Experimental Assessment and Implementation of Photoelastic Tomography

Samantha Giovana Abrego Hernández

Department of Mechanical engineering

University of Sheffield

This dissertation is submitted for the degree of

Doctor of Philosophy

October 2018

I would like to dedicate this thesis to my beloved parents Enrique and Melly for their unconditional love and support during all my life. You are always there in my moments of doubt and frustration with the correct words to make me feel better and encourage me to carry on. . . .

Declaration

I hereby declare that except where specific reference is made to the work of others, the contents of this dissertation are original and have not been submitted in whole or in part for consideration for any other degree or qualification in this, or any other university. This dissertation, entitled "Experimental Assessment and Implementation of Photoelastic Tomography", is my own work and contains nothing which is the outcome of work done in collaboration with others, except as specified in the text and acknowledgements.

Samantha Giovana Abrego Hernández
October 2018

Acknowledgements

My sincerest gratitude to my supervisor, Dr. Rachel Tomlinson, for her continuous guidance, encouragement, advice and proof-reading.

I am deeply grateful to the Mechanical Engineering department, LEA lab and the workshop especially to Richard Kay, David Webster and Kieren Howarth for being always supportive and kind when I asked for help with my experiments.

I would also like to thank Dr. Michael Croucher, Dr. Tania Allard from the Computer Science department, Dr. Chris Holland, Dr. Joel Foreman, Dr. Richard Hodgkinson, Professor Russell Hand and Dr. Lisa Holland from the Department of Materials Science and Engineering, also to Dr. Naeem Desai and Professor Bill Lionheart from the School of Mathematics in the University of Manchester and MSc. Martín Ortiz from the Centro de Investigaciones en Optica A.C. Unidad Aguascalientes, México.

I would like to offer my special thanks to Susana Chávez, Elenja Vogel, Li Tang, Ramón Fuentes, Gabriel Kapellmann, Edgar Covantes, Jose Daniel Muñoz, Julian García, Juan Francisco Mujíca Alarcón, Pablo Ordoñez, Paulina Díaz, Gabriela Villarreal, Alejandra Peñuelas, Niloufar Motazedi, Sarah Falconer, Monyka Szczyrba, Zainab Al Tai which are the people that I have met in Sheffield that have become friends and even my family during this long journey. To my best friends in México willing to make a call whenever I need it to keep myself sane María Carrillo, Eduardo Vilchez, Jessica Villalón, Jahaira Saldivar, Samuel Noguera, Ulises Suárez, Aarón Villarreal, Angel Salazar González.

To all my family but especially my father José Enrique Abrego Mora, my mother Melly Hernández, my brother Sergio Abrego, my cousin Damaris Abrego and my uncle Juan Abrego, I would not make it without your love, care and support.

And finally to the Science and Technology Council of México, (Consejo Nacional de Ciencia y Tecnologia, CONACYT) to believe and sponsor me during this PhD.

Abstract

3-D photoelasticity is a destructive and time-consuming experimental stress analysis technique that assesses internal stress by the construction of a stress frozen polymeric prototype that is sliced and analysed section by section by 2-D photoelasticity. Non-destructive 3-D internal stress reconstruction, such as Photoelastic Tomography has been the main subject of this research. Photoelastic Tomography can be taken as an optical tomography. However, it is not possible to apply directly the equations used in conventional tomography since the mathematical approach of the Radon equation is just for scalar fields but Photoelastic Tomography intends to obtain a tensor stress field. The directions and values of the principal stresses vary through the thickness of the material which makes it difficult to process and to relate the measured data with the non-linear stress distribution. Szotten, in his thesis "Limited data problems in X-Ray and polarised light tomography", proposes a mathematical method for the solution of the stress tensor using Photoelastic Tomography. Numerical results presented in his thesis showed evidence that this mathematical approach could be used to reconstruct the internal stress. This research aims to experimentally assess the mathematics and the tensor stress reconstruction algorithms developed by Szotten to obtain quantitative measurements of the 3-D internal stress in birefringent materials. The research began with a critical audit of an existing rig used in previous preliminary research of Szotten's method. As a result of this audit, essential and considerable improvements were made to the photoelastic tomography apparatus, methodology and software. The assumptions of the mathematical approach require no refraction of the light passing through the specimen, so key developments were made in the refractive index matching procedure within a tolerance of 0.001-2. Szotten's method also requires rotations of the specimen about three different axes. In previous work, this repositioning of the sample was initially carried out manually. In this work, an automated repositioning system and associated control programs were designed, manufactured and commissioned, avoiding contamination of the matching fluid which may introduce noise into the results. The introduction of a new camera to improve the signal to noise ratio in the characteristic parameters was validated by a comparison between Fourier Polarimetry and phase stepping methods. Furthermore, the post-processing of the acquired images was also improved by the development of algorithms that automatically detects the edges of the specimen to cut the unnecessary background information not related to the sample to save computational time. Experimental results in this research showed noise, patterns that did not follow a trend associated with the internal stress and no evidence of the relationship between the signal to noise ratio and the experimental variables tested. The conclusion drawn

from this is that Szotten's mathematical model does not agree with experimentation, and the reconstruction algorithms of the Photoelastic Tomography method need further theoretical developments before they can be used in practice.

Contents

List of Figures

List of Tables

Chapter 1

Introduction

The dynamic environment to which industrial manufacturers belong presents challenges, such as a constant development in technology, globalisation, economic growth, and competitiveness. To excel in this competitive industrial environment processes and products must meet the quality standards defined by the customers. Therefore; the design of processes and components that allow quality control of the produced parts is essential. One method that helps in preventing failure of the products is stress analysis [1].

In order to understand stress analysis, it is essential to define stress. When a body is subjected to a load, its particles exert forces between each other. The quantification of these internal loads in the material is known as stress [2]. After the original load is removed from the body, some of the internal forces of the body remain within it, creating what is known as residual or locked-in stresses. These stresses can be desired or undesired. The most common causes for the residual stresses are the manufacturing processes to which a material is exposed [3]. Hence, to achieve the quality standards for a part, constant control of its locked-in stresses is necessary. The way to monitor the internal stresses is by measuring the magnitude, direction and distribution. These measurements can be performed with techniques such as X-ray diffraction, neutron diffraction [4] and 3-D photoelasticity [5].

3-D photoelasticity is one of the branches of photoelasticity, which is a well-known 2-D experimental stress analysis technique. It is based on the study of the light polarisation when a light ray is passed through a birefringent material under load. A birefringent material is defined as a transparent material that exhibits temporary double refraction or optically anisotropic behaviour when it has been exposed to stress. The polarised light passes through the stressed material and the light splits into two components. These components are orientated according to the direction of the principal stresses and have different velocities due to the change of the refractive indices. The changes in the refractive index of the material can be related to the stress through the stress-optic law, once they leave the stressed material [6].

Each ray beam will have relative retardation which results in the formation of interference fringes. 3-D photoelasticity is used to measure the internal stresses in a birefringent material. To perform a 3-D photoelasticity measurement the creation of a prototype constructed in a polymeric material is required. The prototype is then subjected to a "stress freezing" treatment to lock-in the stresses [7]. Finally, the prototype is sectioned to conduct the 2D photoelasticity analysis. However, even though 3-D photoelasticity analyses the internal stresses, the procedure is time-consuming, expensive, and destroys the specimen. Therefore alternative non-destructive techniques were sought.

Integrated Photoelasticity is a technique that allows internal stress analysis without destroying the specimen [8, 9] and promising results on the internal stress reconstruction for the cases where weak birefringence and axisymmetric conditions have been presented [10–12]. However, variations of the directions and values of principal stresses throughout the thickness of the material make the data processing difficult, hence relating the data measured with the non-linear stress distribution becomes a problem. An optical equivalence was proposed in order to resolve this problem, where three characteristic parameters (axis of the retarder θ_r, the retardation of the retarder 2Δ and the rotatory power of the rotator γ) [13–15] are obtained and analyzed with a digital photoelasticity method, either phase stepping [16, 17] or Fourier polarimetry analysis [18, 19].

The parameters measured in the Integrated Photoelasticity technique are the isoclinic angle and the integral retardation when the polarised light passes through the specimen. It can be considered to be a form of optical tomography; since it measures the line integral of the field studied, therefore it has a similarity with Computed Tomography (CT). Computerized Tomography enables the internal reconstruction of objects. The mathematical approach in which CT is based is the Radon transform [20]. So far it has not been possible to directly apply the equations used in conventional tomography since the mathematical approach of the Radon equations is just for scalar fields, but Integrated Photoelasticity intends to obtain a tensor stress field. Therefore, a mathematical approach using the calculated characteristic parameters to build a reconstruction matrix was proposed by Szotten [21]. The numerical simulations performed by Szotten showed that, in principle, successful experimental implementation could be possible; however, he concentrated his research in theoretical development. Experimental work was carried out years later by students of the University of Manchester using the mathematical approach developed by Szotten. Nevertheless, noisy results were obtained. Drawbacks such as noise in the light system and poor refractive index matching were suspected to be the reasons for these noisy results. Therefore, further investigation and improved experimentation have to be performed to achieve accurate full field internal stress reconstructions.

1.1 Research aim

This research aims to experimentally assess the mathematics and the tensor stress reconstruction algorithms developed in the research “Limited data problems in X-Ray and polarised light tomography” to obtain quantitative measurements of the 3-D internal stress in birefringent materials with a non-destructive technique called Photoelastic Tomography.

1.2 Objectives of research

This research is based on the mathematical approaches and simulated data developed by Szotten that confirmed the possibility of using this technique to obtain the 3D internal stress in a non-destructive way. Previous research has attempted to assess this technique experimentally; however noisy results were obtained. Therefore the objective of this research is to experimentally assess and discard or control the variables that could be affecting the results. The proposed development and application in this research are described as follows:

1. To understand and perform a critical audit of the experimental rig and the stress reconstruction methodology.
2. To perform experimental improvements of the refractive index matching.
3. To implement an automatic repositioning system to avoid manual handling.
4. To develop algorithms that can save computational time and resources when processing the data.
5. To assess the photoelastic characteristic parameters results that are used to perform the internal stress reconstruction.

1.3 Outlines of thesis

This thesis is presented as follows:
Chapter 2 provides background information about Photoelasticity, Integrated Photoelasticity, theories of light, light behaviour, Fourier polarimetry, characteristic parameters and tomography.
Chapter 3 presents a critical audit of the original rig used in previous research to perform the Photoelastic Tomography study.It also provides a detailed explanation of the stages followed and the algorithms used to perform a Photoelastic Tomographic reconstruction.

Chapter 4 introduces the experimental results for the stress reconstruction under different conditions.
Chapter 5 describes the improvements made in the Photoelastic Tomography rig and processes.
Chapter 6 presents the assessment and comparison of the photoelastic characteristic retardation parameters with another optical technique developed by Patterson and Wang using phase stepping instead of Fourier polarimetry [22, 23]. Also, a comparison of these results using a new camera to acquire the light intensity images are displayed. Finally, this chapter provides the Photoelastic Tomography reconstructions with the implemented improvements and automation described in chapter 5.
Chapter 7 concludes the thesis and analyses the results presented in the previous chapters; also it gives a summary of future work within this research topic.

Chapter 2

Literature review

2.1 Introduction

This chapter presents a review of the literature described by previous research [21, 24] regarding non-destructive experimental stress analysis methods. Sections 2.2 and 2.3 provide a brief description of the stress and light concepts. Sections 2.4, 2.5 and 2.6 introduce photoelasticity, the stress optic law and 3-D photoelasticity stating the background of destructive experimental stress analysis. Then, section 2.7 provides background for integrated photoelasticity to establish the starting point of the non-destructive experimental stress analysis methods; then the basic concepts of Tomography in order to be able to understand the Photoelastic Tomography background. Finally, in section 2.8 a review of Szotten's work, which is the starting point of this research, is presented.

2.2 Stress

Stress is defined as the measurement of a force acting on an internal or external section of a body, where its magnitude, direction and plane must be defined [25]. The stress can be represented by a stress tensor formulated by the Euler-Cauchy stress principle. This stress tensor, shown in equation 2.1, consists of 9 elements that fully define the stress at any point in the body [26].

$$\sigma = \begin{bmatrix} \sigma_{11} & \sigma_{12} & \sigma_{13} \\ \sigma_{21} & \sigma_{22} & \sigma_{23} \\ \sigma_{31} & \sigma_{32} & \sigma_{33} \end{bmatrix} \tag{2.1}$$

The first subscript of the stress represents the plane where the traction is measured and the second the direction. Both of these elements defining the same point are represented in Figure 2.1 [26]. In normal stress, the first and the second subscript are equal, while in shear stress these subscripts are different. Due to the symmetry of the shear components, the stress tensor matrix can be reduced to six components [27].

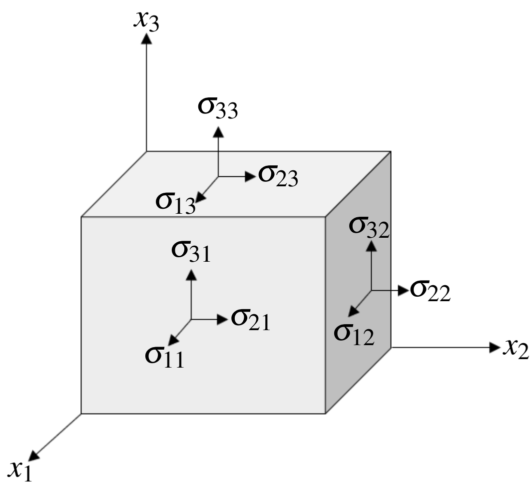

Figure 2.1 Cauchy stress tensor physical representation [27].

The Cauchy stress tensor is composed of the hydrostatic and deviatoric stress tensor [28]. The hydrostatic stress tensor characterises the stress state causing volume change without shear distortion while the remaining stress is the deviatoric stress tensor. The equation 2.2 shows how these stresses are represented mathematically, where the matrix in the middle of the equation corresponds to the deviatoric stress, and the one on the right represents the hydrostatic stress [27].

$$\begin{bmatrix} \sigma_{11} & \sigma_{12} & \sigma_{13} \\ \sigma_{21} & \sigma_{22} & \sigma_{23} \\ \sigma_{31} & \sigma_{32} & \sigma_{33} \end{bmatrix} = \begin{bmatrix} \sigma_{11}-\sigma_{ave} & \sigma_{12} & \sigma_{13} \\ \sigma_{21} & \sigma_{22}-\sigma_{ave} & \sigma_{23} \\ \sigma_{31} & \sigma_{32} & \sigma_{33}-\sigma_{ave} \end{bmatrix} + \begin{bmatrix} \sigma_{11}-\sigma_{ave} & 0 & 0 \\ 0 & \sigma_{22}-\sigma_{ave} & 0 \\ 0 & 0 & \sigma_{33}-\sigma_{ave} \end{bmatrix} \tag{2.2}$$

The deviatoric stress is used within the mathematical operator known as the truncated transverse ray transform (TTRT) used by Szotten [21] to create an algorithm which is able to reconstruct internal stresses. Detailed information relating to the mathematical approach and this research is explained in the section 2.8.

2.3 Light

Several theories about the nature of light have been developed throughout history. One theory developed by Huygens in 1690, proposed light as a wave and its phenomena such as reflection, refraction and diffraction was explained by its wave-fronts. On the other hand, in 1704 Newton stated that light was made of particles that travelled in lines defined as rays [29]. Nevertheless, experiments carried out by Young in 1801 and by Fresnel in 1814-15 left Newton's proposal as an unacceptable theory, mainly because several phenomena, such as diffraction and interference of light, could only be explained by the wave behaviour theory [30]. In 1864 Maxwell developed the electromagnetic theory, which supports the wave theory and explains the light as an electric and magnetic orthogonal vector. Later, this theory was experimentally validated by Hertz in 1886. Nowadays Maxwell's theory is widely accepted; however, it has certain gaps, for example, it does not explain what light is, it just explains its behaviour, and estimates infinite energy in a small wavelength. Some of these shortcomings presented by the electromagnetic theory are overcome by the quantum model proposed by Planck in 1900, which generally describes the conformation of light by bundles of photons [31]. To understand light, it is needed to explore the wave equations starting from the simple harmonic wave movement described by the equation 2.3.

$$y_1 = Asin\frac{2\pi}{\lambda}(x - ct) \tag{2.3}$$

where A is the amplitude, λ is the wavelength, x is the propagation plane, c is the velocity of light which is dependent on the medium and t is the time. If two waves are in the same propagation plane, as the Figure 2.2 shows, with the same wavelength but with a linear phase difference, δ, the second wave with this linear phase difference is represented by the equation 2.4 [29].

$$y_2 = Asin\frac{2\pi}{\lambda}(x + \delta - ct) \tag{2.4}$$

The linear phase difference, caused by the specimen exposed to stress, when expressed in terms of the light wavelength is known as the relative linear phase difference, R, as shown in equation 2.5.

$$R = \frac{\delta}{\lambda} \tag{2.5}$$

where the relative linear phase difference, δ, can be expressed in terms of indices of refraction n_1, n_2 and the distance (or thickness), d, leaving the relative linear phase difference

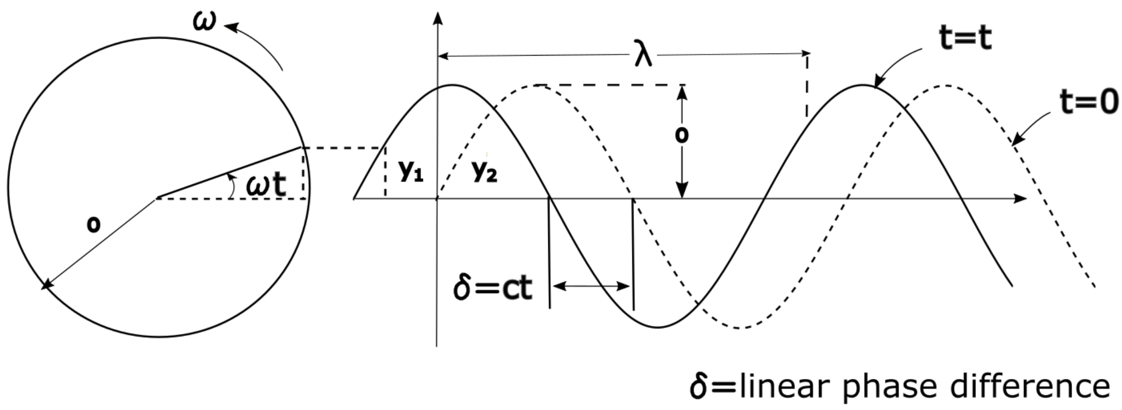

Figure 2.2 Two simple harmonic waves with linear phase difference.

expressed as the equation 2.6 [29].

$$R = \frac{d}{\lambda}(n_1 - n_2) \tag{2.6}$$

Equation 2.6 is also called relative retardation when is expressed in terms of the angular phase difference, α, as shown in equation 2.7

$$R = \frac{\alpha}{2\pi} = \frac{\delta}{\lambda} \tag{2.7}$$

where α is:

$$\alpha = \frac{2\pi d}{\lambda}(n_1 - n_2) \tag{2.8}$$

2.3.1 Interference of plane waves

The light waves can travel in the same propagation plane, meaning they can interfere at some point with one another. If this happens it is necessary to represent this resultant wave as the sum of both waves equations 2.3, 2.4 giving as a result the equation 2.9 where A is the amplitude of the wave.

$$E_s = 2Acos\frac{\pi\delta}{\lambda}cos[\frac{2\pi}{\lambda}(x - ct - \frac{\delta}{2})] \tag{2.9}$$

The key point in interferometry methods is to measure the light phase differences, however the human eyes and other equipment are not able to distinguish this change. They are only able to recognize the intensity, or in other terms, the irradiance. The irradiance can be obtained by the amplitude squared, as it can be seen in equation 2.10 [32].

$$I_s = 4A^2 cos\frac{\pi\delta}{\lambda} \tag{2.10}$$

The kind of interference that is possible to observe (constructive or destructive) depends on the irradiance type (maximum or minimum) and those variations creates observable fringes.

2.4 Photoelasticity

Photoelasticity is an experimental stress analysis technique based on classic interferometric measurements of light. It is used to visualise and quantify stress distributions as patterns which arise from optical anisotropy of the material under stress, through which light is transmitted [32]. The principle of photoelasticity is based on the phenomenon of temporary double refraction or optical birefringent behaviour. A birefringent material, observed for the first time by David Brewster in 1816 [33], is described as a transparent material that exhibits temporary double refraction or optically anisotropic behaviour when it is under stress [34]. This behaviour consists of the light split into two perpendicular beams when passing through a transparent material that is stressed as illustrated in Figure 2.3. These beams take the direction of the principal planes which are termed the fast and slow planes. Each light beam exhibits its own refractive index, (n_1,n_2), and light beam velocity propagation [32]. When the beams come out from the specimen they enter into the analyser which integrates them again as illustrated in Figure 2.4 [29, 34–36].

2.4.1 Polariscopes

When the light does not present an ordered travelling plane direction as shown in Figure 2.5 it is classified as unpolarized light [37].

A polariscope is an instrument that polarises the light in a well-defined plane and allows the observer to see the birefringence of the materials through fringe patterns [37]. It is composed of a light source (laser, white or monochromatic), a polariser and an analyser [38], which helps to define the plane of polarisation. The most common types of this apparatus are the plane polariscope and the circular polariscope. A circular polariscope beside the components described before is composed by two quarter wave plates which introduce a phase shift δ equal to $\frac{\lambda}{4}$, where λ is the wavelength of the light source. The parameters observed with this apparatus are termed as the isoclinic and the isochromatic fringes.

The isochromatics represent contours of principal stress difference, Figure 2.6 a), and the

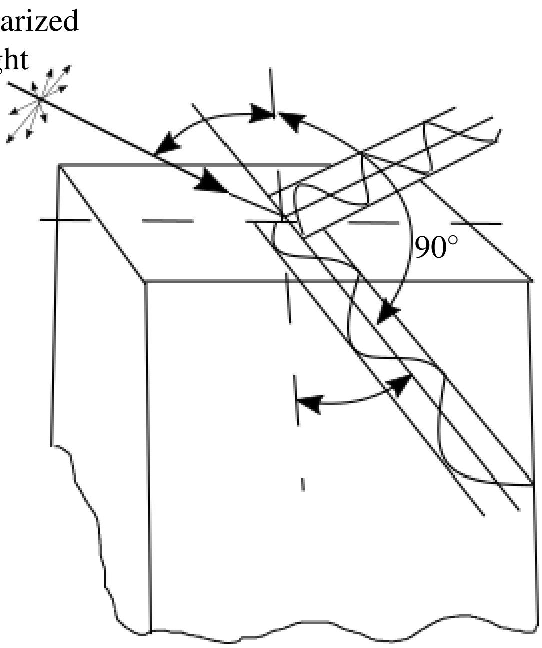

Figure 2.3 Unpolarized light beam split in a stressed birefringent material.

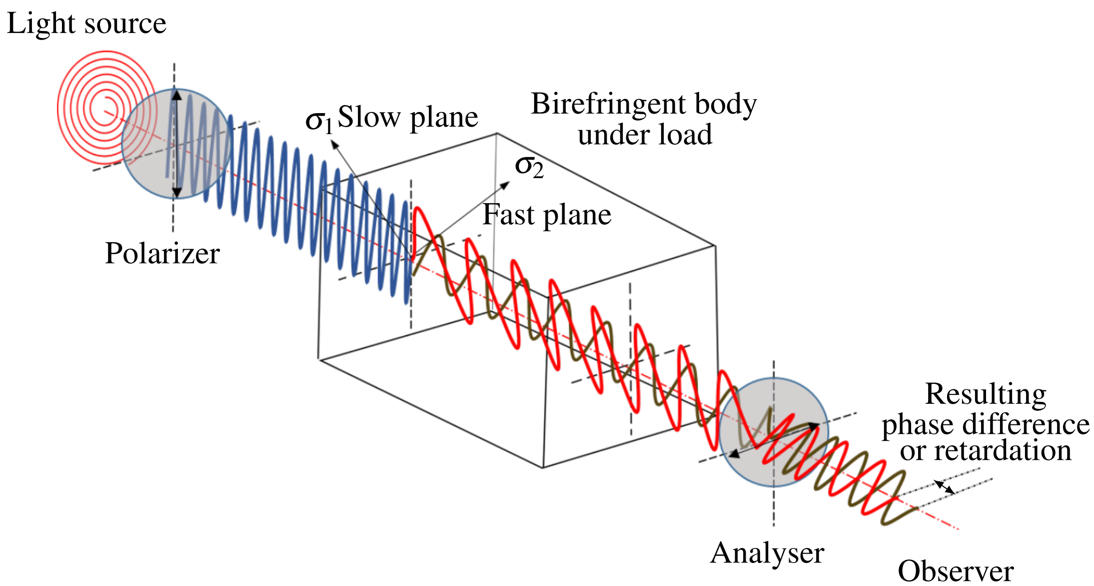

Figure 2.4 Plane polarized polariscope.

isoclinics represents the contours of principal stress direction with respect to the polariser axis, Figure 2.6 b) [39].

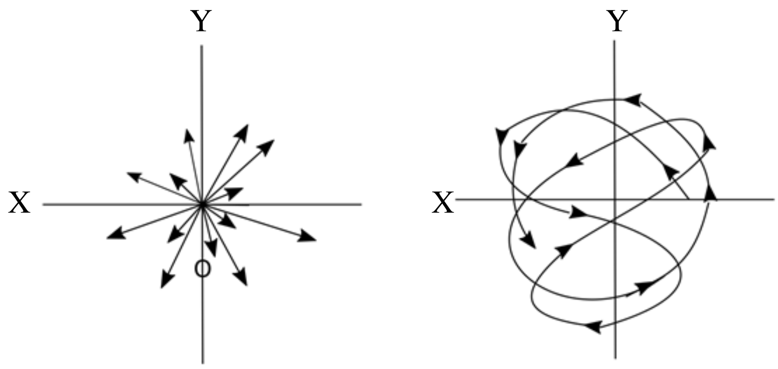

Figure 2.5 Unpolarized light

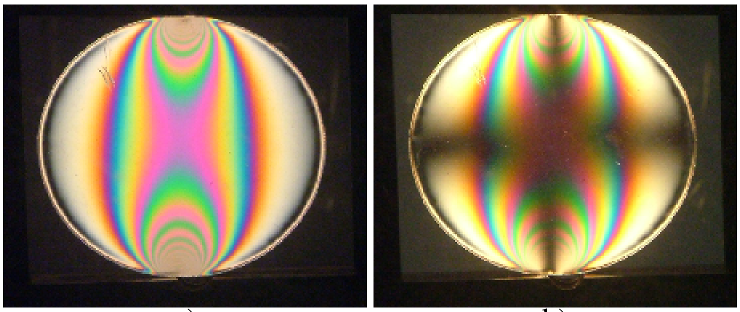

a) b)

Figure 2.6 a) Isochromatic fringes and b) Isoclinic fringes [39].

2.5 Stress-optic law

The isoclinics can be easily separated from the isochromatics if white light is used as the light source. This is because the isoclinics and the zero order fringes are exhibited as black fringes, while the isochromatic fringes are coloured. Also, the isochromatic zero order fringes can be differentiated from the isoclinic fringes because they do not move when the polariser or analyser changes its angle. Nevertheless, when monochromatic light is used as a light source, it is not possible to separate them, due to both of the fringes appearing as dark patterns. In this condition, the circular polariscope helps to separate them with the quarter wave plates, where mainly this quarter wave plates acts as an isoclinic fringes filter.
The formulation of the Maxwell-Neumann stress-optic law in 1853, as shown in equations 2.11, 2.12 and 2.13 [40], established the relationship between the principal values of refractive index and the principal stresses. These absolute changes in the refractive indexes are used to measure the stress.

$$n_1 - n_0 = C_1\sigma_1 - C_2(\sigma_2 + \sigma_3) \tag{2.11}$$

$$n_2 - n_0 = C_1\sigma_2 - C_2(\sigma_3 + \sigma_1) \tag{2.12}$$

$$n_3 - n_0 = C_1\sigma_1 - C_2(\sigma_1 + \sigma_2) \tag{2.13}$$

Where σ_1, σ_2 and σ_3 are the principal stresses at a point, n_0 is index of refraction of material unstressed, n_1, n_2, n_3 are the principal indices of refraction which coincide with principal stress directions and C_1, C_2 are the stress optic coefficients.
For practical purposes in three dimensional measurements, these equations are applied just for the cases where the stresses are in plane, meaning that $\sigma_3 = 0$.
Therefore the previous equations are simplified as shown in equations 2.14 and 2.15

$$n_1 - n_0 = C_1\sigma_1 + C_2\sigma_2 \tag{2.14}$$

$$n_2 - n_0 = C_1\sigma_2 + C_2\sigma_1 \tag{2.15}$$

Photoelasticity uses the stress-optic law expressed in terms of the relative retardation, instead of absolute retardation therefore n_0 is eliminated from the previous equations as shown in equations 2.16, 2.17 and 2.18.

$$n_2 - n_1 = (C_1 + C_2)(\sigma_1 - \sigma_2) = C(\sigma_1 - \sigma_2) \tag{2.16}$$

$$n_3 - n_2 = (C_1 + C_2)(\sigma_2 - \sigma_3) = C(\sigma_2 - \sigma_3) \tag{2.17}$$

$$n_1 - n_3 = (C_1 + C_2)(\sigma_3 - \sigma_1) = C(\sigma_3 - \sigma_1) \tag{2.18}$$

where C = $(C_1 + C_2)$, is the relative stress-optic coefficient expressed in Brewsters which equals to 1 brewster= 10^{-12} Pa^{-1}. From equations 2.6 and 2.22 the relative retardation is related with the stress-optic law as shown in equation 2.19

$$R = \frac{d}{\lambda}(n_2 - n_1) = \frac{(C_1 + C_2)d}{\lambda}(\sigma_1 - \sigma_2) \tag{2.19}$$

The equation 2.19 can be expressed in terms of the photoelastic constants or fringe order N as shown in equation 2.20.

$$N = \frac{(C)d}{\lambda}(\sigma_1 - \sigma_2) = 2\frac{(C)d}{\lambda}\tau_{max} \tag{2.20}$$

were τ_{max} is the secondary maximum shear stress an is equal to 2.21.

$$\tau_{max} = \frac{N\lambda}{2Cd} = NF \tag{2.21}$$

where F is the stress fringe value or the model fringe value. This value is defined as the difference needed in order to create a new order of fringe and its units are MPa/fringe [29]. The stress fringe value can be expressed in the function of the material stress fringe value, defined as the same as the stress fringe value with the difference on the measurement in a unit thickness, whose units are MPa-mm/fringe [29].

$$Fd = \frac{\lambda}{2C} = f \tag{2.22}$$

2.5.1 Numerical methods and photoelasticity

Numerical methods, such as Finite Element Methods (FEA) are used to solve complex stress analysis problems. The first FEA paper was published in 1956 by Turner, M. J., Clough, R. W., Martin H. C. and Topp, L. J [41]. Nevertheless; it was not until the '70s-'80s with the advent of computer development that software such as NASTRAN, Abaqus and Ansys were created to perform FEA [42–44]. FEA offers the possibility of predicting the reaction of an object to physical effects, e.g. external forces, heat, vibration. To make an FEA simulation, a mesh made of small elements that forms the shape of the analysed object needs to be created. Then, the mathematical calculations on each of these elements are made. Finally, the results of all the mesh are combined to get the final result or approximations depending if the element or node is a boundary element. Different approximations, such as linear, quadratic and cubic are used [45]. There are some cases where numerical methods are not suitable to apply in stress analysis such as in parts assemblies, e.g. bolting, residual stress from manufacturing processes, e.g. welding and casting; stresses caused by complex working forces which make difficult to define the loading and boundary conditions; and stresses resulting from geometric imperfections [46]. Therefore, photoelasticity is used as an experimental technique that complements, verifies and validates the FEA results. Within the advantages of photoelasticity it can be found that [47]:

- It is an economic method to obtain a reliable quantitative solution for the stress measurement.
- It is applicable to all types of contact stress problems.
- It can obtain a general picture of the stress distribution, instead of a point by point output in comparison with other techniques such as the mechanical, electrical and optical strain gauges.
- It can be used for a broad range of contact stress problems.

- No size limitation, since the specimens can be scaled according to the requirements.
- Boundary and high stress concentration are easily obtained.
- Applications in several fields e.g. engineering, medicine and biology.
- Thermal and impact dynamic studies can be analysed under this technique.

2.6 3D Photoelasticity

In Photoelasticity or 2-D Photoelasticity it is assumed a plane stress condition and therefore the stresses and orientation through the material thickness does not change, however in a 3-D internal analysis they vary. The process to accomplish a 3-D internal stress analysis starts with a load application. A careful selection of loads on the specimen must be done, since a large load can distort it and a low load can give a poor optical effect. This loading procedure is accompanied by a thermal cycling process which is well known as stress freezing [48, 5]. This stress freezing is used due to the di-phase property that polymers exhibit. Polymers have two type of bonds,the primary and secondary. When the temperature reaches the critical temperature (T_g= glass transition temperature) of the material [49], the secondary bonds break, leaving the load acting only on the primary bonds leading to a deformation in the material. Then when the temperature decreases the secondary bonds reform locking the deformation in the primary bonds.
After the loading and stress-freezing, the model should be sliced into thin layers so it can be analysed as a 2D specimen. This step must be conducted in a way that no machining stresses are involved. It can be accomplished by using single point cutting tools and coolants [48]. Even though this technique offers the 3-D internal stress analysis it can be concluded that is time consuming and destructive, therefore alternative to this technique have been developed.

2.7 Integrated photoelasticity

As previously stated, 3D photoelasticity is used to obtain the internal stress distribution in a model, however this technique is described as costly, time-consuming and destructive, because the model needs to be sliced to perform its analysis upon it. Integrated photoelasticity could provide a method that allows the performance of a 3D analysis without the necessity of destroying the specimen. This technique consists of a light beam that passes through all the directions and orientations of the specimen in order to reconstruct the internal stress tensor [50]. The basic elements of this method are: the transmission polariscope, a bath which is filled with a fluid that must match the refractive index of the analysed material, and a beam of polarised light conducted through the bath and the specimen. If the specimen is not axisymmetric, it needs to be rotated in several angles for it to be analysed. A schematic drawing is shown in the Figure 2.7 [51][24].

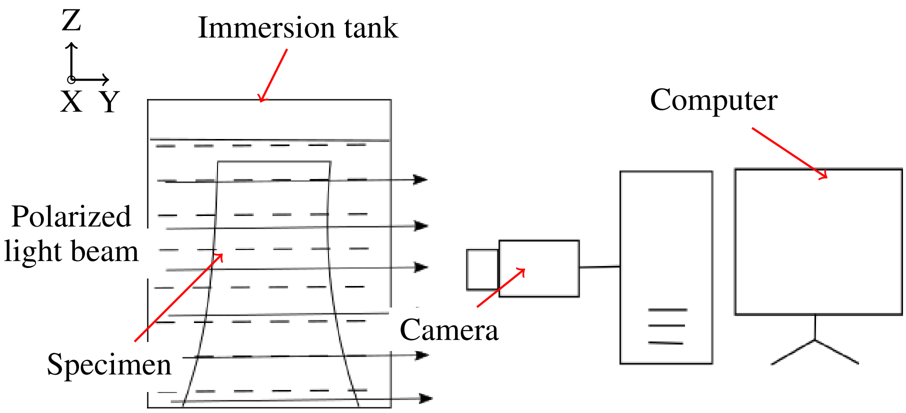

Figure 2.7 Experimental setup in integrated photoelasticity

However this technique does not reconstruct the stress tensor for all cases. This method can be useful under two particular conditions, in a weakly birefringence material or a constant principal stress axes [24] .

Also, the measurements of each ray to find the stress through the calculation of the variables called characteristic parameters are needed [52]. Detailed information about these characteristic parameters will be presented in section 2.7.1. Integrated photoelasticity is considered as a form of optical tomography since it obtains the stresses in slices. However tomography is based on an equation that just solves scalar fields. When talking about stress measurements,tensor stress fields are expected as a result [8]. Hammer and Lionheart [53] proposed a mathematical method called “Tomographic photoelasticity” for weakly birefringent materials, where the 2-D Inverse Radon equations are used in order to obtain the dielectric tensor. The input information to solve these 2-D Inverse Radon equations are the characteristic parameters described in section 2.7.1.

2.7.1 Characteristics parameters

In previous sections it has been stated how difficult it is to analyse the stresses in a 3-D photoelastic model. The fact that the orientation and the magnitude of the stresses are changing within the material represents a challenge. In general, a concept defined as optical equivalence was created to solve this. This optical equivalence creates another system with

discrete elements, that represent the changing model. These elements are the axis of the retarder θ_r, the retardation of the retarder 2δ and the rotatory power of the rotator γ, known as the characteristic parameters [54].
The characteristic parameters have a physical meaning. The emerging light from the analysed material gets linearly polarised in two positions of the polariser. These two positions are termed as the primary and secondary characteristic retardation. An illustration of them is presented in Figure 2.8 [55].

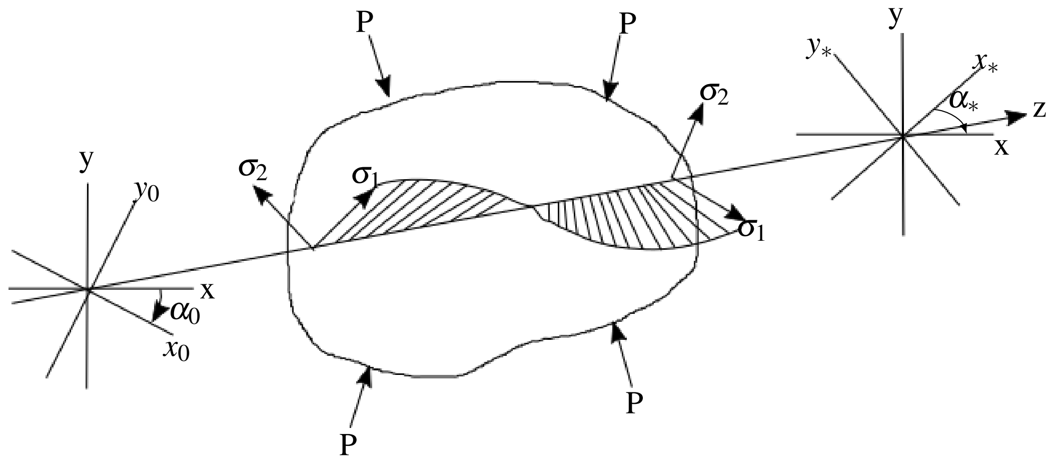

Figure 2.8 Illustration of the rotation of the principal stress axes; primary x_0 ,y_0,a_0 and secondary x_* ,y_*,a_* characteristic directions.

2.7.2 Obtaining the characteristic parameters through Fourier polarimetry

The Fourier polarimetry method allows the determination of the characteristic parameters. The equation that defines the light intensity for Fourier polarimetry is presented in equation 2.23 [56].

$$i(\omega) = \int_{-\infty}^{\infty} i(\beta)e^{-j\omega\beta}d\beta \tag{2.23}$$

where i(β) is:

$$i(\beta) = \sum_{n=-\infty}^{\infty} i_n e^{-jn\omega\beta} \tag{2.24}$$

and i_n is equal to:

$$i_n = \frac{1}{T}\int_{\frac{-T}{2}}^{\frac{T}{2}} i(\beta)e^{-j\omega_0\beta}d\beta \tag{2.25}$$

The analyser angle (β) gives the intensity variations through Fourier transform, while the isoclinic angle is obtained from the ratio of the real and imaginary parts of the Fourier transform. The light vector is obtained by the Jones calculus matrix, equation 2.26 [18]

$$\begin{bmatrix} E_\beta \\ E_{\beta+\frac{\pi}{2}} \end{bmatrix} = \begin{bmatrix} \cos\beta & \sin\beta \\ -\sin\beta & \cos\beta \end{bmatrix} \times \begin{bmatrix} \cos\delta\cos\gamma - isin\delta\cos(2\theta_r+\gamma) & -\cos\delta\sin\gamma - i\sin\delta\sin(2\theta_r+\gamma) \\ \cos\delta\sin\gamma - i\sin\delta\sin(2\theta_r+\gamma) & \cos\delta\cos\gamma + i\sin\delta\cos(2\theta_r+\gamma) \end{bmatrix} \times \begin{bmatrix} cos\alpha \\ \sin\alpha \end{bmatrix} ke^{i\omega t} \tag{2.26}$$

where E_β and $E_{\beta+\frac{\pi}{2}}$ are components of the electric vector, α is the angular polarizer position, β is the angular position of the analyser, k$e^{i\omega t}$ is the incident light vector, δ is a linear retarder or the characteristic retardation, θ_r is the primary characteristic direction and γ is a rotator represented by the characteristic angle. Then the intensity output though the polariscope is represented by equation 2.27.

$$I_{out} = I_b + \frac{I_{in}}{2} \begin{bmatrix} 1+\cos^2\delta\cos2\gamma\cos2(n-1)a \\ +\cos^2\delta\sin2\gamma\sin2(n-1)a \\ +\sin^2\delta\cos(4\theta_r+2\gamma)\cos2(n+1)a \\ +\sin^2\delta\sin(4\theta_r+2\gamma)\sin2(n+1)a \end{bmatrix} \tag{2.27}$$

where I_{out} is the output periodic intensity, I_b is the background intensity and I_{in} is the intensity of incident light. The next step is to define the magnitudes of the spectrum in order to get the three characteristic parameters as seen in equation 2.28.

$$F(I_{out}) = I_b\delta(\omega_f) + \frac{I_in}{2} \begin{bmatrix} \delta(\omega_f) + A_{2(n-1)}\delta[\omega_f - 2(n-1)] + \delta[\omega_f - 2(n-1)] \\ -iB_{2(n-1)}\delta[\omega_f - 2(n-1)] - \delta[\omega_f - 2(n-1)] \\ +A_{2(n+1)}\delta[\omega_f - 2(n+1)] + \delta[\omega_f - 2(n+1)] \\ -iB_{2(n+1)}\delta[\omega_f - 2(n+1)] - \delta[\omega_f - 2(n+1)] \end{bmatrix} \tag{2.28}$$

where

$$A_{2(n-1)} = \frac{1}{2}\cos^2\Delta\cos2\gamma \tag{2.29}$$

$$B_{2(n-1)} = \frac{1}{2}\cos^2\Delta\sin2\gamma \tag{2.30}$$

$$A_{2(n+1)} = \frac{1}{2}\sin^2\Delta\cos(4\theta_r + 2\gamma) \tag{2.31}$$

$$B_{2(n+1)} = \frac{1}{2}\sin^2\Delta\sin(4\theta_r + 2\gamma) \tag{2.32}$$

Finally,the characteristic parameters are obtained by the equations 2.33, 2.34, and 2.35.

$$\gamma = \frac{1}{2}\arctan[\frac{B_{(2(n-1))}}{A_{(2(n-1))}}] \tag{2.33}$$

$$\theta_r = \frac{1}{4}\arctan[\frac{B_{(2(n+1))}}{A_{(2(n+1))}}] - \frac{\gamma}{2} \tag{2.34}$$

$$2\Delta = 2\arctan[\frac{A^2_{(2(n+1)} + B^2_{(2(n+1)}}{A^2_{(2(n-1)} + B^2_{(2(n-1)}}]^{\frac{1}{4}} \tag{2.35}$$

There are similar methods to Fourier such as Phase stepping, which uses the assumption of a constant wavelength.The light intensity output is defined by the equation 2.36.

$$I = \frac{A^2}{2}\begin{bmatrix} 1 + \sin2(\beta-\phi)\cos\alpha \\ -\sin2(\theta-\phi)\cos2(\beta-\phi)\sin\alpha] \end{bmatrix} \tag{2.36}$$

where β and ϕ are the output positions of the optical elements (analyzer and quarter wave plate), A represents the amplitude, α the relative retardation and θ the isoclinic angle [56].

2.7.3 Obtaining the characteristic parameters with phase stepping

The main differences between phase stepping and Fourier polarimetry are the accuracy that Fourier polarimetry can reach and the need of quarter wave plates in phase stepping. However, Fourier polarimetry is not the best method in matters of efficiency due to the number of images required [18]. In order to obtain the characteristic parameters through phase stepping the light output, equation 2.37, needs to be solved by defining vectors and Mueller matrices for each components of the polariscope [57].

$$S_{out} = P_\beta Q_\phi R_\chi M_\theta(\delta) Q_p P_o S \tag{2.37}$$

Starting from the light source which is represented by a vector called the Stokes vector in the equation 2.38.

$$S = \begin{bmatrix} 1 \\ 0 \\ 0 \\ 0 \end{bmatrix} \tag{2.38}$$

Then the analyzer matrix, is represented by the equation 2.39.

$$P_\beta = \frac{1}{2} \begin{bmatrix} 1 & \cos 2\beta & \sin 2\beta & 0 \\ \cos 2\beta & \cos^2 2\beta & \cos 2\beta \sin 2\beta & 0 \\ \sin 2\beta & \cos 2\beta \sin 2\beta & \sin^2 2\beta & 0 \\ 0 & 0 & 0 & 0 \end{bmatrix} \tag{2.39}$$

The quarter wave plate matrix is defined as the equation 2.40

$$Q_\phi = \begin{bmatrix} 1 & 0 & 0 & 0 \\ 0 & \cos^2\phi & \cos 2\phi \sin 2\phi & -\sin 2\phi \\ 0 & cos 2\phi \sin 2\phi & \sin^2 2\phi & \cos 2\phi \\ 0 & \sin 2\phi & -\cos 2\phi & 0 \end{bmatrix} \tag{2.40}$$

The specimen or the retarder matrix is represented by the equation 2.41.

$$M_\theta \delta = \begin{bmatrix} 1 & 0 & 0 & 0 \\ 0 & \cos^2\theta + \sin^2 2\theta \cos\delta & (1-\cos\delta)\sin 2\theta \cos\theta & -\sin 2\theta \sin\delta \\ 0 & (1-\cos\delta)\sin 2\theta \cos\theta & \cos^2\theta + \sin^2 2\theta cos\delta & \cos 2\theta \sin\delta \\ 0 & \sin 2\theta \sin\delta & -\cos 2\theta \sin\delta & \cos\delta \end{bmatrix} \tag{2.41}$$

The rotator matrix is represented by the equation 2.42, where χ is the rotator angle.

$$R_\chi = \frac{1}{2} \begin{bmatrix} 1 & 0 & 0 & 0 \\ 0 & cos 2\chi & -\sin 2\chi & 0 \\ 0 & \sin 2\chi & \cos 2\chi & 0 \\ 0 & 0 & 0 & 1 \end{bmatrix} \tag{2.42}$$

In order to obtain the six phase steps the positions of the quarter wave plates and the analyser must be defined as the Table 2.1 shows. The system is represented in the Figure 2.9. Then the six phase stepped images can be solved through the next equations 2.43, 2.44, 2.45, 2.46, 2.47 and 2.48.

$$i_1 = \frac{A^2}{2}(1 + \sin\delta \cos 2(\theta + \chi)) \tag{2.43}$$

Table 2.1 Orientation of the input and output quarter wave plates (Q_ρ and Q_ϕ) and the analyser (P_β) relative to the polarizer for the six phase-stepped images.

Image number	Q_ρ	Q_ϕ	P_β
i_1	$\frac{\pi}{4}$	$\frac{\pi}{4}$	$\frac{\pi}{4}$
i_2	$\frac{\pi}{4}$	0	0
i_3	$\frac{\pi}{4}$	0	$\frac{\pi}{2}$
i_4	$\frac{\pi}{4}$	0	$\frac{\pi}{2}$
i_5	$\frac{\pi}{2}$	0	$\frac{\pi}{4}$
i_6	$\frac{\pi}{2}$	0	$\frac{\pi}{2}$

$$i_2 = \frac{A^2}{2}(1 - \sin\delta\cos 2(\theta+\chi)) \tag{2.44}$$

$$i_3 = \frac{A^2}{2}(1 + \sin\delta\sin 2(\theta+\chi)) \tag{2.45}$$

$$i_4 = \frac{A^2}{2}(1 + \cos\delta) \tag{2.46}$$

$$i_5 = \frac{A^2}{2}(1 + \sin 2(\theta\sin\delta)) \tag{2.47}$$

$$i_6 = \frac{A^2}{2}(1 - \cos 2\theta cos 2(\theta+\chi) - \sin 2\theta\sin 2(\theta+\chi)cos\delta) \tag{2.48}$$

Finally the characteristics parameters can be obtained from the equations 2.49, 2.50 and 2.51.

$$(\theta+\chi) = \frac{1}{2}tan^{-1}\frac{(i_2 - i_3)}{(i_3 + i_2 - 2i_1)} \tag{2.49}$$

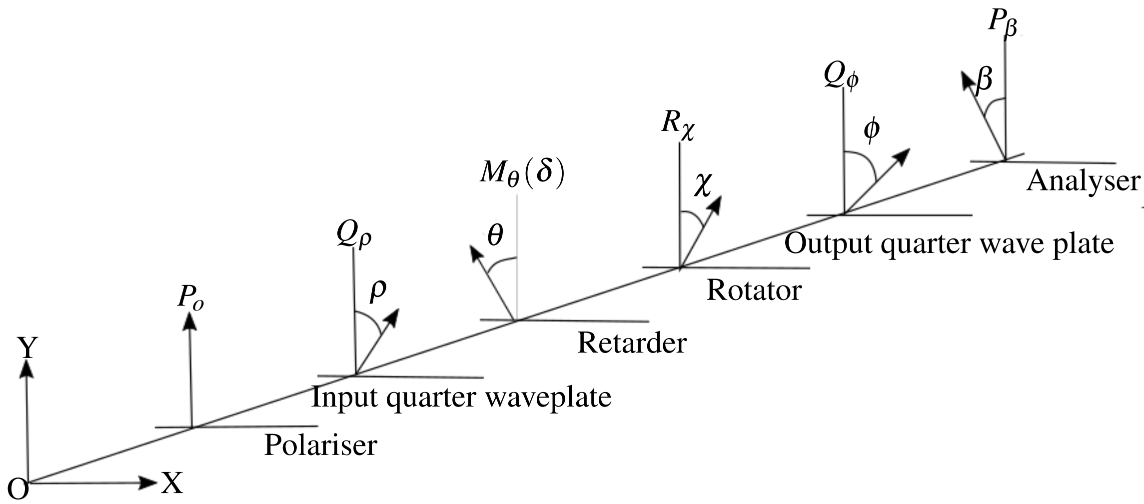

Figure 2.9 Schematic diagram of the polariscope showing the optically equivalent.

$$\delta = tan^{-1}\frac{i_2 - i_3}{\sin 2(\delta+\chi)(i_2+i_3-2i_4)} \tag{2.50}$$

$$\theta = \frac{1}{2}tan^{-1}\frac{\sin 2\theta(\cos 2(\theta+\chi))}{1-\frac{2i_6}{i_2+i_3}-\sin 2(\theta+\chi)\sin 2\theta\cos\delta} \tag{2.51}$$

where $\sin 2\theta$ is equal to:

$$\sin 2\theta = \frac{\frac{2i_5}{i_2-i_3}-1}{\sin\delta} \tag{2.52}$$

After the solution of these characteristic parameters the unwrapping algorithm must be applied in order to obtain the continuous fringe maps.

2.7.4 Computer Tomography

The origin of the word tomography comes from two Greek words: *tomos* which means slice or section and *grapho* which means write [58]. Tomography can be briefly described as the determination of an internal picture of an object where a radiation (x-rays, gamma ray, laser or acoustic) is passed through the object and a characteristic of the radiation (intensity, phase or polarization) is measured. This information is then used to reconstruct the internal picture of the object. Tomography has wide application in different fields such as astrophysics, ocean science, atmospheric science, archeology, geophysics, molecular biology, medical, engineering and nanotechnology [59]. One of the most popular concepts related with tomography is X-ray computed tomography (CT), used mainly in the medical applications, where its mathematical foundation of linear algebra to obtain the projections were proposed by G.N. Hounsfield and A. Cormack in 1979 [60]. Also another mathematical approach of tomography called convolution back projection is used, proposed by G.N.Ramachandran and A. V. Laxminarayanan [61]. The most common mathematical approach of tomography is based on the Radon equations [62], as it can be seen in the equation 2.53 and Figure 2.10.

$$g(l,\theta^*) = \int_{-\infty}^{\infty} f[r(l,\theta^*,z),\theta(l,\theta^*,z)]dz. \tag{2.53}$$

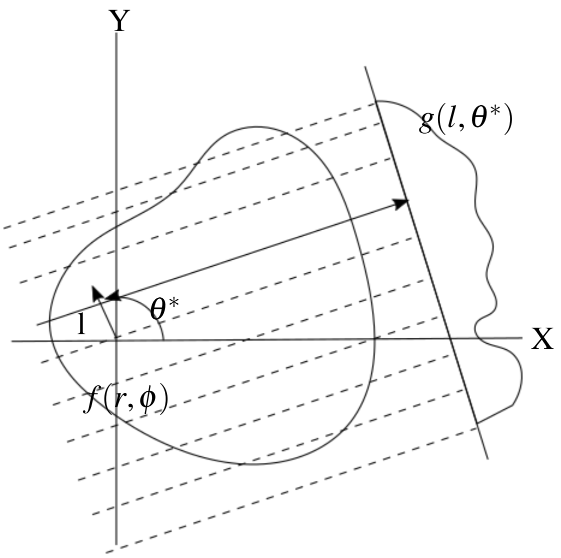

Figure 2.10 The Radon transform.

where $g(l,\theta^*)$ represent the experimental data for different angles of θ^* defined as the projections for several values intended to be pictured. The most convenient algorithm to use in order to make a tomographic reconstruction is the Radon inversion function $f(r,\phi)$ as it is shown in the equation 2.54 [22].

$$f(r,\phi) = \frac{1}{2\pi^2}\int_0^{\pi} d\theta \int_{-\infty}^{\infty} \frac{\partial g(l,\theta^*)}{\partial l} \frac{dl}{rcos(\theta^* - \phi) - l} \tag{2.54}$$

The mathematical foundation of Computer Tomography requires the measurement of projected data and the reconstruction of this data into a virtual model. When a 3-D object is scanned, these scans are translated into projections of the object at different angles, then this information is saved as 2 dimensional images. Each of these 2 dimensional images are converted into one dimension vector. A sinogram is an image composed of all the one dimensional vectors as illustrated in the right rectangle of Figure 2.11 [63].

CT works in two different domains which are defined as the volume domain and the projection domain. The volume domain obtains the scanned object and the volume reconstruction in a spatial domain with a Cartesian coordinate system. The projection domain saves the data projected from the volume domain and its coordinate system involves the projection direction and the detector position. When the acquired information is translated from the volume domain into the projection domain the operation is defined as a forward projection. On the other hand when the operation is translated from the projection into the volume domain the action is defined as a back-projection as it can be seen in Figure 2.11.

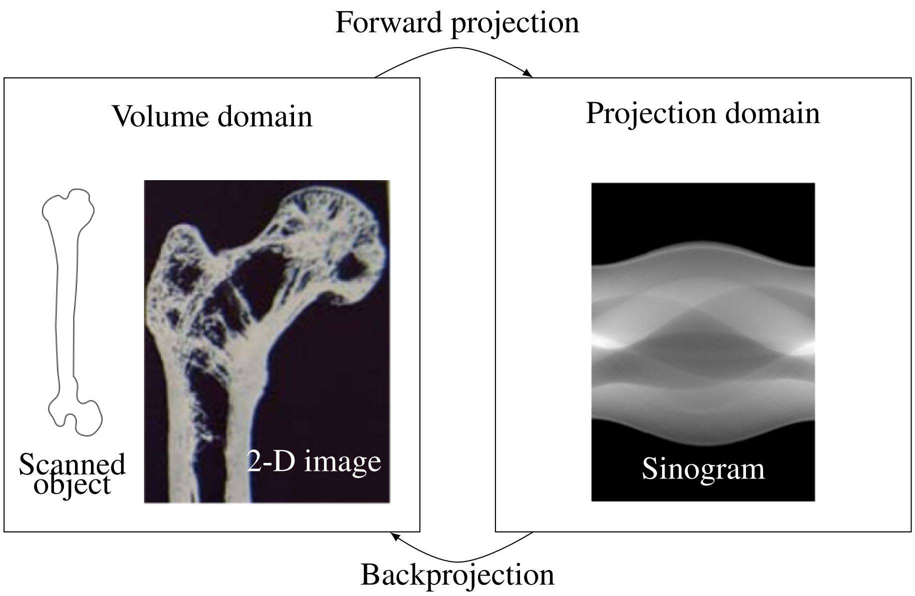

Figure 2.11 Forward and backforward projection schematic [63].

Two approaches for these projection operators are the analytical and the algebraic [64, 65]. Where an analytical approach defines the projections as line integrals in the volume domain for each projection and for each detector point, it is a summation of a large number of incremental effects. In the algebraic approach the projection is represented by a matrix vector as shown in Figure 2.12. The analytical approach is the sum of the line integrals over the volume domain for each projection of the detector line through the volume. On the other hand the algebraic approach is a matrix vector W which is known as the projection matrix which is equal to V, the detector vector, multiply by p, the projection angles. When back-projecting the data with the analytical solution the integrals are passed back over the volume with its corresponding integral, whereas for the algebraic case the projection matrix is transposed.

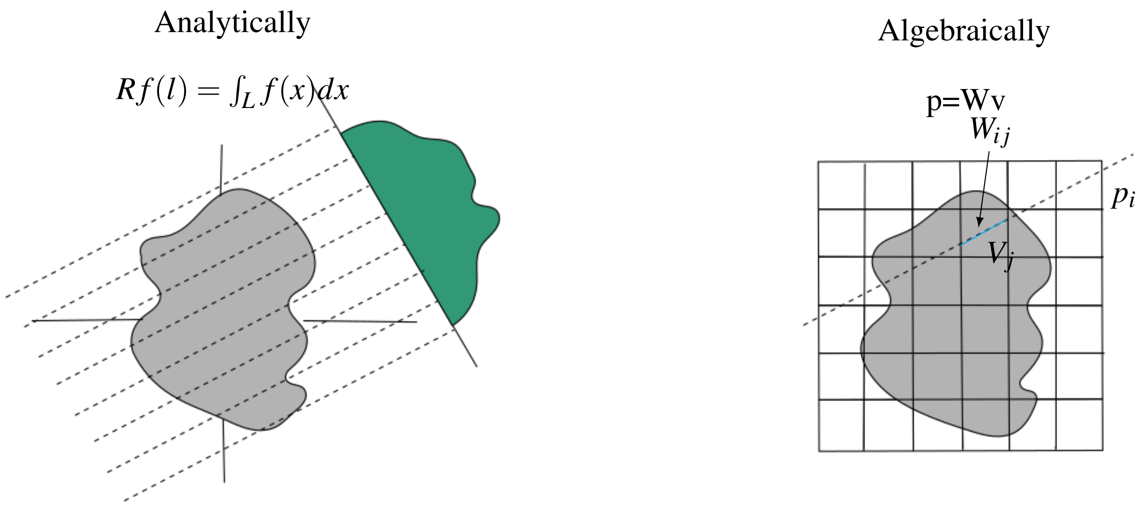

Figure 2.12 Analytical and algebraic approach illustration [63], where the analytically approach use the radon equations and gives the integral of the scanned volume represented in green. The algebraically approach is sectioned by a matrix and the scanned area is a portion of this matrix.

2.7.5 Fourier slice theorem

The backprojection analytical approach is based on the Fourier slice theorem, which is the operator that relates the Fourier transform of any function with the Fourier transform of the Radon transformations. The detailed mathematical explanation can be found in the papers presented by Rosenfeld, Kak and Slaney [66, 67]. When an object is scanned the 2-D Fourier transform function is unknown. The Fourier slice theorem states that it is possible to get the 1-D Fourier function for each angle of the scanned object, and this 1-D lines in the Fourier domain will construct the 2-D Fourier transform which when completed can be back projected as shown in the Figure 2.13.

However, this back projection faces some drawbacks since the information in the origin of the scanned object contains low frequencies information and the borders contain high frequencies information as shown in Figure 2.14. High frequencies contain information about small details. Less high frequencies information gives as a result blurry reconstructions, [68]. To improve the back projection quality the low frequencies are filtered. This is what it known as filtered back projection.

The filter back projection, FBP, is used to get a defined reconstruction [69] by using filters such as Ram, Shepp, Hann to cut out the high frequencies [70]. Reconstructions created with filtered backprojection are closer to the original images as it can be seen in Figure 2.15.

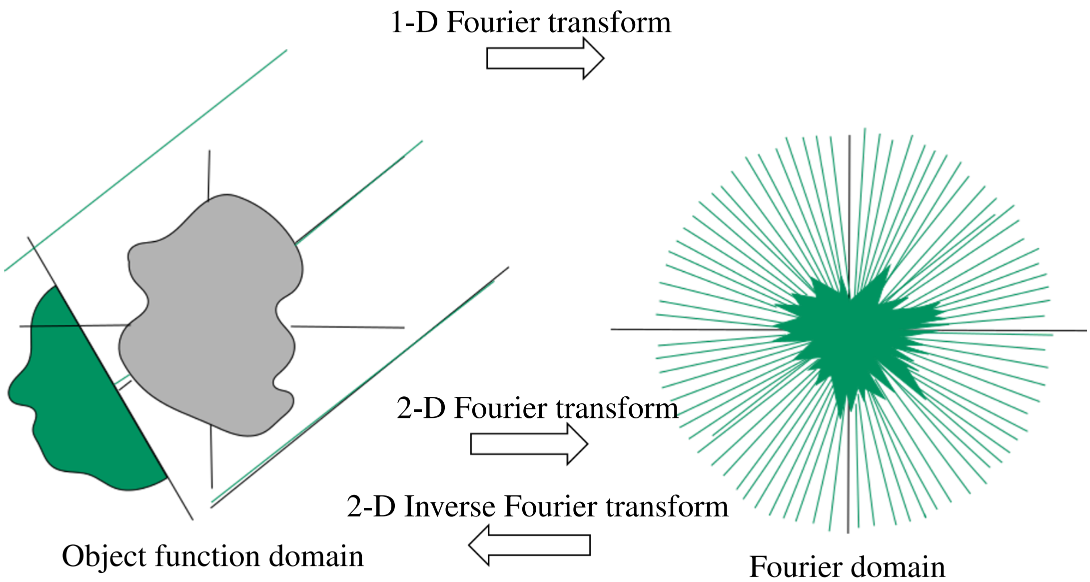

Figure 2.13 1-D Fourier transform into 2-D Fourier transform and inversion schematic [63]. The Fourier domain is represented by a volume that is scanned in each angle represented by each single line in green.

2.8 Limited data problems in X-Ray and polarized light tomography review

A rank two tensor provides information about the internal stress in a more complicated way than a scalar field. Therefore, new mathematical approaches to represent the 3-D internal stress were presented in Szotten's thesis based on Lionheart and Sharafutdinov's previous research [71]. In this section, a brief description of this mathematical approach developed by Szotten is presented [21].

The structure of his research is as follows:

- Introduction of Tomography mathematics which was previously defined in section 2.7.4. The Radon transform is invertible and was demonstrated by the Fourier slice theorem. However, the Fourier slice is considered a complicated algorithm to use in practice. Therefore an algebraic approach to perform this inversion was sought. These algebraic equations are known as filtered back projection. The advantages of this algebraic method is the reduction of noise by applying filters by limiting the low frequencies, for instance by using Hamming window as shown in Figure 2.16.

  Szotten modelled the linear Radon transform as a matrix that allows to discretises images and sinograms as vectors and constructed a matrix.

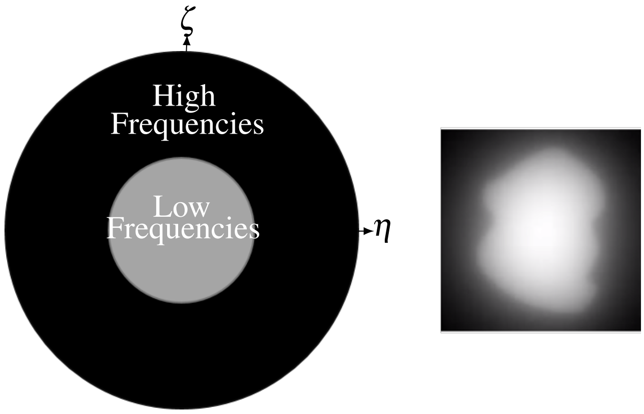

Figure 2.14 Back projection schematic representation with blurred edges due to less high frequencies information than low frequencies [42].

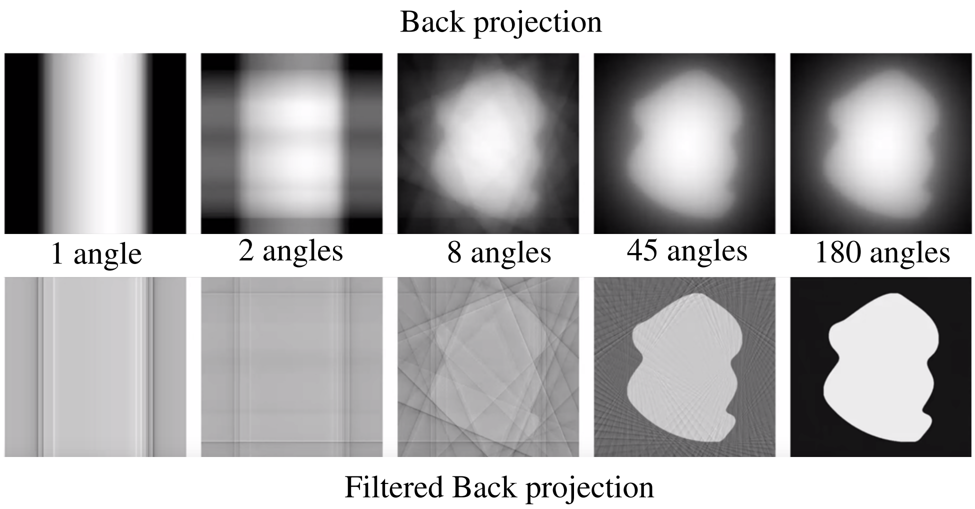

Figure 2.15 Back projection and Filtered back projection results comparison [42].

Then, an operator was applied to work out the Radon transform where the 3-D model was a stack of 2-D functions as shown in Figure 2.17.

Data were collected by measuring the rotation of the specimen at certain angles of the detector; in this case a camera. Szotten described that the tomographic reconstructions based on the Radon transform are known only for some cases such as limited angle, exterior and interior problem as shown in Figure 2.18 where the white areas symbolise the limitations.

The algorithms developed in Szotten's research were built under the interior problem limitation, as shown in Figure 2.18, because is the typical situation where the width of the camera, is smaller than the scanned object.

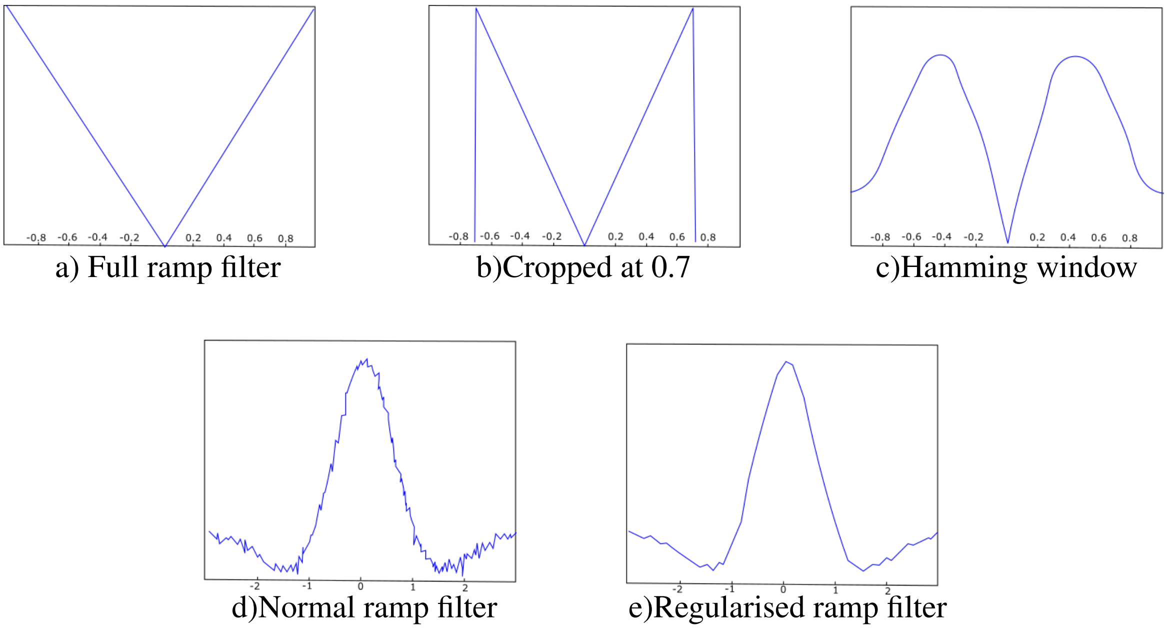

Figure 2.16 Ramp filters options that can be applied in the back projection reconstruction, extracted from [21].

- Introduction to photoelasticity mathematics.
  The mathematics of photoelasticy were also analysed, where it was stated that the stress-optics law proposed that the permittivity tensor depends linearly on the stress tensor, under the assumptions where the forces are small enough to be linearly related in the equation 2.55.

$$\varepsilon = C_0 D(\sigma) + C_1 H(\sigma) \tag{2.55}$$

where ε is the permittivity, C_0, C_1 are the optical coefficients, D is the deviatoric stress and H is the hydrostatic stress. The deviatoric stress can be related to the von Mises field stress, J, and it is expressed in eigenvalues λ_i, λ_j as the equation 2.56 shows.

$$J = \sqrt{\frac{1}{2}\sum_{n=1}(\lambda_i - \lambda_j)^2} \tag{2.56}$$

However the permittivity is difficult to measure by the use of polarimetric methods, therefore an approximation to Maxwell equations, in this case the Rytov-Kravtsov law, models the light through the photoelastic object. This model was expanded by the Neumman series and then truncated to first order linear approximation by

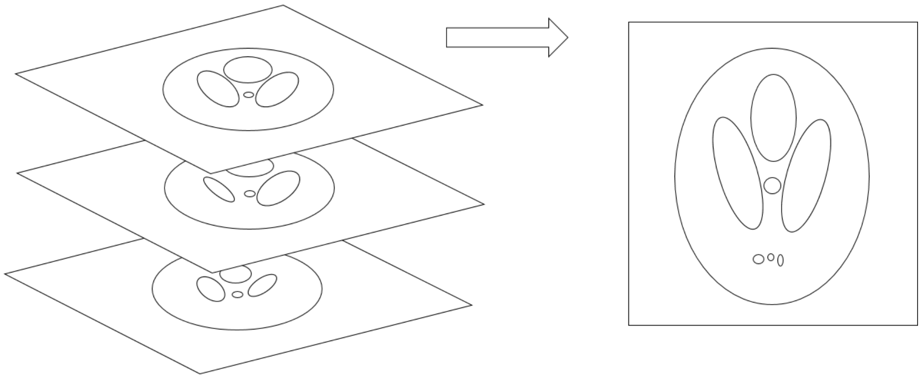

Figure 2.17 Planes of 2-D functions for 2-D Radon collection data [21].

Sharafutdinov [72]. This model is defined as truncated because it does not take into account the hydrostatic part of the Cauchy stress tensor since the von Mises criterion is not dependent of this variable. An experimental approach was proposed to collect the Truncated Transverse Ray Transform, TTRT, with Fourier polarimetry to measure the light intensity variations when a photoelastic material has been exposed to an stress. Then the TTRT, developed by Sharafutdinov and Lionheart [71] was expresed in terms of the filtered backprojections instead of the backprojection. Finally, the Radon transverse inversion is performed. Szotten explored two types of tensor the potential which is a symmetrised derivative of a vector field, and the solenoidal which is a divergence free vector. These tensors are the foundations of the reconstruction method for Photoelastic Tomography by Aben [73] which is better known as Integrated photoelasticity as explained in section 2.7. From the work developed by Lionheart and Sharafutdinov the assumption where the field is solenoidal is not required. Once the two type of tensor were converted into the Radon inversion domain, a Hilbert transform, which is a technique for certain types of data truncation was applied. This technique is helpful in cases where a clamping apparatus is obscuring some views or when elongated specimens which detectors are not wide enough to fit the field view. These new algorithms provided theoretical inversion methods which were implemented to obtain numerical results.

- Numerical findings from the general reconstruction algorithm

  The first step in Szotten's numerical simulation was to develop a simulator to generate the data to test the values of the TTRT instead of taking light intensity measurements with Fourier polarimetry. Then, the tensor field values were discretized to build a 5-D matrix array. The experimental setup described by Szotten, Lionheart and Tomlinson [74] was simulated by Szotten with parallel light beams passing trough the specimen as

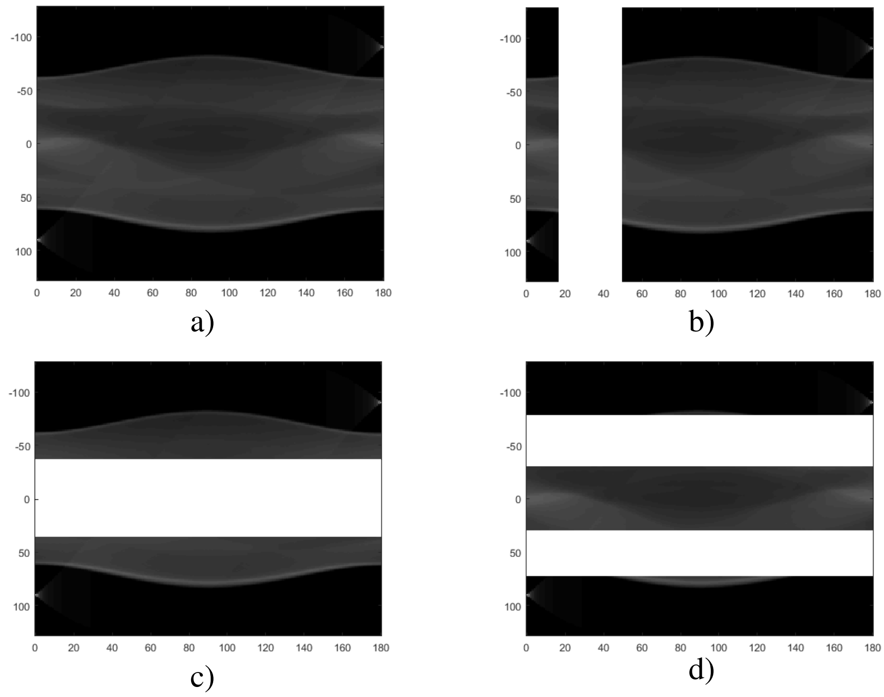

Figure 2.18 Type of limitations faced when acquiring data: a) not limited sinogram, b) limited angle, c) interior limitation and d) exterior limitation [21].

shown in 2.19. This light beam path through the voxel grid was based on the methods proposed by Siddon and Jacobs [75, 76]. Where a voxel is defined as a 3-D pixel that does not contain information about the position in the 3-D space. The width and height ratio were simulated as 4:3 to match the supposed camera in the system. The rotation of the tomographic data was made around the Z axis by the use of a rotational matrix. Finally, the projection of the tensor field was calculated in the plane perpendicular to the ray and the filtered back projection was performed.

Numerical results for photoelastic tomography were performed collecting six and three axes of the simulated object as shown in Figure 2.20 a) and b) respectively [21]. Szotten defined the reconstruction from data collected from six and three axes as stable and unstable reconstruction respectively. He concluded that both reconstructions showed promising results; however, it was demonstrated that three-dimensional scalar tomography using six axes was dimensionally overdetermined. Therefore, three axes (Unstable reconstruction) were used in the experimental reconstruction since it was simpler to collect the data and less time-consuming.

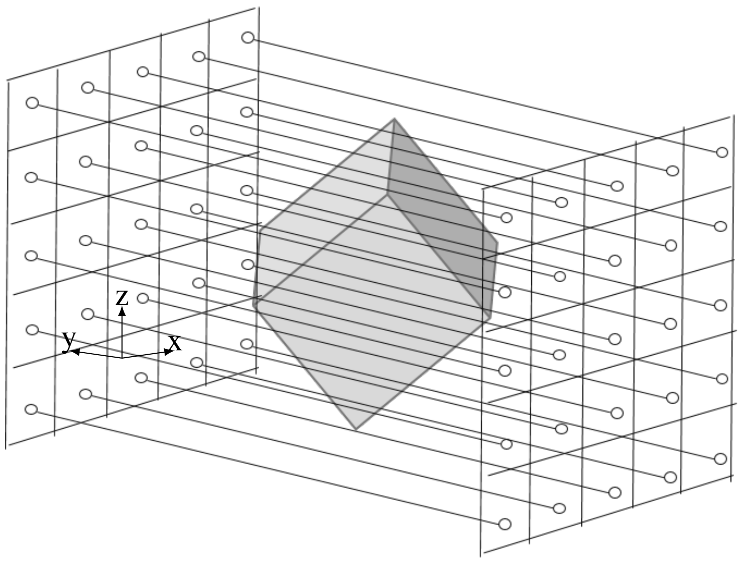

Figure 2.19 Simulated experimental setup [21].

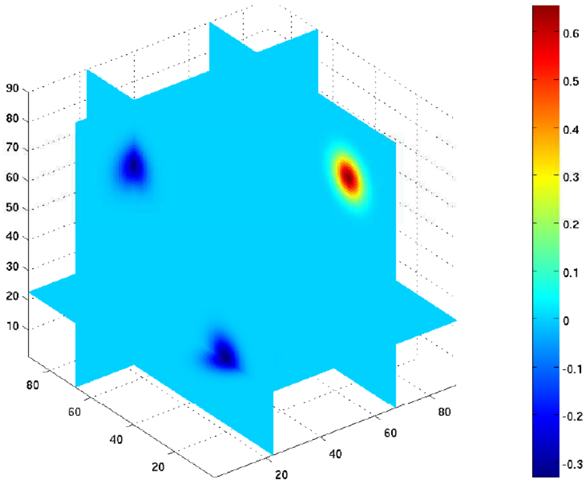

a)Original phantom

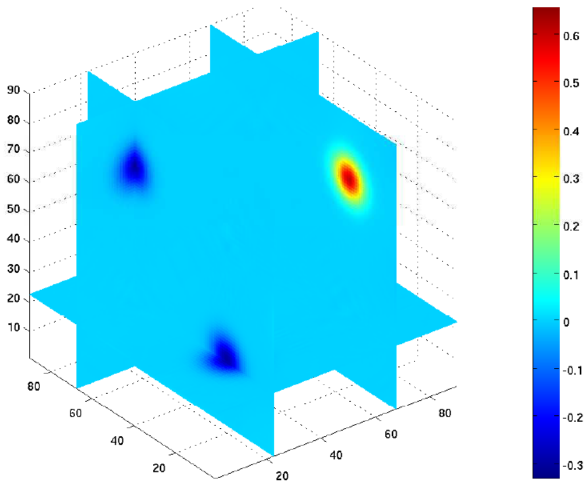

b) Six axes reconstruction (Stable)

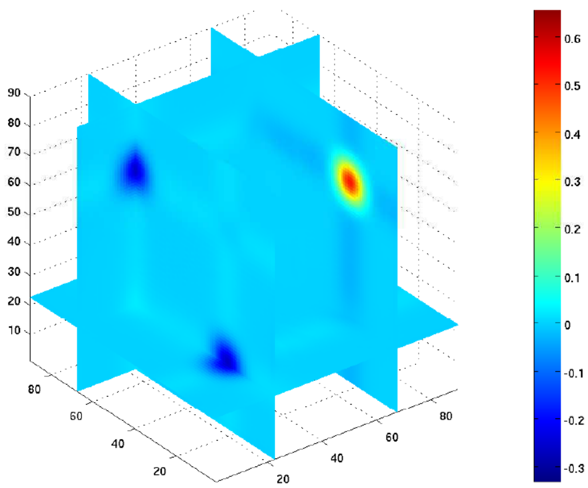

c) Three axes reconstruction (Unstable)

Figure 2.20 Numerical results from Szotten research [21], for three (unstable) and six (stable) scanned axes of the simulated object.

2.9 Literature review conclusion

The literature review presented in this chapter covered the essential background to understand stress, the light behaviour and the experimental stress analysis techniques, such as photoelasticity, 3D photoelasticity. It also gave the insight to alternative non-destructive experimental stress analysis such as Integrated Photoelasticity and Photoelastic Tomography and background of Computer Tomography. Also a review of Szotten's research was made. In his work he presented a novel mathematical approach that evidenced the possibility of non-destructive internal stress reconstruction and concludes that it could be implemented experimentally. Therefore, the aim of this research was clear and settled to work towards the adequate experimental implementation of this mathematical approach that avoids the destruction of the specimen. In the following chapter the experimental apparatus and the methodology proposed by Szotten, Lionheart and Tomlinson to obtain an internal stress reconstruction is described [74], this description is complemented with a critical audit of the state of the apparatus and software and the implementations to improve the photoelastic tomography rig.

Chapter 3

Photoelastic tomographic rig and software review

The aim of this chapter is to understand the state of Photoelastic Tomography in previous research [77–81] to improve the experimental conditions. This chapter provided a critical audit of the components that comprise the Photoelastic Tomographic apparatus and the physical improvements implemented where they were required. Also, a brief explanation of the stress treatment for the specimen and the immersion fluid refractive index matching with the specimen to avoid light refraction is explained in section 3.2 and 3.3. Finally, the steps involved to perform the internal stress reconstructions with the explanation of each program developed in previous Szotten research [21] are described in section 3.4.

3.1 Photoelastic tomography apparatus description

The initial design for the Photoelastic tomography apparatus proposed by previous research [21],[82] is shown in Figure 3.1. The light path travelling through the optical devices is represented by a schematic drawing as shown in Figure 3.2. A detailed explanation and a critical audit of each optical device referenced numerically in Figure 3.2 will be listed throughout this section.

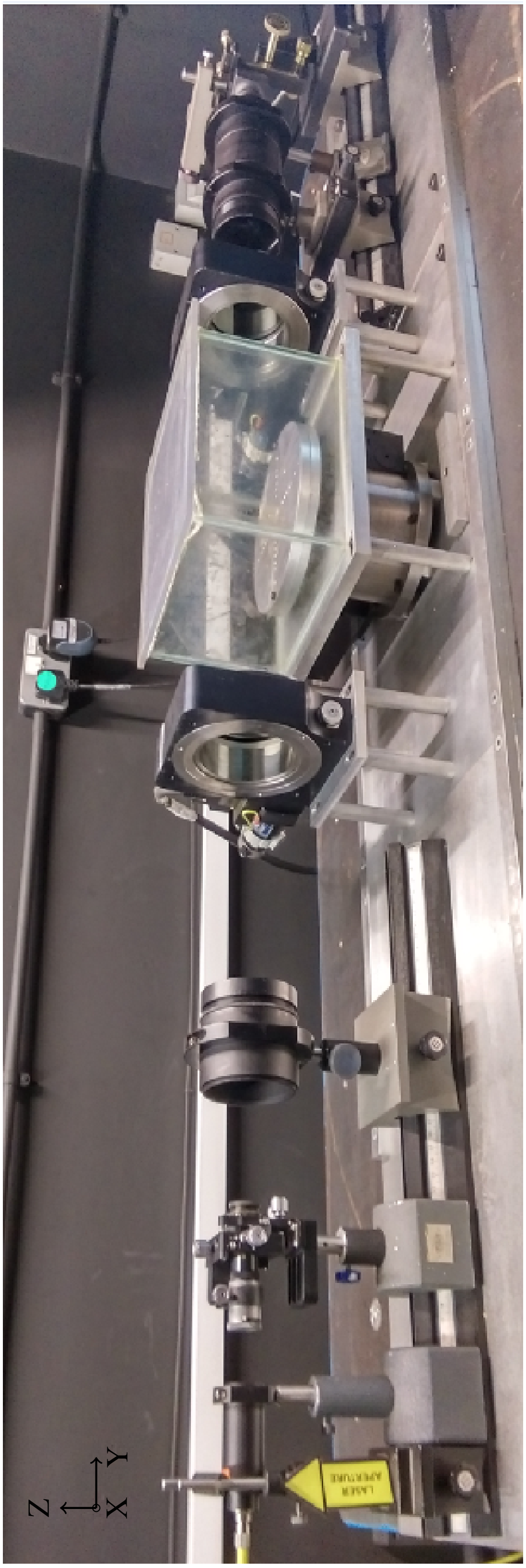

Figure 3.1 Photoelastic tomography apparatus picture.

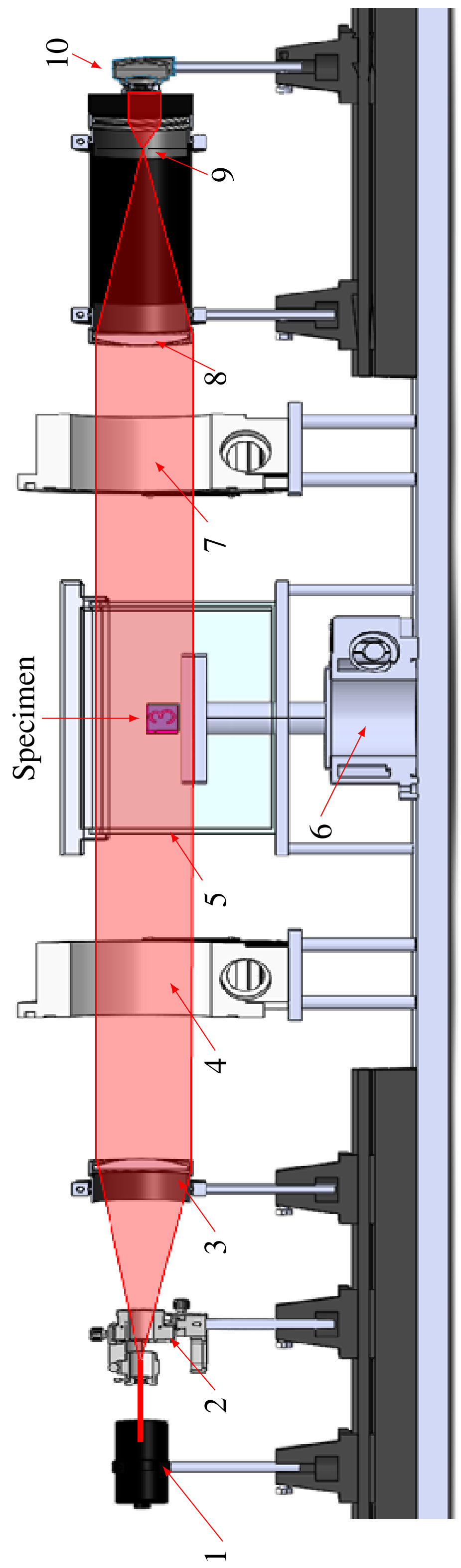

Figure 3.2 Photoelastic tomography schematic:
1) Laser, 2) Spatial filter, 3) Plano-convex aspherical lens, 4)Polarizer, 5) Immersion tank, 6) Motorized rotation stage, 7) Analyser, 8) Plano-convex aspherical lens , 9) Iris diaphragm, 10) CMOS camera.

1. Laser:
   A monochromatic 3R class laser with a wavelength of 635 nm is used as the light source for the system. The reason a laser was chosen as a light source was because it provides a means to create a collimated, parallel beam of light which is required by the mathematical approach proposed by Szotten. This device fits in the experimental purpose, therefore, no changes are needed regarding the light source.

2. Spatial filter:
   A spatial filter that consists of a microscope objective, a pinhole aperture and a positioning system as Figure 3.3 a) illustrates. The spatial filter eliminates the scattering light that creates Airy disks. The Airy disks are defined as series of concentric rings of decreasing intensity around a bright region of light in the centre due to diffraction when the light passes through an aperture as shown in Figure 3.3 b). With the employment of this device, only the maximum intensity and peaks of the beam will go through, leaving a clean Gaussian beam as a result, Figure 3.3 c). This device works as expected within the experimental rig and expands the light source without the presences of the Airy disk. The only downside about it is its difficulty to align it. A person without previous experience in optical devices alignment will struggle to do it. Therefore, a detailed explanation for the spatial filter alignment is provided in section A.1.2.

3. Lens:
   A plano-convex aspherical lens, is an optical device that collects the light rays in order to join them into a focus length. The focus length is the distance at which the lens or various lenses bring light rays that are parallel to a coincide on a single point to form a sharp image. In this experimental setup the light source reaches the plane face first and exits by the convex face, which gives as a result an expanded and collimated light beam. Figure 3.4 represents a plano-convex lens [83]. It has to bear in mind that the position of the focus depends on the refractive index, it is not always on the back of the sphere as is shown in Figure 3.4. These lenses work as expected but the focal length was unknown. An attempt to find out this information from the manufacturer specifications was made, however, no serial numbers were found, therefore an experiment to measure the focal length was performed. The results of the focal length measured experimentally and the procedure followed to align the lenses are shown in section A.1.3.

4. Polarizer:
   A polarizer which acts as a filter with the property of changing the light direction and rotation (linearly or circularly) as explained in Appendix A. In this experiment, the

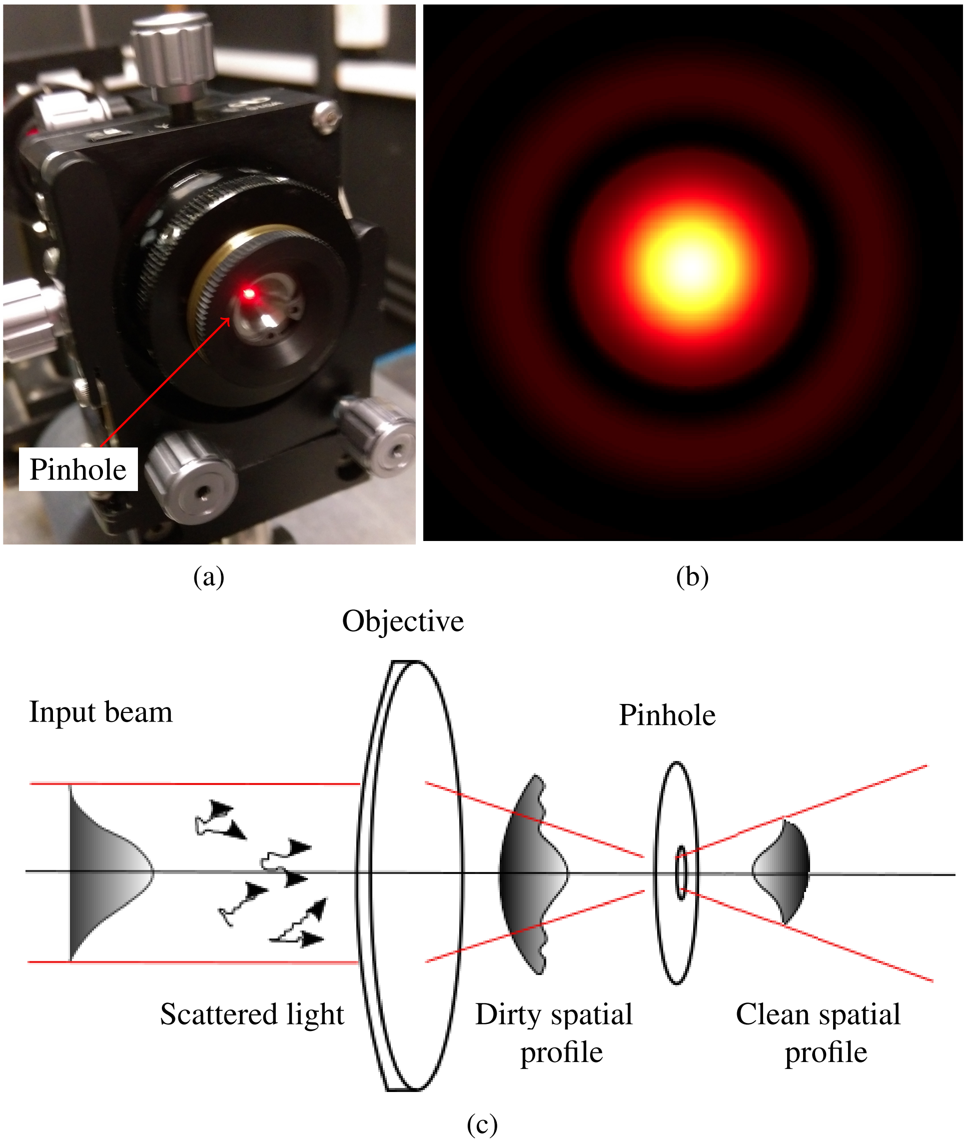

Figure 3.3 a) Spatial filter b) Airy disk example c) clean Gaussian beam example.

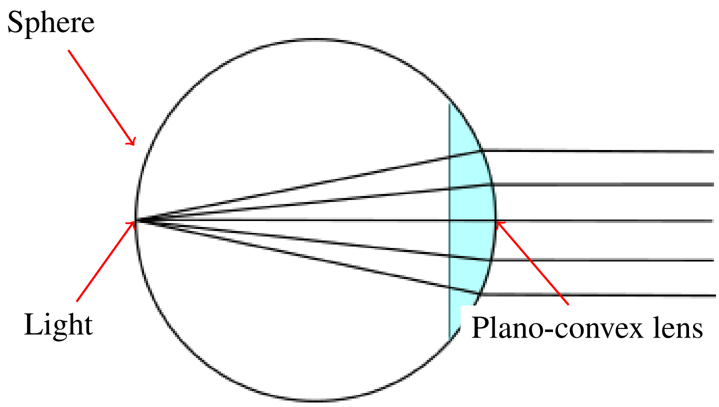

Figure 3.4 Plano-convex lens schematic diagram.

polarization filter is fitted in a rotational motor to change the polarization axis during the data acquisition. This optical device works as expected but due to its proximity to the immersion tank greasy spots on its surface could be found which affects the image quality and visibility of the specimen. Consequently, a methodology to clean up the optical devices before each experimental data acquisition is described in Appendix A.

5. An immersion tank:
   Contains the specimen and is filled with a fluid that matches the refractive index of the specimen; this avoids the light refraction in the surfaces of the specimen as required by the mathematical approach developed by Szotten [21]. This cubical tank is large enough to contain the rotatory plate of the system and is made of an aluminum plate as a bottom and four glass walls. It works, however, design improvements are needed such as the addition of a proper lid to enclose the immersion liquid to avoid its contamination and evaporation which affects the refractive index. Also, the addition of a drainage system is needed since the procedure to empty the tank is difficult. The experimentalist has to manually unscrew the rotatory table of the tank when it is with the immersion liquid, this action needs to be performed to be able to lift the tank and transfer the fluid to another container. This emptying procedure is also dangerous since lifting a 2 kg glass tank with approximately 5 litres of an immersion fluid is not exactly the safest way to do it. Hence, implementations for the tank improvement were made and shown in chapter 5, section 5.2.

6. A motorized rotation plate:
   A circular aluminium plate is placed inside the immersion tank attached to the engine through a manufactured shaft. This plate is where the sample is positioned and its role is to change the specimen rotational position about the Z axis from 0 to 180 degrees.

This component rotates the specimen, but it does not have a reference where to place it. The repeatability of the position of the specimen within the tank can enhance the cut and shift process, as explained in section 3.4.1. Thus, a new rotational plate design adding a reference to place the specimen is needed.

7. Analyser filter:
   Which has the same functionality and setup as the polarizer.

8. A detection tube:
   Consists of 2 plano-convex spherical lenses and an iris diaphragm. The plano-convex spherical lenses reduce the diameter of the light beam before entering the camera. In this stage of the experiment,the light beam enters by the curved section of the first plano-convex spherical lens and exits from the plane area. In Figure 3.5 [84] this in-house made detection tube that acts as an afocal telescope is illustrated. In this device nothing else than the height adjustment that coincide with the optical axis of the system is needed. In this device no improvements are required.

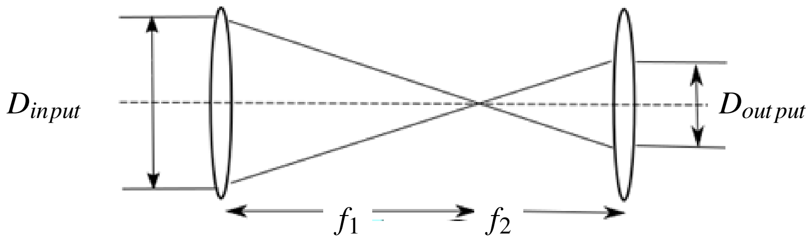

Figure 3.5 Schematic diagram of plano-convex lens afocal telescope.

9. Iris diaphragm:
   positioned between the 2 plano –convex spherical lenses, it restricts the light entering into the camera to prevent over-saturation and to act as a spatial filter. In this device no improvements are required.

10. CMOS camera:
    A DC1545M camera with a pixel resolution of 1280x1024 pixels is connected to a computer to perform the data acquisition of the light intensity images. The configurations settings for this camera is shown in Appendix D.

3.2 Specimen preparation

Polymeric materials, polymers epoxy, poly methyl methacrylate and polycarbonate, have been tested during previous research [77–81] and in the beginning of this one due to their characteristics: transparency, manufacturing ease and weak birefringence [85]. These polymers were exposed with different loads to a stress freezing cycle to induce internal stresses to be able to measured it with the Photoelastic Tomography rig. The thermal stress cycle procedure is performed in an oven that was configured to increase its temperature at a rate of 20 °C per hour until it reach the glass transition temperature, T_g, of the material. Once this temperature is reached the oven is held at the T_g temperature for two hours. Then the specimen is cooled down at a rate of 5 °C per hour. Details about the glass transition temperature measurement for the tested material used in these experiments will be given in section 4.2.

3.3 Refractive index matching

The Photoelastic tomography technique requires the sample to be immersed in a liquid that equal its refractive index in order to eliminate the light refraction in its surfaces because the mathematical approach that performs the stress reconstruction assumes straight light rays passing through the solid [86]. Attempts in previous research [78, 77, 79–81] has been made to calculate the exact ratio proportion of each component , however the lack of equipment or a methodology could not give the desired results, an example of this results is given in Figure 3.6. In section 4.3 the proposed methodology followed to perform the index matching will be presented.

3.4 Photoelastic tomography software review

In this section the programs needed to perform the 3-D stress reconstruction will be described. A brief outline of this reconstruction process is shown in Figure 3.7. This outline is divided by the data acquisition and post processing applied to reduce the amount of data and the internal 3-D reconstruction programs developed by [21]. The aim of this review was to understand these processes in order to identify what needs to be improved in this data acquisition and post-processing of the images as the first stage. This research is based on the assumption that the reconstruction algorithms works since Szotten showed numerical results and simulations as evidence that they could work experimentally as reviewed in section 2.8 therefore the reconstruction part of the process will not be improved in this research but tested. Nevertheless, the reconstruction algorithms will be described in this chapter and experimentally tested in the following chapter.

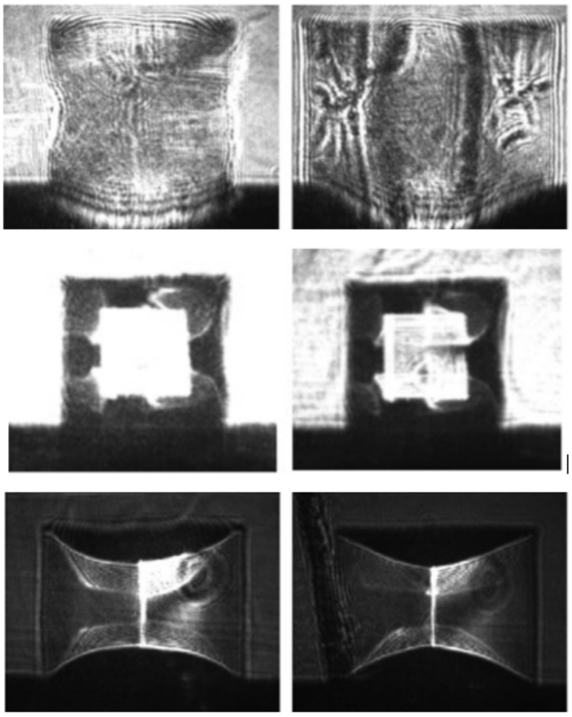

Figure 3.6 Examples of refractive index matching performed in previous research [70].

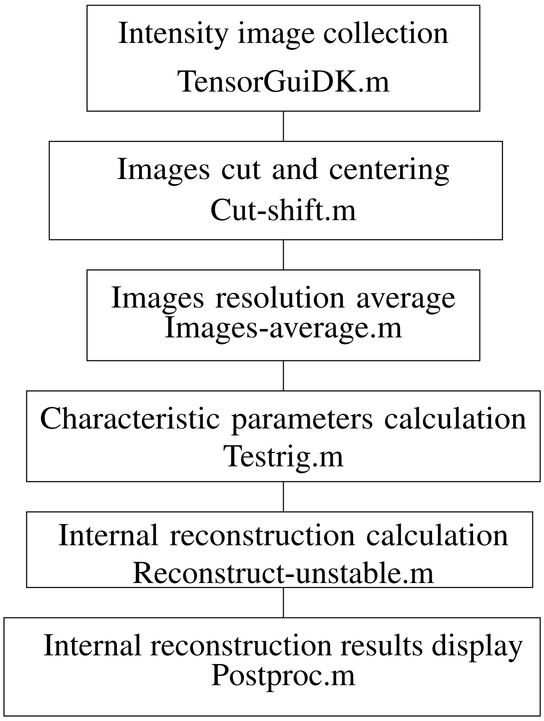

Figure 3.7 Internal stress reconstruction processes.

3.4.1 Data acquisition and image processing

Collection of intensity images

The data acquisition starts with the execution of the program called *"TensorGUIDK"* which is a program developed in MATLAB by Yang [82]. This program, creates a Graphical User Interface (GUI) as shown in Figure 3.8 that helps to make an easy interaction with the electronic devices within the apparatus. In other words,*"TensorGUIDK"* controls the camera, the rotational base plate, the rotation of polariser and analyser configuration in order to acquire the light intensity images. These light intensity images are captured under 18 different polarisation states and will be used to calculate the characteristic parameters through Fourier Polarimetry [18] as reviewed in section 2.7.2.

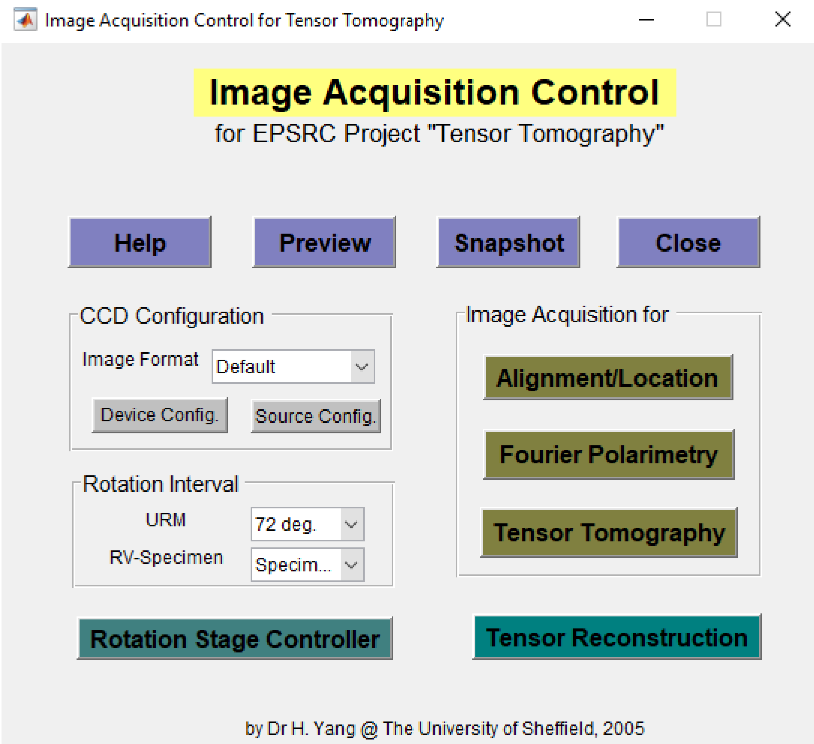

Figure 3.8 Photoelastic tomography interface.

The complete data acquisition consists of a collection of light intensity and position images. The set of light intensity images involves the rotation of the sample from 0 to 180 degrees in increments of 1 degree. Every time the specimen is rotated 1 degree a total of 18 images with different polarization states are captured, as shown in Figure 3.9. These pictures are the inputs to a program, described in section 3.4.2, that calculates the characteristic parameters. The ratio between polariser and analyser rotations was 2:1 based on Yang and Tomlinson

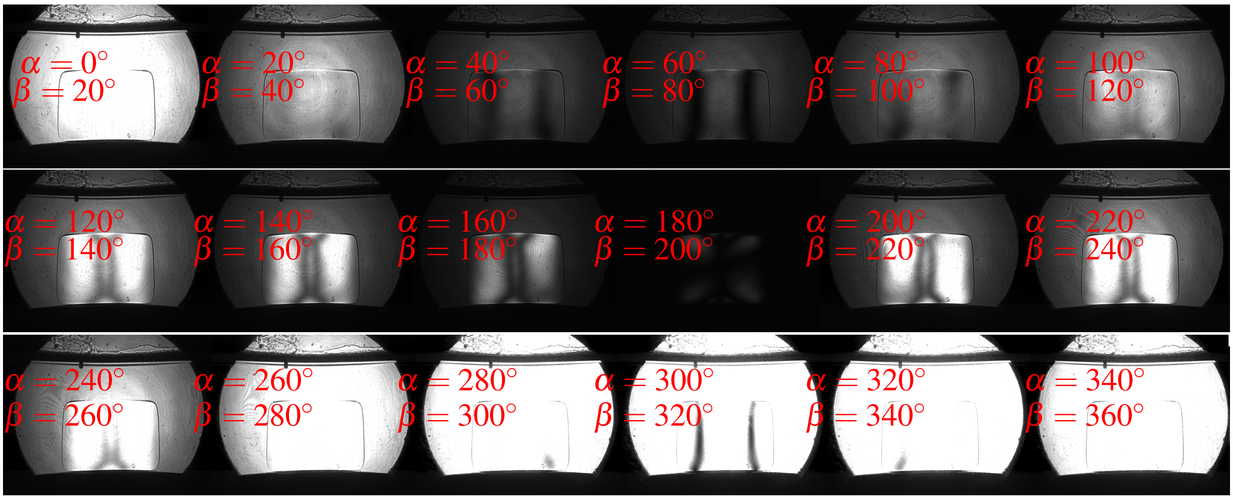

Figure 3.9 Polarization states where α is the polarizer and β the analizer.

[18]. Furthermore, the set of position images involves the rotation of the sample from 0 to 360 degrees in steps of 90 degrees, resulting on a total of 5 images. These images are used in the second step of the data processing procedure,*"Cut-shift"* which is detailed in section 3.4.1. To accomplish a full reconstruction the data acquisition has to be performed in each axis, *"X"*, *"Y"*, and*"Z"* of the specimen, meaning that the sample has to be flipped as shown in Figure 3.10.

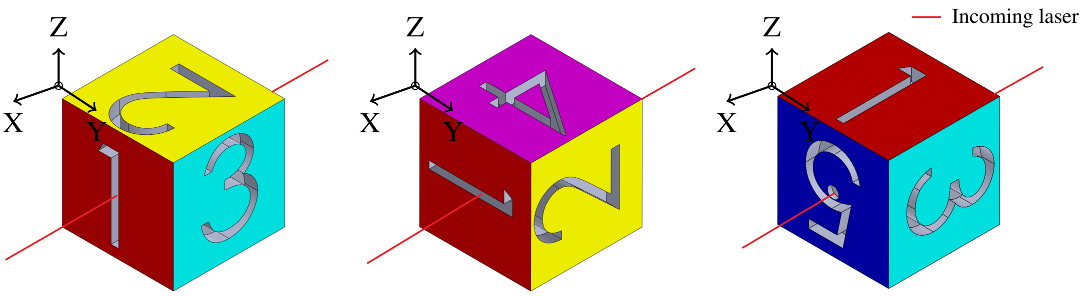

(a) (b) (c)

Figure 3.10 Rotations of the specimen on a) Z axis b) Y axis c) X axis.

Positioning and cropping the images

A program known as "$Cut - Shift$" that cuts the extra information in the light intensity images and centres them within the image frame was developed by Yang [18]. The aim of this program was to optimize the computational time and resources needed in the stress reconstruction. An example of the applied program is shown in Figure 3.11.

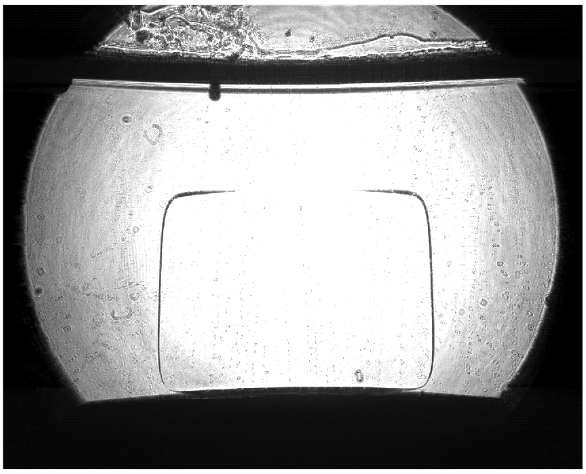

(a)

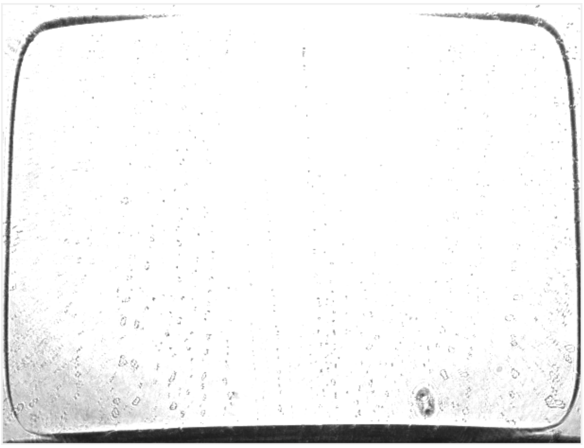

(b)

Figure 3.11 Intensity image a) before centre and cropping with a size of 1280 x 1024 pixels and b) after with a size of 918 x 697 pixels.

The rotational base plate in previous research did not have a physical reference where to place the specimen, meaning the specimen varied its position every time that an experiment was performed. The original cut and shift program needs the measurement of the edges of five pictures with different rotational degrees.This measurements in the *"X"* edge of the position images, was obtained by the MATLAB command known as *"Data cursor"*. This command allows to know the exact position of a point in an image by positioning the cursor on it, as illustrated in Figure 3.12. These measurements tells us how the specimen is moving when it is being rotated on the rotational stage by first calculating the specimen's polar coordinates. Then the radius and the angle of the position must be changed in the program.

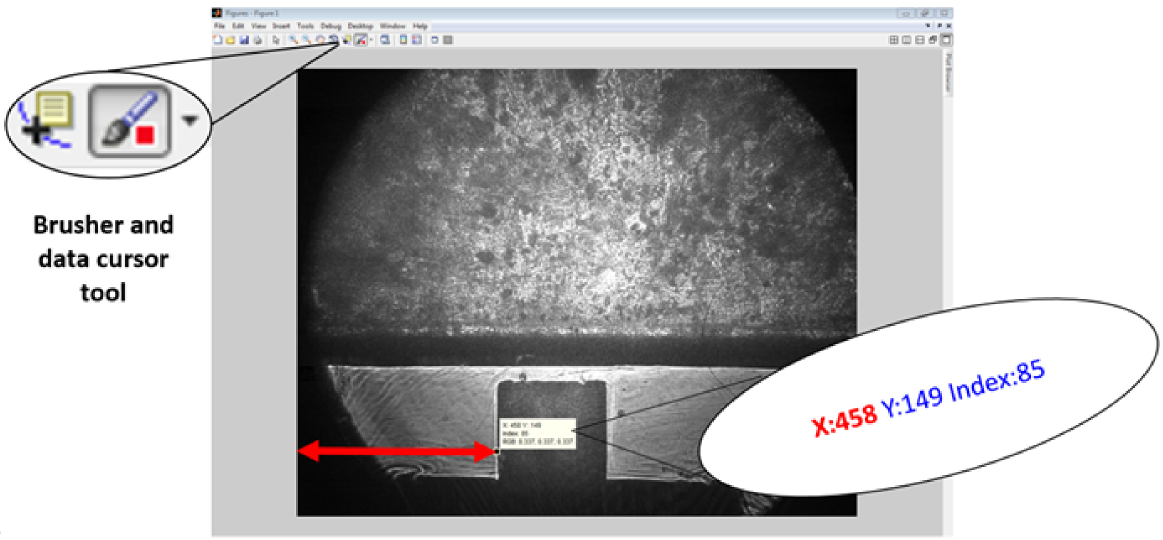

Figure 3.12 Matlab print screen measuring the specimen displacement within the X axis.

These measurements need to be analysed to determinate the values a, b, and c (Figure 3.12), which represent the specimen's displacement from the original image as shown in Figure 3.13. Once the values a, b and c have been determined, the values of Δx and Δy can be calculated by the Figure B.1 in appendix B. These values help us to obtain the values of r and θ, equation 4.2 and 4.3 respectively, which are the inputs needed in the program *"Cut and shift"*. These polar coordinates relate the cube centre position with the centre of the rotational plate.

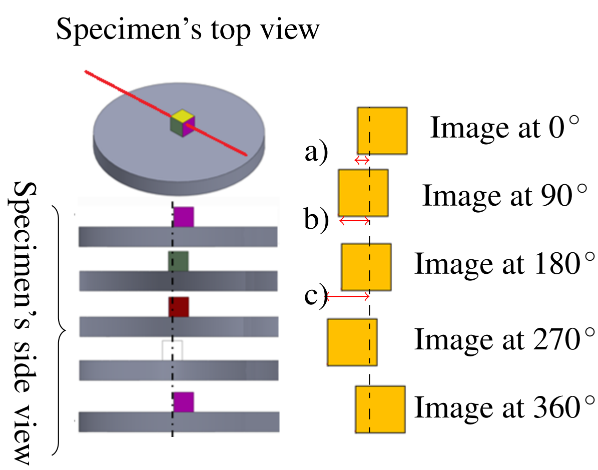

Figure 3.13 Specimen position measurement during rotations from 0 to 360 degrees in 90 degrees steps

$$r = \sqrt{\Delta_x^2 + \Delta_y^2} \tag{3.1}$$

$$\theta = \tan^{-1}\frac{\Delta_y}{\Delta_x} \tag{3.2}$$

This program is time-consuming and tedious, since 5 position images, with the rotation of the specimen from 0 to 360 degrees must be acquired, then the measurement of the edges of each image must be done. Moreover, calculate the polar coordinates which will be the inputs of the programs. This program is also exposed to human error due to the manual measurements. Results from this program are shown in the Figure 3.14 where it can be seen that the shifting of the image is not working properly.

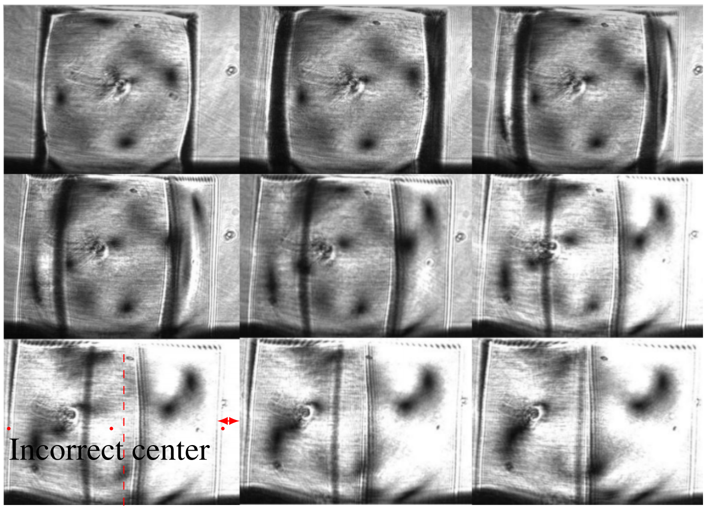

Figure 3.14 Cut and shift program results developed in previous research.

Image average

The following step, after the images have been cropped and centred, is to average them at a number of pixels to reduce the amount of data processed by the computer since a large number of images are analysed. Hence,a program called ”*Image* − *average.m*” was developed. This program calculates the pixel’s mean values for each 3 by 3 or 4 by 4 columns and rows. This calculation will generate a new image with a resolution and size reduction of the image as depicted in Figure 3.15 c) [81, 77, 80, 78, 79].

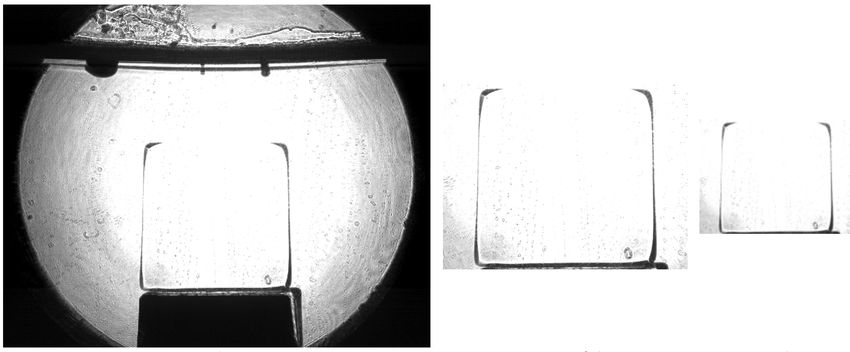

Figure 3.15 a) Light intensity image 1280 x 1024 pixels , b) cropped and centered image (611 x 463 pixels), c) averaged image (114 x 156 pixel).

One has to bear in mind that the image height:width ratio must be 3:4, and the height must be divisible by three to be able to perform the reconstruction as required by the program in section 3.4.2.

3.4.2 3-D stress reconstruction

Once the data acquisition and image processing has been done the reconstruction programs need to be run.

Testrig

The first program to be run is *"Testrig"*. This program helps to merge the information from the 3 axes and is made of two main functions,*"Intensity2characparams"* and *"ReconstructUnstable.m"*, which helps to perform the 3-D stress reconstruction calculation. These functions will be described in the following sections.

Intensity2characparams

This function generates a 5 dimensional matrix where the calculated values of the characteristic parameters are saved. This 5 dimensional matrix is the input for the next function *"ReconstructUnstable.m"*. Detailed description about the calculation is presented in section 2.7.1. Since this calculation involves a huge amount of images, 4320 in total, the aid of a supercomputer (150 GB RAM) is needed.

ReconstructUnstable

After this function processed the 5 dimensional matrix, it generates a 1 by 6 cell array that contains the reconstructed stress information with the aid of the following sub-functions:

MakeRotationMatrixUnstable

This sub-function rotates the 5-D matrix to make the given axis of rotation lined up with the z-axis, which is the axis taken as the original axis for the reconstruction as it can be seen in Figure 3.10.

Apply a filter

This sub-function applies a filter needed as explained in section 2.7.5 in this case the filter called Hilbert is applied. After this filter application the Fourier Transform is calculated in order to be used to filter the projections. Then the backprojections are combined and finally the function *"finalFourierStepUnstable"* is calculated to generate the cell array.

Postproc

Then after the 1 by 6 cell array was obtained by *"ReconstructUnstable"*. Each of these matrices represent the stress in each direction at a point in the sample. To display the stress in an illustrative way the matrices have to be manipulated to obtain the eigenvalues of each matrix by the program *"postproc.m"*. These values represent the maximum values of the stress tensor matrices. To view the data of the reconstructed specimen, Figure 3.16 a), it is divided in slices. The command *contourf(allmax(:,:,n))* can be used to plot in a contour map plot the stress reconstruction as shown in Figure 3.16 b), where n is the number of the slice attempted to be seen, the Figure 3.16 c) how the relationship of this slices with the sample. The number of slices obtained in the reconstruction depends on the averaged images size, e.g. an image of 114 x 200 pixels will be reconstructed in a total of 114 slices because the data is processed as a stack of 2-D images as explained in chapter 2, section 2.8
Detailed information about the theory for the mathematical approaches used to create these programs is found in section 2.8. With this last program the internal stress reconstruction is finished, the improvements that can be done is the integration of each program in a main one and modify the directories to automatically obtain the data instead of writing down the address manually. Other than that, it is not in the scope of this research to change the mathematical approach developed by Szotten rather than test it.

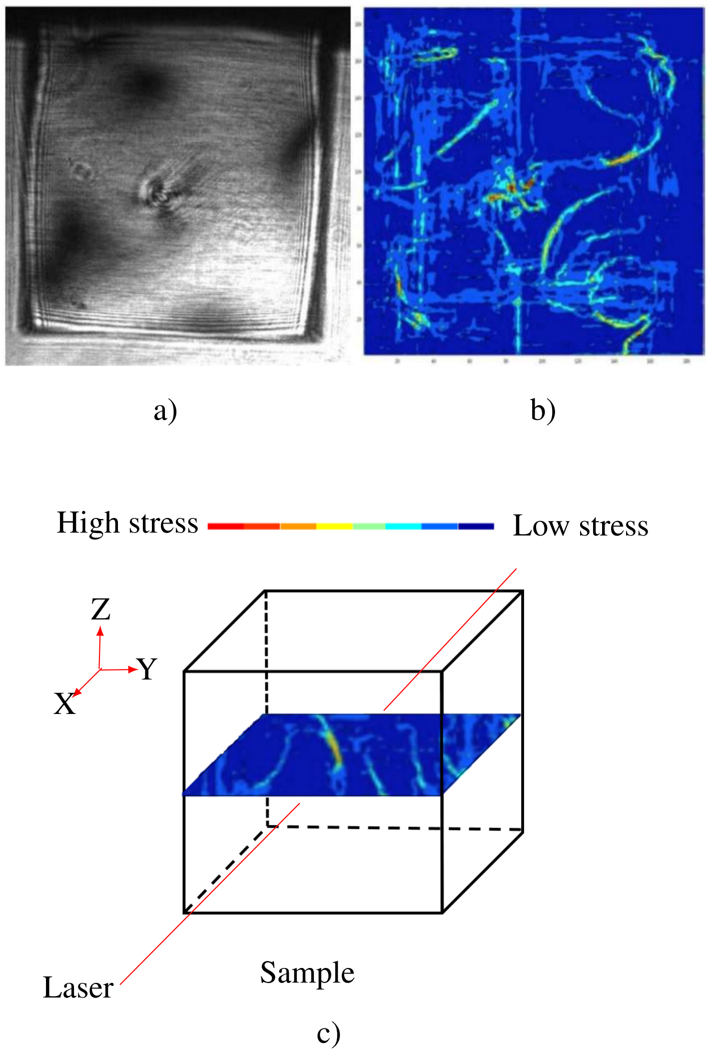

Figure 3.16 Sample of results obtained by Flemming and Rodak [77,78] where a) is the sample as viewed by the CMOS camera and b)a reconstruction slice, c)schematic diagram showing the slice stress pattern relationship with the sample.

3.4.3 Conclusion

This section concludes the Photoelastic tomography apparatus and software review by giving the description of each component of the experimental apparatus with its respective critical audit. A methodology to perform an alignment of the optical devices is explained in order to be performed to remove the Airy disk of the laser light beam. Within the physical implementations e.g. the manufacture of new base plates to assure a constant laser height passing through the optical axis of each component is presented.

A brief introduction of the refractive index matching which is one of the variables suspected to be affecting the stress reconstruction is described in this chapter however the followed methodology will be presented in the next chapter in section.

Finally the observations about the programs used to perform the internal reconstruction were explained and critically examined. These processes are divided by the data acquisition, the image processing, and the internal stress reconstruction as shown in Figure 3.7. Improvements of the data acquisition and post-processing will be presented in Chapter 5. In the case of the internal stress reconstruction, we will narrow this research just to the experimental part and testing of the existent algorithms developed by Szotten [21].

Chapter 4

Photoelastic tomography experimental work

4.1 Introduction

In the previous chapter a critical audit of the apparatus and software developed by Szotten [21, 18] to perform 3-D internal stress reconstruction through Photoelastic Tomography was presented and areas of improvement in the apparatus and methodology were identified. It was shown by previous research [78, 77, 80, 81, 79], that the 3-D internal stress reconstruction results contained a lot of noise. The aim of this chapter is to improve the refractive index matching by following a quantitative methodology and test if this makes a difference in the internal stress reconstruction results. A series of experiments were performed on four PMMA cubes of 1 inch cubic size exposed to a stress freezing methodology [34, 87] varying the loads as presented in section 4.2. This samples were immersed in a blend of oils prepared with the mentioned refractive index matching methodology in section 4.3. Furthermore, the image averaging under two windows sizes of 3 by 3 pixels and 4 by 4 pixels were carried out. All these experiments were made in order to test the influence of these variables in the internal stress reconstruction and the results are presented in section 4.4.

4.2 Experimental preparation of the specimen

In the next experiments, four PMMA cubes from different batches were tested. The first two cubes, from left to right in Figure 4.1, were obtained directly from a manufacturer and the next two cubes were cut from a PMMA square beam. The main differences between these PMMA batches are: the roughness, its transparency and glass transitional temperature.

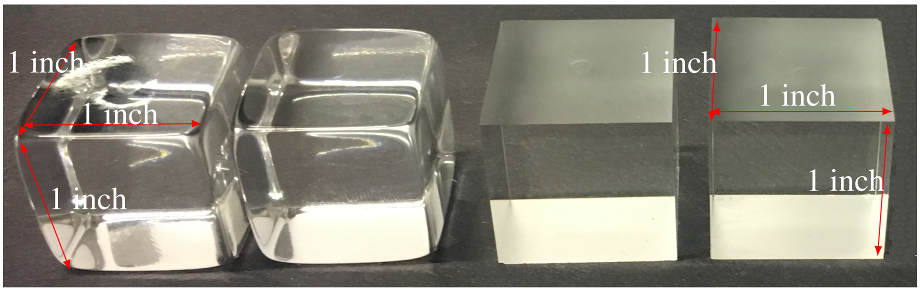

Figure 4.1 Tested PMMA specimens from two different batches.

These samples were exposed to a thermal cycle treatment in order to induce residual stresses to be able to measure it with the Photoelastic tomography method. The measurement of the glass transition temperature was required to avoid notches on the surface of the specimen due to the applied loads. This measurement was made with the Dynamic Mechanical Analysis machine, DMA, from the Department of Materials Science and Engineering of the University of Sheffield, Figure 4.2.

Figure 4.2 DMA machine used to measure the glass transition temperature, Tg, of the PMMA samples.

The glass transition temperature obtained for the manufactured cubes batch was 118 °C, whereas for the cubes cut out from the PMMA square beam the glass transition temperature was 128 °C as shown in the graph in Figure 4.3.

These results were within the range value according to the literature review, therefore they were the values used to perform the thermal cycle [88]. Once the glass transition temperature

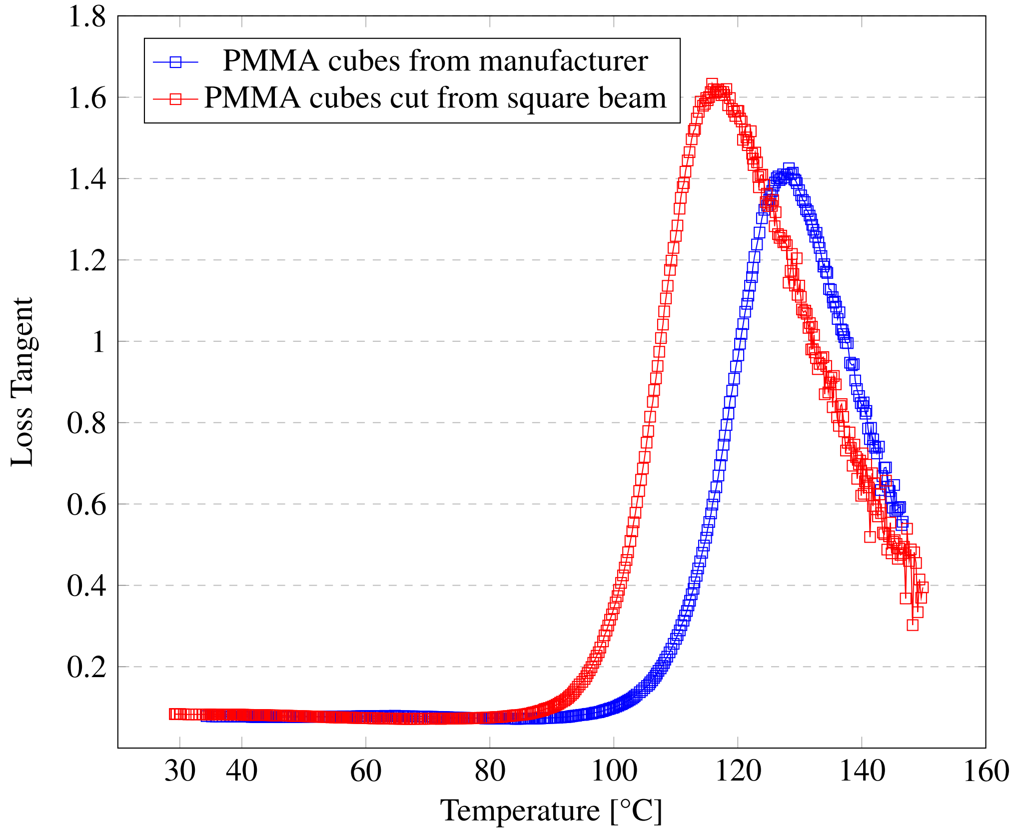

Figure 4.3 Tg measurement of PMMA specimens.

was known, the cycle thermal stress was performed in an oven of the Mechanical Engineering Department of The University of Sheffield as shown in Figure 4.4. Two different weights of 0.300 kg and 1 kg were applied to the specimens by using a loading device which gives a mechanical advantage that multiplies the weights by three. Therefore the loads are P_1 =8.829 N and P_2 =29.43 N respectively as shown in Figure 4.5. The stress freezing process previously performed by Burguete and Patterson [89] was followed in this research to induce the stress. Where the temperature was increased at a rate of 20 °C per hour and held at the critical temperature for two hours. Then the specimens were cooled down at a rate of 5 °C degrees per hour.

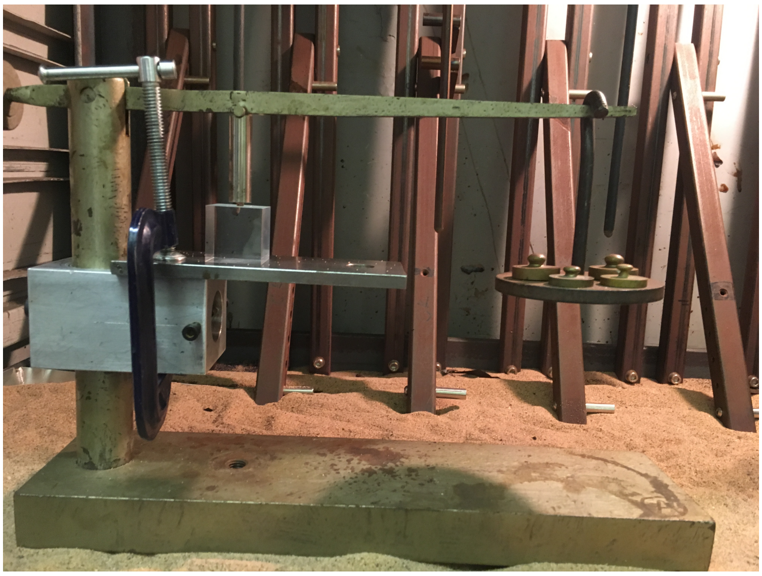

Figure 4.4 PMMA stress freezing treatment.

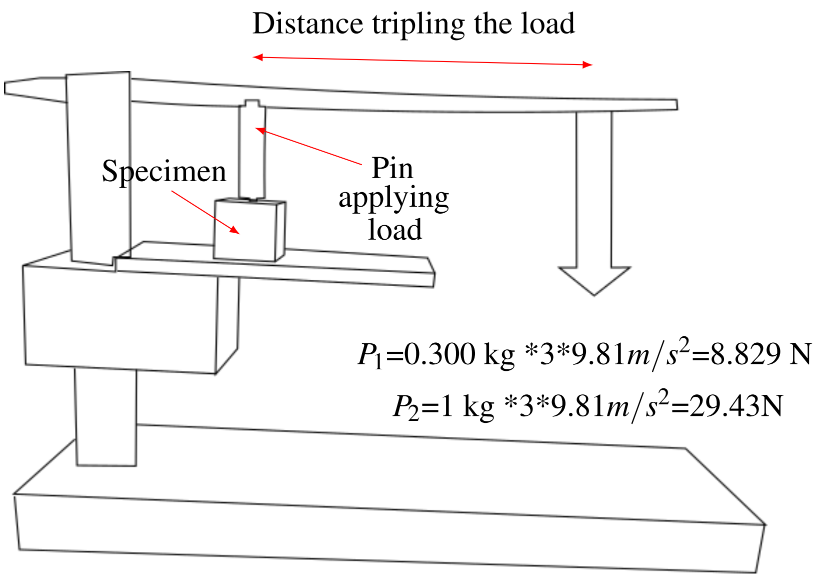

Figure 4.5 Loading device schematic.

4.3 Refractive index matching methodology

The Photoelastic Tomography method requires the sample to be immersed in a liquid that equal its refractive index in order to eliminate the light refraction in its surfaces. This is done because the mathematical approach used to perform the stress reconstruction assumes straight light rays passing through the solid [86]. Attempts to calculate the ratios of the blend of liquids needed in refractive index matching has been tried. This blend is usually made of two fluids, where the first fluid has a lower and the second fluid has a higher refractive index than the specimen. Therefore the exact ratios of both liquids in order to achieve the best match of refractive index according to the tolerance was sought. The mismatch tolerance suggested is about a difference of 0.001 and 0.002 [90]. Theoretical mixing rules such the ones presented in the equations 4.1, 4.2, 4.3, 4.4, 4.5, 4.6 and 4.7 can be used to calculate the ratio of the blend [91]:

- Lorentz-Lorentz

$$\frac{n_{12}-1}{(n_{12}^2+2)\rho_{12}} = \frac{n_1^2-1}{n_1^2+2}\frac{p_1}{\rho_1} + \frac{n_2^2-1}{n_2^2+2}\frac{p_2}{\rho_2} \tag{4.1}$$

- Wiener equation

$$\frac{n_{12}^2-n_1^2}{n_{12}^2+2n_1^2} = (\frac{n_2^2-n_1^2}{n_2^2+2n_1^2})\phi_2 \tag{4.2}$$

- Heller equation

$$\frac{n_{12}-n_1}{n_1} = (\frac{3m^2-1}{2m^2+2}) \tag{4.3}$$

with

$$m = (\frac{n_2}{n_1}) \tag{4.4}$$

- Dale-Gladston equation

$$\frac{n_{12}-1}{\rho_{12}} = (\frac{n_1-1}{\rho_1})\rho_1 + (\frac{n_2-1}{\rho_2})\rho_2 \tag{4.5}$$

- Arago-Biot equation

$$n_{12} = \phi_1 n_1 + \phi_2 n_2 \tag{4.6}$$

- Lichtenecker equation

$$lnn_{12} = \phi_1 lnn_1 + \phi_2 lnn_2 \tag{4.7}$$

- Newton equation

$$n_{12}^2 = \phi_1 n_1^2 + \phi_2 n_2^2 \tag{4.8}$$

where:
n_i, (i=1,2), is the index of refraction of the pure fluid
n_{12} correspond to the blended refractive index
ϕ_i is the component volume fraction in the mixture of the pure fluid
p_i, (i=1,2) being the component weight fraction in the blend of the fluid.
Even though some predictive ratios can be calculated from these formulas presented in equations 4.1 to 4.8 there are some shortcomings related with the incapacity to measure the change in volume and refractivity since these rules are based mainly in volume addition [92]. Therefore an experimental approach was taken for this methodology.
The first step of this process must be the accurate determination of the specimen refractive index. Although the values of this parameter can be found in literature, a measurement to obtain an accurate value after the sample has been exposed to a stress freezing treatment measurements must be done. This results in difficulties when calculating the exact refractive index needed for the liquid's blend. The refractive index value depends on the light wavelength and the temperature. For the case of the light wavelength a refractometer that could use the same light source as the Photoelastic Tomography experiment was required. In the case of the temperature dependency, implementations for the temperature control within the tank have not been performed yet, therefore our blend will be affected by these changes.
In order to obtain the most accurate measurement possible an Abbe 60 (E/D) refractometer, from the Chemical Engineering Department of The University of Sheffield which can measure solid and liquids was used. To verify the accuracy of the refractometer, the refractive index of water was measured using the same wavelength as the Photoelastic Tomography apparatus. According to literature, the refractive index of water at 635 nm is 1.33033, as shown in Figure 4.6 [93]. The experimental measured value was 3.659 in Abbe scale that equals to 1.33030, which is close to the theoretical value.
Once the accuracy of the refractomer was proved, the specimens measurements were performed as depicted in Figure 4.7 a). A liquid with a high refractive index (1.79) is used to make the optical coupling between the specimen and the refractometer prism as shown in Figure 4.7 b).

4.3.1 PMMA refractive index matching.

The refractive index measured for the unstressed PMMA specimen with a 635nm wavelength laser at 20°C, approximate temperature, was 20.112 in Abbe scale reading. This Abbe reading can be translated into the refractive index value with the 'Abbe Utility Program 7.0' , which 20.112 equals to 1.4876. The two synthetic oils used in the blend to match the refractive index of the PMMA sample were obtained from the Chemical Engineering

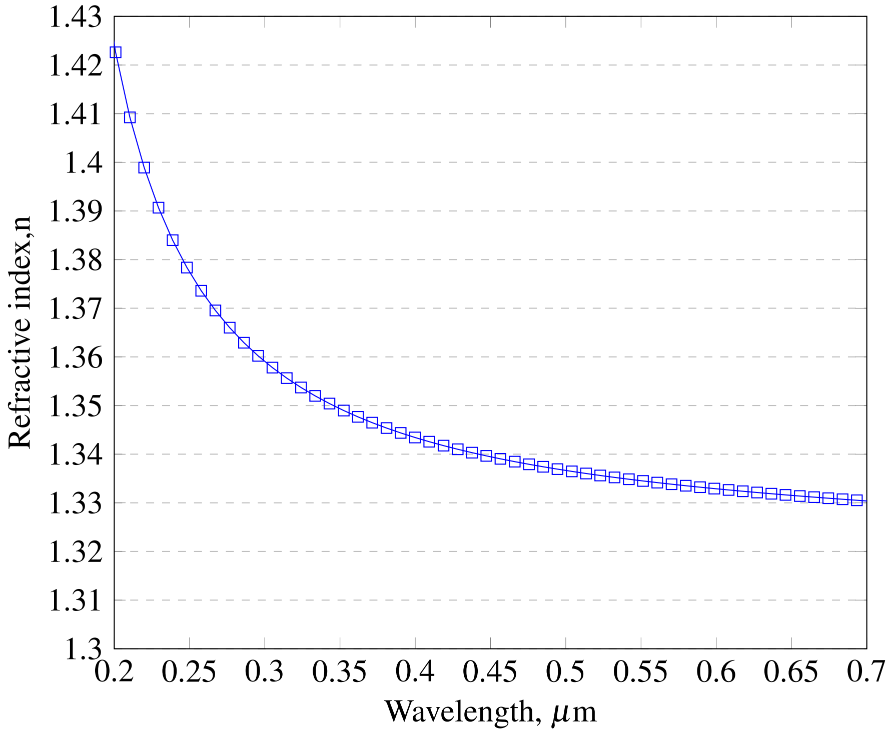

Figure 4.6 Refractive index measurement of distilled water with different wavelenghts.

Department of the University of Sheffield from Exxon Mobil company free of charge. These donated oils were the Synesstic 5, with an index of refraction of 1.522 at 25 °C [94], and SpectraSyn 2, with an index of refraction of 1.4418 at the same temperature [95] in accordance with the manufacturer and the Standard Test Method for Refractive Index and Refractive Dispersion of Hydrocarbon Liquids, ASTM D1218 [96]. The refractive index of each oils was measured with the same refractometer previously mentioned because it was needed to experimentally get the values with the environmental temperature and the specific wavelength in our experiment. The results were a measurement of 23.586 in Abbe scale which equals to n=1.51824 for Synesstic 5 oil and 14.887 in Abbe scale which equals to n=1.43968 for SpectraSyn 2. Even though the values from the literature review and the experimental measurement were obtained, it was needed to work out the ratios values. Comparing the theoretical and experimental values and considering the differences of the light source and temperature conditions affecting the accuracy [97], the approach taken was the experimental one. Therefore, solutions with different concentration ratios were prepared [98] as Figure 4.8b and Table 4.1 shows. These solutions were weighted on an electronic balance (Kernel PLB 1000-2), Figure 4.8a, with an accuracy of 0.01 gr, then they were mixed with the aid of an ultrasonic bath (Fisherbrand FB11020) for 15 min, Figure 4.8c.

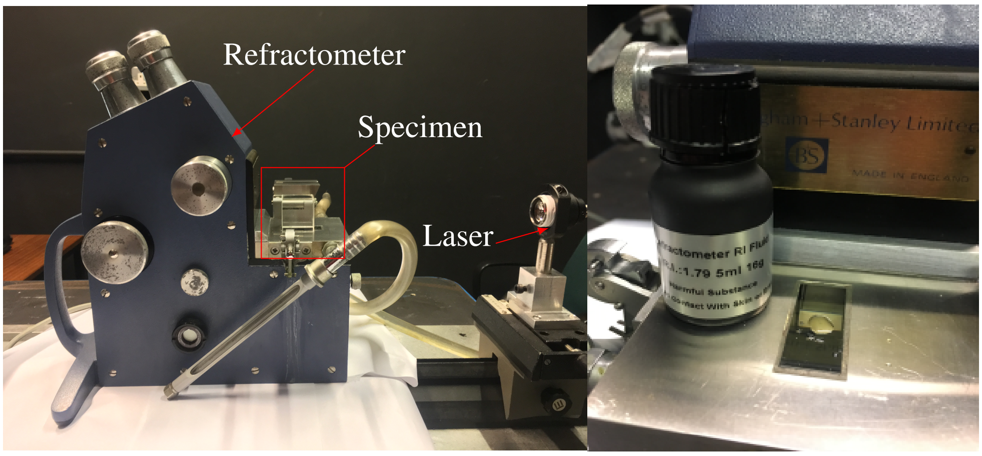

Figure 4.7 Measurement of PMMA specimen:a) Abbe 60 E/D refractometer, b) Coupling measurement liquid.

The measured refractive index measurements from these solutions were plotted as presented in Figure 4.9. The concentration of the Synesstic 5 oil is plotted on the abscissa axis and the value of the refractive index value is plotted in the ordinate axis. With this plot it was possible to obtain a trend in order to approximate the solution ratio near the refractive index of the specimen. The trend obtained from the different blends showed that the refractive index increase linearly with the increase of the concentration [97].
After the ratio that approximates the refractive index of the sample was obtained, a batch of 3 Kg to fill the tank was performed using the electronic balance (ML3002T). This solution was mixed with the SciQuip Digital Overhead Stirrer at 1250 rpm for 15 min. The oil refractive index was compared with the specimen. The oil's refractive index was higher than the specimen, therefore addition of the Spectrsyn oil was needed. After several iterations, the desirable refractive index matching of 20.112 on Abbe scale was obtained by the ratio of 65 wt% of Synesstic 5 and 35 wt% of SpectraSyn 2. The results for the PMMA refractive index are shown in the following Figure 4.10. In this images it can be seen that the edges completely disappear for an angle of 45 degrees
Even though a matching according to the tolerance suggested could be obtained, it has to be taken into account that several drawbacks in R.I.M techniques could affect the results [91], e.g. impurity on the particles of the fluid or the solid (gas bubble), temperature differences in the liquid, humidity (vapour losses), the change of the refractive index with the light wavelength [97].

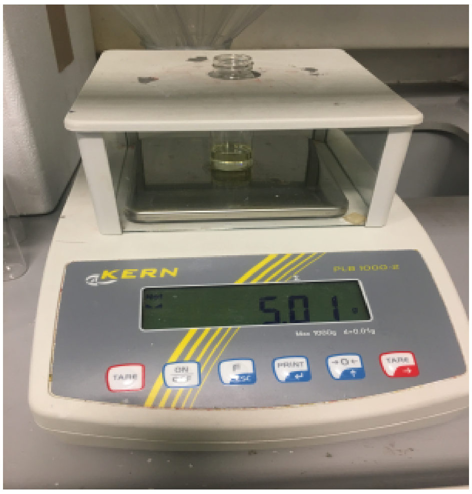

(a)

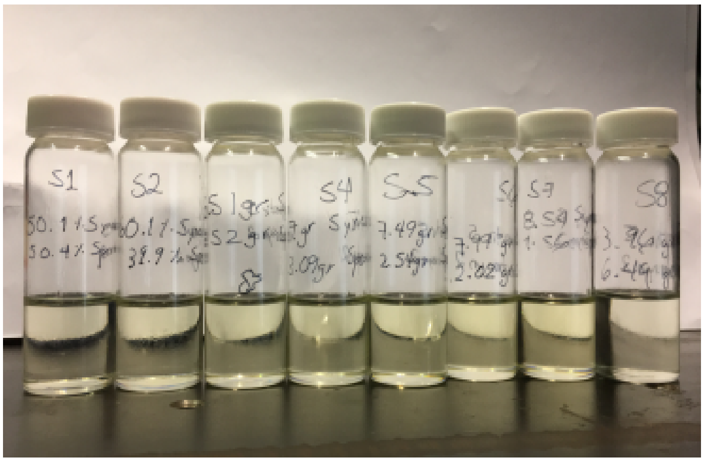

(b)

(c)

Figure 4.8 Oil solutions preparation: a) Oil blend weighted in electronic balance, b) Oil solutions with different weight ratios, c) Fisher ultrasonic bath mixing the prepared solutions.

Table 4.1 Concentration ratios of blend of oils used as immersion fluid for Photoelastic Tomography

Solution number	% of Synesstic 5	% of SpectraSyn 2	Refractive index (Abbe scale)
1	37.89	62.11	17.8
2	49.85	50.15	18.8
3	60.1	39.9	19.7
4	64.9	35.1	20.1
5	69.375	30.625	20.5
6	74.675	25.325	21
7	79.82	20.18	21.45
8	84.55	15.45	21.85

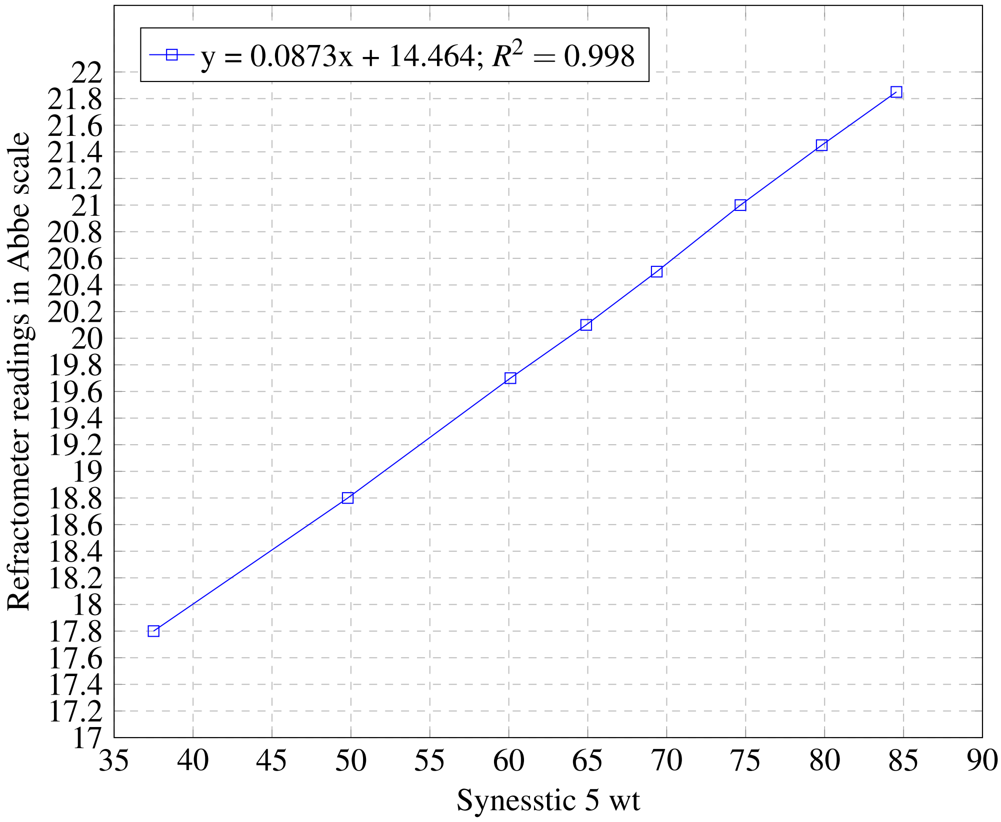

Figure 4.9 Synesstic 5 oil and Spectrasyn 2 calibration curve.

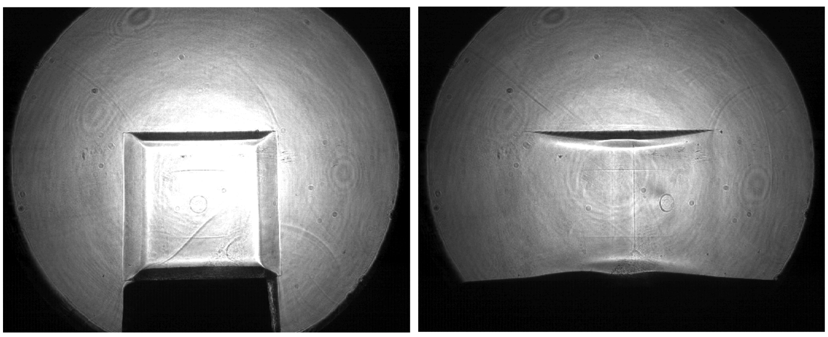

(a) (b)

Figure 4.10 Refractive index matching of PMMA sample rotated at a) 0 degrees and b) 45 degrees.

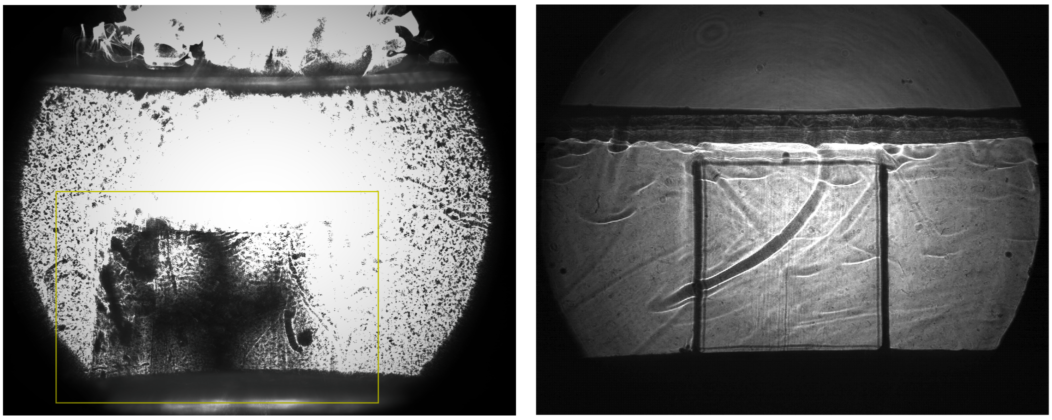

a) b)

Figure 4.11 Example of bubbles and flow lines visible when the immersion fluid has not settled.

After the immersion fluid preparation, the next step to follow is to place the specimen inside the tank and wait for the immersion fluid to settle down between 8-12 hours before the data acquisition. This procedure was followed to avoid as much as possible the bubbles and the liquid's flow lines that affect the images quality as it can be observed in Figure 4.11.

4.4 Experimental work with PMMA specimens

The description of the conducted experiments with different loads, immersion and averaging conditions carried out with 0.1 mW power as the light source for the experiments are summarized in Table 4.2 and the results of them are shown in the following sections.

Table 4.2 Experimental work with PMMA samples

№	Sample	Load	Immersion fluid	Averaging	Aim
1	PMMA 1 (batch 1)	None	None	3x3 pixels 4x4 pixels	Test the worst condition of refractive index matching.
2	PMMA 1 (batch 1)	None	Yes	3x3 pixels 4x4 pixels	Test the specimen unloaded but immersed in the refractive index matching fluid.
3	PMMA 1 (batch 1)	8.82 N	Yes	3x3 pixels 4x4 pixels	Test the specimen loaded and immersed in the refractive index matching fluid to see the difference induced by the stress by comparing experiment 1 and 2.
4	PMMA 2 (batch 1)	29.43 N	Yes	3x3 pixels 4x4 pixels	Test the specimen loaded with a higher load and immersed in the refractive index fluid to see the difference induced by a higher stress by comparing experiment 1 and 2 and 3.
5	PMMA 3 (batch 2)	8.82 N	Yes	3x3 pixels 4x4 pixels	Test the specimen loaded and immersed in the refractive index fluid to see the difference with an specimen from another batch of PMMA.
6	PMMA 4 (batch 2)	29.43 N	Yes	3x3 pixels 4x4 pixels	Test the specimen loaded with a higher load and immersed in the refractive index fluid to see the difference with the experiment 4 in the reconstruction results.

PMMA sample 1

The first experiment performed was with a PMMA cube from the manufactured batch. This sample was not exposed to the thermal cycle stress previously described and it was not immersed to the refractive index matching liquid. This was done in order to make a comparison of the results regarding the refractive index matching with the worst condition. The complete data acquisition and stress reconstruction for this and the following experiments was performed as shown in Figure 4.12.

Collection of 180 light intensity images where the rotation of the sample from 0 to 180 degrees in the *"Z"* axis in increments of 1 degree were taken.

↓

Cut and shift process, where measurements of the edges of the specimen in 5 different positions were done.

↓

Averaging process at a number of pixels (3 x 3 or 4 x 4) to reduce the amount of data processed by the program called "*Image – average.m*".

↓

The characteristic parameters calculation, using Fourier polarimetry.

↓

Stress reconstruction performed by the program "*Testrig*".

Figure 4.12 Data acquisition and stress reconstrucion process.

The images for the *"X"* axis at 0 and 45 degrees position of the specimen are presented in 4.13 a) and e). The cut and shift images are presented in Figure 4.13 b) and f). Then, the averaged images with two windows pixels of 3 by 3, Figure 4.13 c) and g), and 4 by 4, Figure 4.13 d) and h) are shown. Finally, the characteristic parameters calculations and the 3-D internal stress reconstruction results using the averaged images 3 by 3 and 4 by 4 are displayed in Figures 4.14, 4.15, 4.16 respectively.

For the second experiment with this sample, the tank where the sample was positioned was filled with the immersion fluid that matches the refractive index of the unstressed sample. To prepare the immersion fluid the unstressed sample was measured, giving a result of 20.112 in Abbe scale which equals to n=1.48777. The results for the PMMA sample 1 immersed and unstressed are shown in Figures 4.17, 4.18, 4.19 and 4.20.

The third experiment involved the stress treatment where a load of 8.82 N was applied during the thermal cycle, therefore the refractive index value change to 19.763 in Abbe scale which equals to n=1.48464.The result of this stress reconstruction are displayed in Figures 4.21, 4.22, 4.23 and 4.24.

PMMA sample 2

For the PMMA sample 2, which was the second manufactured cube, the thermal cycle was performed with a load of 29.43N, the refractive index measured with this stress was 19.663 in Abbe scale which equals to n=1.48374, therefore the immersion fluid was prepared for this refractive index. The methodology to acquire the data was the same as followed in the first experiment 4.4 and it will be the same for the upcoming experiments. The result of this stress reconstruction are displayed in Figures 4.25, 4.26, 4.27 and 4.28.

PMMA sample 3

For the PMMA sample 3, which was cut out from the square PMMA beam, the thermal cycle was performed with a load of 8.82 N, the refractive index measured with this stress was 20.241 in Abbe scale which equals to n=1.48892, therefore the immersion fluid was prepared for this refractive index. The result of this stress reconstruction are displayed in Figures 4.29, 4.30, 4.31 and 4.32.

PMMA sample 4

For the PMMA sample 4, which is the second cube cut out the square PMMA beam, the thermal cycle was performed with a load of 29.43N, the refractive index measured with this stress was 20.263 in Abbe scale which equals to n=1.48912, therefore the immersion fluid was prepared for this refractive index. The result of this stress reconstruction are displayed in Figures 4.33, 4.34, 4.35 and 4.36.

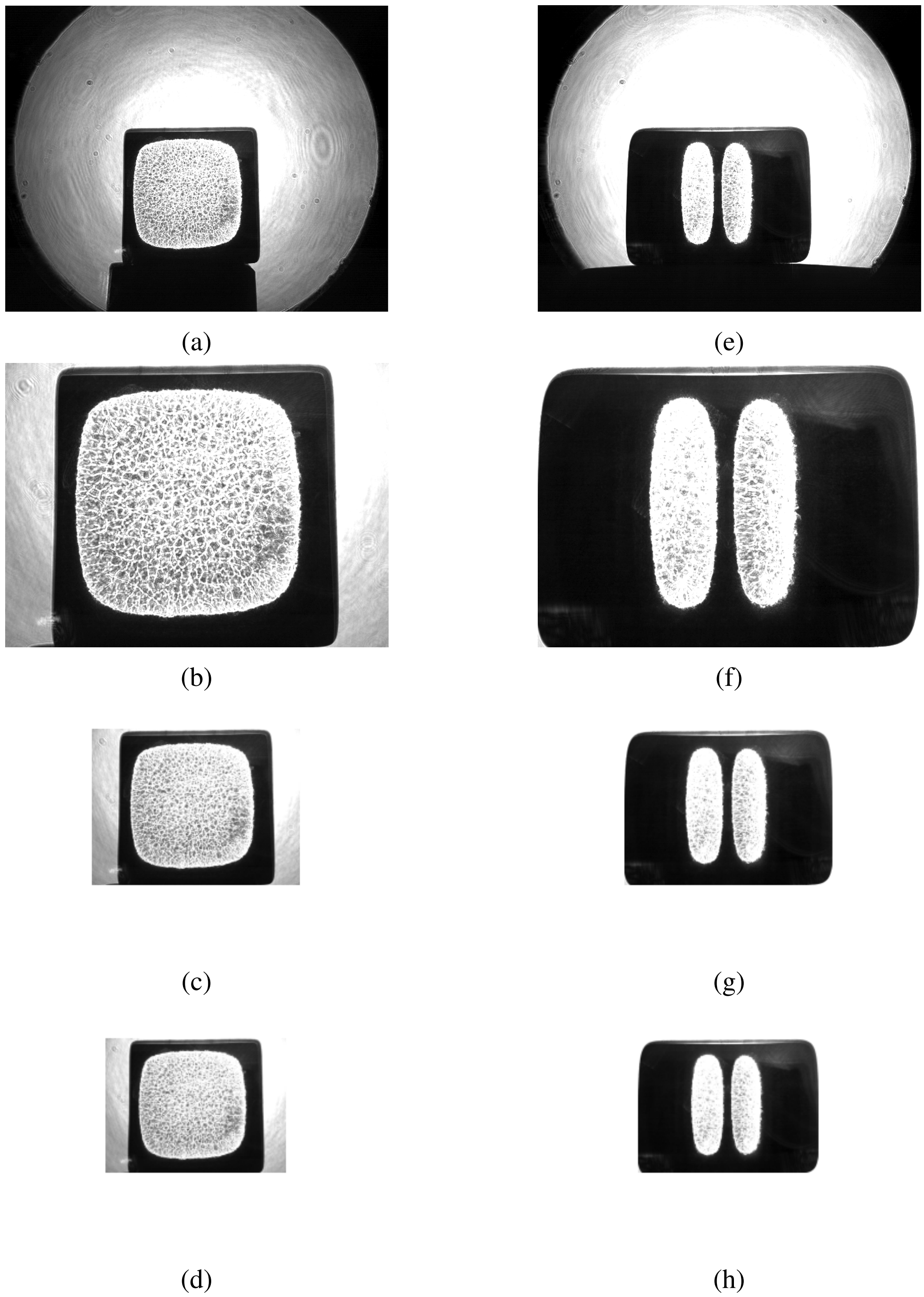

Figure 4.13 Light intensity images for experiment 1: unstressed and not immersed specimen with the polariser and analyser set at 0 and 20 degrees respectively. Where a) shows the data acquisition for PMMA 1 at 0 degrees and e) at 45 degrees, b) shows the cut image at 0 and f) at 45 degrees, c) shows the 3 by 3 pixels averaged images at 0 and g) at 45 degrees. Finally, d) shows the 4 by 4 pixels averaged images at 0 degrees and g) at 45 degrees.

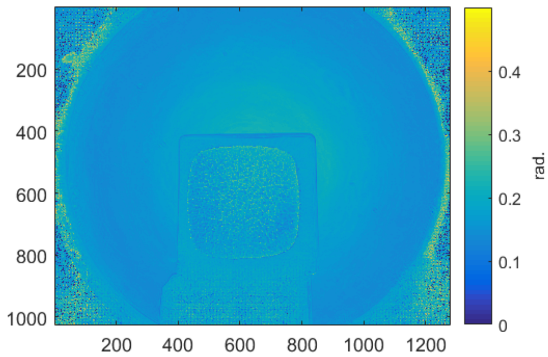

(a) Characteristic retardation at 0 degrees

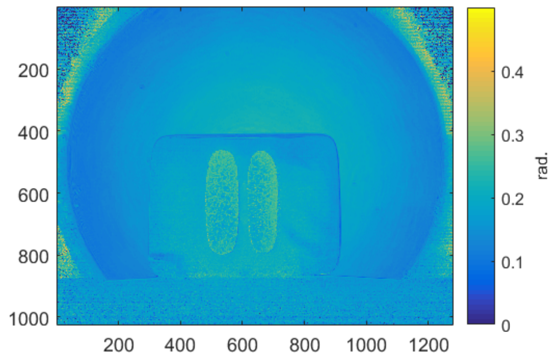

(d) Characteristic retardation at 45 degrees

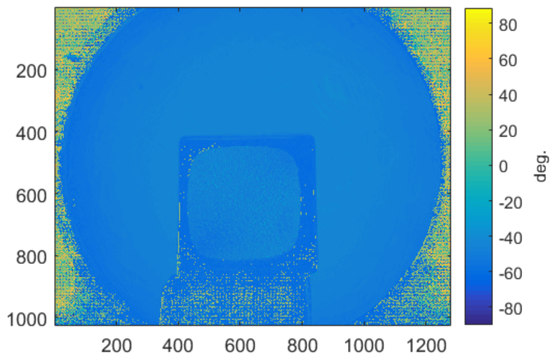

(b) Primary characteristic direction at 0 degrees

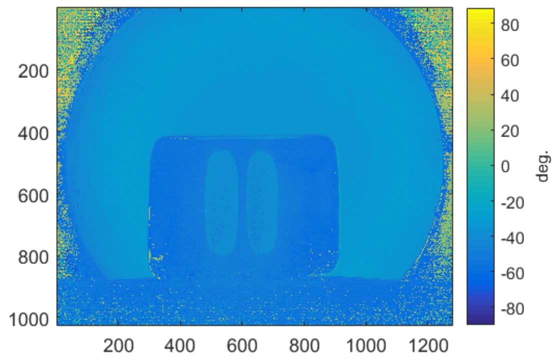

(e) Primary characteristic direction at 0 degrees

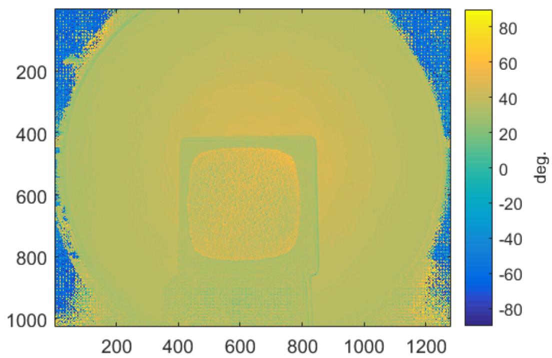

(c) Characteristic angle at 0 degrees

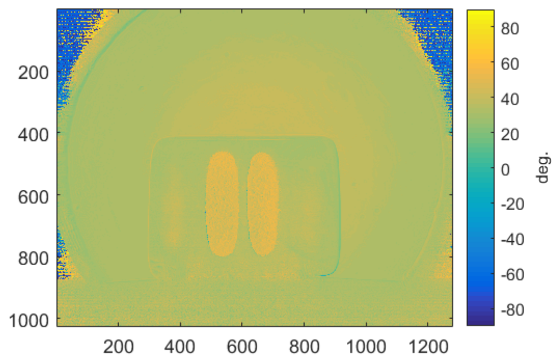

(f) Characteristic angle at 45 degrees.

Figure 4.14 Characteristic parameters calculation for experiment 1: unstressed and not immersed PMMA 1 at 0 degrees and 45 degrees position.

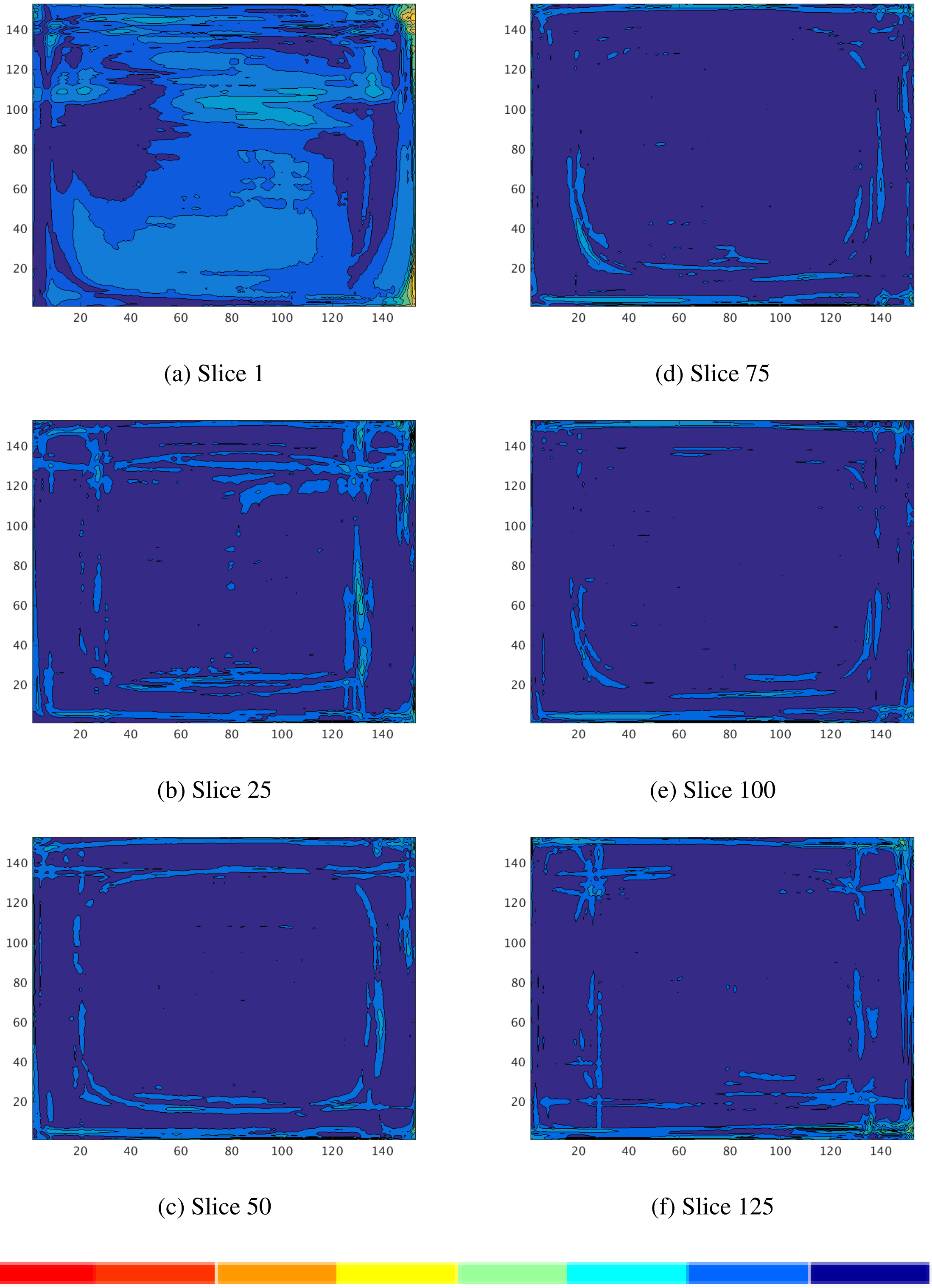

(a) Slice 1

(d) Slice 75

(b) Slice 25

(e) Slice 100

(c) Slice 50

(f) Slice 125

High stress Low stress

Figure 4.15 3-D reconstruction for experiment 1: unstressed and not immersed using 3 by 3 averaged images.

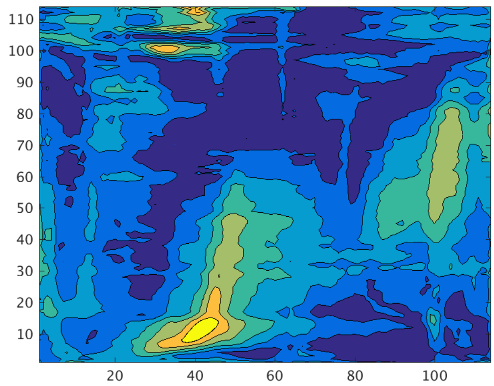

(a) Slice 1

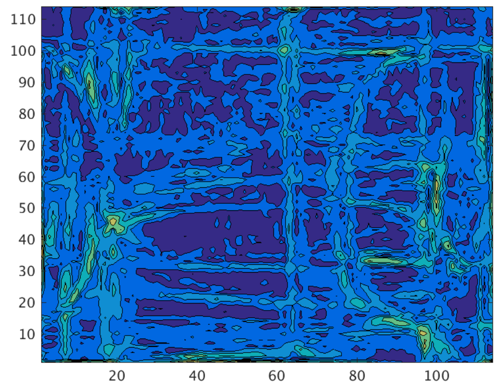

(d) Slice 57

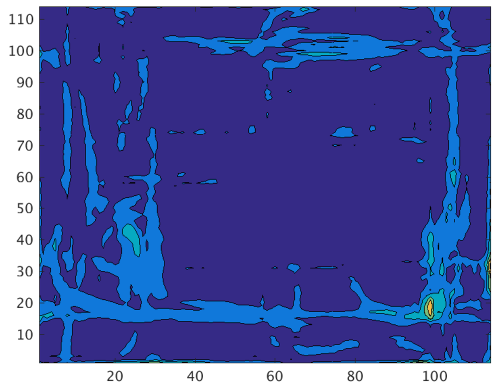

(b) Slice 19

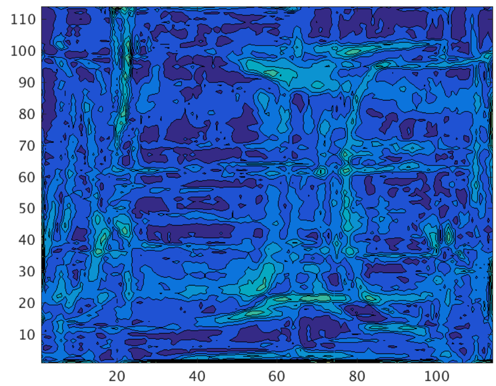

(e) Slice 76

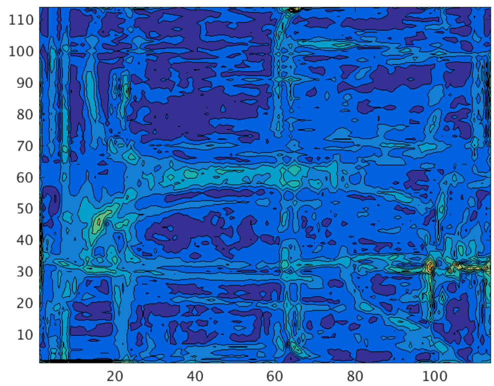

(c) Slice 38

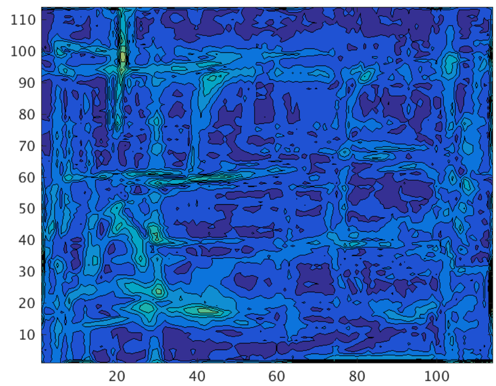

(f) Slice 95

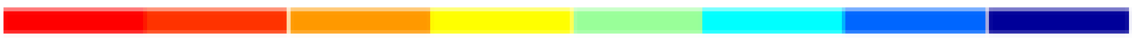

High stress Low stress

Figure 4.16 3-D reconstruction for experiment 1: unstressed and not immersed using 4 by 4 averaged images.

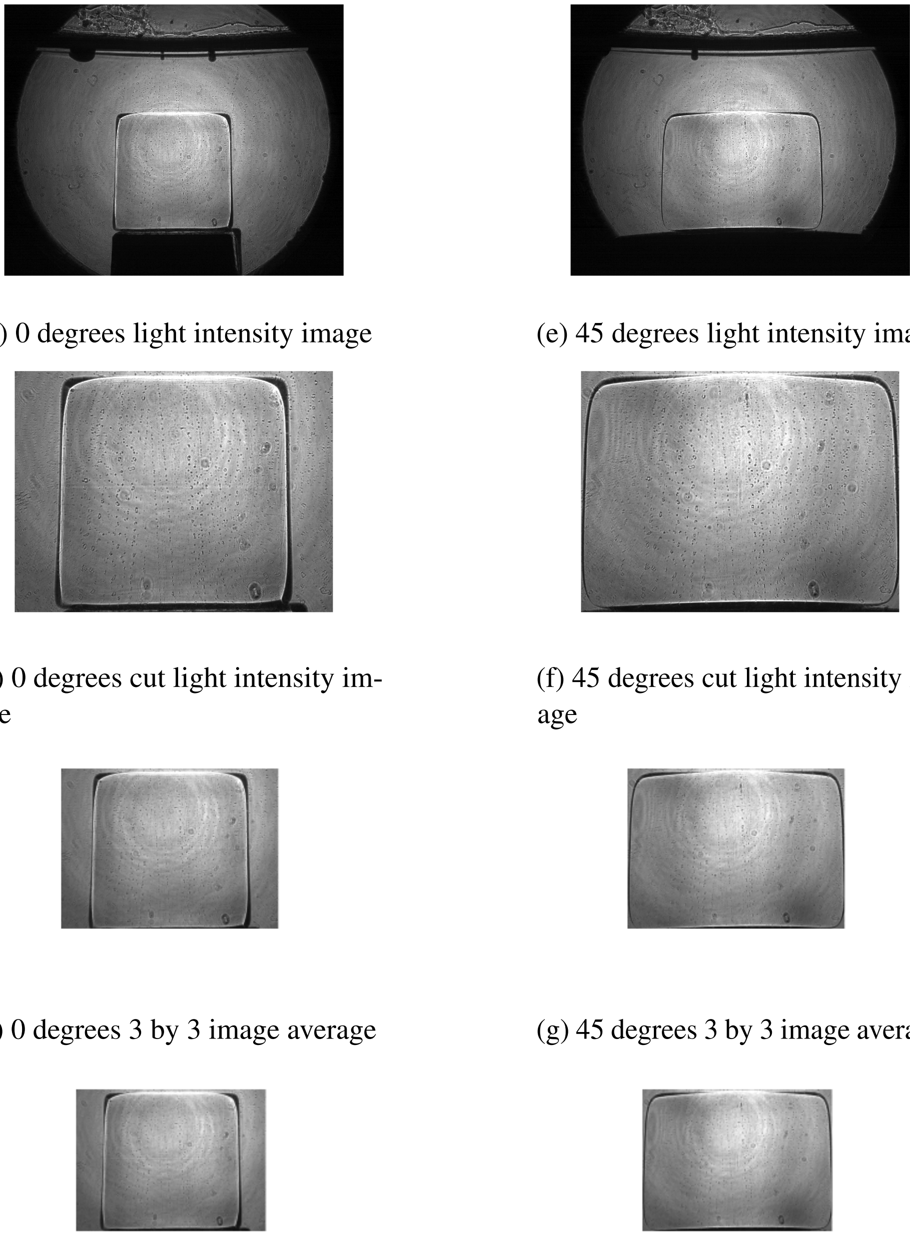

(a) 0 degrees light intensity image

(e) 45 degrees light intensity image

(b) 0 degrees cut light intensity image

(f) 45 degrees cut light intensity image

(c) 0 degrees 3 by 3 image average

(g) 45 degrees 3 by 3 image average

(d) 0 degrees 4 by 4 image average

(h) 45 degrees 4 by 4 image average

Figure 4.17 Light intensity images for experiment 2 unstressed and immersed with the polariser and analyser set at 0 degrees and 20 degrees respectively. Where a) shows the data acquisition for PMMA 1 at 0 degrees and e) at 45 degrees, b) shows the cut image at 0 degrees and f) at 45 degrees, c) shows the 3 by 3 pixels averaged images at 0 degrees and g) at 0 degrees. Finally, d) shows the 4 by 4 pixels averaged images at 0 degrees and g) at 45 degrees.

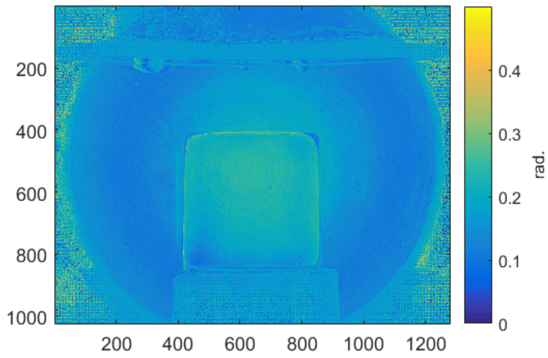

(a) Characteristic retardation at 0 degrees

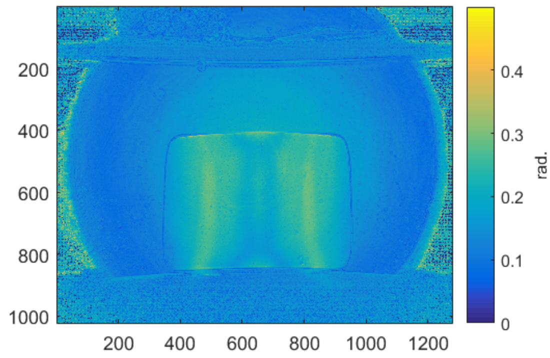

(d) Characteristic retardation at 45 degrees

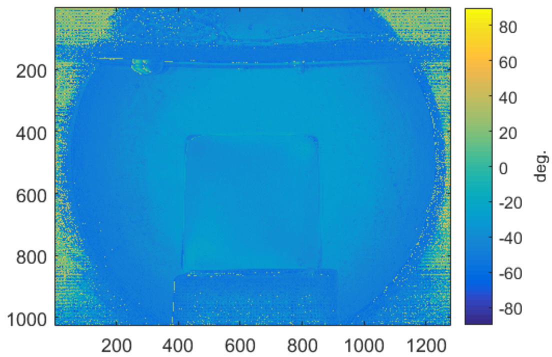

(b) Primary characteristic direction at 0 degrees

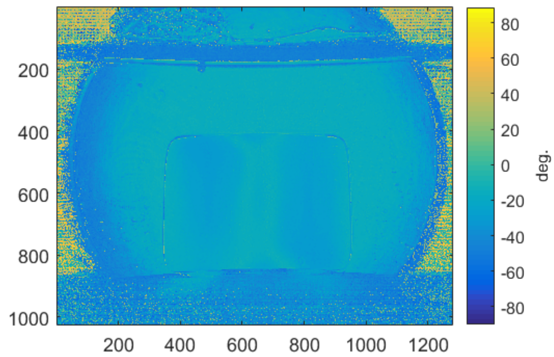

(e) Primary characteristic direction at 45 degrees

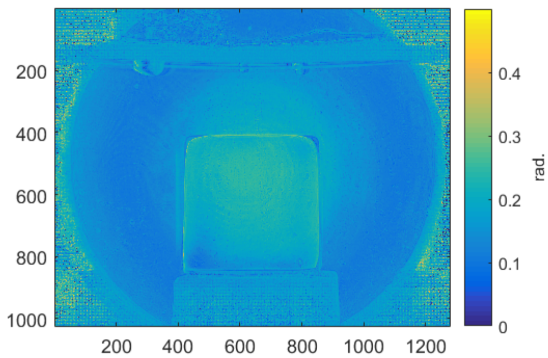

(c) Characteristic angle at 0 degrees

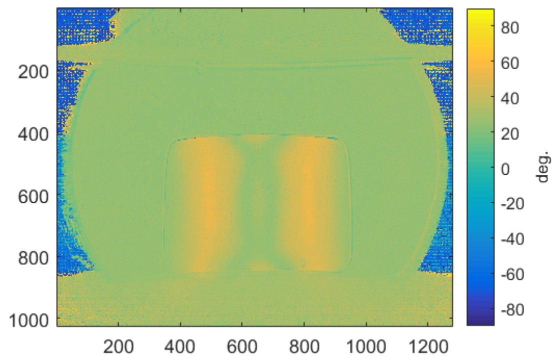

(f) Characteristic angle at 45 degrees

Figure 4.18 Characteristic parameters calculation for experiment 2: unstressed and immersed PMMA 1 at 0 degrees and 45 degrees position.

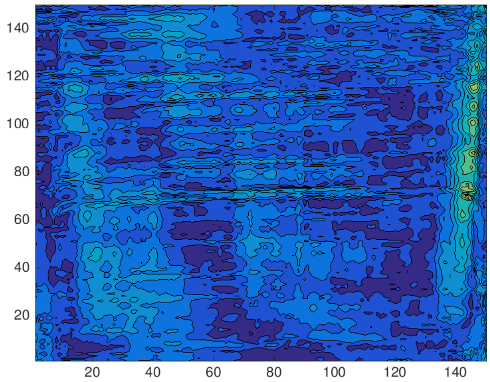

(a) Slice 1

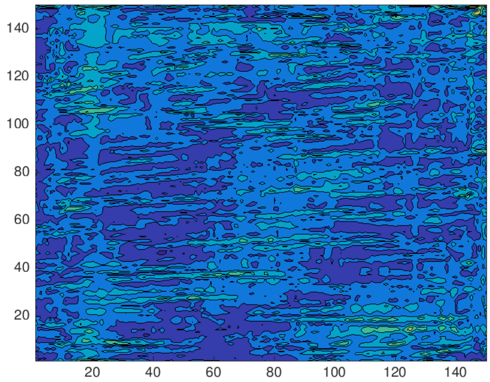

(b) Slice 25

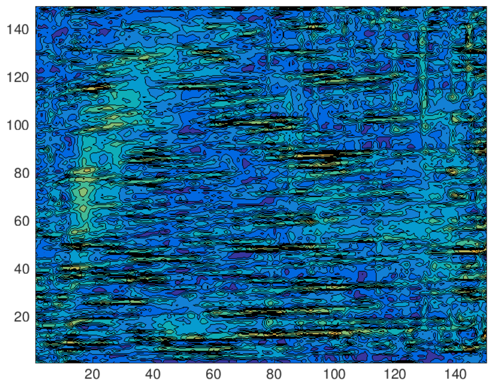

(c) Slice 50

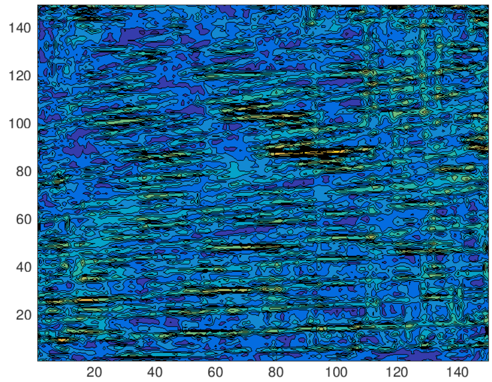

(d) Slice 75

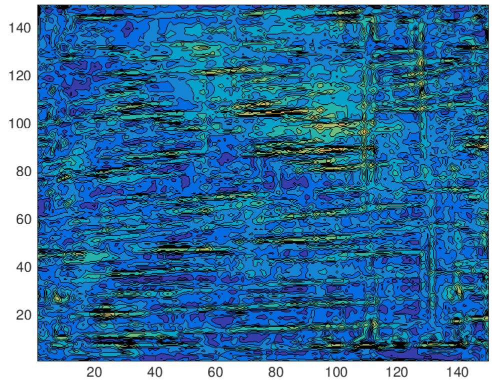

(e) Slice 100

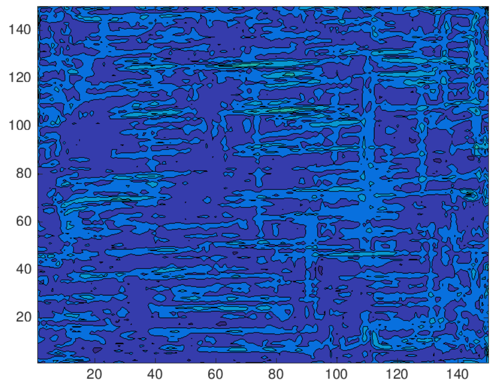

(f) Slice 125

High stress Low stress

Figure 4.19 3-D reconstruction for experiment 2: unstressed and immersed using 3 by 3 averaged images.

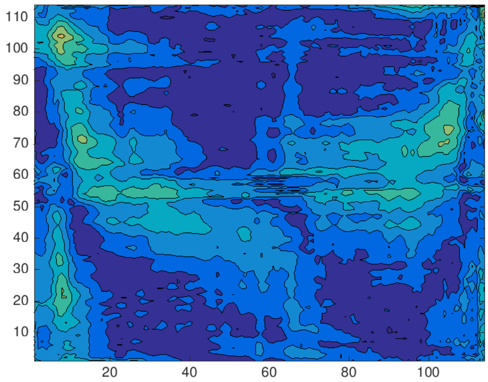

(a) Slice 1

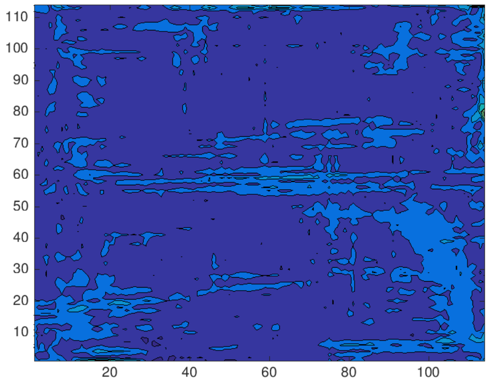

(b) Slice 19

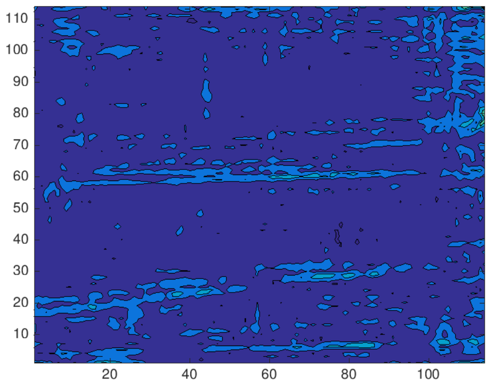

(c) Slice 38

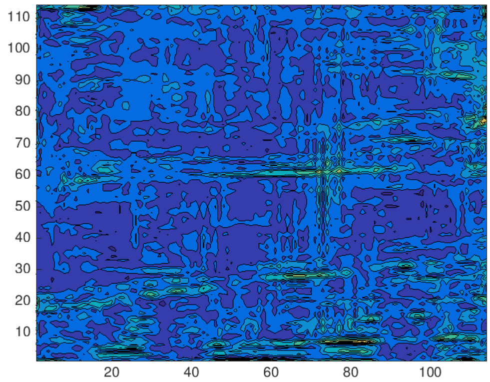

(d) Slice 57

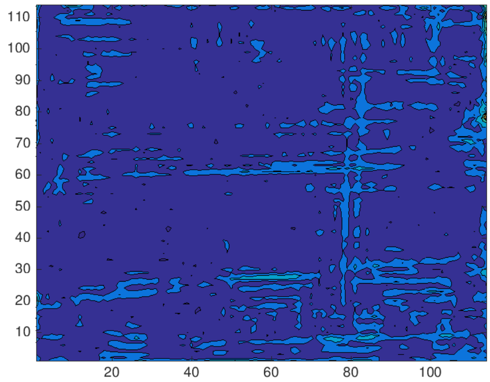

(e) Slice 76

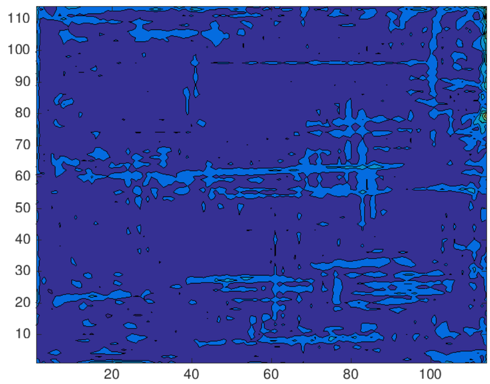

(f) Slice 95

High stress Low stress

Figure 4.20 3-D reconstruction for PMMA 2: unstressed and immersed using 4 by 4 averaged images.

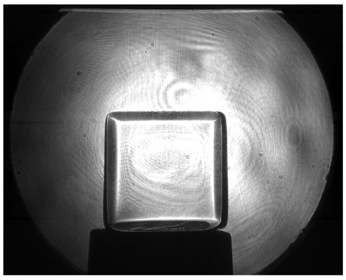

(a) 0 degrees light intensity image

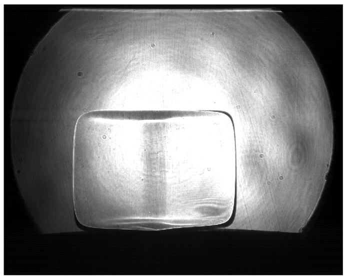

(e) 45 degrees light intensity image

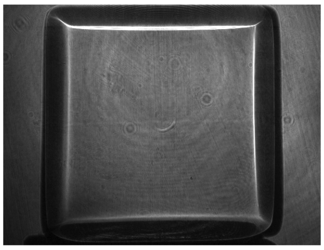

(b) 0 degrees cut light intensity image

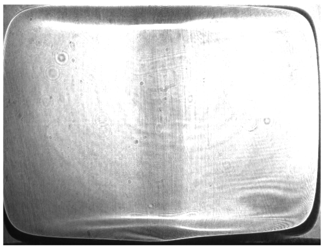

(f) 45 degrees cut light intensity image

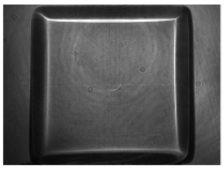

(c) 0 degrees 3 by 3 image average

(g) 45 degrees 3 by 3 image average

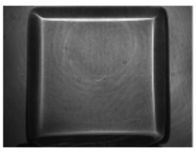

(d) 0 degrees 4 by 4 image average

(h) 45 degrees 4 by 4 image average

Figure 4.21 Light intensity images for experiment 3: stressed and immersed specimen with the polariser and analyser set at 0 degrees and 20 degrees respectively. Where a) shows the data acquisition for PMMA 1 at 0 degrees and e) at 45 degrees, b) shows the cut image at 0 degrees and f) at 45 degrees, c) shows the 3 by 3 pixels averaged images at 0 degrees and g) at 45 degrees.

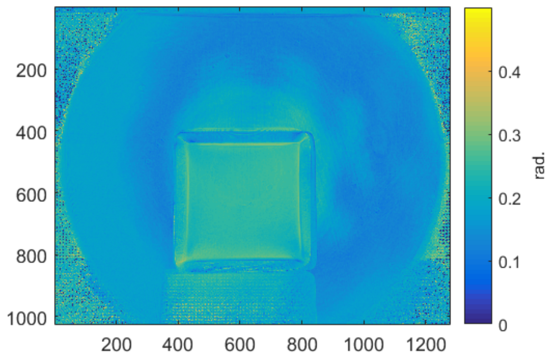

(a) Characteristic retardation at 0 degrees

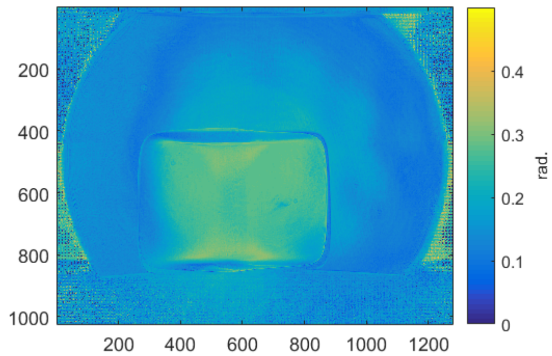

(d) Characteristic retardation at 45 degrees

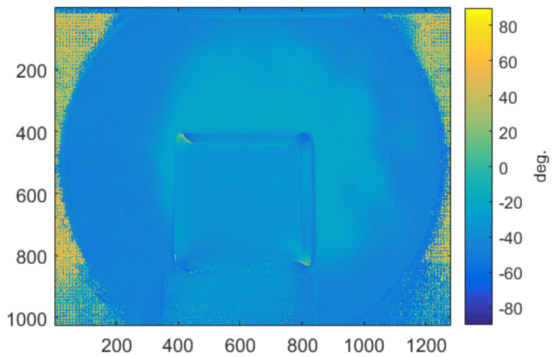

(b) Primary characteristic direction at 0 degrees

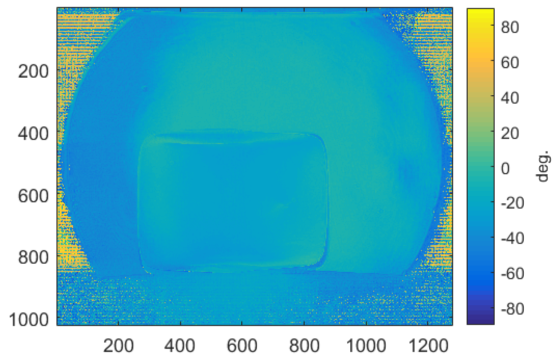

(e) Primary characteristic direction at 45 degrees

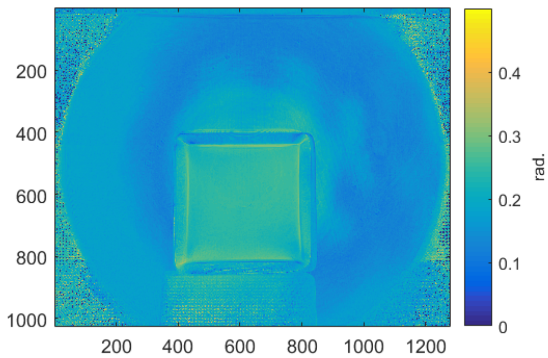

(c) Characteristic angle at 0 degrees

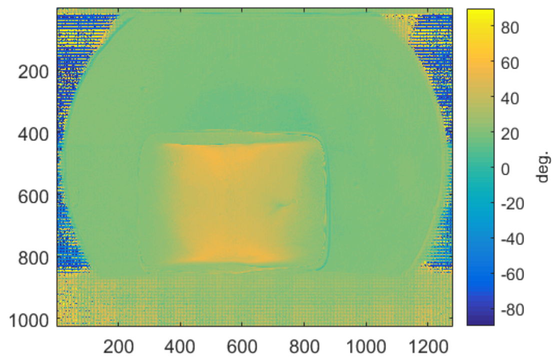

(f) Characteristic angle at 45 degrees

Figure 4.22 Characteristic parameters calculation for experiment 3: stressed and immersed PMMA1 at 0 degrees and 45 degrees position.

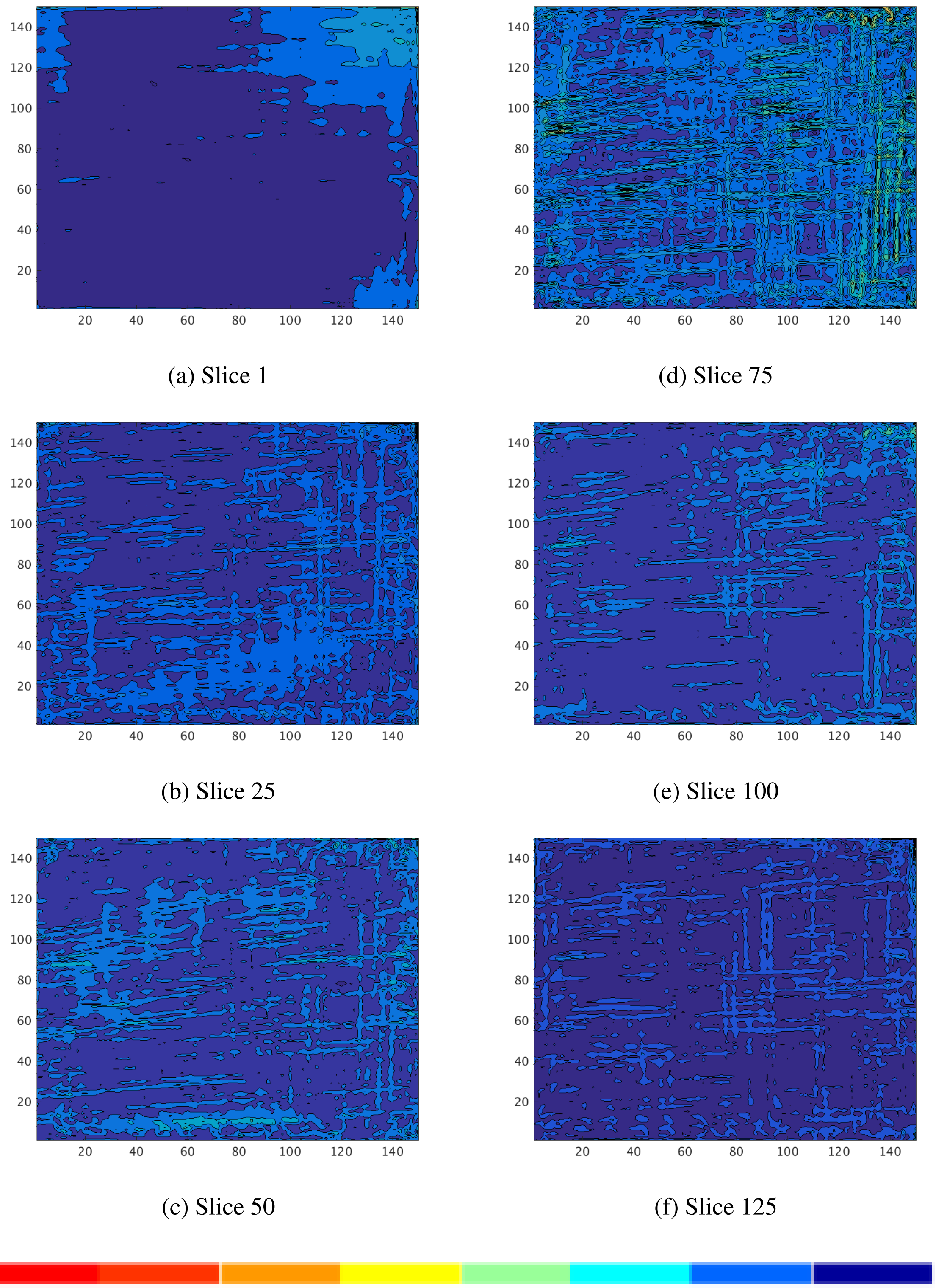

(a) Slice 1

(d) Slice 75

(b) Slice 25

(e) Slice 100

(c) Slice 50

(f) Slice 125

High stress

Low stress

Figure 4.23 3-D reconstruction for PMMA 3: stressed and immersed using 3 by 3 averaged images.

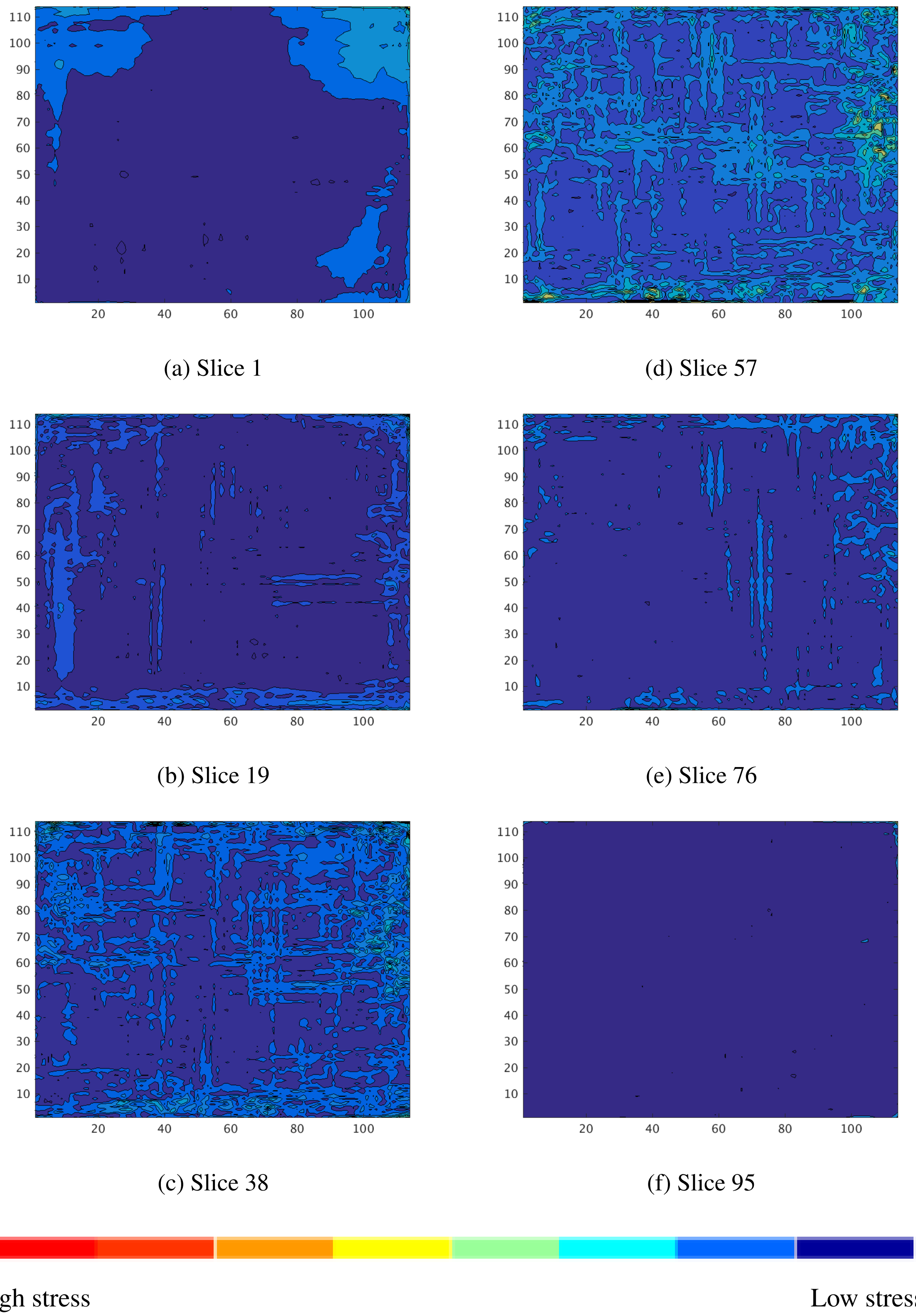

(a) Slice 1 (d) Slice 57

(b) Slice 19 (e) Slice 76

(c) Slice 38 (f) Slice 95

Figure 4.24 3-D reconstruction for PMMA 3: immersed and stressed using 4 by 4 averaged images.

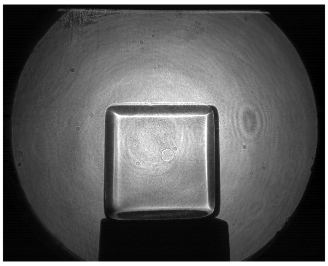

(a) 0 degrees light intensity image

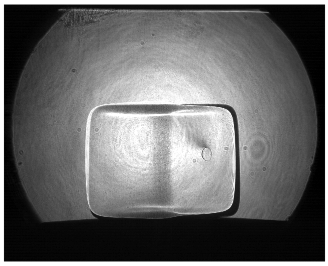

(e) 45 degrees light intensity image

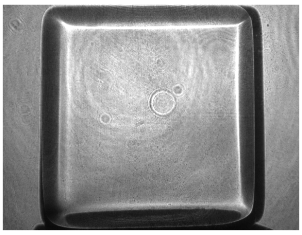

(b) 0 degrees cut light intensity image

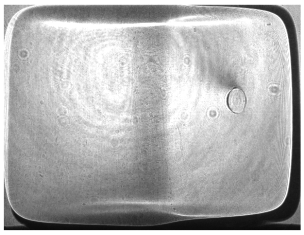

(f) 45 degrees cut light intensity image

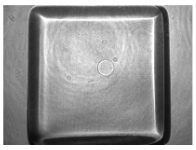

(c) 0 degrees 3 by 3 image average

(g) 45 degrees 3 by 3 image average

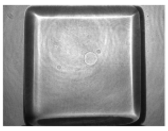

(d) 0 degrees 4 by 4 image average

(h) 45 degrees 4 by 4 image average

Figure 4.25 Light intensity images for experiment 4: stressed and immersed specimen with the polariser and analyser set at 0 degrees and 20 degrees respectively. Where a) shows the data acquisition for PMMA 2 at 0 degrees and e) at 45 degrees, b) shows the cut image at 0 degrees and f) at 45 degrees, c) shows the 3 by 3 pixels averaged images at 0 degrees and g) at 45 degrees.

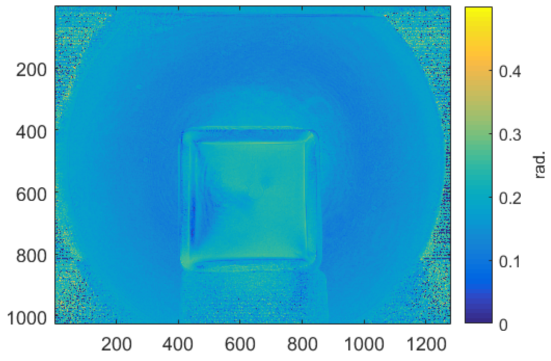

(a) Characteristic retardation at 0 degrees

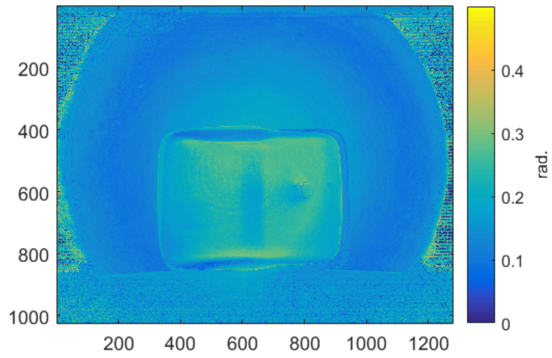

(d) Characteristic retardation at 45 degrees

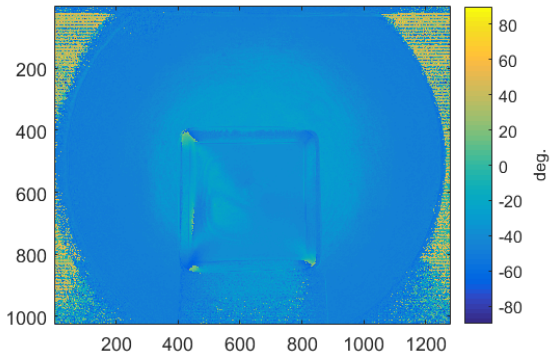

(b) Primary characteristic direction at 0 degrees

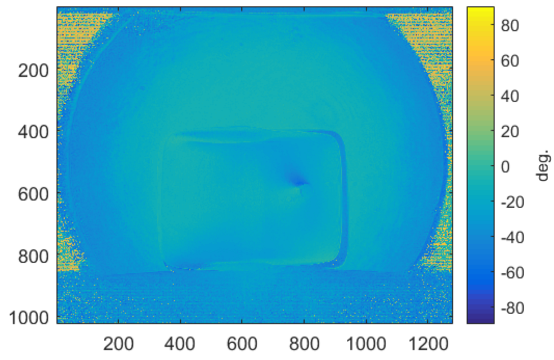

(e) Primary characteristic direction at 0 degrees

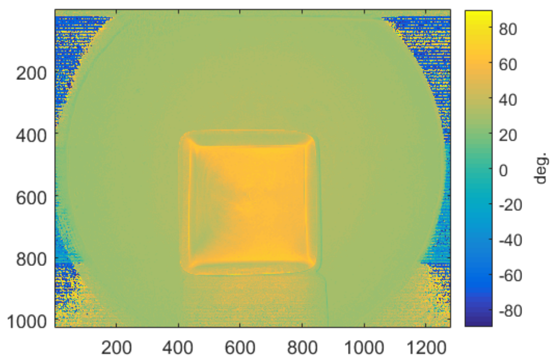

(c) Characteristic angle at 0 degrees

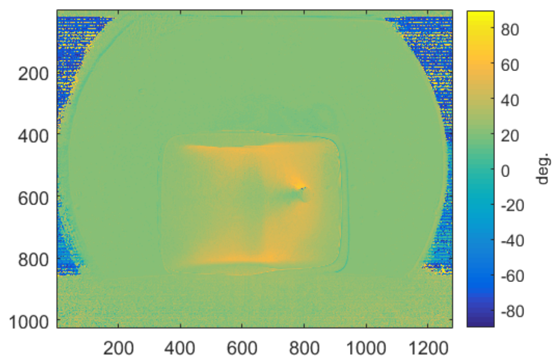

(f) Characteristic angle at 45 degrees

Figure 4.26 Characteristic parameters calculation for experiment 4: stressed and immersed PMMA 2 at 0 degrees and 45 degrees position.

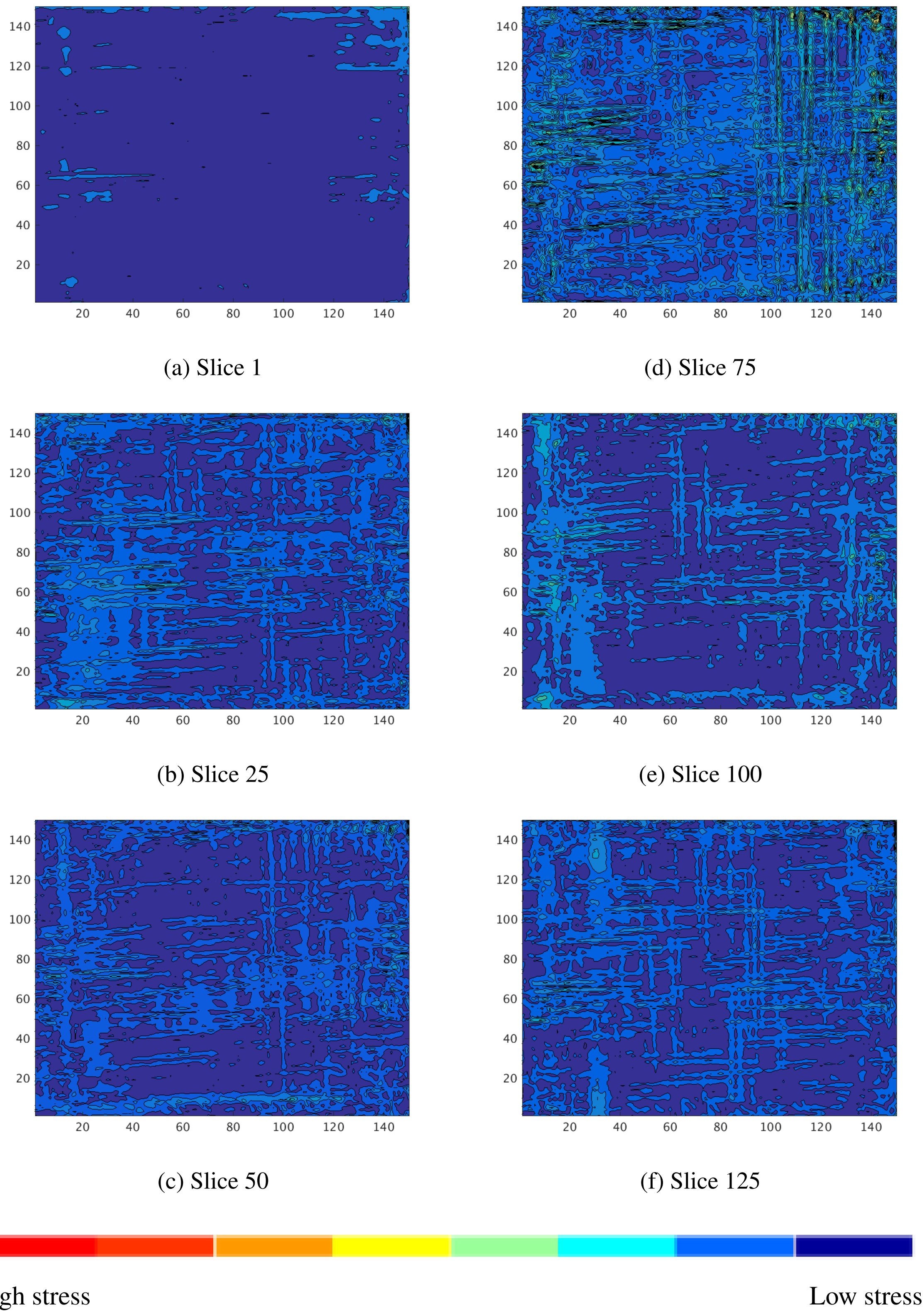

Figure 4.27 3-D reconstruction for PMMA 2: immersed and stressed using 3 by 3 averaged images.

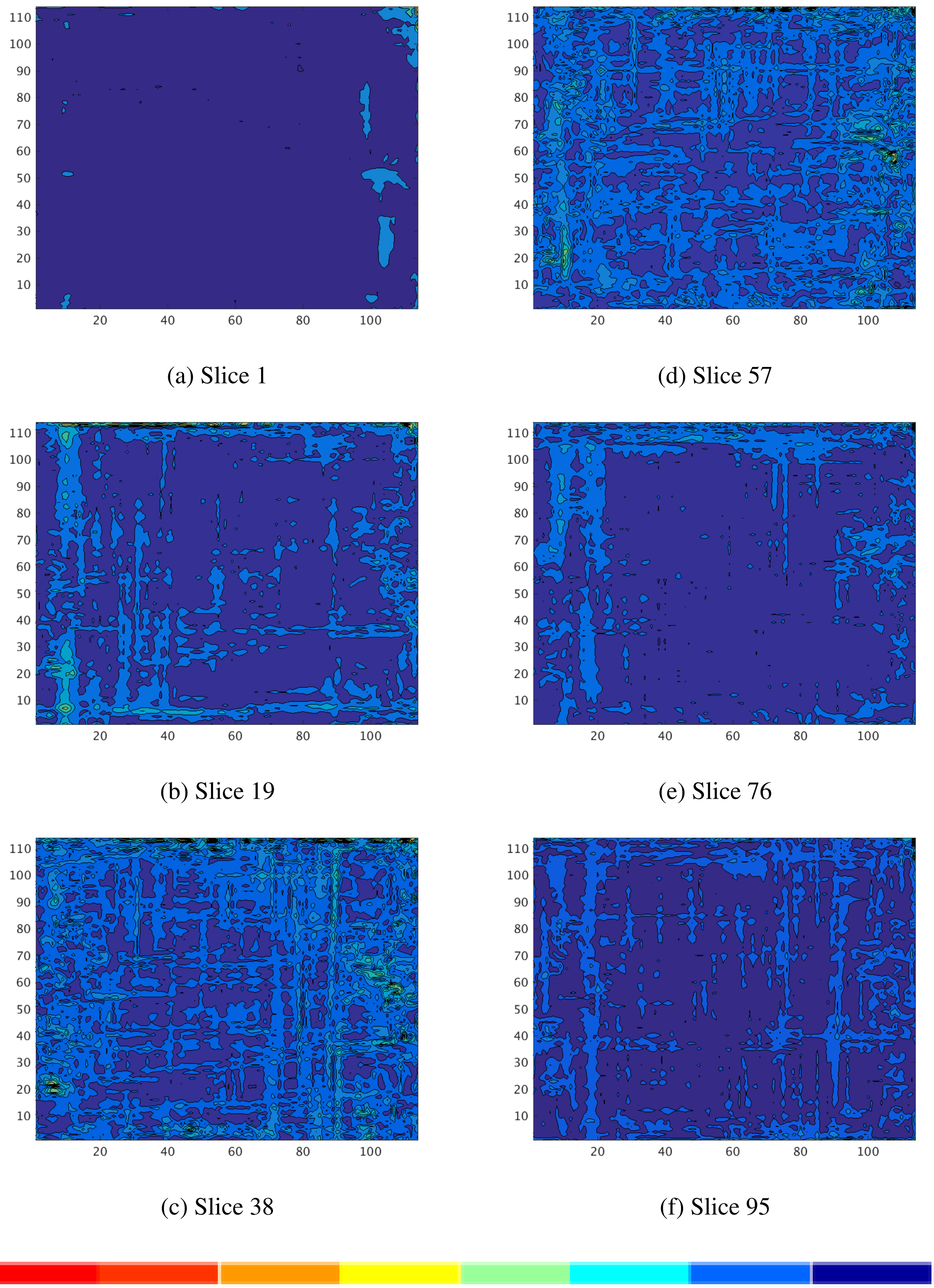

(a) Slice 1

(d) Slice 57

(b) Slice 19

(e) Slice 76

(c) Slice 38

(f) Slice 95

High stress Low stress

Figure 4.28 3-D reconstruction for PMMA 2: immersed and stressed using 4 by 4 averaged images.

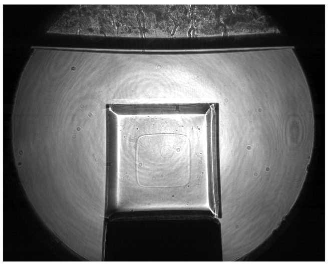

(a) 0 degrees light intensity image

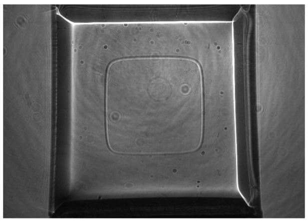

(b) 0 degrees cut light intensity image

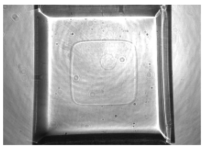

(c) 0 degrees 3 by 3 image average

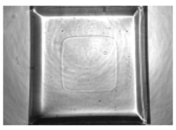

(d) 0 degrees 4 by 4 image average

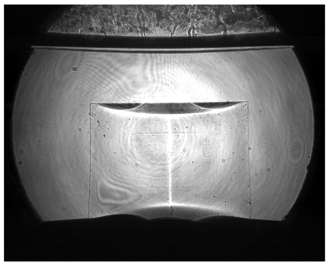

(e) 45 degrees light intensity image

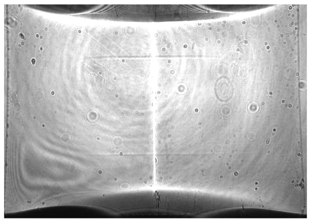

(f) 45 degrees cut light intensity image

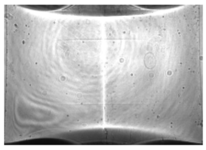

(g) 45 degrees 3 by 3 image average

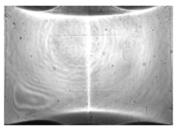

(h) 45 degrees 4 by 4 image average

Figure 4.29 Light intensity images for experiment 5: stressed and immersed specimen with the polariser and analyser set at 0 degrees and 20 degrees respectively. Where a) shows the data acquisition for PMMA 3 at 0 degrees and e) at 45 degrees, b) shows the cut image at 0 degrees and f) at 45 degrees, c) shows the 3 by 3 pixels averaged images at 0 degrees and g) at 45 degrees.

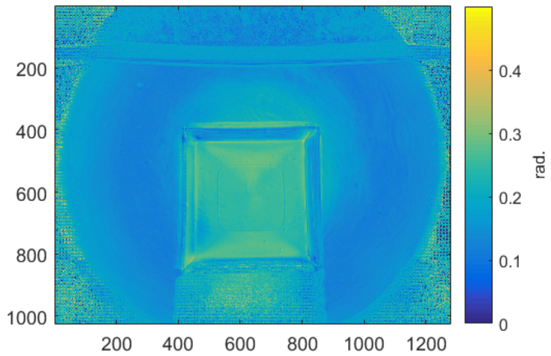

(a) Characteristic retardation at 0 degrees

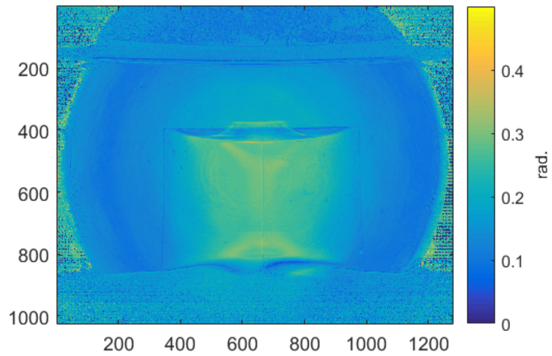

(d) Characteristic retardation at 45 degrees

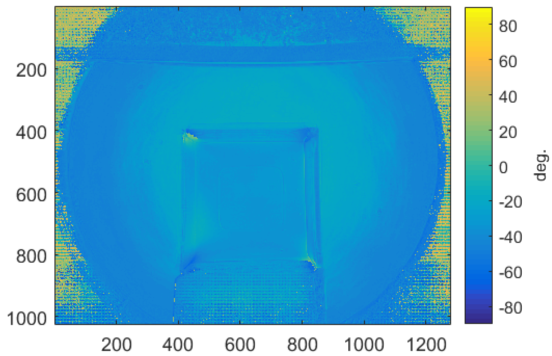

(b) Primary characteristic direction at 0 degrees

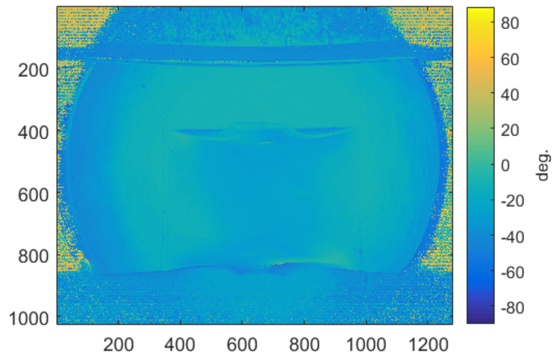

(e) Primary characteristic direction at 45 degrees

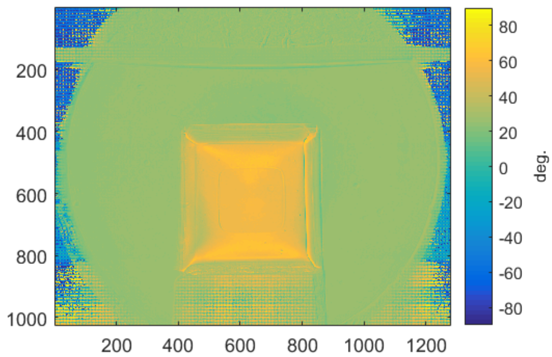

(c) Characteristic angle at 0 degrees

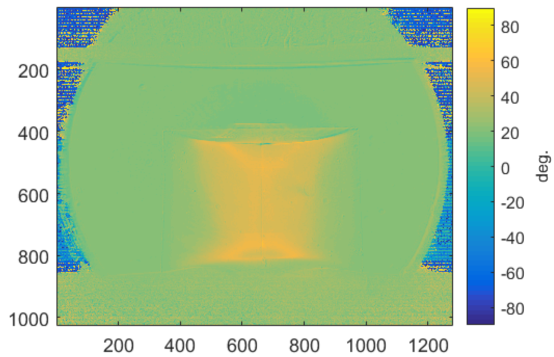

(f) Characteristic angle at 45 degrees

Figure 4.30 Characteristic parameters calculation for experiment 5: stressed and immersed PMMA 3 at 0 degrees and 45 degrees position.

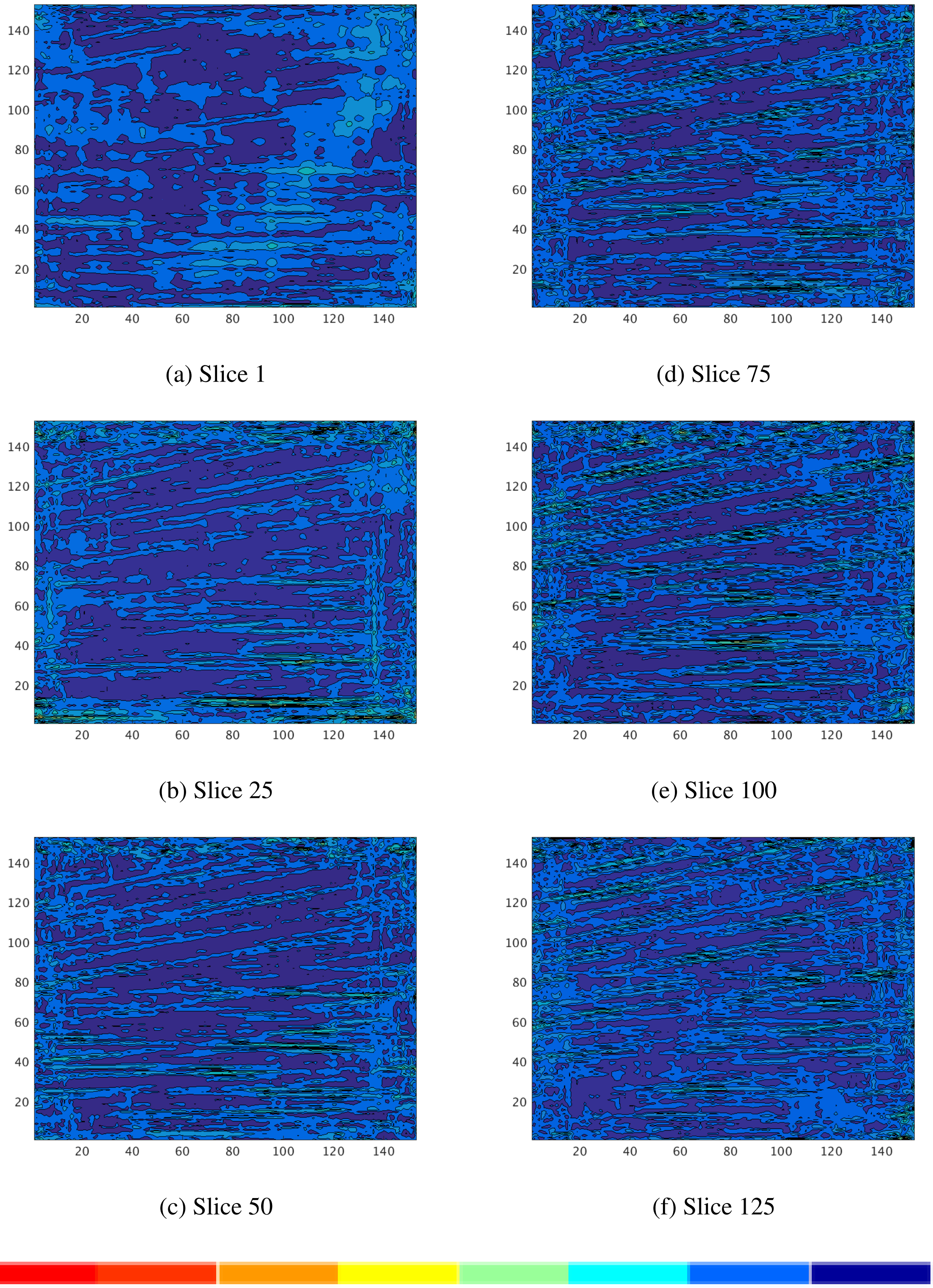

(a) Slice 1

(d) Slice 75

(b) Slice 25

(e) Slice 100

(c) Slice 50

(f) Slice 125

High stress

Low stress

Figure 4.31 3-D reconstruction for PMMA 3: immersed and stressed using 3 by 3 averaged images.

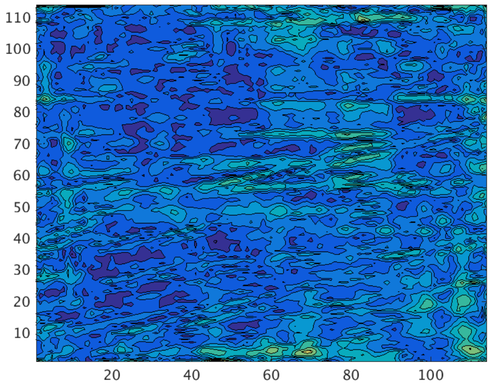

(a) Slice 1

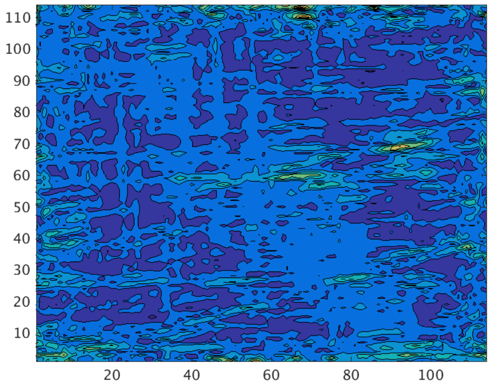

(b) Slice 19

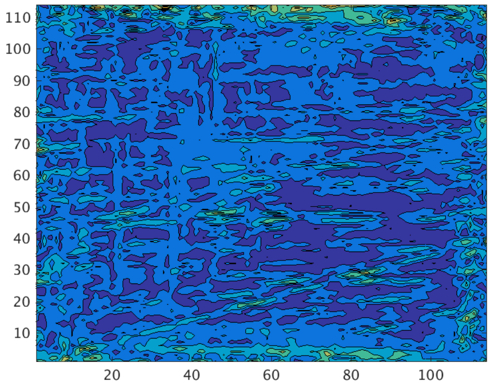

(c) Slice 38

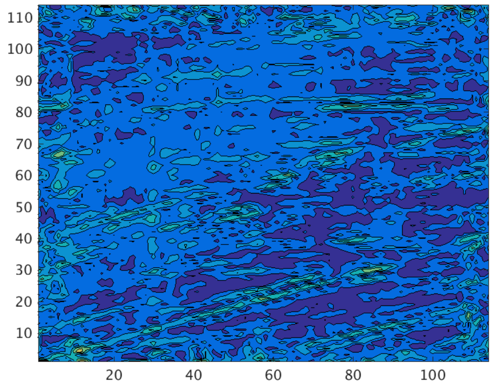

(d) Slice 57

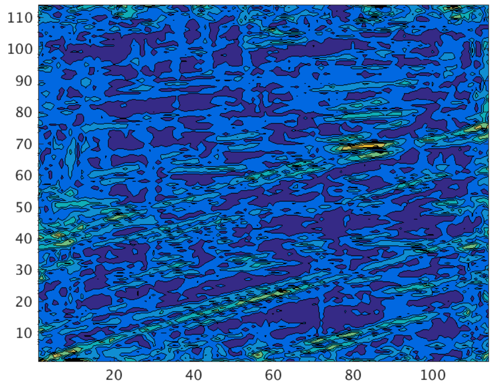

(e) Slice 76

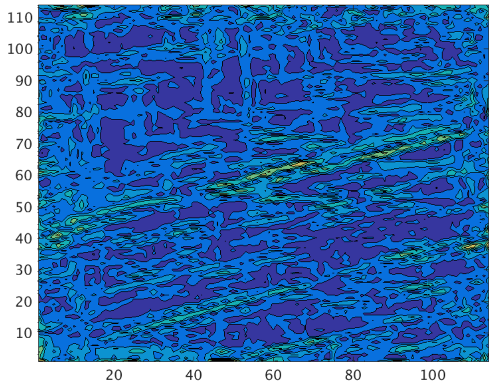

(f) Slice 95

High stress Low stress

Figure 4.32 3-D reconstruction for PMMA 3: immersed and stressed using 4 by 4 averaged images.

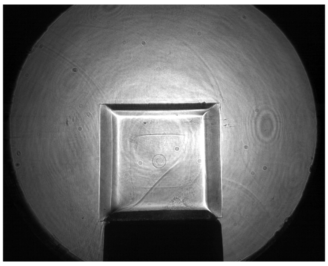

(a) 0 degrees light intensity image

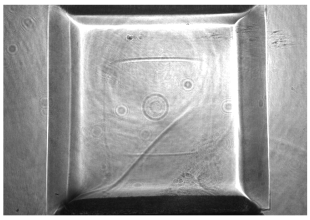

(b) 0 degrees cut light intensity image

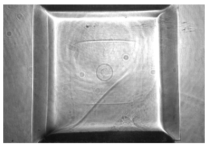

(c) 0 degrees 3 by 3 image average

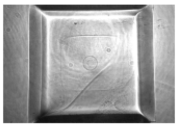

(d) 0 degrees 4 by 4 image average

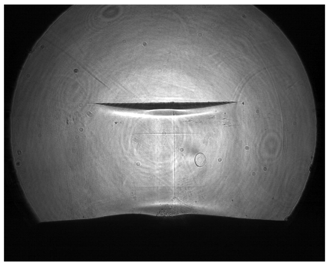

(e) 0 degrees light intensity image

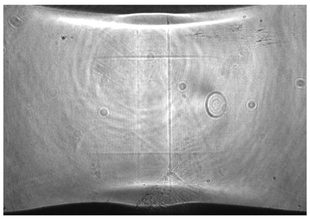

(f) 0 degrees cut light intensity image

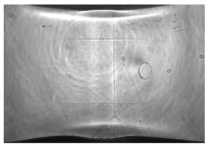

(g) 45 degrees 3 by 3 image average

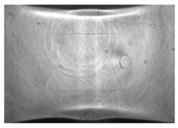

(h) 45 degrees 4 by 4 image average

Figure 4.33 Light intensity images for experiment 6: stressed and immersed specimen with the polariser and analyser set at 0 degrees and 20 degrees respectively. Where a) shows the data acquisition for PMMA 4 at 0 degrees and e) at 45 degrees, b) shows the cut image at 0 degrees and f) at 45 degrees, c) shows the 3 by 3 pixels averaged images at 0 degrees and g) at 45 degrees.

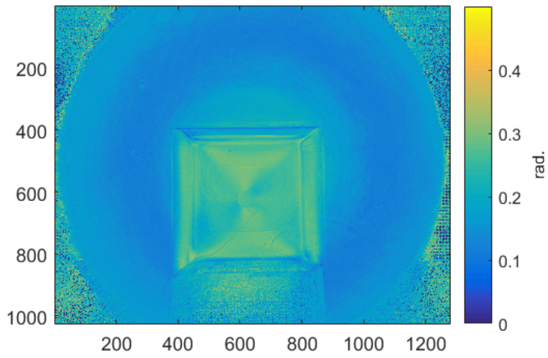

(a) Characteristic retardation at 0 degrees

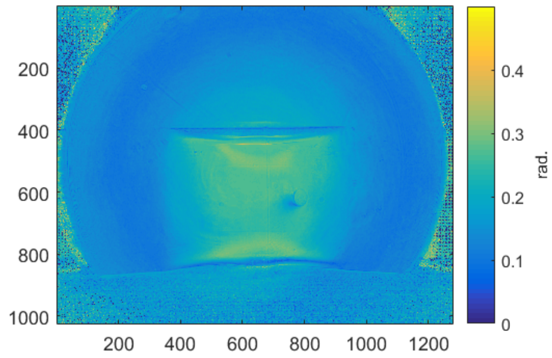

(d) Characteristic retardation at 45 degrees

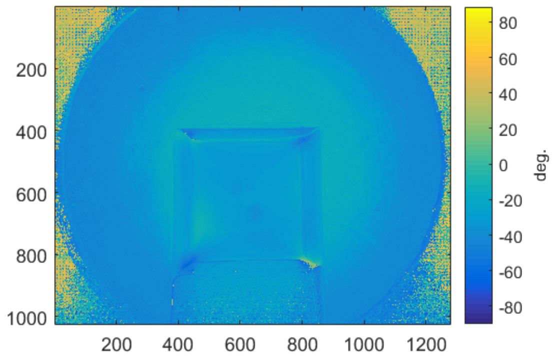

(b) Primary characteristic direction at 0 degrees

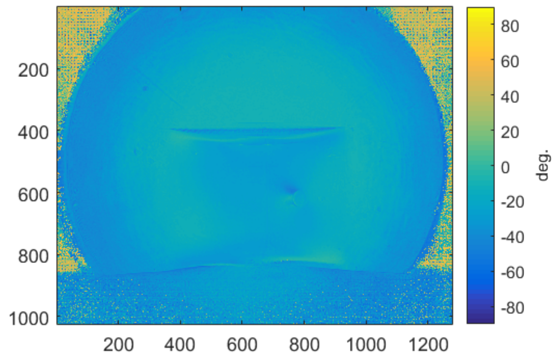

(e) Primary characteristic direction at 0 degrees

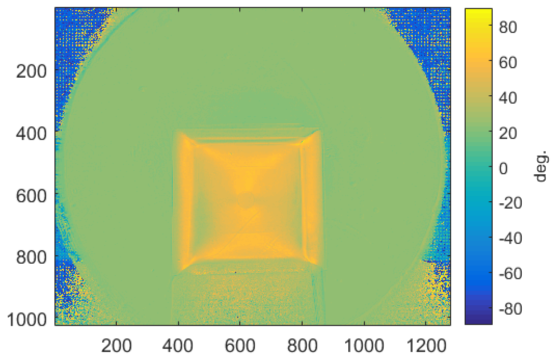

(c) Characteristic angle at 0 degrees

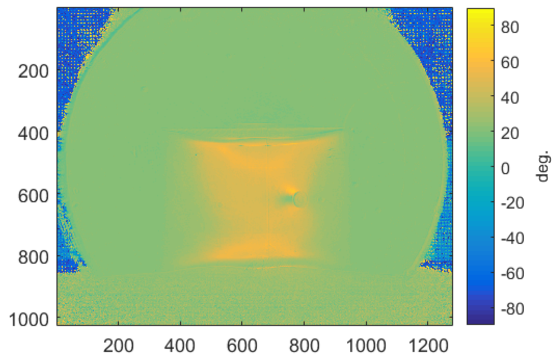

(f) Characteristic angle at 45 degrees

Figure 4.34 Characteristic parameters calculation for experiment 6: stressed and immersed PMMA 4 at 0 degrees and 45 degrees position.

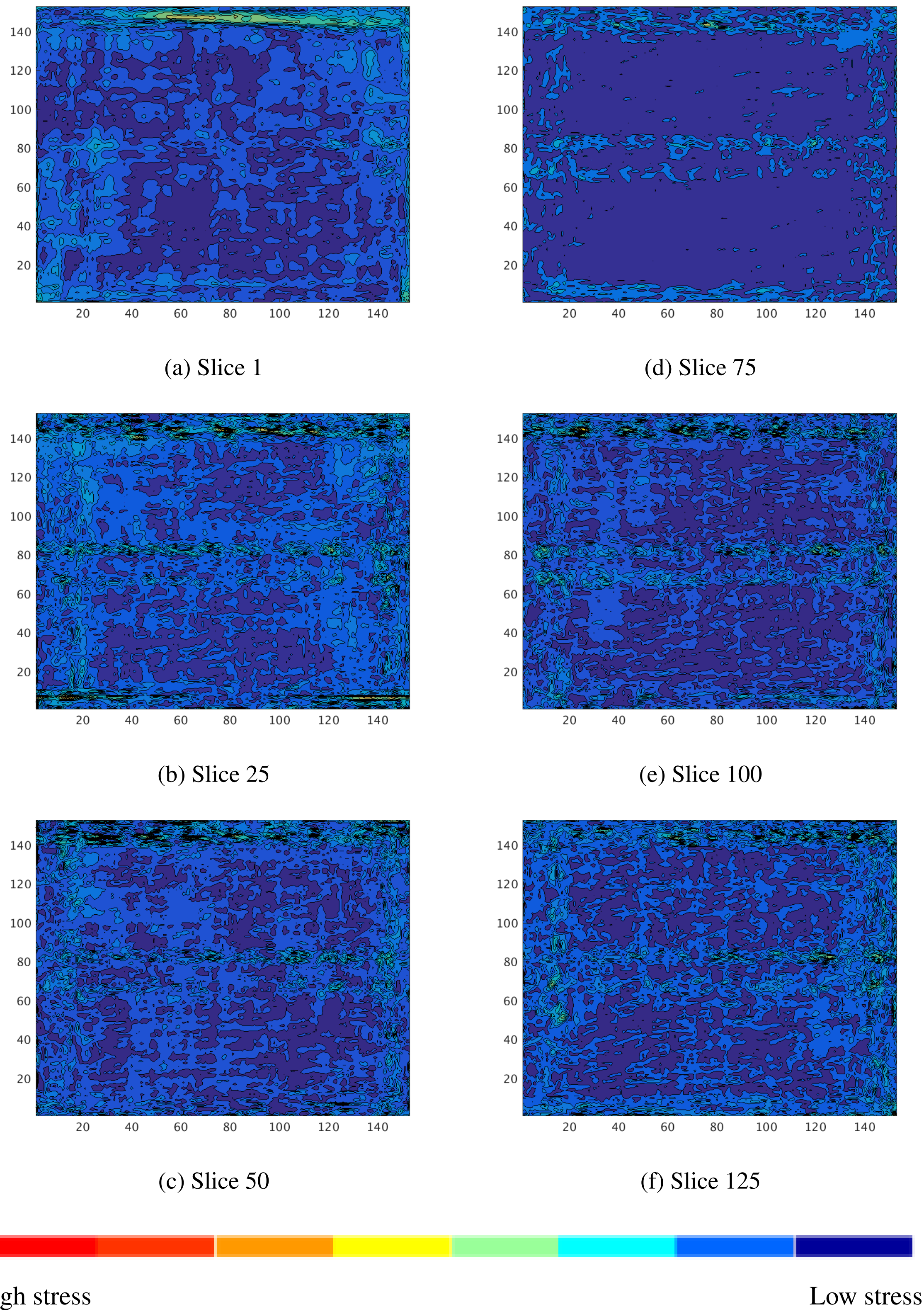

(a) Slice 1
(d) Slice 75
(b) Slice 25
(e) Slice 100
(c) Slice 50
(f) Slice 125

Figure 4.35 3-D reconstruction for PMMA 4: immersed and stressed using 3 by 3 averaged images.

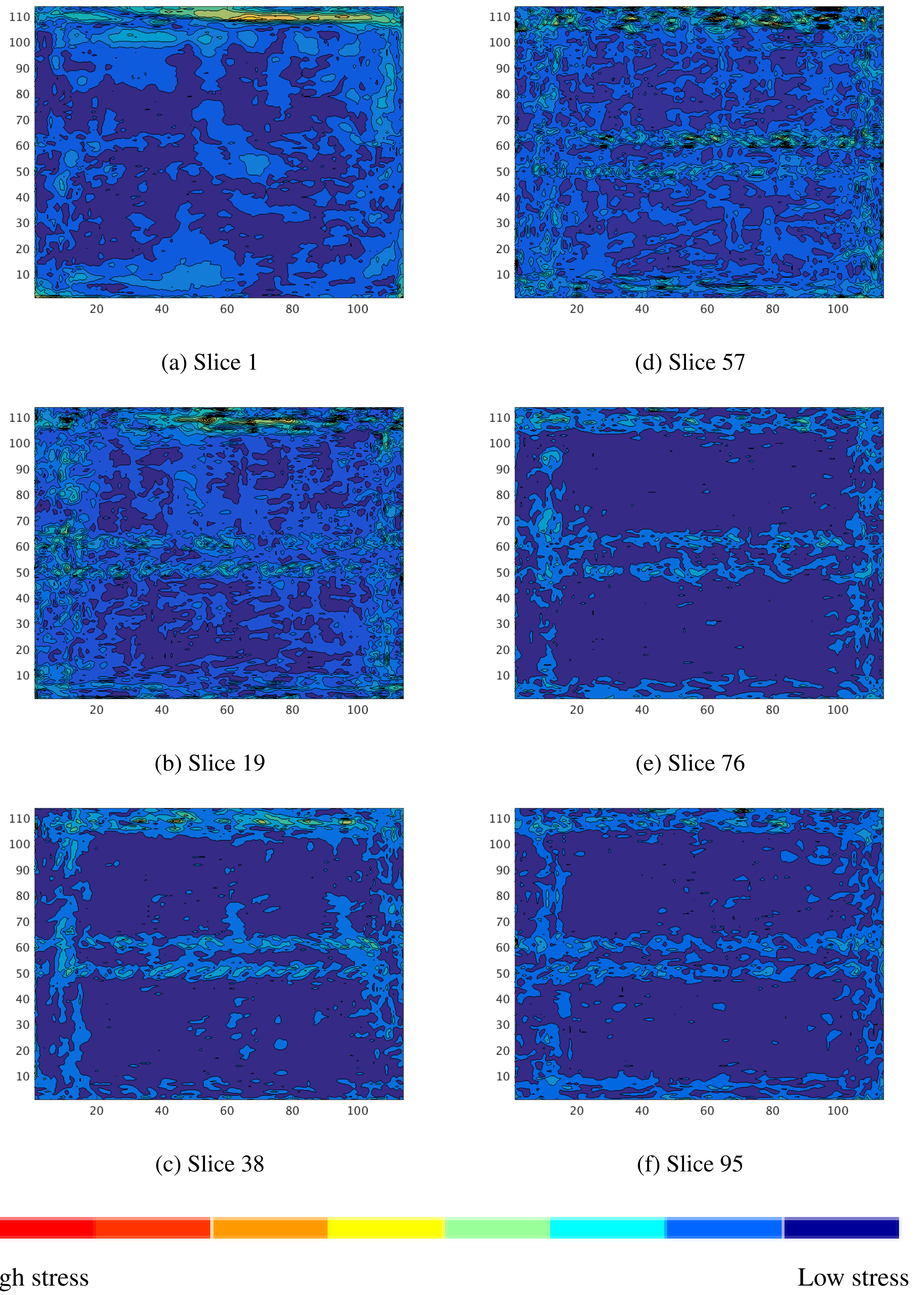

(a) Slice 1

(b) Slice 19

(c) Slice 38

(d) Slice 57

(e) Slice 76

(f) Slice 95

Figure 4.36 3-D reconstruction for PMMA 4: immersed and stressed using 4 by 4 averaged images.

4.5 Discussion of the results

Experiment 1 was performed on a manufactured cube, as shown in Table 4.2. This sample was tested under the worst-case scenario which is when the specimen is not immersed. The data acquisition images showed a dark square on the edges meaning that the light was refracted. When looking at the reconstructions performed it can be seen that the reconstruction performed with the 3 by 3 pixels averaged images show less noisy results in comparison with the 4 by 4 averaged images. In fact, a silhouette that resembles the shape of the acquired images of the specimen is observed.

The experiment number 2 was performed with the same unstressed sample but this time immersed in the index matching fluid. It can be noticed that the black edges from the previous experiment disappeared meaning that the light is passing through the sample. The results of the reconstructions for both of the averages showed higher noise than the sample which was not immersed.

The experiment number 3 was performed on the PMMA 1 specimen stressed with a load of 8.82 N and immersed to compare with the previous results. A dark square on the edges was noted, it is believed this is due to the subjected stress. The refractive index for this sample had to be tuned up since a slight change that falls out of the suggested tolerance occurred due to the stress treatment. It is extremely difficult and tedious to approximate the refractive index since is quite sensitive to small additions however it was performed. Regarding the reconstruction results with both of the averaged images cases, noisy lines were observed, however there was not a trend that indicate that the specimen had been subjected to stress as expected. The experiment number 4 was performed on the PMMA 2 exposed to a load of 29.43 N, this was made to observe if by increasing the internal stress will impact the reconstruction, however, the obtained results were noisy lines with no trend.

For the experiments 5 and 6 PMMA 3 and PMMA 4 specimens were used respectively. With the experiments performed in these specimens, it was aimed to test the impact of the opacity of the material since these specimens were cut from a square PMMA beam. This cut leaves higher roughness surface than the surface of the manufactured cubes. These specimens, PMMA 3 and PMMA4, where exposed to a stress freezing treatment with loads of 8.82 and 29.43 N to observe if some kind of trend was obtained. The results obtained were noisy and did not follow any valid pattern that could be related with the internal stress.

4.6 Conclusion

From the results presented in this chapter, it was concluded that the 3-D internal residual stress measurement in the PMMA specimens under the conditions of the different experiment did not show a trend regardless of the stress and refractive index conditions. It was observed that in the first reconstruction shown in Figure 4.15 under the case of no stress and no immersion of the sample the reconstruction results using the 3 by 3 pixels averages followed the silhouette of the specimen in comparison with the acquired image shown in Figure 4.12. In theory, the immersion fluid is needed since the mathematical approach that reconstructs the internal stress assumes a straight light beam passing through the specimen. However, for the cases where the PMMA samples were immersed and not stressed more noise and straight lines that did not follow a trend was observed. In this chapter, an improved refractive index methodology from the previous research has been presented therefore the results were expected to show an improvement, since the refractive index is according to tolerance. Also, it was expected to see some kind of trend related to the stress conditions but this was not the case. The methodology process for the data acquisition and the post-processing of the images works even when this can be automated. So the variables left to test are the characteristic parameters calculation and the algorithms used to perform the internal stress reconstruction. However, the scope of this research is limited to the experimental improvements of the system since what is intended to test is that the reconstruction algorithms proposed by Szotten [21] could be implemented experimentally. This means that from now on the research work will be focused on the validation of characteristic parameters calculation. In chapter 6, the validation of these characteristic parameters, specifically the characteristic retardation by performing a comparison with the phase stepping methodology instead of Fourier polarimetry and the implementation of a new camera to test the noise introduction will be presented.

Chapter 5

Photoelastic tomography automation

During the critical audit performed in chapter 3, an understanding of the experimental workflow was gained and areas to improve the data acquisition were identified. Drawbacks such as the manual repositioning of the specimen, which could contaminate the refractive index, and the manual cut and shift program presented in chapter 3, section 3.4.1 were faced in the original state of the apparatus. In this chapter the implementations to automate the Photoelastic Tomography apparatus will be shown. In section 5.1 a proposed repositioning system and the design criteria followed is described. The sequence of movements required are illustrated step by step in sections 5.1.3. The algorithms developed to automate the cut and shift process are presented in section 5.3. Finally, the integration of the data acquisition and the image post processing programs is presented in section 5.4.

5.1 Re-positioning system design for data acquisition.

In this section, the development of an automated repositioning system to change the axis of the specimen is proposed. Its design, implementation and operation are explained in detail.

5.1.1 Instrument design criteria:

The Photoelastic Tomography system requires the rotational change of the specimen in three axis, as shown in Figure 5.1, to perform the 3-D stress reconstruction.
In previous research, these position changes were made manually by the experimentalist and several disadvantages were detected, such as:

- Manual replacement affects the continuity and therefore, the efficiency of the image acquisition since the experiment is stopped until the reposition for either the *"X"* or *"Y"* axis is made. Also, the re-set of the TensorGUI.mat program in Matlab is needed.

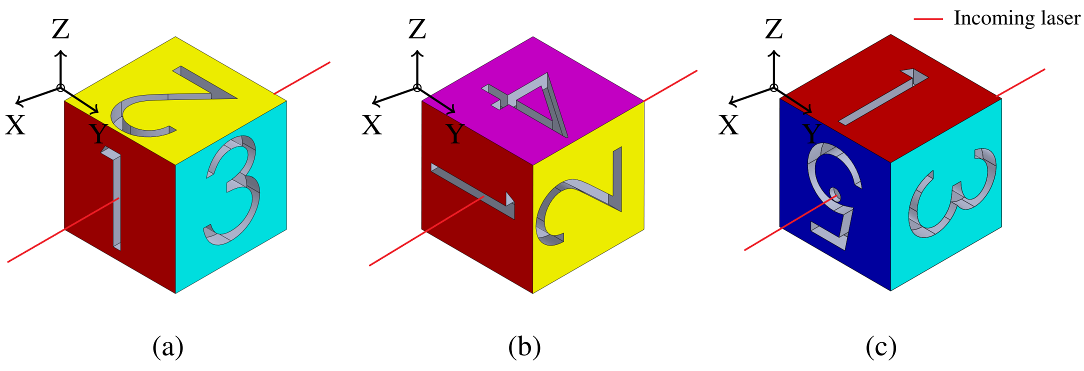

Figure 5.1 Specimen's rotations on a) Z axis b) Y axis c) X axis.

These two actions are performed by the experimentalist manually meaning that the flow of the data acquisition is broken every time that a new axis position is attempted to be acquired.

- There is no repeatability in the manual placement of the specimen, meaning that the zero position between each axis varies.
- Manual replacement can contribute to the contamination of the immersion fluid used to match the specimen's refractive index.
- Skin exposure to the immersion fluid. This can be avoided with the use of latex gloves, however, during experimentation, it was noted that gloves leave a whitish trail in the immersion fluid. This whitish trail may disappear approximately after a day, however, this interferes with the visibility of the images collection.

The following conditions were considered for the conceptual design of the re-positioning system of the specimen, where the most important were:

- Interferences with the line of sight must be avoided while data collection is performed.
- The repositioning system must be contained completely inside the tank, therefore inner size and height of the tank must be considered.
- Interferences between the devices immersed in the tank must be avoided while rotating the specimen.
- The centre of the specimen and height must be kept constant relative to the optical axis of all the devices of the experiment.

- Waterproof electronic devices and non-rusting materials for the structural parts of the repositioning system must be used and the materials must no react with the chemicals of the refractive index fluid.

5.1.2 Design description:

The Photoelastic Tomography system requires the axis change of the specimen, as shown in Figure 5.1, to perform the 3-D stress reconstruction. In order to avoid the disadvantages previously mentioned in section 5.1.1 a reposition system design was proposed by the autor based on the operating principle of a gimbal. A gimbal can be defined as a mechanical device that allows rotating an object in a pivoted supported axis. The re-positioning system is comprised of electronic devices, mechanical and structural components. The electronic devices are four SW-0230MG waterproof servomotors used to move the frames of the repositioning system and an Arduino Uno controller which controls the positions of these servomotors accurately. Arduino hardware has serial ports, known as universal asynchronous receiver-transmitter, (UART) which are part of an integrated circuit (IC) used for serial communications over a computer or peripheral device serial port. In each serial port one serial information can be send and received. Matlab software allows the installation of add-on libraries that easily access and communicates with Arduino UNO without the need to work in the Arduino environment but within the Matlab. The user can create custom add-on libraries by using the Matlab class and creating the C++ code that includes the librarybase.h from arduino to control different devices such as sensors, servomotors, LCD dislays and so on. An schematic of the process where it shows the construction of the Arduino add-on library and how it is related with the hardware is presented in Figure 5.2 [99].

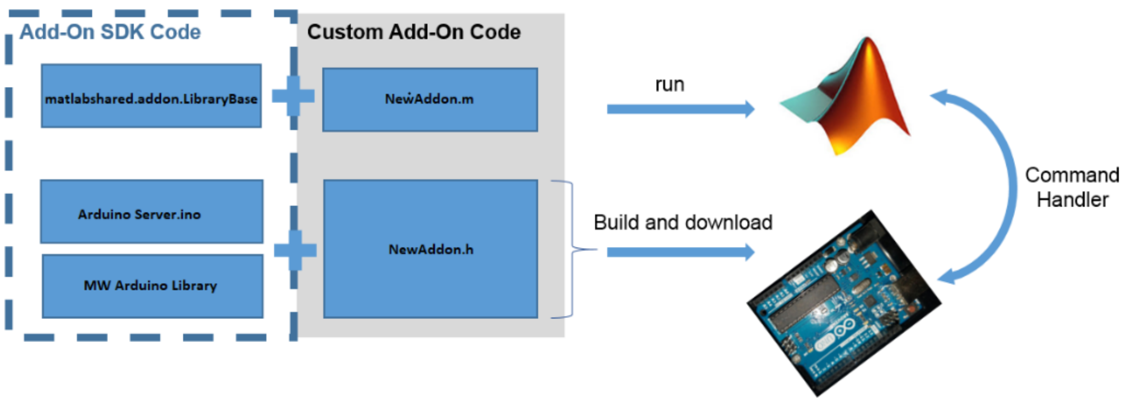

Figure 5.2 Construction of a custom Arduino add-on library and its relation to the hardware extracted from [99].

The steps to transmit and receive data through a serial port on the Arduino hardware with Matlab to control a servomotor are described in the following steps:

- Connect the Arduino UNO to the PC.
- Run the following command arduino() in Matlab to verify the correct connection
- Connect the servomotor that needs to be controlled as shown in Figure 5.3 [100].
- Define the Matlab objects for the servomotor and the functions to work with e.g.:
  »servomotor = servo(arduinoObject, pinAtWhichServoIsAttached)
  »writePosition(motorObject, angle) which is the command used to rotate the servomotor shaft to a specific angle from 0 to 1.
  »readPosition(motorObject) which is the command used to read the current position of shaft.

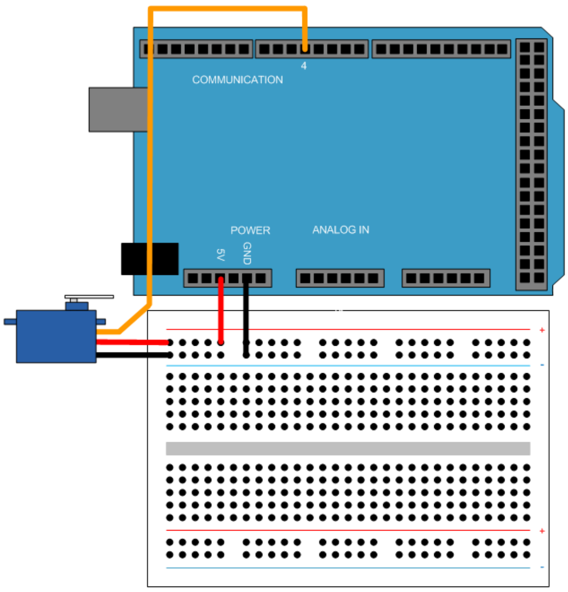

Figure 5.3 Schematic connection diagram of servomotor to the Arduino Board, image extracted from [100].

These components were selected because they are easy to program and interact with Matlab.

The mechanical components involved in this system include bearings that allows the rotational movement while reducing the friction between the components of the system and the worm drive which converts the rotational movement of the servomotors into a linear movement. The structural components consists mainly of two structural frames manufactured in aluminum, defined by the author as the *"outer frame"* and *"inner frame"* as shown in 5.4 .

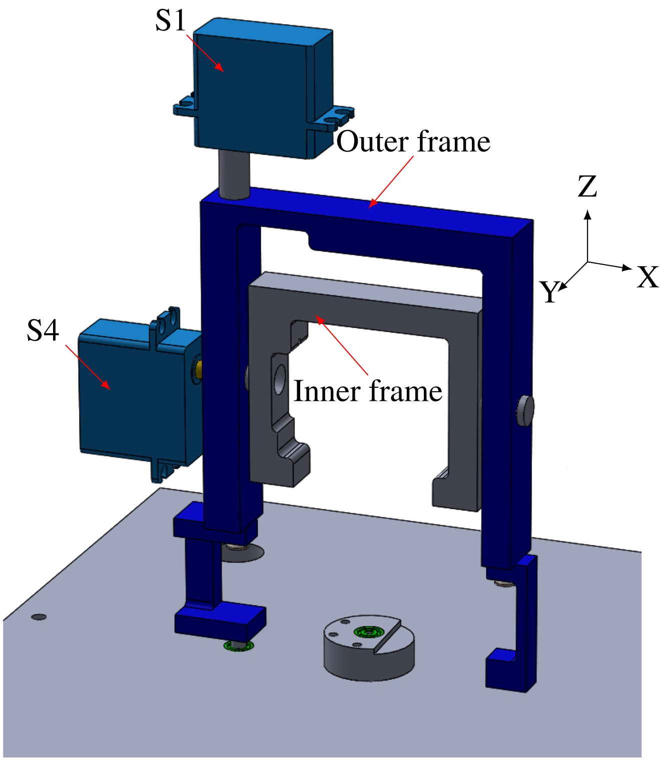

Figure 5.4 Inner and outer frame isometric view.

The outer frame acts as the structural support for the inner frame and the servomotor *"S4"* that rotates the inner frame. Also, it places the system in the position to rotate the specimen as shown in Figure 5.5 a) and b) or in the home position out of the camera viewing, see Figure 5.5 c) and d). This rotation is made by a servomotor,*"S1"*, that is linked through a pin to the outer frame.

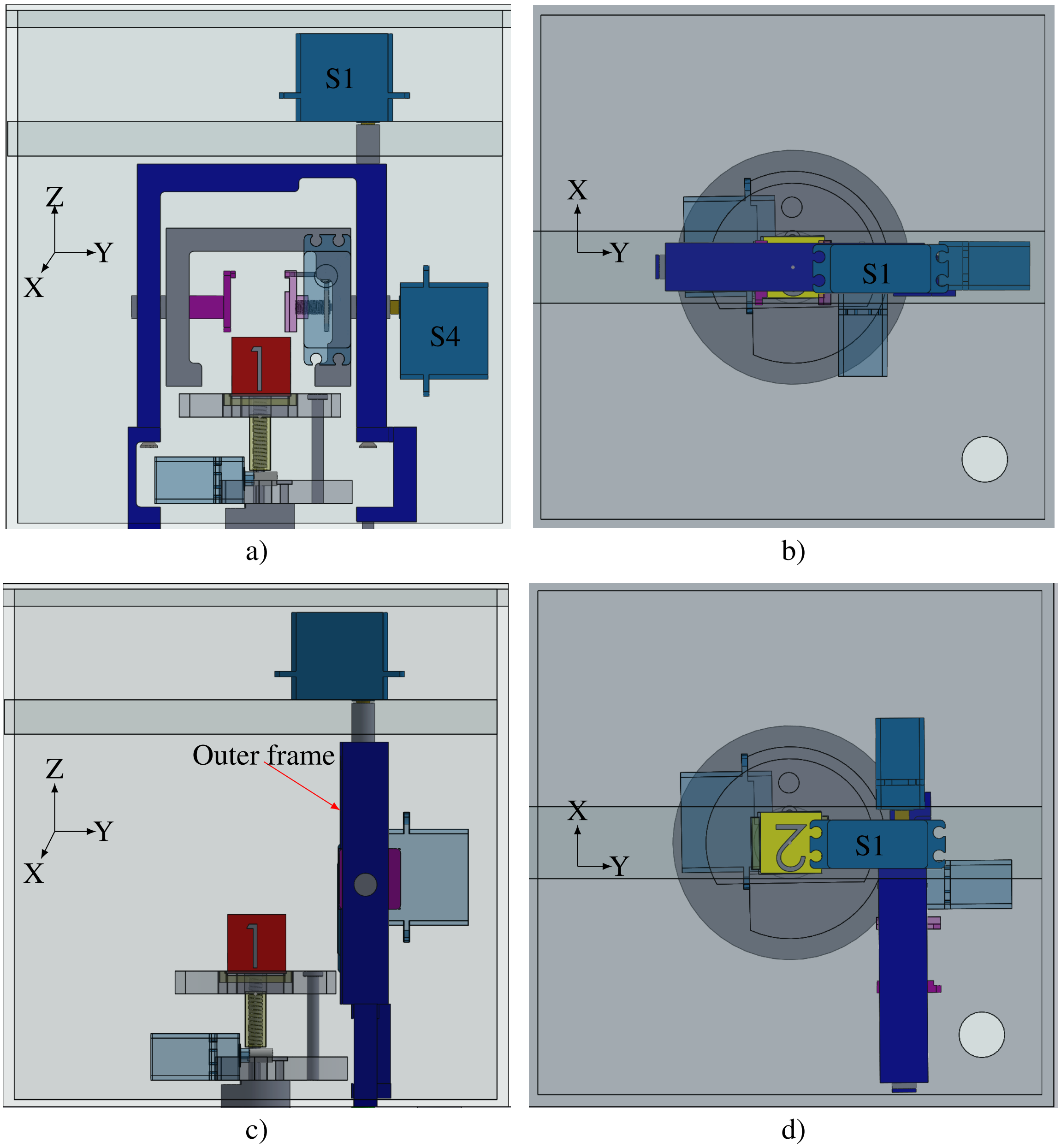

Figure 5.5 Outer frame home position a) front view and b) top view and working position to rotate the specimen c) front view d) top view.

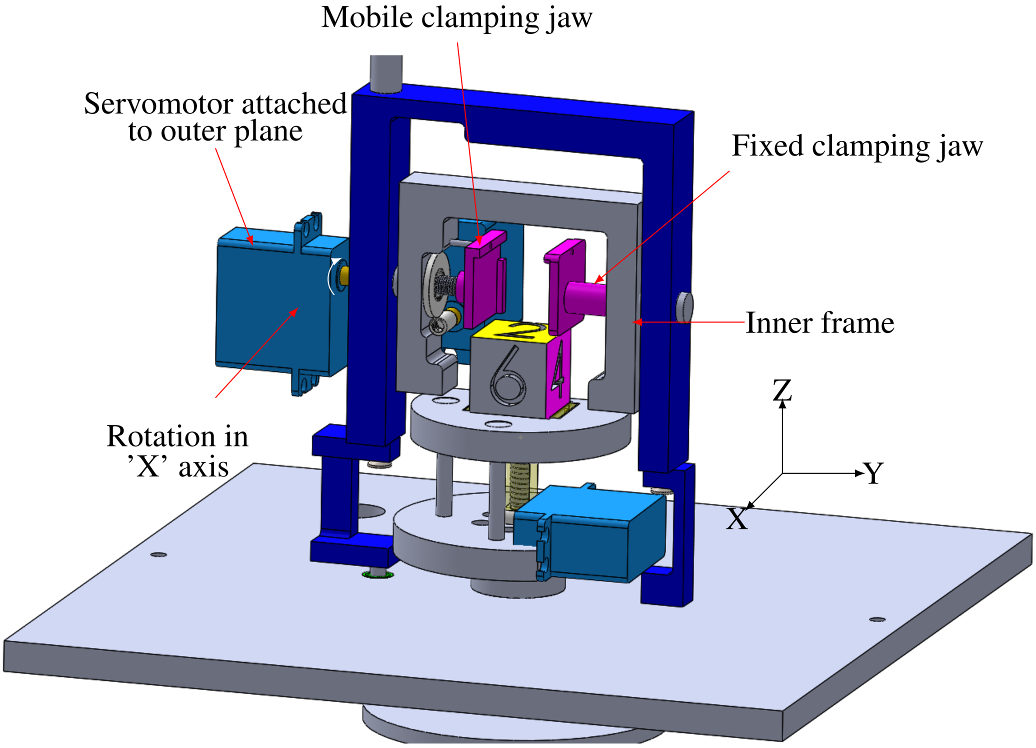

Figure 5.6 Inner frame description.

The function of the inner frame is to rotate in the *"X"* axis and to serve as structural support for the clamping jaws for the servomotor that makes the mobile clamping jaw hold or release the specimen, as shown in Figure 5.6 . In this case the design could be categorized as a single axis gimbal, since only the *"X"* axis position changes through the inner frame.
Additionally to the parts previously described, the repositioning system is composed by the top and bottom rotational plates for *"Z"* axis and the mobile holder, as shown in Figure 5.7. The specimen's mobile holder moves up and down to reach the clamping jaws or to sit the specimen in the turning table as shown in Figure 5.8.
This movement is made with the aid of a servomotor that is connected to a crown and gear worm screw that helps to convert the rotational movement into a linear one as it is shown in Figure 5.7. The vertical stage servomotor was modified mechanically and electronically to obtain continuous rotation. The first step was to remove the physical servomotor rotational limit. Then, the calibration potentiometer, included in the servomotor's circuit, has to be positioned in a neutral point by measuring the resistance between the first and second pin and the second and third pin to allow the change of direction. This is because the servomotors position is controlled by the pulse width. This pulse is normally of 1.5 ms to maintain the position centred. If the pulse is shorter, e.g. 1 ms, the servomotor turns to the left, if the

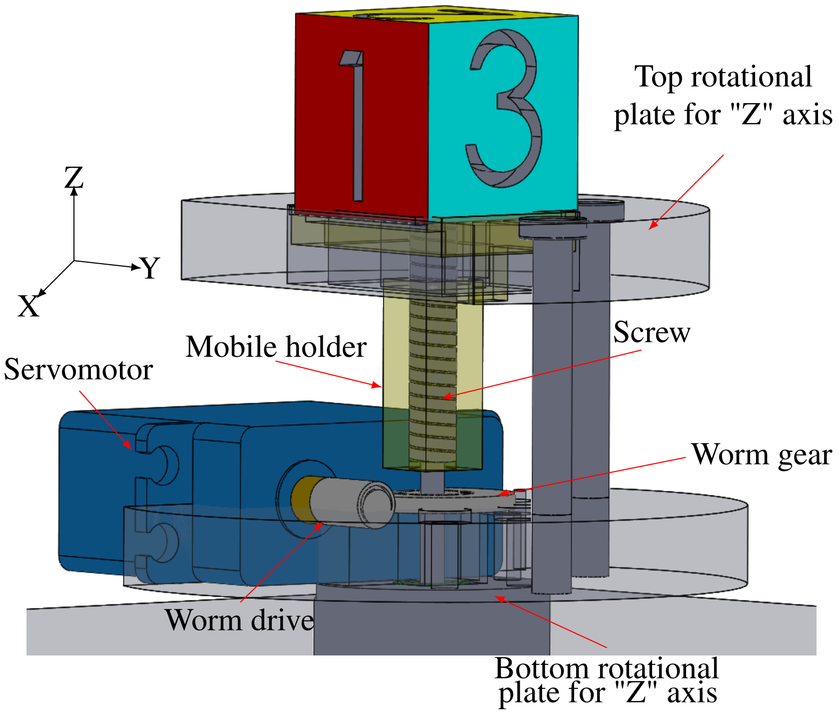

Figure 5.7 Top and bottom rotational plates components.

pulse is longer, e.g 2 ms, the servomotor turns to the right. From the electronically point of view, what happens is that the servomotor state is in equilibrium when the potentiometer is in its neutral position. The servomotor moves when a send pulse decompensates the circuit. The modified servomotor was programmed by time to know when to stop its rotation. This system has no feedback yet to see the position of the specimen; future improvement of this design could include sensors to give this feedback.

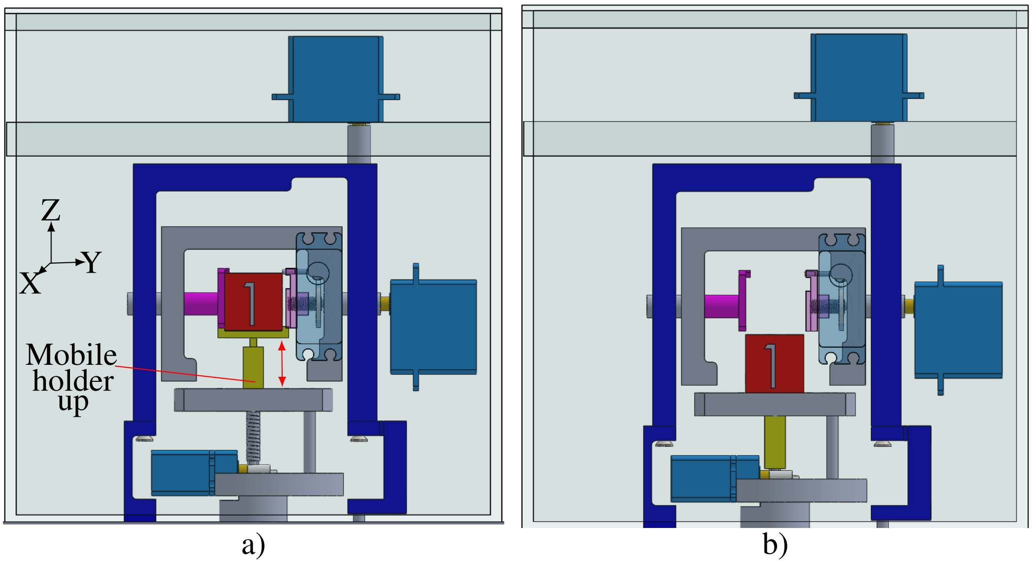

Figure 5.8 Mobile holder: a) upper position reaching the clamping jaws, b) lower position sited in the turning table.

5.1.3 Repositioning system sequence description

In this section the sequence of the servomotors movement required to accomplish the rotation for *"X"* and *"Y"* axes are described step by step. This sequence description is helpful to define the programming work flow, but before the sequences description, the servomotors shown in Figure 5.9 must be defined. S1 is the servomotor responsible for the outer frame movement, S2 is the servomotor in charge of the movement of the mobile holder, S3 moves the mobile clamping jaw and S4 rotates the inner frame. In addition to the servomotors, the rotational motor for Z axis will be needed within the sequences.

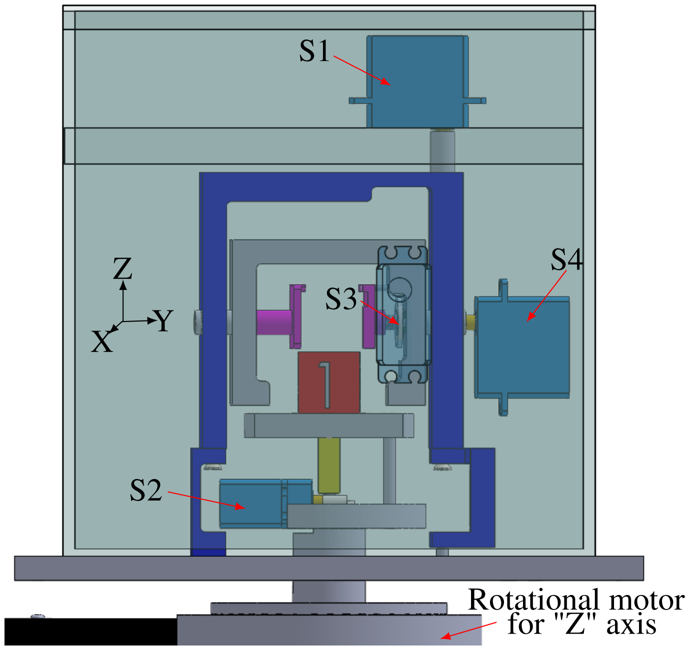

Figure 5.9 Repositioning system front view with servomotors 1,2,3 and 4.

Sequence for rotation of specimen about *"Y"* axis

The rotation required to change the position of the specimen is illustrated in Figure 5.10.

All the sequences must start from the home position as Figure 5.11 a) shows.

1. Rotate servomotor "S1" 90 degrees anti-clockwise about the *"Z"* axis, to move outer and inner frame as Figure 5.11 b) illustrate.

2. Rotate servomotor "S2" until it reach the adequate height to get the fixed left grip, as illustrated in Figure 5.11 c).

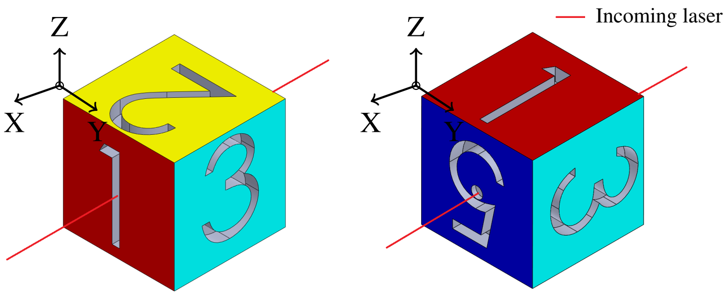

(a) (b)

Figure 5.10 Specimens rotation in "Y" axis

3. Rotate servomotor “S3” to move right grip to hold the specimen, as shown in Figure 5.11 d).

4. Rotate servomotor “S2” backwards to remove the movable holder, as it can be seen in Figure 5.12 e).

5. Rotate servomotor “S4” 90 degrees about the *"Y"* axis until the inner frame is perpendicular to the outer frame, as it is shown in Figure 5.12 f).

6. Rotate servomotor “S2” until the movable holder reach the bottom of the specimen, as shown in Figure 5.12 g).

7. Rotate servomotor “S3” backwards to remove the movable right grip, as demostrated in Figure 5.12 h).

8. Rotate servomotor “S2” until the movable holder is totally hidden in the rotational plate for ‘’Z” axis, as shown in Figure 5.13 i).

9. Rotate servomotor “S4” about the *"Y"* axis to home position to get the inner frame parallel to the outer frame, as presented in Figure 5.13j).

10. Rotate servomotor “S1” to place the outer and inner frame in home position as displayed in Figure 5.13 k).

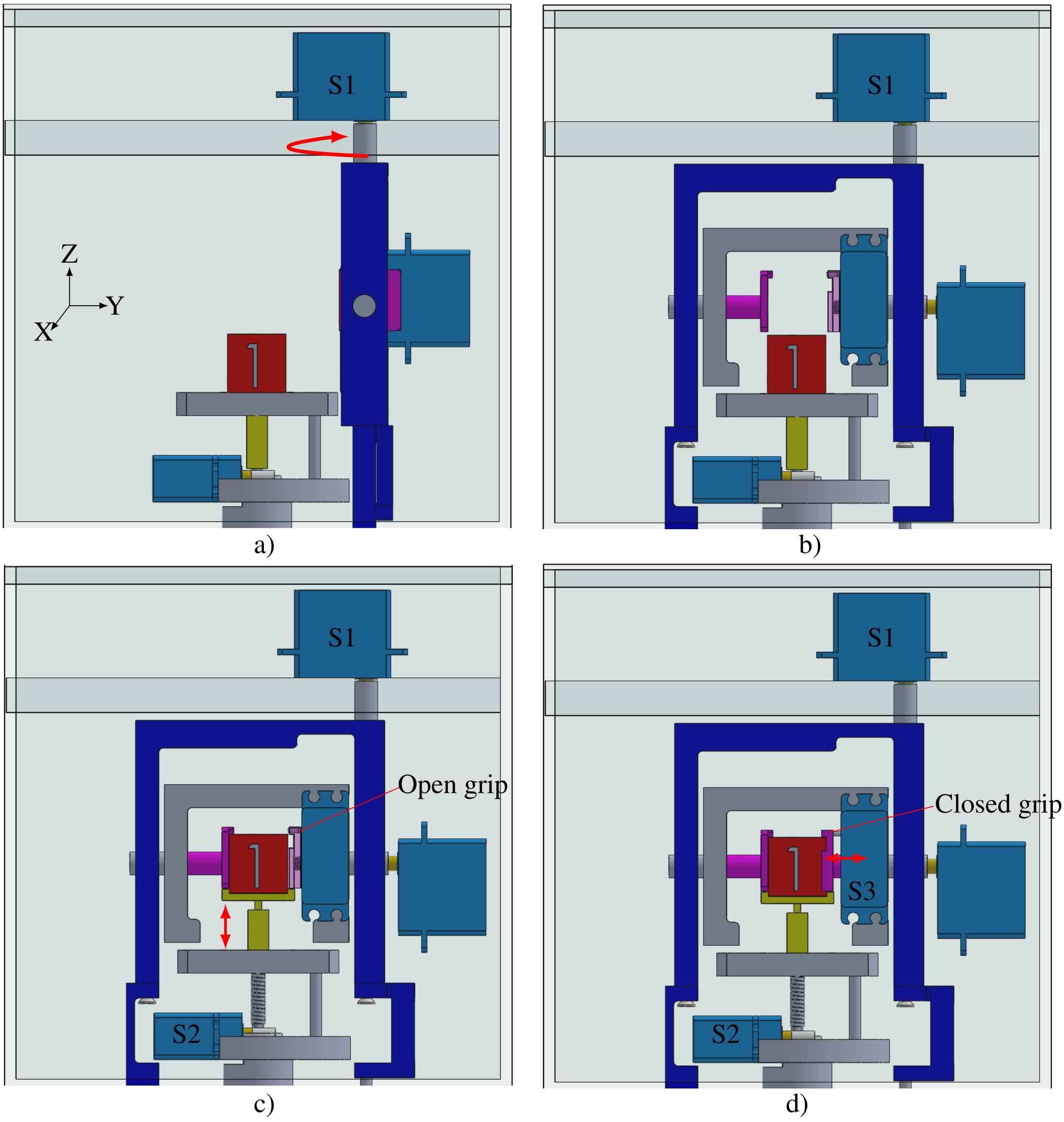

Figure 5.11 Sequence to move the specimen to the gripping jaw.

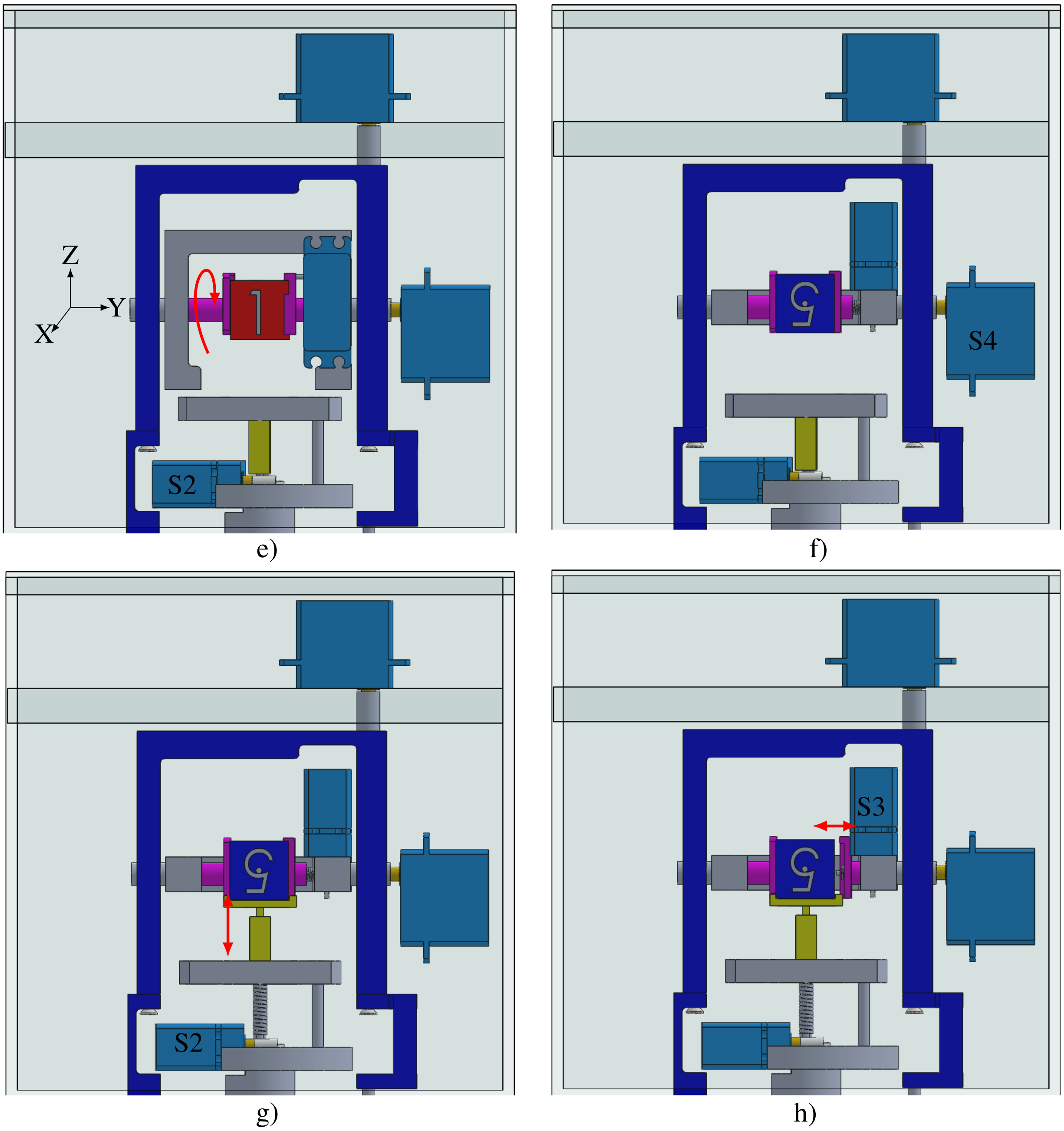

Figure 5.12 Sequence to rotate the specimen about the *"Y"* axis.

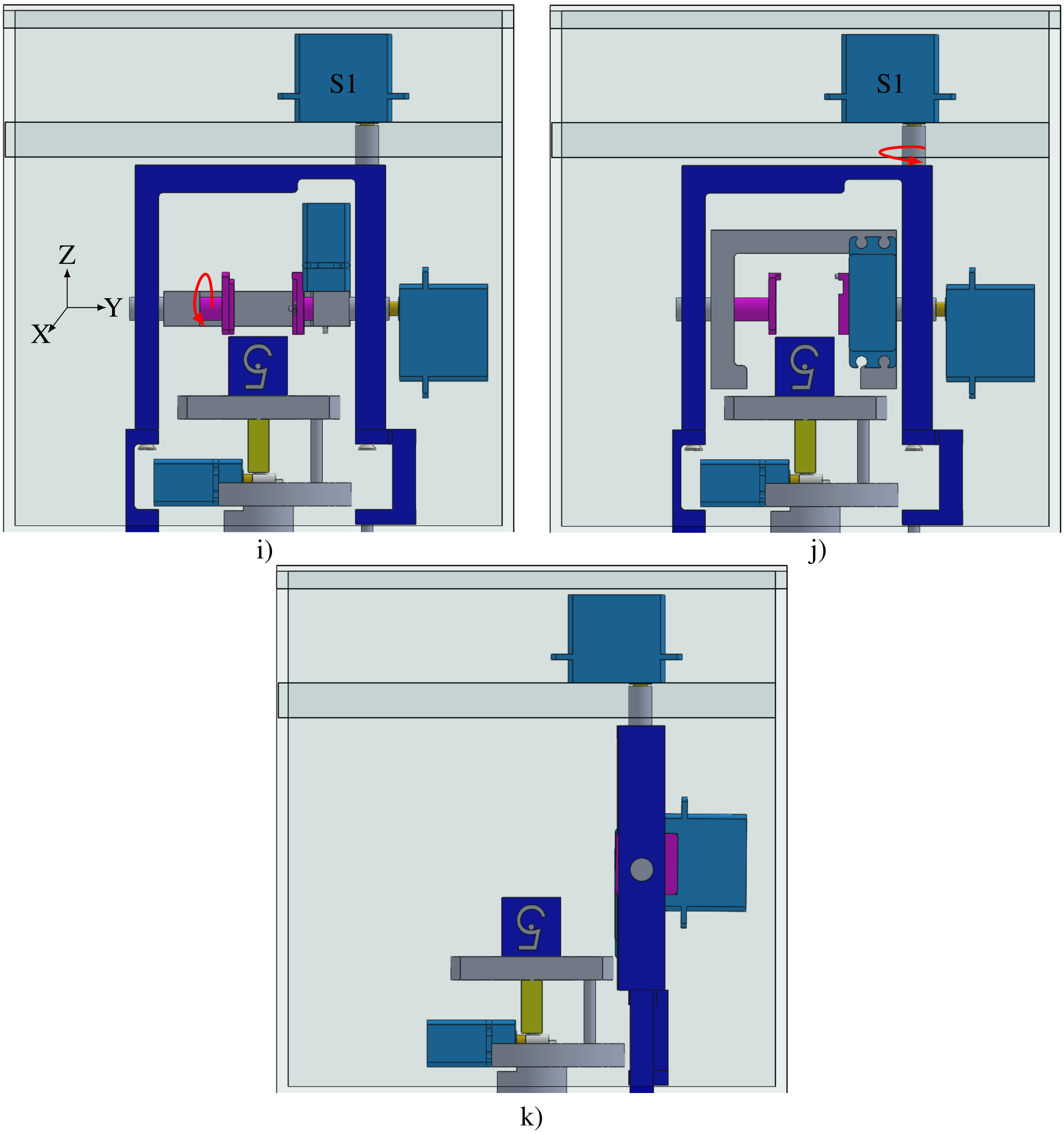

Figure 5.13 Sequence to rotate inner frame and outer frame at home position.

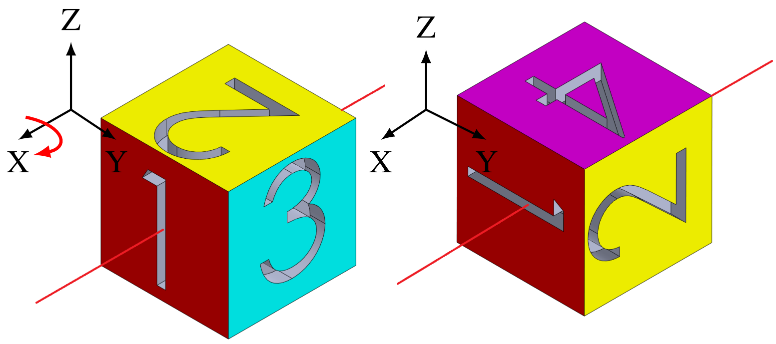

Figure 5.14 Rotation of the specimen about the *"X"* axis

Sequence for rotation of the specimen about the *"X"* axis

After the data acquisition of the *"Y"* axis of the specimen the last rotation needed is in the *"X"* axis as shown in Figure 5.14 .
Where the proposed sequence to perform this rotation is presented in the following steps:

1. Move the specimen to home position, without the *"X"* axis rotation, as shown in Figure 5.15 a).

2. Move the rotational plate motor for *"Z"* axis 90 degrees, as shown in the Figure 5.15 b).

3. Rotate servomotor "S1", 90 degrees anti-clockwise about the *"Z"* axis to move outer and inner frame as shown in Figure 5.15 c).

4. Rotate servomotor "S2", until it reach the adequate height to get the fixed left grip, as illustrated in Figure 5.15 d).

5. Rotate servomotor "S3" to move right grip to hold the specimen, as shown in Figure 5.16 e).

6. Rotate servomotor "S2" backwards to remove the movable holder, as shown in Figure 5.16 f).

7. Rotate servomotor "S4", 90 degrees,about the *"Y"* axis until the inner frame is perpendicular to the outer frame, as it is shown in Figure 5.16g).

8. Rotate servomotor "S2" until the movable holder reach the bottom of the specimen, as shown in Figure 5.16 h).

9. Rotate servomotor “S3”, backwards to remove the movable right grip, as shown in 5.17 i).

10. Rotate servomotor “S2” until the movable holder is totally hidden in the rotational plate for ‘’Z” axis, as shown in 5.17 j).

11. Rotate servomotor “S4”,about the *“Y”* axis until the inner frame is parallel to the outer frame, as it is shown in Figure 5.17 k).

12. Move the rotational plate motor for “Z” axis to home position , as shown in the Figure 5.17 l).

13. Rotate servomotor “S1” to place the outer and inner frame in home position as shown in Figure 5.18 m).

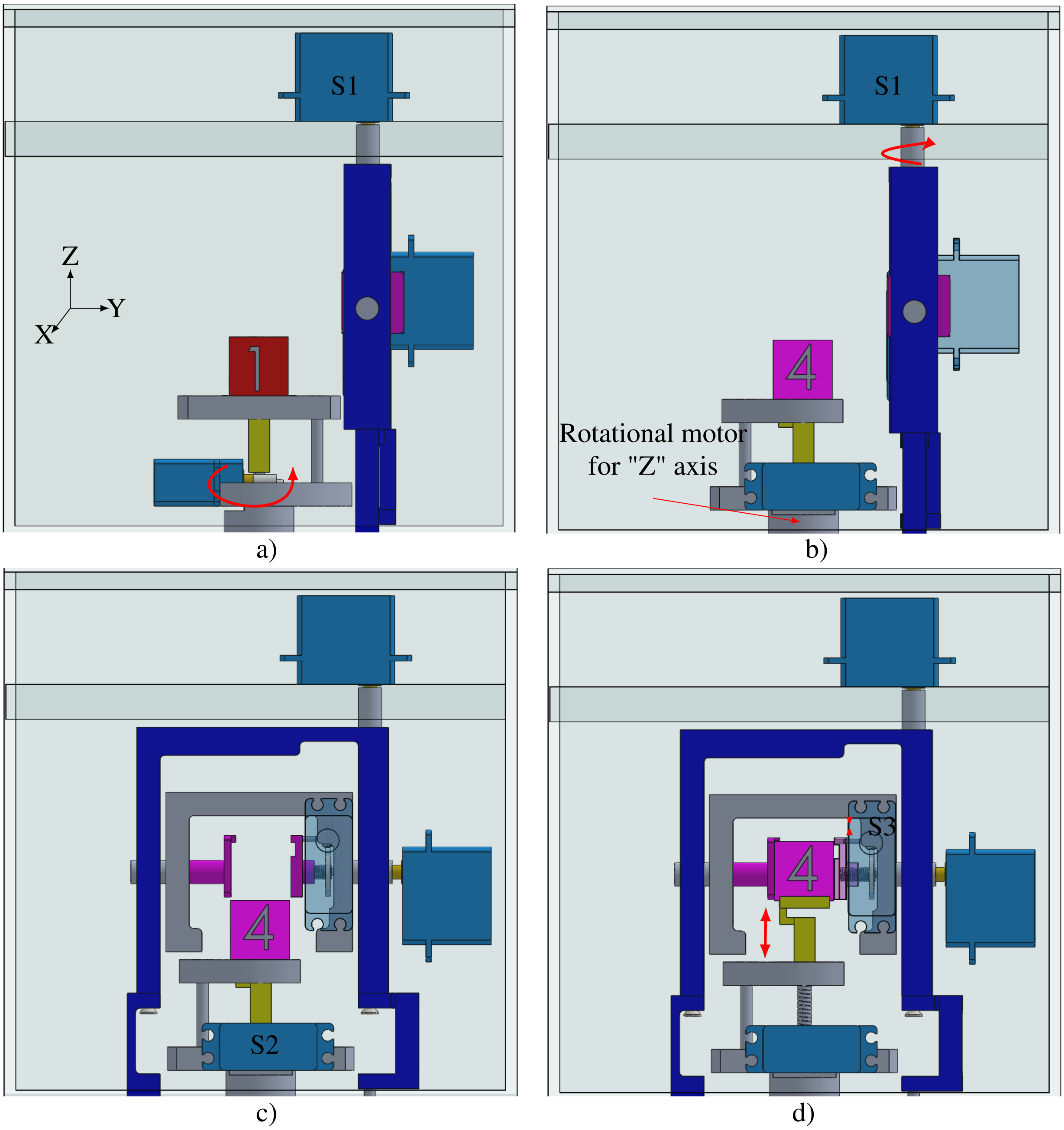

Figure 5.15 Sequence to move the specimen to gripping jaw.

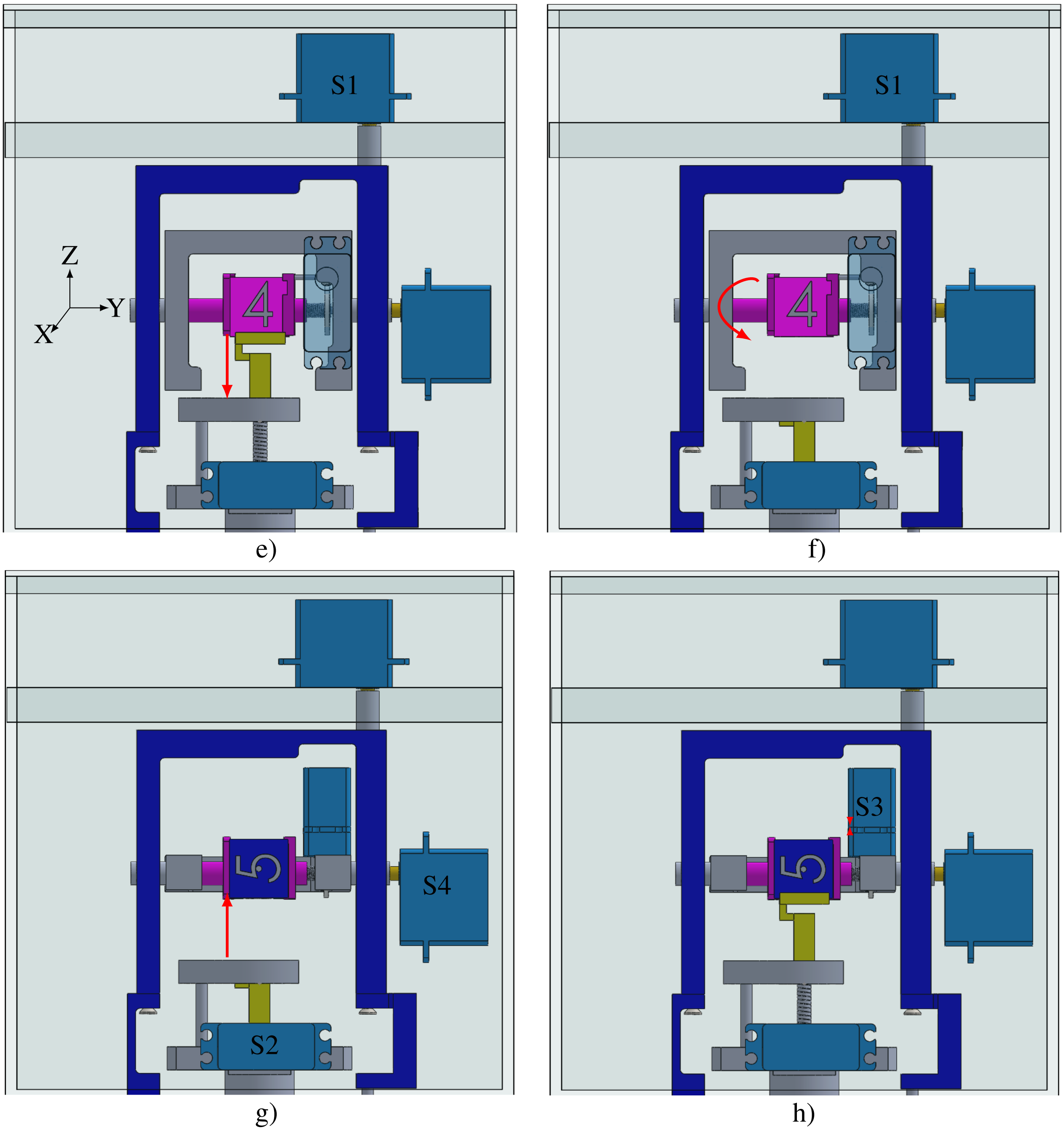

Figure 5.16 Sequence to rotate the specimen about the "X" axis.

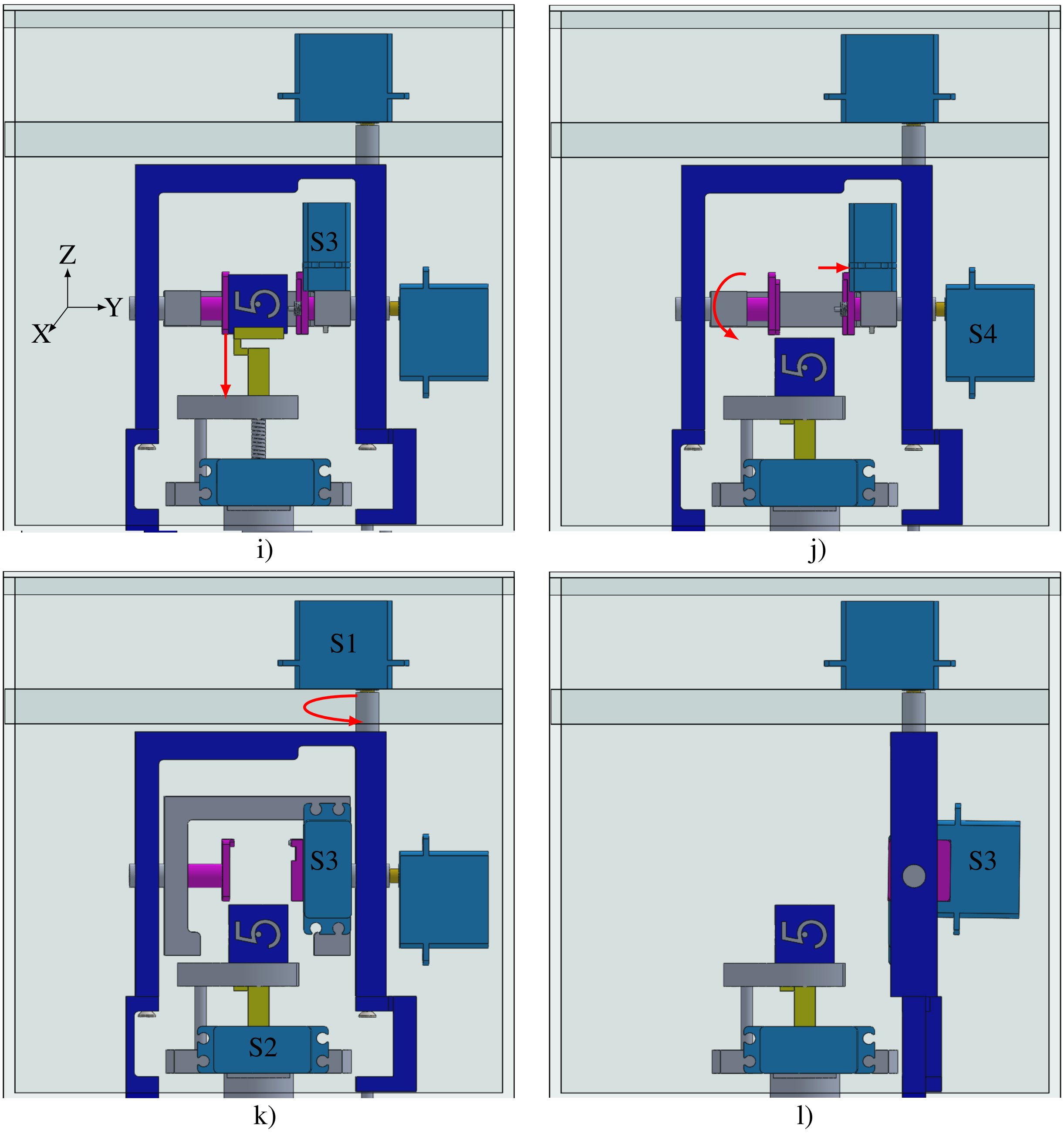

Figure 5.17 Sequence to rotate inner frame and outer to the home position.

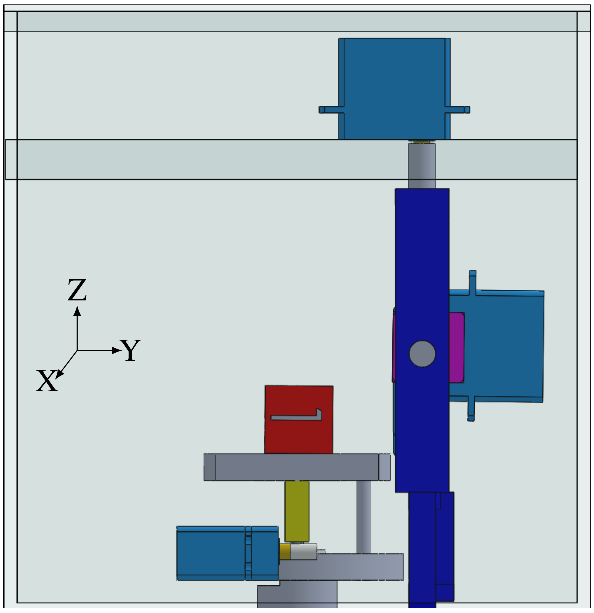

m)

Figure 5.18 Rotation plate motor for *"Z"* axis in its home position.

5.2 Repositioning system implementation

In this section, pictures of the implemented repositioning system which was manufactured in the Mechanical Engineering department workshop are shown as in Figure 5.19.

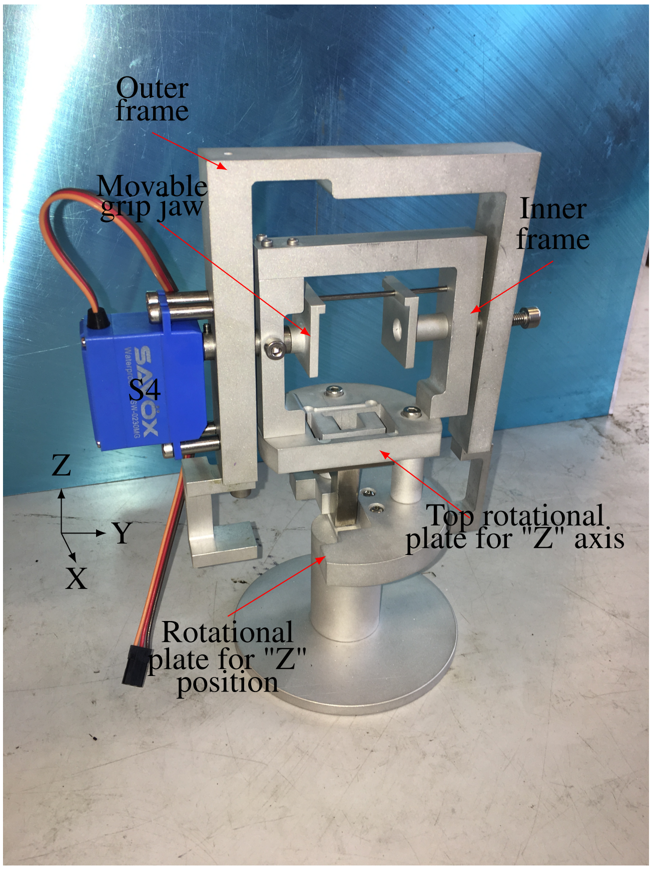

Figure 5.19 Repositioning system implementation.

The previous design for the rotational plate for the specimen did not have a reference to position the specimen in a consistent position. Therefore in this implementation a new rotational plate for the specimen was made with a reference to be able to repeat the position of the sample as shown in Figure 5.20 a) and b).

The tank was changed from a glass tank, Figure 3.1, to a PMMA tank in order to be able to contain the repositioning system as shown inside the red squares Figure 5.21. The faces of this PMMA tank, where the laser passes through, were modified to fit two windows made of glass in order to avoid birefringence interference from the tank as shown in Figure 5.22 a). Moreover, a lid that is screwed to the top of the tank to avoid the immersion fluid contamination and evaporation loss as shown in Figure 5.21 was added. And finally a

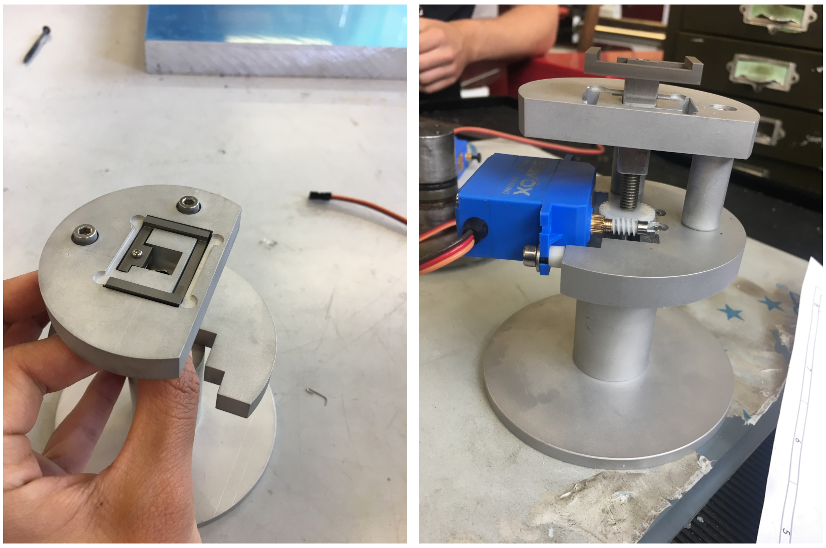

a) b)

Figure 5.20 New rotational plate for the specimen a) top view and b) side view with servo-motor assembled.

drainage valve in order to empty the tank in a safer and cleaner way was installed as shown inside red ellipse in Figure 5.22 b).

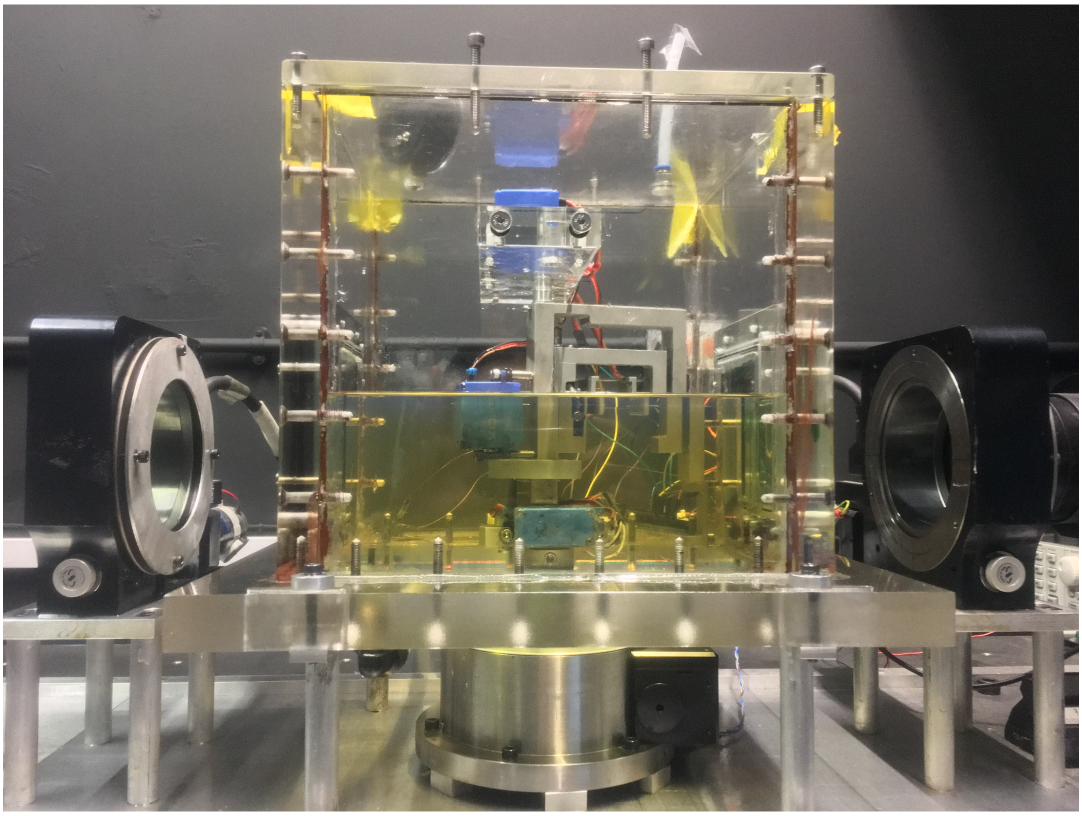

Figure 5.21 New PMMA tank

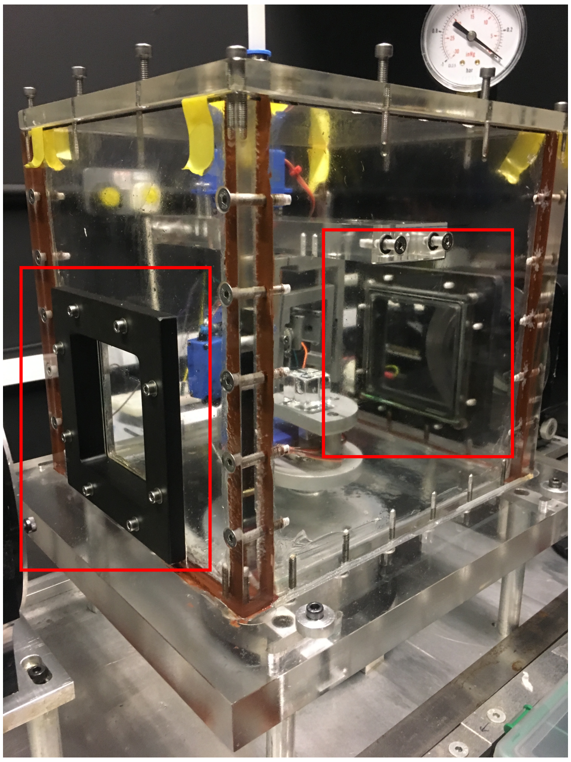

a)

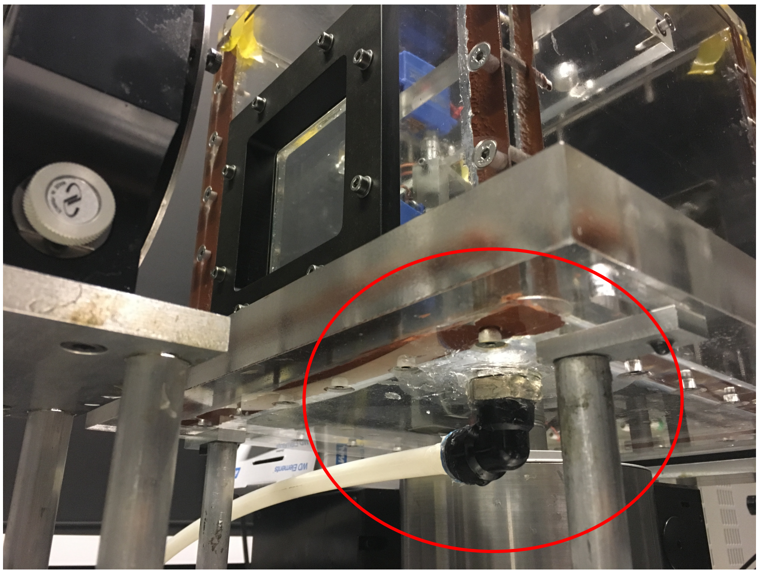

b)

Figure 5.22 PMMA tank where a) shows the glass windows to avoid birefringence from PMMA material and b) shows the draining system implemented.

5.3 Automated cut and shift program

As mentioned in section 3.4.1 after the light intensity images acquisition, in order to remove extra information that does not include the specimen an algorithm called cut and shift is used. This algorithm involves several steps that the experimentalist has to perform before being able to cut the image e.g. the specimen measurement in 5 different pictures, the calculation of its polar coordinates of the position of the specimen and change the program manually. This methodology is subject to human errors, is time-consuming and tedious. Therefore an attempt was made to improve this feature and also to be able to automate the post-processing methodology. In this section, alternative algorithms are proposed where the edges of the specimen are automatically detected. The different algorithms used the functions *regionprops*, *improfile*, and *Gaussian filters and Hough transform* to detect vertical lines are presented in the algorithm 1, 2 and 3. Examples of this algorithms implementations are shown in Figures 5.23,5.24 and 5.25

Algorithm 1: Automated cut and shift program using *regionprops*.

Input: Light intensity image in .mat files.
Output: Cut and centred light intensity image in .mat files.

1 Load the light intensity images .mat files.
2 Change the format of the light intensity images from .mat files to .jpg.
3 Define working width of the specimen at 45 and 135 degrees position.
4 Load the .jpg images
5 Crop the images according to the width of the specimen at 45 degrees.
6 Convert the .jpg images to black and white images.
7 Detect the white connected pixels in the black and white image.
8 Obtain the areas of the connected white pixels.
9 Obtain the coordinates position of the biggest area.
10 Obtain the centroid of the biggest area in the image.
11 Save the coordinate values in a table.
12 Run this process to generate the position coordinates for all the images.
13 Cut the .mat files according to this coordinates.

Algorithm 2: Automated cut and shift program using improfile function where a) is the image profile an

Input: Light intensity image in .mat files.
Output: Cut and centred light intensity image in .mat files.

Load the light intensity images .mat files.
Change the format of the light intensity images from .mat files to .jpg.
Definethe width of the specimen at 45 and 135 degrees position.
Load the .jpg images.
Crop the images according to the width of the specimen at 45 degrees.
Convert the .jpg images to black and white images.
Apply the improfile function.
Calculate the pixel average and obtain the coordinate of the pixel that gets out of this mean value for each 50 pixe
Save the coordinate values in a table.
Run this process to generate the position coordinates for all the images.
Cut the .mat files according to this coordinates.

Algorithm 3: Automated cut and shift program using filters and Hough transform function.

Input: Light intensity image in .mat files.
Output: Cut and centred light intensity image in .mat files.

Load the light intensity images .mat files.
Change the format of the light intensity images from .mat files to .jpg.
Define width of the specimen at 45 and 135 degrees position.
Load the .jpg images.
Crop the images according to width of the specimen at 45 degrees.
Apply gaussian filter.
Convert the previous filtered image into a black and white image.
Apply the Hough transform function to detect vertical lines at 90 degrees.
Save the coordinate values in a table.
Run this process to generate the position coordinates for all the images.
Cut the .mat files according to this coordinates.

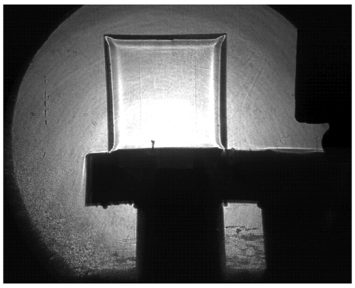

(a)

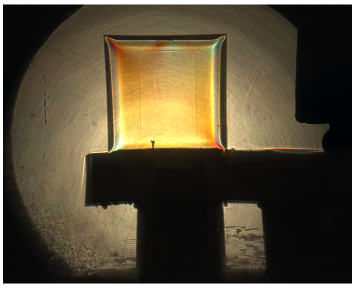

(b)

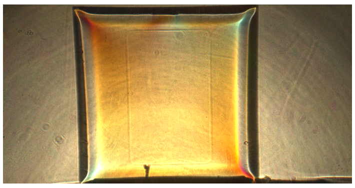

(c)

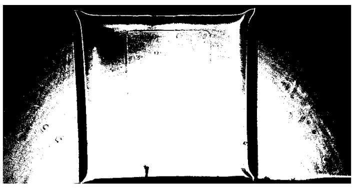

(d)

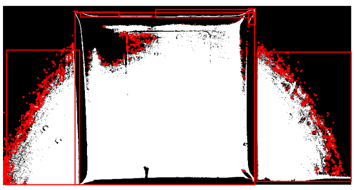

(e)

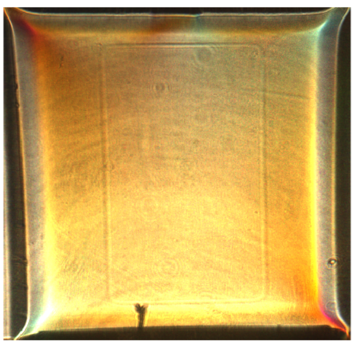

(f)

Figure 5.23 Automated cut and shift program using regionprops function where: a) is the Original light intensity image, b) the converted light intensity image to RGB format, c) the cropped RGB image according to defined working window, d) the RGB image converted to black and white, e)the detected edges by *regionprops* function and f) the cropped light intensity image.

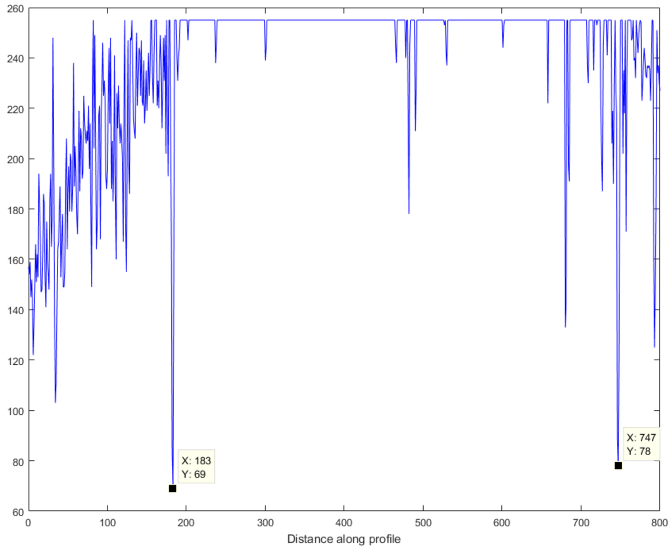

(a)

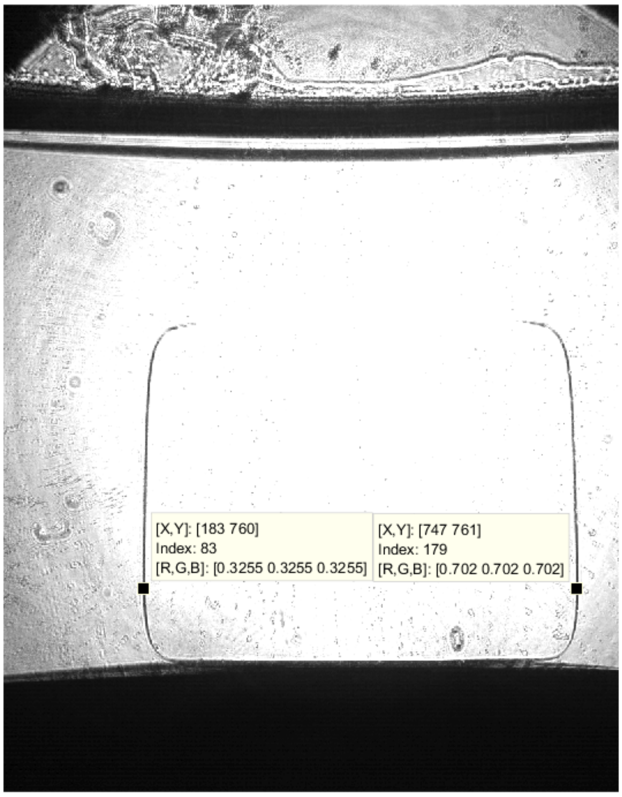

(b)

Figure 5.24 Automated cut and shift program using improfile function where a) shows the intensity values of the pixels of an image and b) shows the image where the profile path was obtained. In this image the left and right edge location was performed correctly.

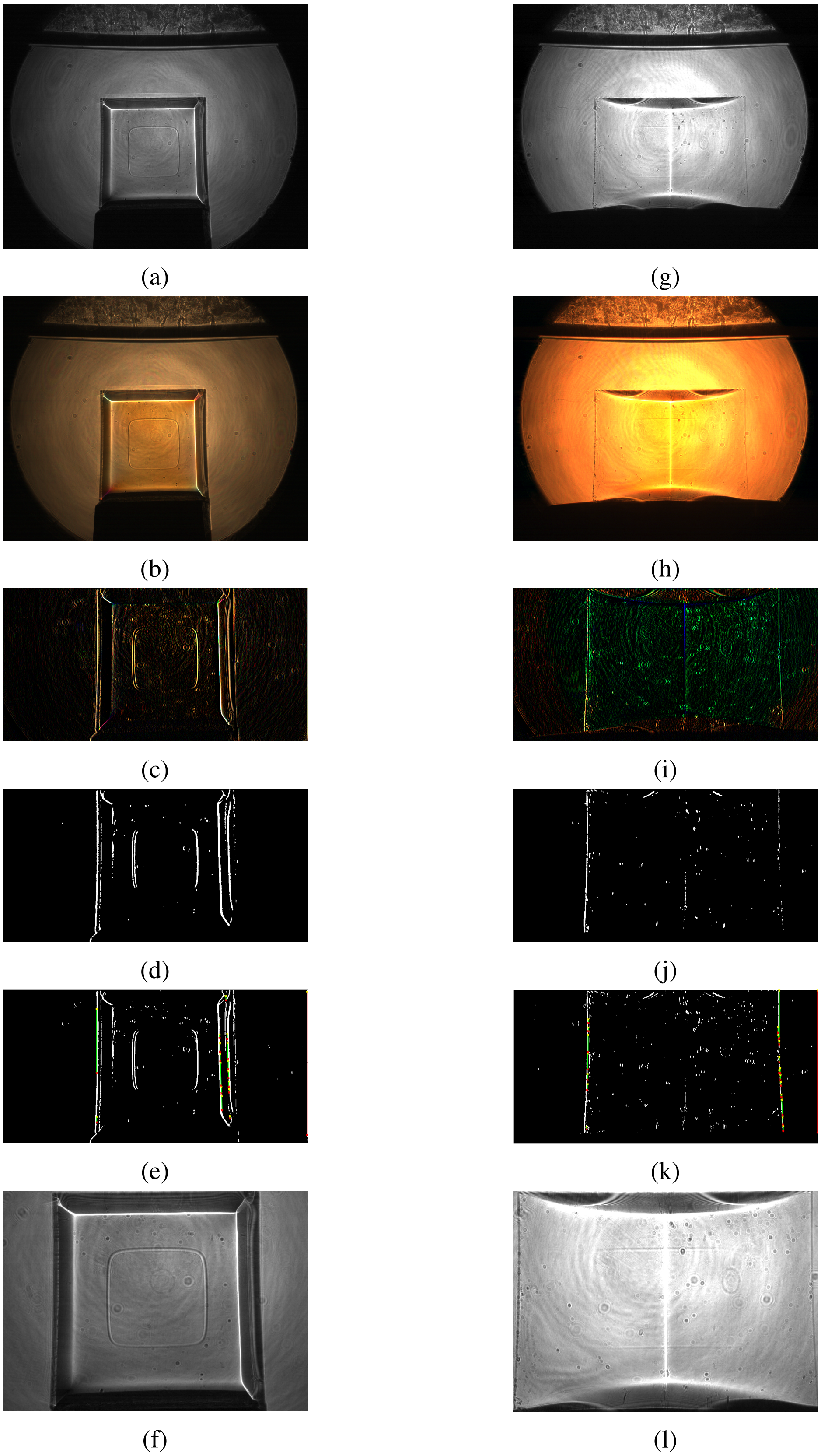

Figure 5.25 Automated cut and shift program using filters and Hough transform function pictures where a) and g) are the original light intensity image, b) and h) are the converted light intensity image to RGB format, c) and i) are the cropped and filtered Gaussian RGB images, d) and j) are the RGB image converted to black and white, e) and k) are the edge detected by *Hough transform* function and finally f) and l) are the cropped light intensity images.

5.4 Integration of the programs

The first step in the programs integration started by the hardware and software upgrade, since the Photoelastic Tomography programs were installed in a Windows 7 computer and Matlab 2009a version. The main reason for this upgrade it was to speed up the data acquisition process since the computer and the Matlab software use to crashed quite often. Also this upgrade will allow the installation of the Arduino package used by Matlab 2018 to be able to control the servomotors of the repositioning system.
Matlab handles different types of files. The most common file extensions to work with MATLAB are the '.m' file which is defined as a script that uses the MATLAB functions.In the case of Photoelastic Tomography apparatus, the program TensorGUIDK.m developed by Yang [18] controls the images acquisition. This program controls USB port the camera and serial port the motors that rotate the polarizer, analyser and the circular plate where the specimen is placed. Nevertheless to control certain devices, like the Thorlabs camera DC1545X, Matlab requires to use a translator. The drivers, software and libraries for this mentioned camera [101] are compiled in other language by the manufacturer, in this specific case C++. The files to control the camera are written as '.cpp' files which need to be converted in a compatible file that Matlab can read and execute. This translator is a .MEX file which is a type of file that provides information between MATLAB and functions written in other languages such as C, C++ or Fortran. MEX stands for "MATLAB executable". The migration of the .m files and drivers was not straight forward. Several attempts to recompile the .m files and drivers with the help of software literature was made without success. Therefore help from Dr. Michael Croucher [102] and Dr. Tania Allard from the Research Software Engineers (RSEs) [103] was required to update the .MEX files. They updated and migrated successfully the programs by the recompilation of the .cpp files with the MinGW64 compiler and also create algorithm 4 to avoid errors in the recompilation of this files, giving as a result the .mexw64 files which Matlab 2018 can read without problem.

Algorithm 4: Cpp files recompilation for programs migration

Input: .cpp files.

Output: .mexw64 files.

```
mex openCamera.cpp CXXFLAGS=CXXFLAGS -fpermissive C:\Program Files \Thorlabs \Scientific Imaging\D
mex loadParameters.cpp C:\Program Files\Thorlabs\Scientific Imaging\DCx Camera Support\Develop\Lib\uc480
```

Once the program migration was done the Photoelastic Tomography interface including the repositiong system and the cut and shift program was completed as it is shown in Figure 5.26

Algorithm 5: Data acquisition and post-processing image integration.

Input: Light intensity image acquisition.

Output: Averaged images.

1 Define polarizer and analyzer rotation ratio.
2 Load camera parameters and communicate through serial port to the motor controller for the polarizer analyzer and s
3 Rotate the polarizer and analyzer to obtain the eighteen polarization states.
4 Change the position of the specimen by rotating 1 degree clockwise from 0 until 180 degrees.
5 Rotate the specimen with the repositionig system in the X axis.
6 Wait for the immersion fluid to settle down 6 hours.
7 Rotate the polarizer and analyzer to obtain the eighteen polarization states.
8 Change the position of the specimen by rotating 1 degree clockwise from 0 until 180 degrees.
9 Rotate the specimen with the repositionig system in the Y axis.
10 Wait for the immersion fluid to settle down 6 hours.
11 Rotate the polarizer and analyzer to obtain the eighteen polarization states.
12 Change the position of the specimen by rotating 1 degree clockwise from 0 until 180 degrees.
13 Cut and shift the light intensity images for all the axis.
14 Average the light intensity images for all the axis.

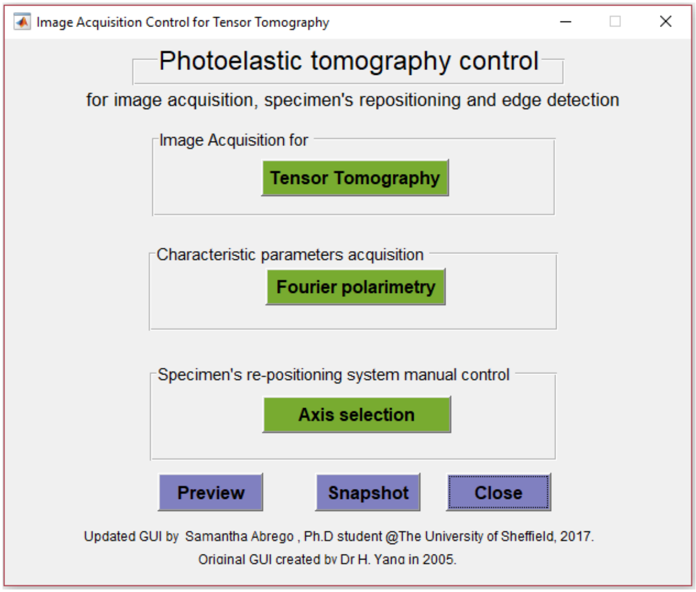

a)

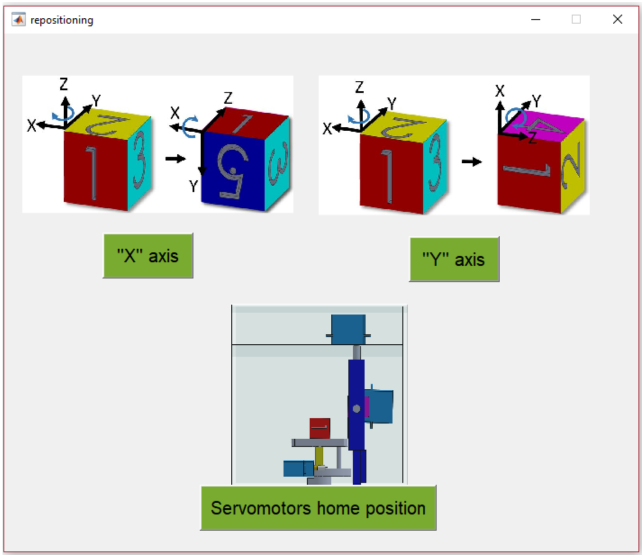

b)

Figure 5.26 Photoelastic Tomography new interface.

5.5 Discussion

This post-processing process involved the cut and shift of the light intensity image and the image averaging of the cut and shifted images. Therefore algorithms to detect automatically the edges are presented in this chapter. All these algorithms needs the image binarization in order to be able to use the image processing functions offered by Matlab. The algorithm 1 used the Matlab function *regionprops*, however some problems were faced such as the detection of the fluid flow lines as edges. Therefore, a second attempt using the function improfile was made. This function worked better than the previous algorithm since a higher quantity of images were cut and centred correctly. Nevertheless, it did not work for all the images due to the light intensity changes. A third attempt using Gaussian filters and the Hough transform to detect vertical lines at a defined angle, in this case 90 degrees was implemented. This algorithm worked better than the previous algorithms however still not getting all the 180 images cut and centred correctly. Nevertheless this algorithm was the one selected to include in the main integrated data acquisition program which as well have a new interface including the repositioning system in case that manual controlling of the servomotors is needed.

5.6 Conclusions

This chapter explained the improvements made to the Photoelastic Tomography apparatus in this research. Where a repositioning system has been implemented to avoid manual handling and to acquire data automatically. Therefore its design, the sequence to control the movements and implementation were presented. Additionally, the program migration process to upgrade the hardware and software of the rig was made. The results adding these improvements will be tested and shown in the following chapter.

Chapter 6

Characteristic parameters assessment

In chapter 4 results of the 3-D reconstructions were shown under different experimental conditions. Even when the refractive index matching was according to the tolerance suggested by McKenzie [90] and the samples were exposed to different loads, these stress reconstruction results were noisy and did not show any trend.
A second attempt to find what variables could be affecting the results was made by validating one of the characteristic parameters. This validation is important since the characteristic parameters are the main input for the stress reconstruction as explained in section 3.4.2.
In this chapter the comparison of the characteristic retardation between the Photoelastic Tomography rig and the Computed Aided Photoelastic Analysis, COPA, software designed by Siegmann, Patterson and Wang [104, 23, 22] is performed for 2 PMMA disks and 2 PMMA cubes. The main difference in these methods is the use of Fourier polarimetry to calculate the characteristic parameters in the case of the Photoelastic Tomography rig and the use of phase stepping in the case of the software COPA and its hardware as shown in Figure 6.1. The camera used for the image acquisition in COPA was a CCD XCD710 Sony camera, and the light source was a sodium lamp with a wavelength of 589 nm.

The mathematical approach of both methods has been explained in section 2.7.2 and 2.7.3 respectively. A brief review of the use of this software is given in section 6.1
Besides the comparison of the methods, a comparison of the characteristic parameters calculation using two cameras of the same model, DC1545M Thorlabs, is presented in section 6.2. The main difference between these cameras is the usage time, one of them has been used for minimum 5 years and the other camera is brand new. Results of the stress reconstruction with the implementation of this new camera are presented in section 6.3

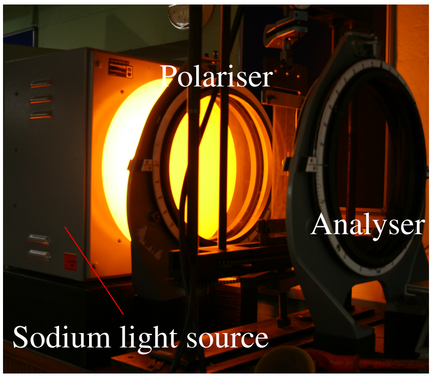

Figure 6.1 Experimental setup to acquire images with COPA software.

6.1 Computer Aided Photoelastic Analysis (COPA), review

Computer Aided Photoelastic Analysis, COPA, software was developed by Siegmann et. al [104, 23, 22]. COPA analyze and process the acquired intensity images through phase stepping methodology. These images are acquired by a programme called CatchSix which produce the file that contains 6 images with different polarization states using a circular polariscope rotated according to the Table 6.1.

Table 6.1 Six step phase stepping positions for quarter waveplate ϕ and analyzer β

Image number	ϕ	β	Light intensity
I_1	0	$\frac{\pi}{4}$	$I_1 = I_m + I_v cos\alpha$
I_2	0	$-\frac{\pi}{4}$	$I_2 = I_m - I_v cos\alpha$
I_3	0	0	$I_3 = I_m - I_v sin\alpha sin2\theta$
I_4	$\frac{\pi}{4}$	$\frac{\pi}{4}$	$I_4 = I_m - I_v cos\alpha sin2\theta$
I_5	$\frac{\pi}{2}$	$\frac{\pi}{2}$	$I_4 = I_m - I_v cos\alpha sin2\theta$
I_6	$\frac{3\pi}{4}$	$\frac{3\pi}{4}$	$I_6 = I_m - I_v cos\alpha sin2\theta$

A CatchSix file is imported to COPA to start the photoelastic analysis, as shown in Figure 6.2. Once the .six file has been imported the wrapped isoclinic map will be shown initially as shown in Figure 6.3. Then a mask to remove the background information can be drawn or imported as shown in Figure 6.4.

Once the mask has been applied, demodulation of the isoclinic is undertaken to avoid error in the situation where the values of the isochromatics exceed half a fringe, or where the isoclinic angle is at $\pm$ 45 degrees. This demodulation consists of the identification of the zero-crossing boundary which is similar to edge detection in image processing. The first step was to build two matrices, a positive and a negative, these matrices will have the same size as the data array and will be filled with zeros. Then an algorithm scans the isoclinic map pixel by pixel in a window of two by two. If the signs of the analysed window of the isoclinic angle is the same, the value of this pixel does not change, however if a negative value in the analysed window is found the pixel with the different sign value will be filled with a one in the negative matrix. In the case of the positive matrix, if a positive value is found in the analysed window the value of this pixel will be changed to one. This will allow to find the zero-crossing boundaries identified by the ones in the matrices. After these boundaries are detected the unwrapping process starts by the selection of a large area, Figure 6.5 b) and c), and by using a quality map based on a procedure developed by Pritt [105] where the quality of the pixels are estimated by the phase derivative variance. Discontinuities are allowed in the quality map for some values that are according to the classical definition of isoclinic angle and the zero-crossings. This was because the isoclinic was valued as zero and it was discarded, detailed information regarding the formulas and the variables used in this process can be found in [106, 104].

A filter called the Wiener filter [107, 108] is used to smooth the data when a large difference is found in the isoclinic map. This filter could be applied before the isoclinic angle is calculated to save computational time. The percentage of wrapped information left and the isoclinic map can be controlled by selecting the windows pixels in the COPA interface, the difference can be notice in the time calculation and the noise in the zero-boundaries images as Figure 6.5a) shows. One thing to bear in mind with this filtering process is that it is used just to effectively detect the zero-boundaries and the unfiltered isocline data is unwrapped therefore no errors will be induced due to this filtering process.

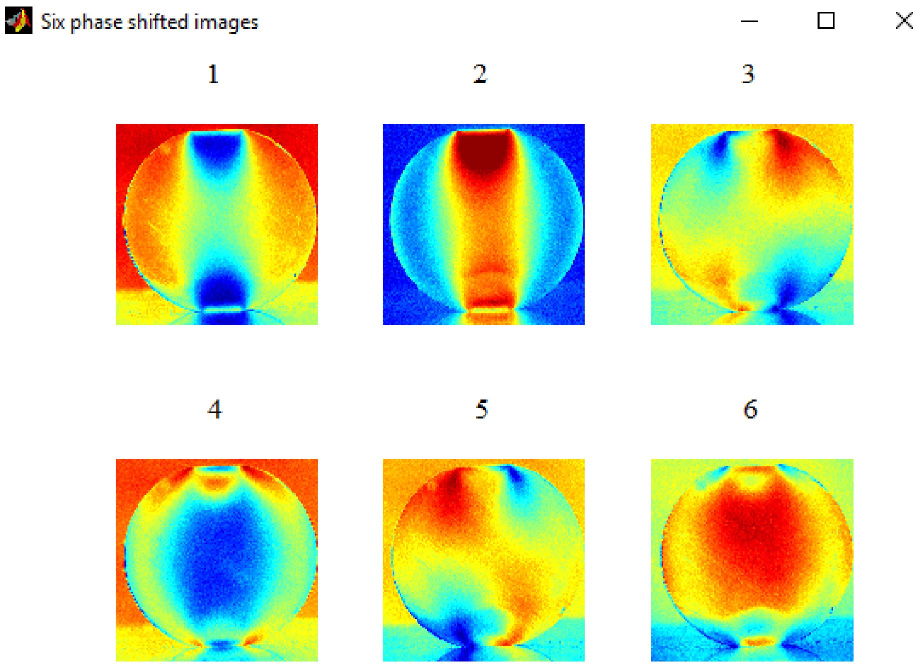

Figure 6.2 Light intensity images acquired through phase stepping.

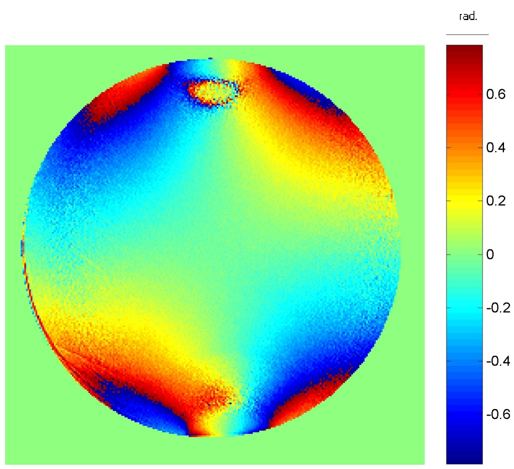

Figure 6.3 Isoclinic map obtained by COPA.

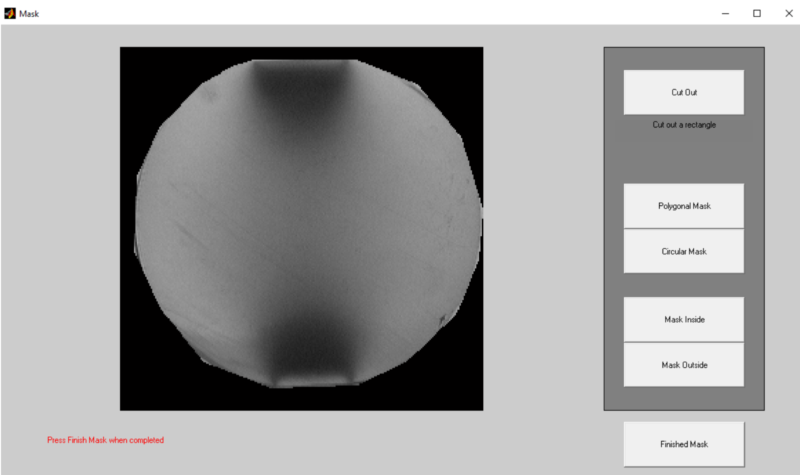

Figure 6.4 Mask drawn to remove background information.

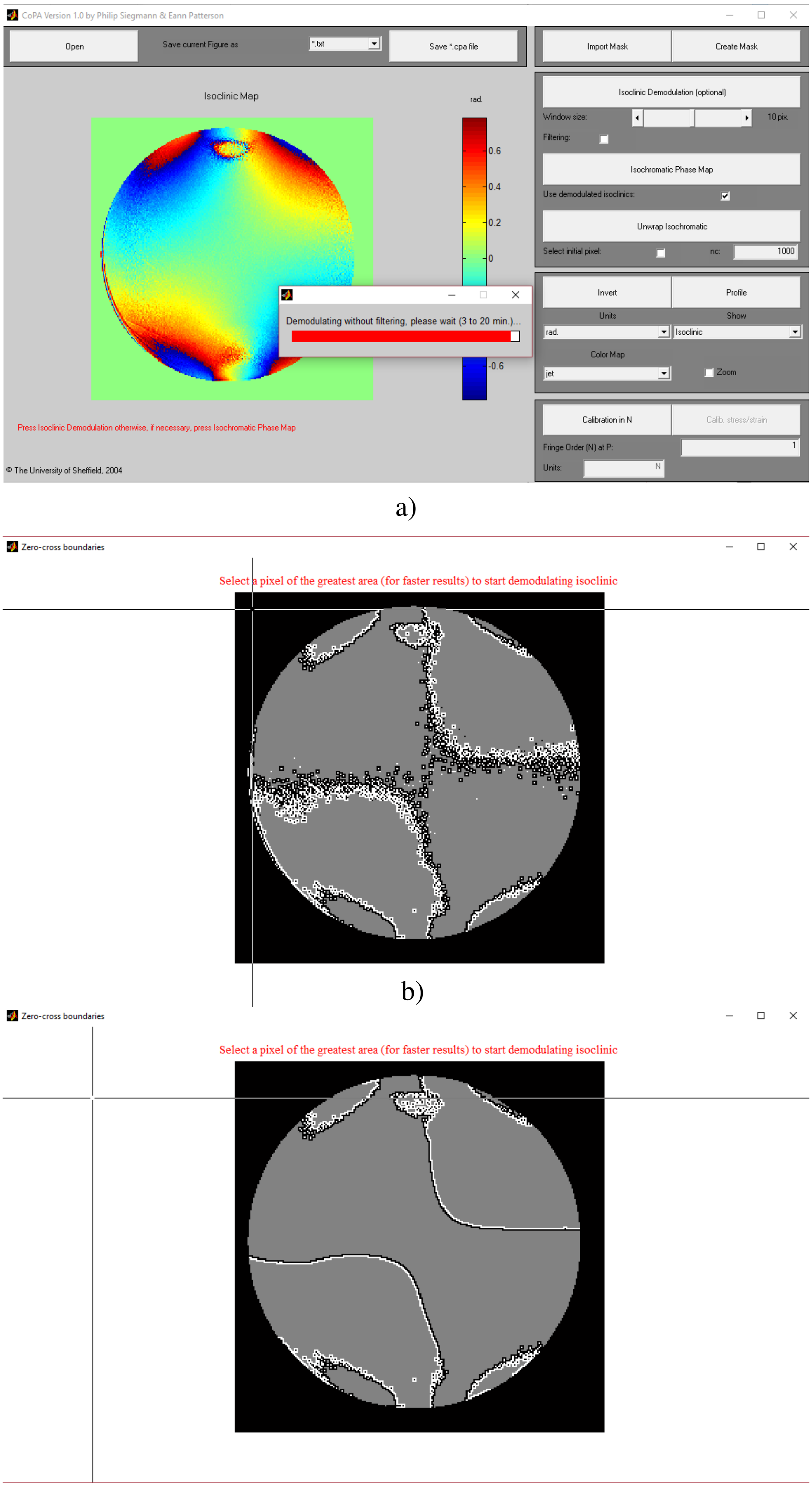

a)

b)

c)

Figure 6.5 a) Demodulating without Wiener filter estimated time from 3 to 20 min, b) Isoclinic map without Wiener filter, c) Isoclinic map with Wiener filter performed in seconds.

Then, the unwrapping algorithm developed by Heredia and Patterson is used [109] over the relative retardation. Finally, the unwrapped isochromatic fringe maps is displayed as fringe orders as shown in Figure 6.6. These fringes are calibrated against the stress at a known point or with the aid of a calibration specimen as displayed in Figure 6.7, otherwise, the software assigns an automatic scale.

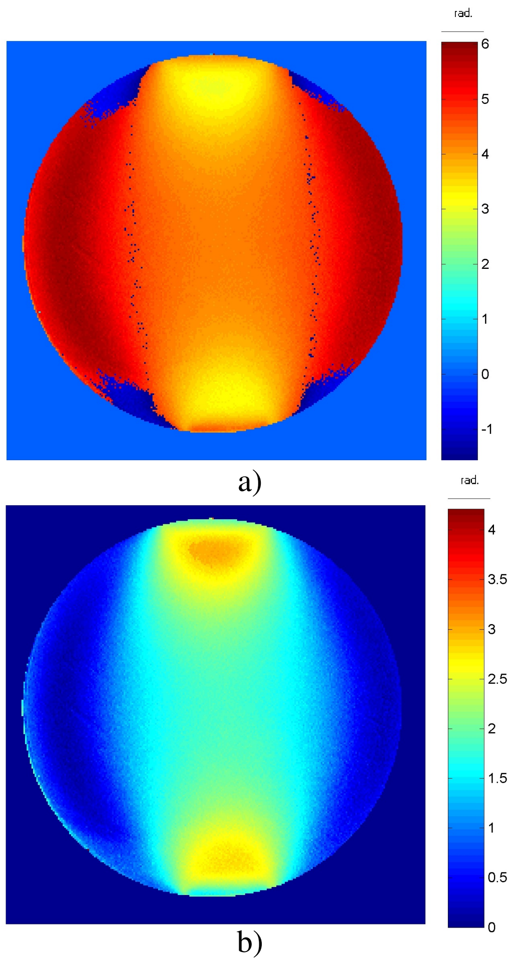

Figure 6.6 a) Wrapped isochomatic map and b) unwrapped isochromatic map.

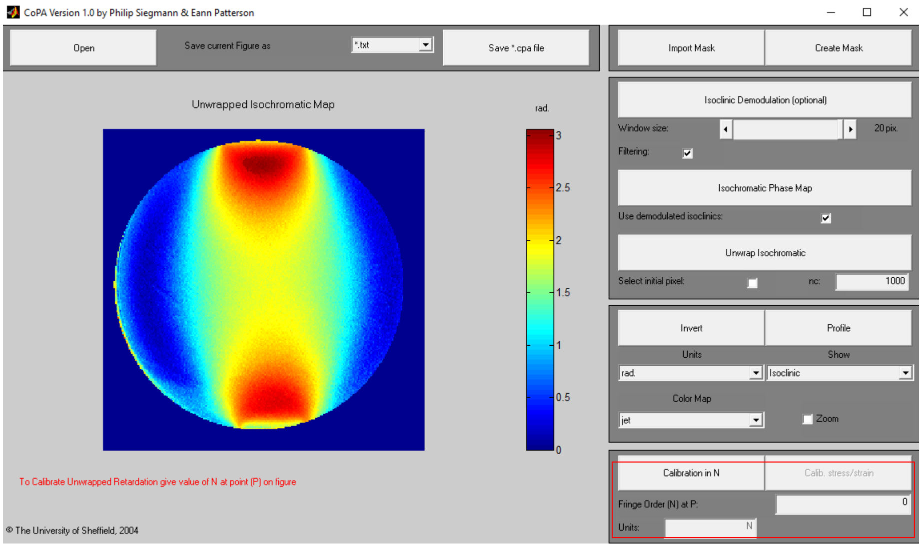

a)

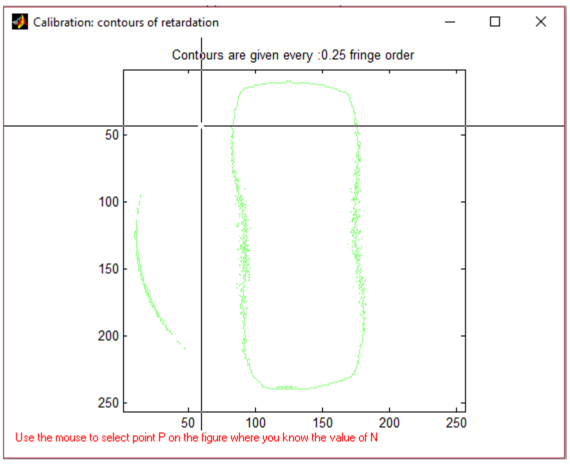

b)

Figure 6.7 Calibration tool in COPA, b) Selecting a known fringe for calibration.

6.2 Characteristic retardation comparison

Two PMMA discs of 18 mm diameter and 3 mm thickness were made from the square PMMA beam of 25.4×25.4 mm. These disks were loaded with 1.5 kg (Disc 1) and 2 kg (Disc 2) which equals to 14.715 N and 19.62 N and exposed to a thermal cycle where the temperature was increased at a rate of $20\,^{\circ}$C per hour and held at the critical temperature for two hours. Then the discs were cooled down at a rate of $5\,^{\circ}$C degrees per hour, hence the strains were locked into the disc through the stress freezing process. The objective was to use these disc to compare the results of the characteristic retardation obtained by the Photoelastic Tomography method with the results obtained by COPA software. The second comparison involved the characteristic retardation for the PMMA cubes previously assessed in chapter 4, which were loaded with 0.300 kg and 1 kg by using a device that triplicate this load therefore it equals to 8.82 N and 29.43 N. Then these cubes were exposed to a thermal cycle were the temperature was increased at a rate of $20\,^{\circ}$C per hour and held at the critical temperature for two hours. Finally the PMMA cubes were cooled down at a rate of $5\,^{\circ}$C degrees per hour. Then 18 polarization states images of these discs and cubes using the old camera and new camera, DC1545M, were taken in order to calculate the characteristic retardation with Fourier polarimetry as described in section 2.7.2. For this comparison only the characteristic retardation will be taken into account since is the parameter that can be directly compared with the isochromatic phase map obtained by COPA. COPA uses the phase stepping methodology to calculate this retardation therefore 6 polarization states images were captured with a circular polariscope and with the CatchSix software by rotating the quarter wave plates the analyser as defined in Table 6.1 [23]. These cameras are compact and uses a high-speed Complementary Metal-Oxide Semiconductor sensor, CMOS, and they are easy to connect to different interfaces such as Matlab. The parameters to control these cameras within the TensorGUI.m program are defined Appendix D. A mask will be applied to the background of all the following data images so that a direct comparison of the retardation determined using both methods may be made.

The results of this comparison between the old camera and new camera were visualized as improvements in the characteristic retardation calculation by using the new camera as they can be seen in Figures 6.10, 6.14 for the discs and in Figures 6.18 and 6.22 for the cubes. By comparing these figures previously mentioned a distinct difference can be seen in the retardation pattern between the old and new camera. Particularly in the discs,Figure 6.10 and 6.14, the new camera gives the shape of fringes expected for a disc in compression, whereas the old camera does not. The reason for this improvement is not confirmed however different variables such as sensor manufacturer defects, exposure to excessive heat, humidity and light for long periods of time could affect the old camera sensor [110]. In the case of sensor manufacturer defects Thorlabs adds in its features a configuration to avoid hot pixels. A hot pixel is defined as a pixel that does not follow a linear behaviour according to the light income to its sensor. Thorlabs offers a configuration to diminish the effect of these hot pixels on the images acquired with their cameras [111]. In the experiments of this research this configuration was made for both cameras as shown in Appendix D, therefore this can be discarded as the reason of the noise source in the old camera. The original experimental rig is not exposed to heat or humidity conditions therefore this could not be the reason of the noisy results with the previous camera. However the camera has been exposed to light for long periods, possibly leading to sensor damage due to thermal or light-induced degradation. For these comparisons only the characteristic retardation was taken into account since it is the parameter that can be directly compared with the isochromatic phase map obtained by COPA.

Six polarization states images were taken using a circular polariscope and the CatchSix software by rotating the quarter wave plates and the analyser as defined in Table 6.1 [23]. Then, the processing of these images by following the steps reviewed in section 6.1 using COPA was made. The results for the discs using COPA are shown in Figure 6.11 and 6.15. The results for the PMMA cubes are shown in Figure 6.19 and 6.23. It can be seen that the Fourier polarimetry results obtained with the new camera differ in magnitude from those obtained using COPA by only 0.1 rad, however the profiles are are similar, as can be seen in Figures 6.12, 6.16, 6.20 and 6.24. The slight difference in the magnitude of these results is related to the light source used in the apparatus of Photoelastic Tomography that calculated the characteristic parameters with Fourier polarimetry and COPA. The first one used a laser of 635 nm wavelength, and COPA apparatus used a sodium lamp of 589.3 nm wavelength. Since retardation is inversely proportional to wavelength of light, the characteristic retardation found using the higher wavelength in the FP method will be slightly lower that that of the COPA method. The algorithm used for Fourier polarimetry did not use an unwrapping filter since the discs and cubes used were loaded with a force that gives as a result fringes lower than half a fringe as it can be seen in Figure 6.8. From these comparisons between the FP method and the phase stepping method, the author is satisfied that the FP method, using the new camera is calculating the characteristic parameters correctly. Therefore this new camera was used in the final test on the whole process of reconstruction as described in the next section.

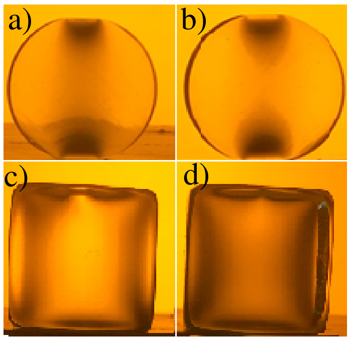

Figure 6.8 Images of light field circular polariscope where the dark fringes shown are an order of 0.5 fringes for a) disc 1, b) disc 2, c) cube 1 and d) cube 2.

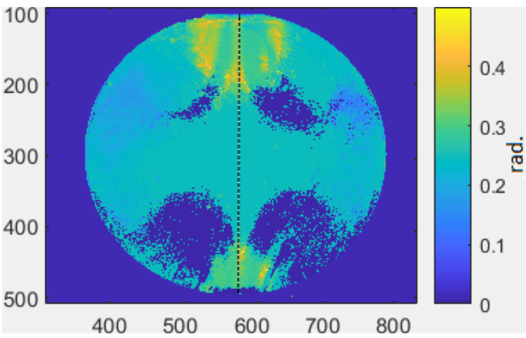

(a) Characteristic retardation image of vertical profile measurement of disc 1 calculated with Fourier polarimetry and taken with old camera.

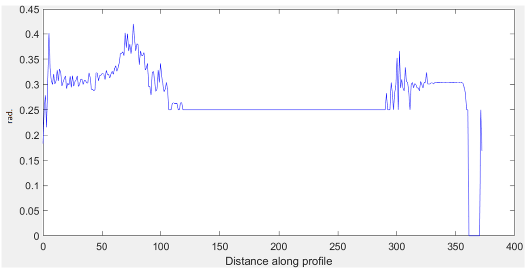

(b) Characteristic retardation graph of vertical profile measurement of disc 1 calculated with Fourier polarimetry and taken with old camera.

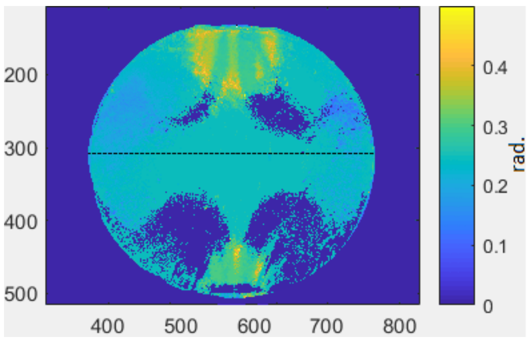

(c) Characteristic retardation image of horizontal profile measurement of disc 1 calculated with Fourier polarimetry and taken with old camera.

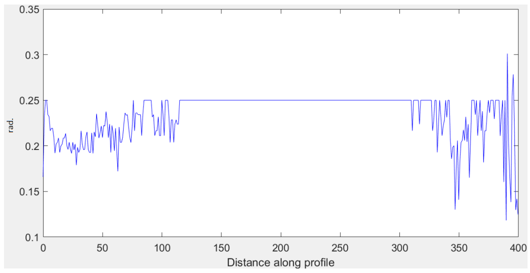

(d) Characteristic retardation graph of horizontal measurement of disc 1 calculated with Fourier polarimetry and taken with old camera.

Figure 6.9 Characteristic retardation for loaded disc 1 (14.715 N) calculated with Fourier polarimetry taken with old camera.

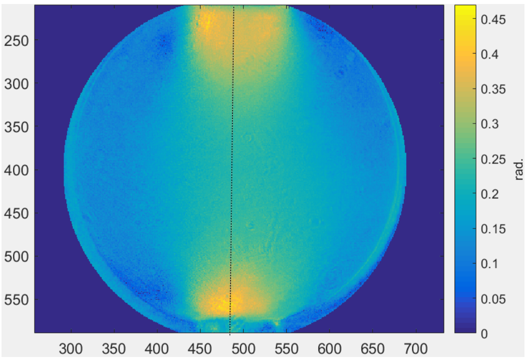

(a) Characteristic retardation image of vertical profile measurement of disc 1 calculated with Fourier polarimetry and taken with new camera.

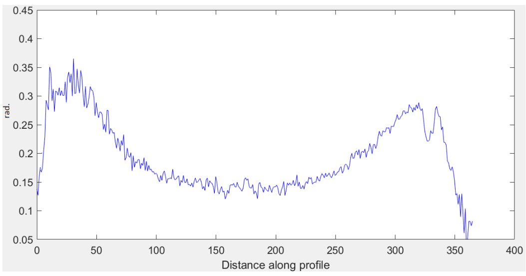

(b) Characteristic retardation graph of vertical profile measurement of disc 1 calculated with Fourier polarimetry and taken with new camera.

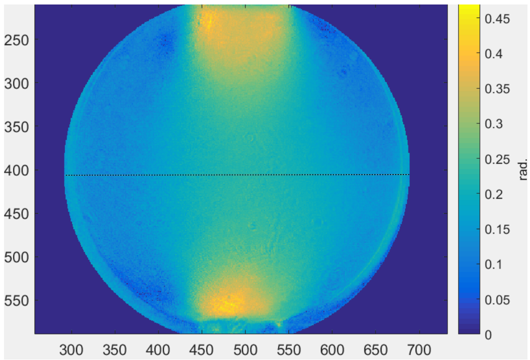

(c) Characteristic retardation image of horizontal profile measurement of disc 1 calculated with Fourier polarimetry and taken with new camera.

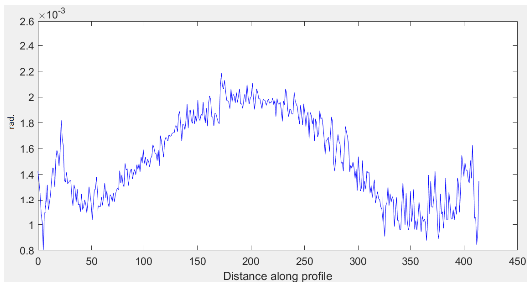

(d) Characteristic retardation graph of horizontal measurement of disc 1 calculated with Fourier polarimetry and taken with new camera.

Figure 6.10 Characteristic retardation for loaded disc 1 (14.715 N) calculated with Fourier polarimetry taken with new camera.

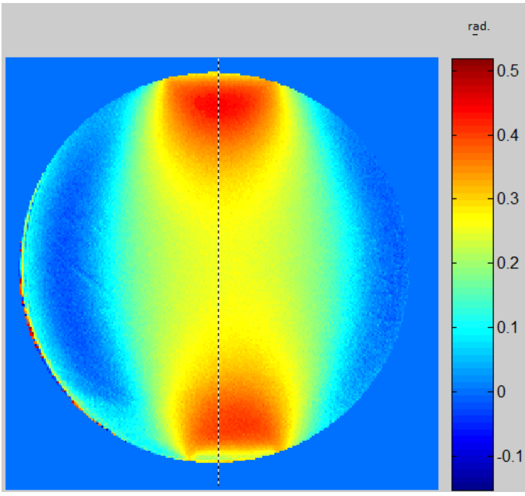

(a) Characteristic retardation image of vertical profile measurement of disc 1 calculated with COPA.

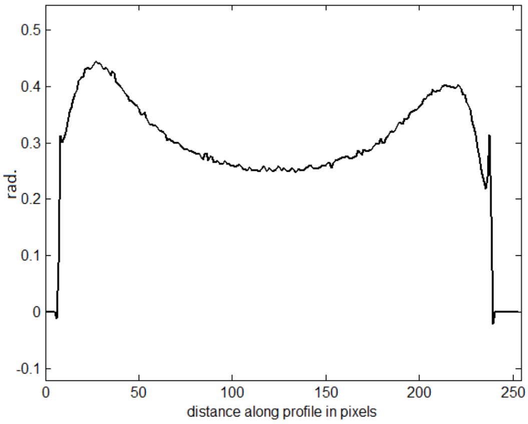

(b) Characteristic retardation graph of vertical profile measurement of disc 1 calculated with COPA.

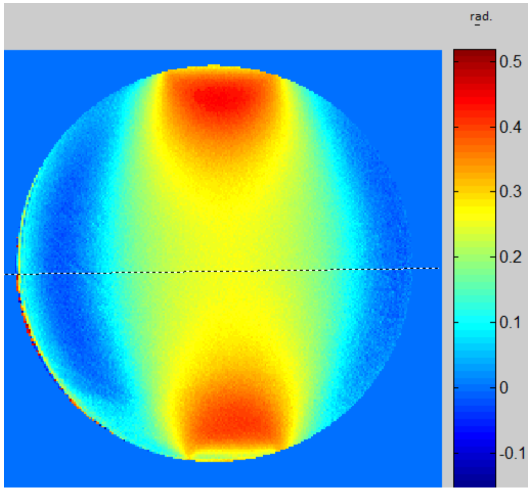

(c) Characteristic retardation image of horizontal profile measurement of disc 1 calculated with COPA.

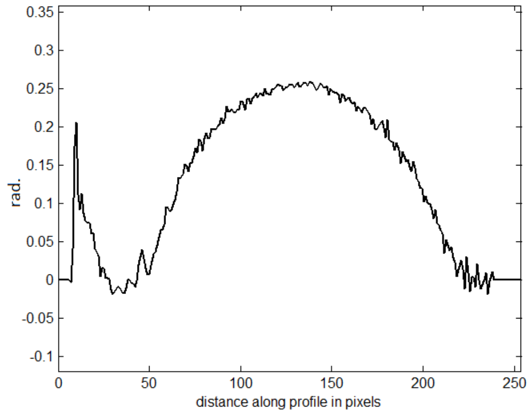

(d) Characteristic retardation graph of horizontal measurement of disc 1 calculated with COPA.

Figure 6.11 Characteristic retardation for loaded disc 1 (14.715 N) calculated with COPA

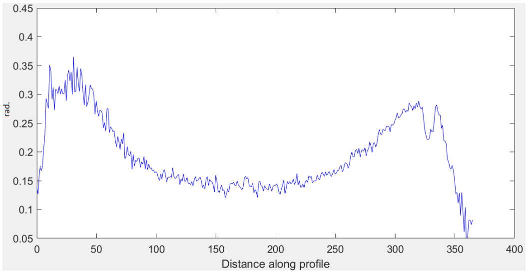

(a) Characteristic retardation graph of vertical profile measurement of disc 1 calculated with Fourier polarimetry and taken with new camera.

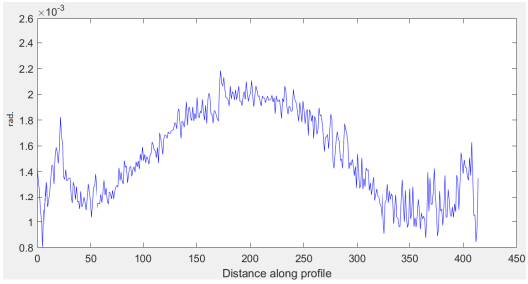

(c) Characteristic retardation graph of horizontal measurement of disc 1 calculated with Fourier polarimetry and taken with new camera.

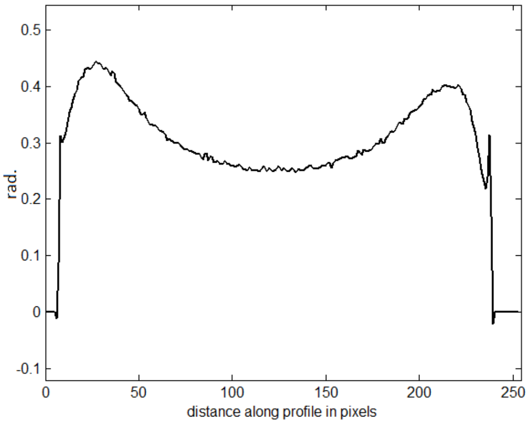

(b) Characteristic retardation graph of vertical profile measurement of disc 1 calculated with COPA.

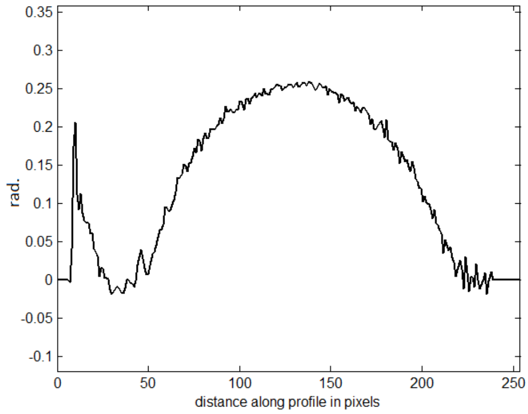

(d) Characteristic retardation graph of vertical profile measurement of disc 1 calculated with COPA.

Figure 6.12 Characteristic retardation direct graphs comparison between Fourier polarimetry (new camera) and COPA results for loaded disc 1 (14.715 N).

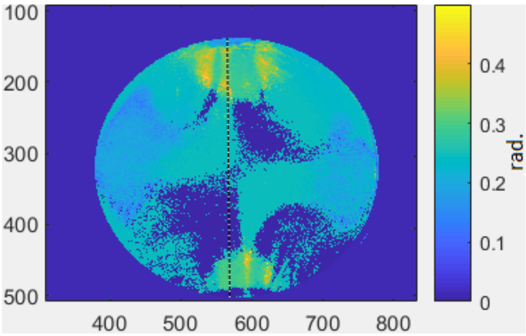

(a) Characteristic retardation image of vertical profile measurement of disc 2 calculated with Fourier polarimetry and taken with old camera.

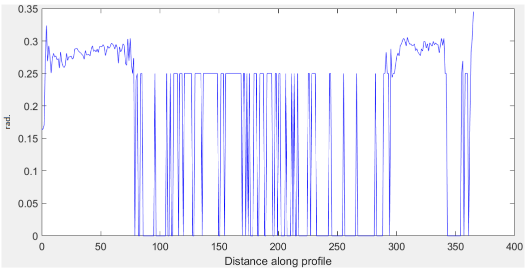

(b) Characteristic retardation graph of vertical profile measurement of disc 2 calculated with Fourier polarimetry and taken with old camera.

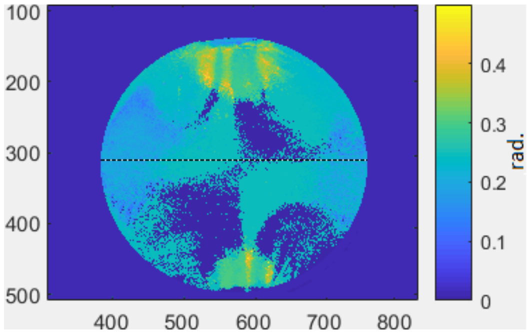

(c) Characteristic retardation image of horizontal profile measurement of disc 2 calculated with Fourier polarimetry and taken with old camera.

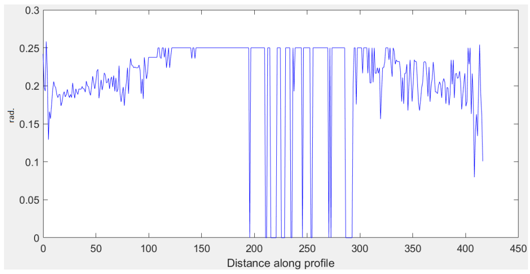

(d) Characteristic retardation graph of horizontal measurement of disc 2 calculated with Fourier polarimetry and taken with old camera.

Figure 6.13 Characteristic retardation for loaded disc 2 (19.62 N) calculated with Fourier Polarimetry taken with old camera.

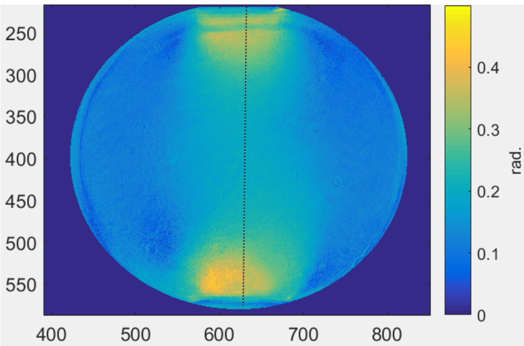

(a) Characteristic retardation image of vertical profile measurement of disc 2 calculated with Fourier polarimetry and taken with new camera.

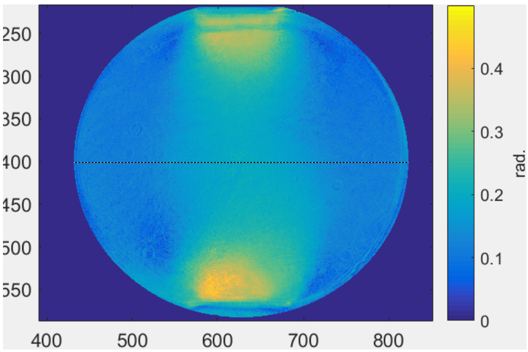

(c) Characteristic retardation image of horizontal profile measurement of disc 2 calculated with Fourier polarimetry and taken with new camera.

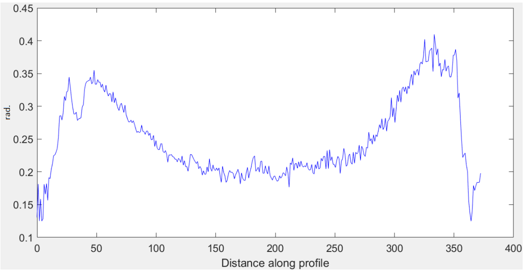

(b) Characteristic retardation graph of vertical profile measurement of disc 2 calculated with Fourier polarimetry and taken with new camera.

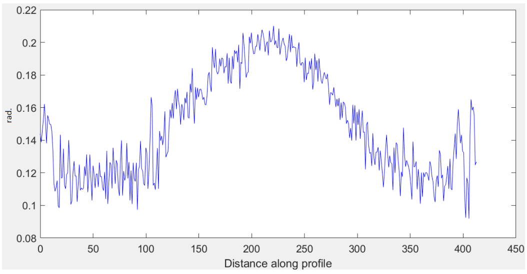

(d) Characteristic retardation graph of horizontal measurement of disc 2 calculated with Fourier polarimetry and taken with new camera.

Figure 6.14 Characteristic retardation for loaded disc 2 (19.62 N) calculated with Fourier polarimetry taken with new camera.

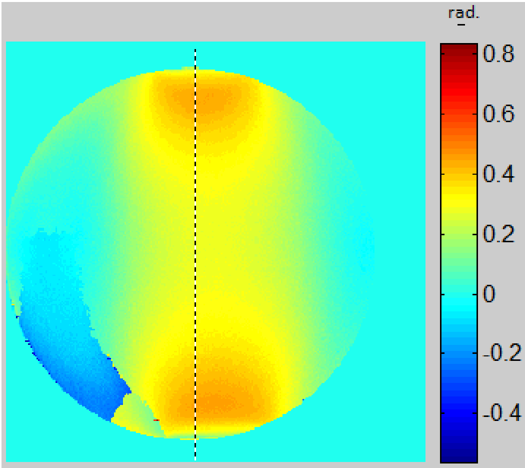

(a) Characteristic retardation image of vertical profile measurement of disc 2 calculated with COPA.

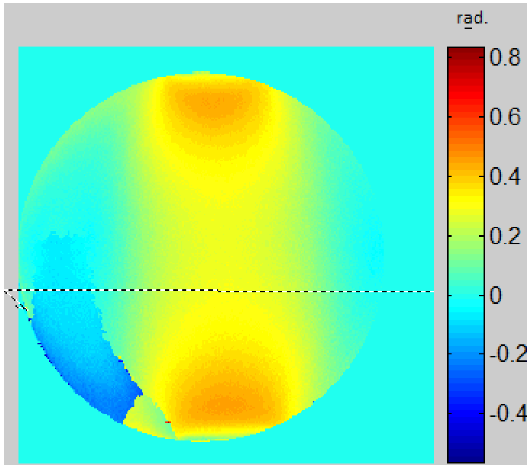

(c) Characteristic retardation image of horizontal profile measurement of disc 2 calculated with COPA.

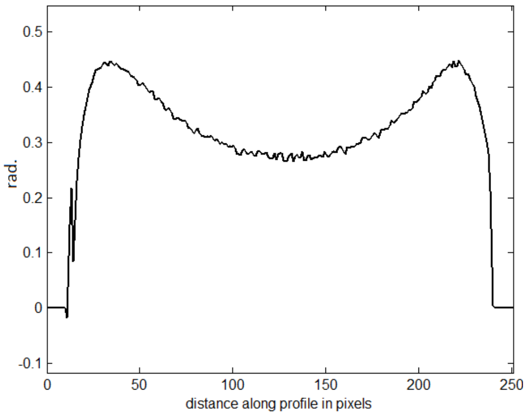

(b) Characteristic retardation graph of vertical profile measurement of disc 2 calculated with COPA.

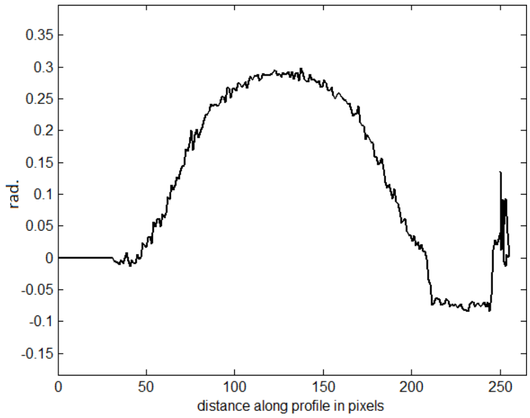

(d) Characteristic retardation graph of horizontal measurement of disc 2 calculated with COPA.

Figure 6.15 Characteristic retardation for loaded disc 2 (19.62 N) calculated with COPA

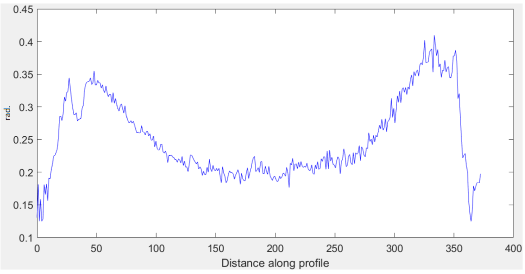

(a) Characteristic retardation graph of vertical profile measurement of disc 1 calculated with Fourier polarimetry and taken with new camera.

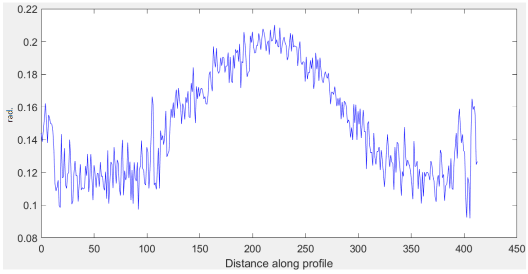

(c) Characteristic retardation graph of horizontal measurement of disc 1 calculated with Fourier polarimetry and taken with new camera.

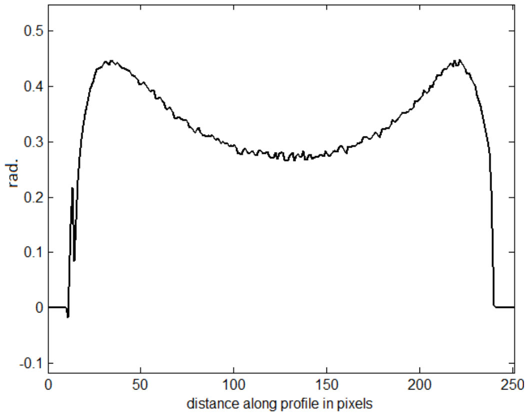

(b) Characteristic retardation graph of vertical profile measurement of disc 1 calculated with COPA.

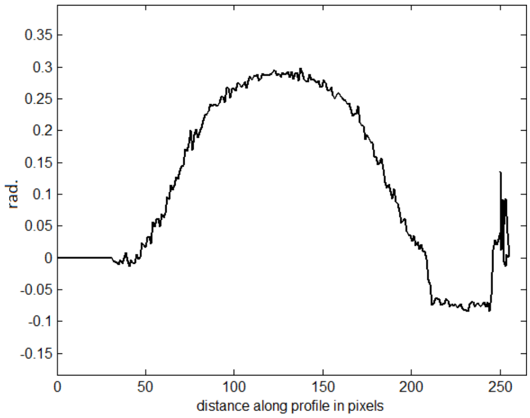

(d) Characteristic retardation graph of vertical profile measurement of disc 1 calculated with COPA.

Figure 6.16 Characteristic retardation direct comparison graphs between Fourier polarimetry (new camera) and COPA results for loaded disc 2 (19.62 N).

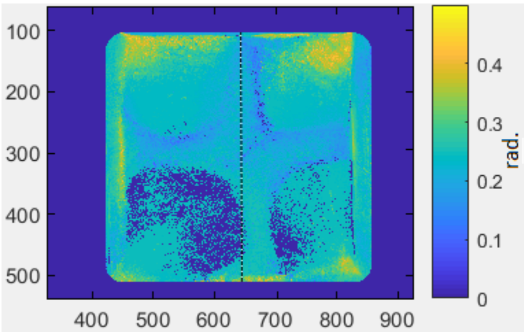

(a) Characteristic retardation image of vertical profile measurement of cube 1 calculated with Fourier polarimetry and taken with old camera.

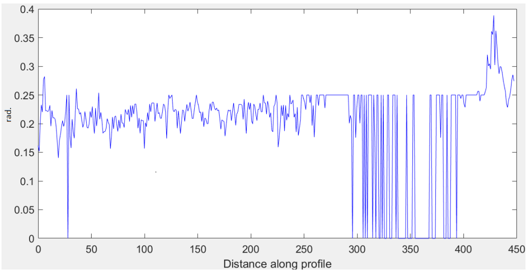

(b) Characteristic retardation graph of vertical profile measurement of cube 1 calculated with Fourier polarimetry and taken with old camera.

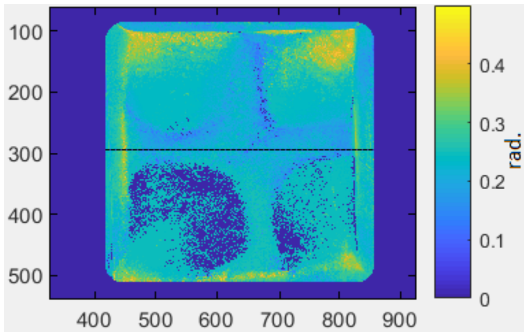

(c) Characteristic retardation image of horizontal profile measurement of cube 1 calculated with Fourier polarimetry and taken with old camera.

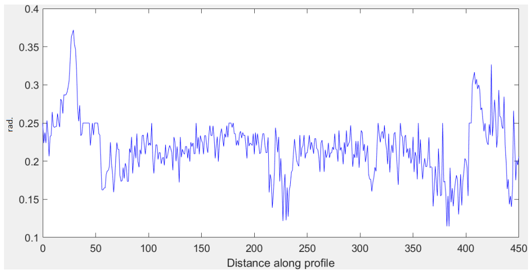

(d) Characteristic retardation graph of horizontal profile measurement of cube 1 calculated with Fourier polarimetry and taken with old camera.

Figure 6.17 Characteristic retardation for loaded cube 1 (8.82 N) calculated with Fourier polarimetry taken with old camera

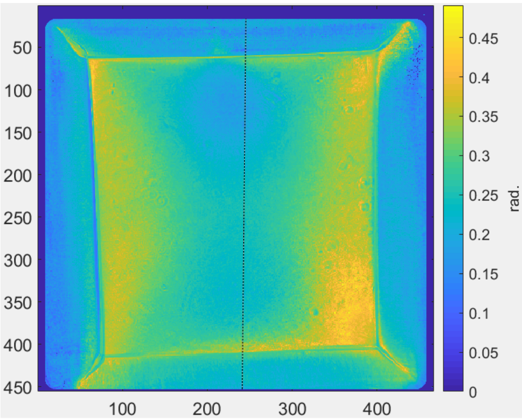

(a) Characteristic retardation image of vertical profile measurement of cube 1 calculated with Fourier polarimetry and taken with new camera.

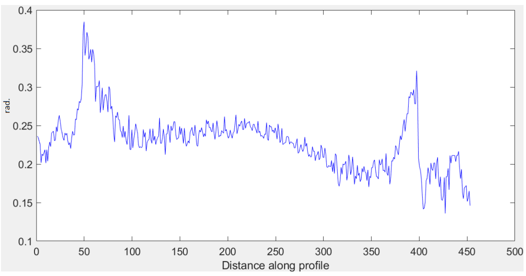

(b) Characteristic retardation graph of vertical profile measurement of cube 1 calculated with Fourier polarimetry and taken with new camera.

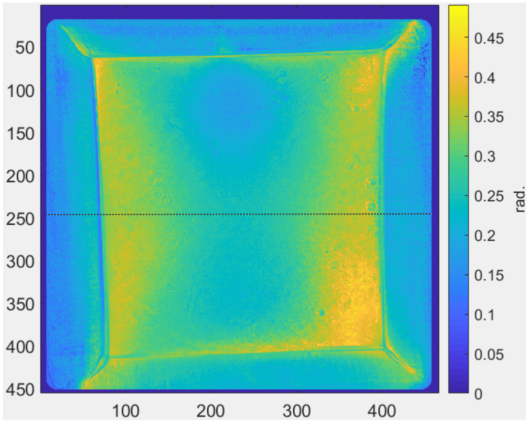

(c) Characteristic retardation image of horizontal profile measurement of cube 1 calculated with Fourier polarimetry and taken with new camera.

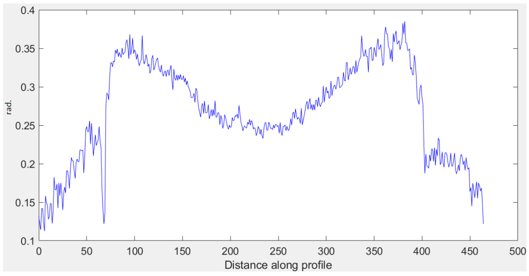

(d) Characteristic retardation graph of horizontal measurement of cube 1 calculated with Fourier polarimetry and taken with new camera.

Figure 6.18 Characteristic retardation for loaded cube 1 (8.82 N) calculated with Fourier polarimetry taken with new camera.

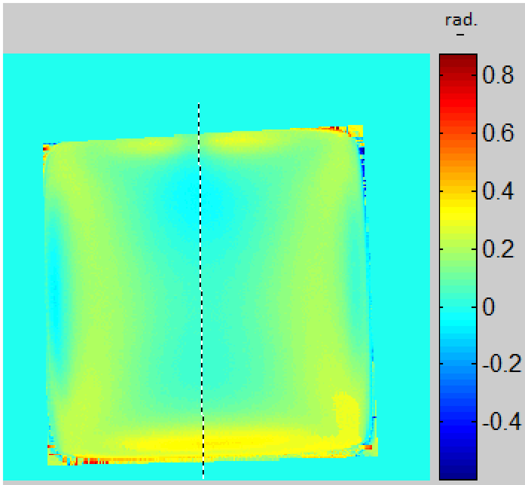

(a) Characteristic retardation image of vertical profile measurement of cube 1 calculated with COPA.

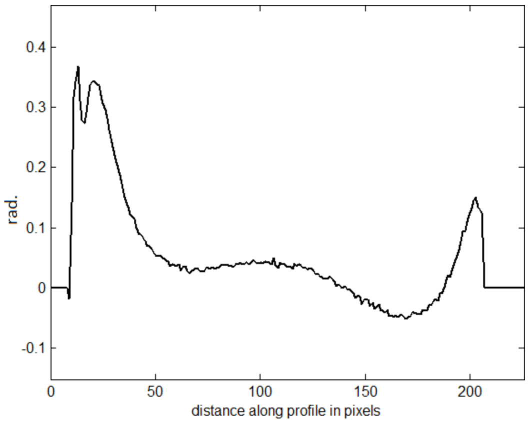

(b) Characteristic retardation graph of vertical profile measurement of cube 1 calculated with COPA.

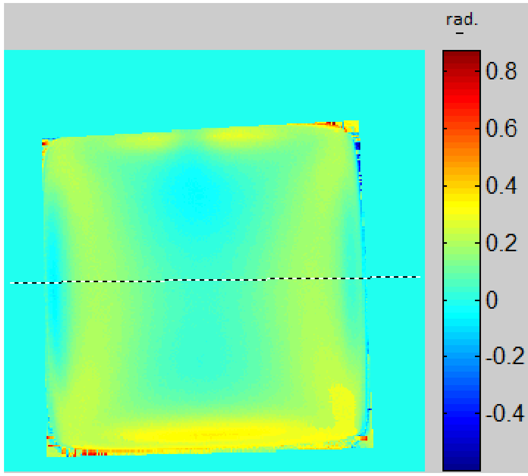

(c) Characteristic retardation image of horizontal profile measurement of cube 1 calculated with COPA.

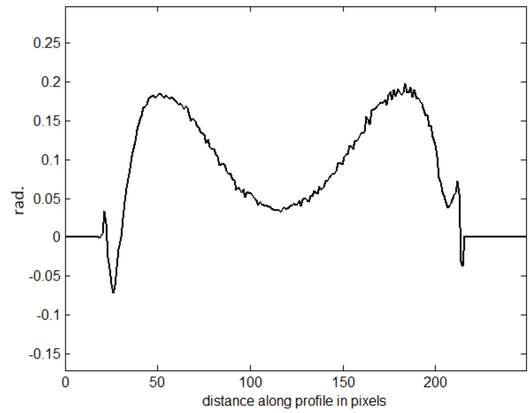

(d) Characteristic retardation graph of horizontal measurement of cbe 1 calculated with COPA.

Figure 6.19 Characteristic retardation for loaded cube 1 (8.82 N) calculated with COPA

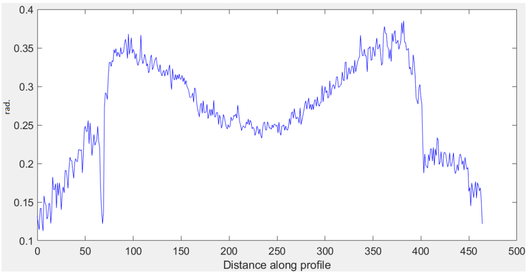

(a) Characteristic retardation graph of vertical profile measurement of cube 1 calculated with Fourier polarimetry and taken with new camera.

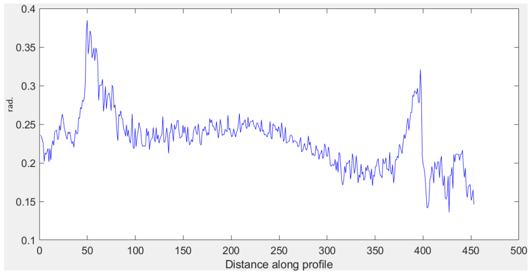

(c) Characteristic retardation graph of horizontal measurement of cube 1 calculated with Fourier polarimetry and taken with new camera.

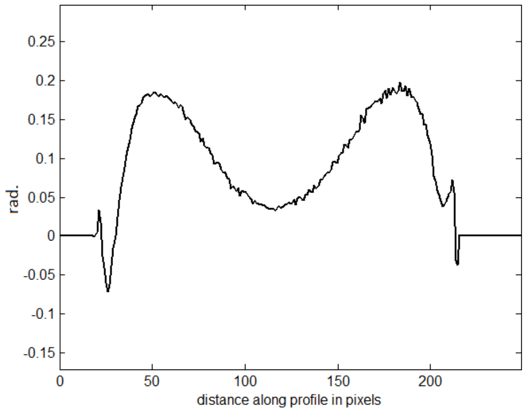

(b) Characteristic retardation graph of vertical profile measurement of cube 1 calculated with COPA.

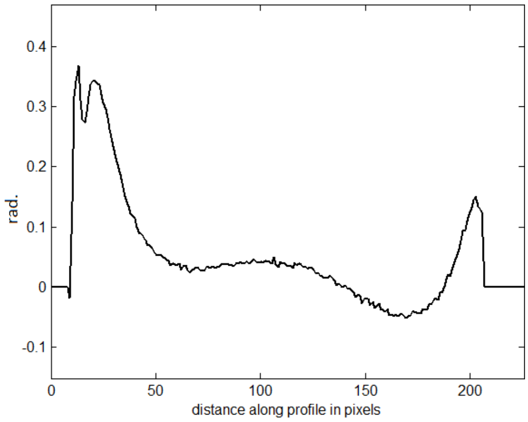

(d) Characteristic retardation graph of vertical profile measurement of cube 1 calculated with COPA.

Figure 6.20 Characteristic retardation direct comparison graphs between Fourier polarimetry (new camera) and COPA results for loaded cube 1 (8.82 N).

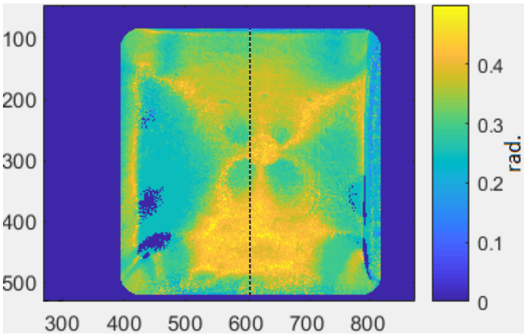

(a) Characteristic retardation image of vertical profile measurement of cube 2 calculated with Fourier polarimetry and taken with old camera.

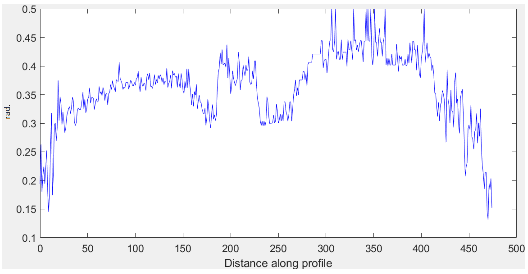

(b) Characteristic retardation graph of vertical profile measurement of cube 2 calculated with Fourier polarimetry and taken with old camera.

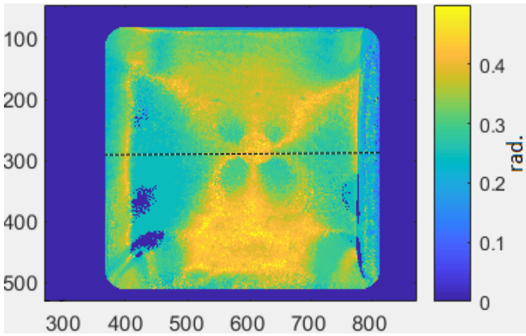

(c) Characteristic retardation image of horizontal profile measurement of cube 2 calculated with Fourier polarimetry and taken with old camera.

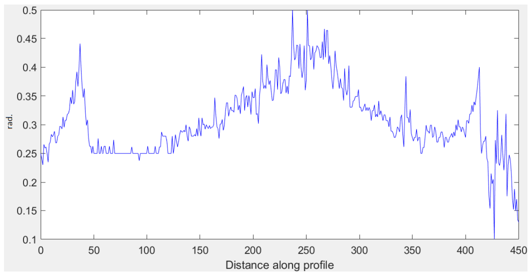

(d) Characteristic retardation graph of horizontal profile measurement of cube 2 calculated with Fourier polarimetry and taken with old camera.

Figure 6.21 Characteristic retardation for loaded cube 2 (29.43 N) calculated with Fourier polarimetry taken with old camera.

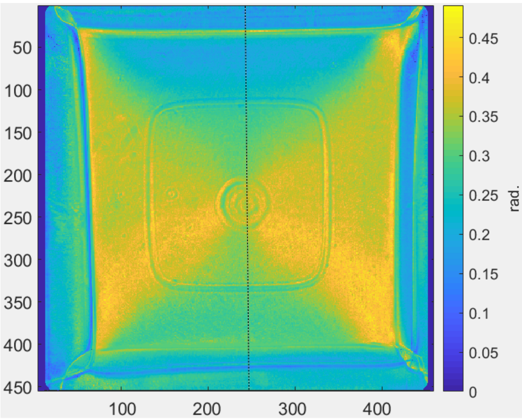

(a) Characteristic retardation image of vertical profile measurement of cube 2 calculated with Fourier polarimetry and taken with new camera.

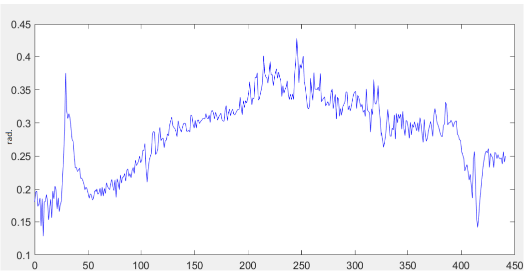

(b) Characteristic retardation graph of vertical profile measurement of cube 2 calculated with Fourier polarimetry and taken with new camera.

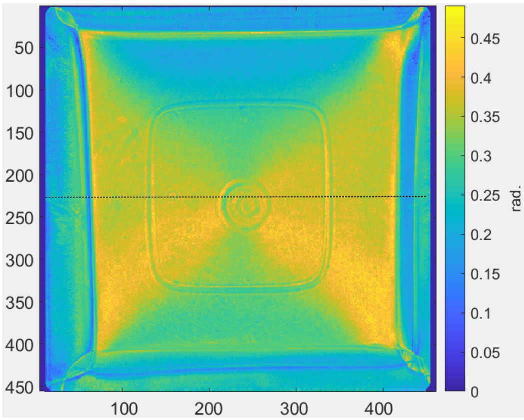

(c) Characteristic retardation image of horizontal profile measurement of cube 2 calculated with Fourier polarimetry and taken with new camera.

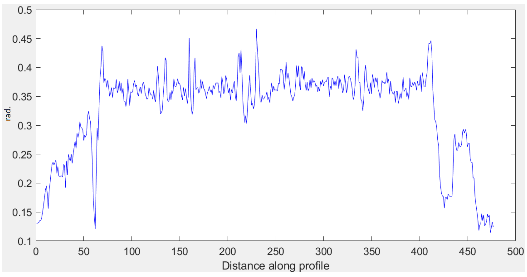

(d) Characteristic retardation graph of horizontal measurement of cube 2 calculated with Fourier polarimetry and taken with new camera.

Figure 6.22 Characteristic retardation for loaded cube 2 (29.43 N) calculated with Fourier polarimetry taken with new camera.

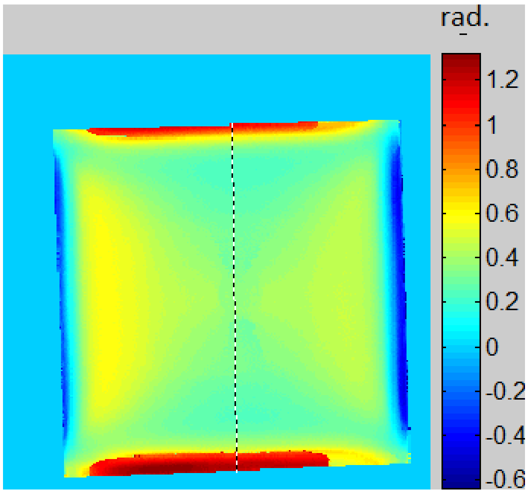

(a) Characteristic retardation image of vertical profile measurement of cube 2 calculated with COPA.

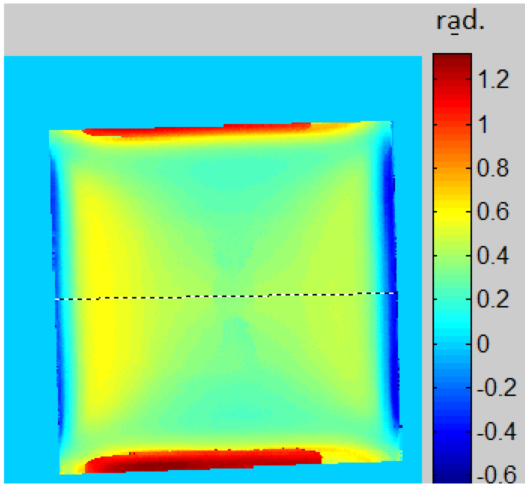

(c) Characteristic retardation image of horizontal profile measurement of cube 2 calculated with COPA.

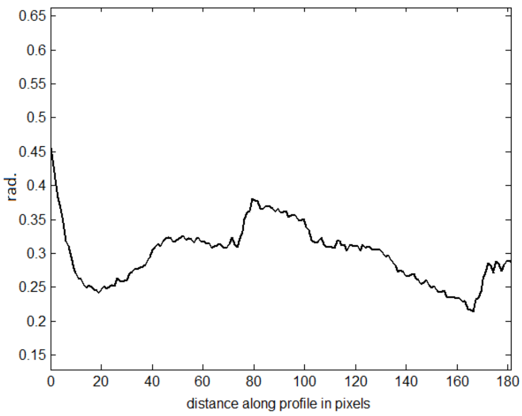

(b) Characteristic retardation graph of vertical profile measurement of cube 2 calculated with COPA.

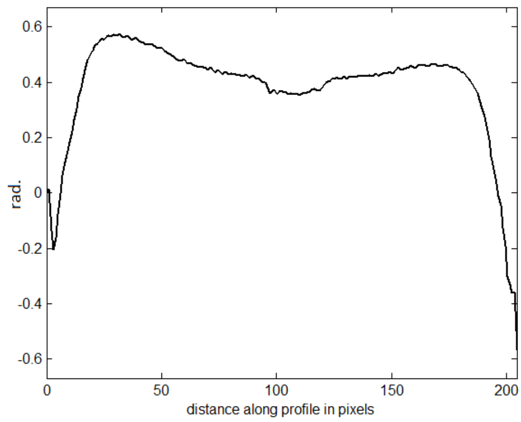

(d) Characteristic retardation graph of horizontal measurement of cube 2 calculated with COPA.

Figure 6.23 Characteristic retardation for loaded cube 2 (29.43 N) calculated with COPA.

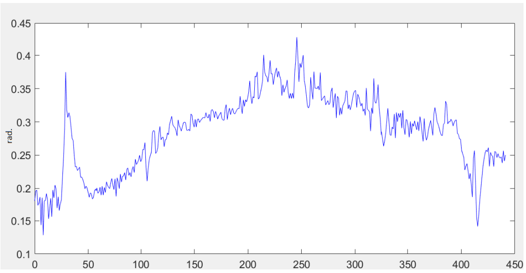

(a) Characteristic retardation graph of vertical profile measurement of cube 2 calculated with Fourier polarimetry and taken with new camera.

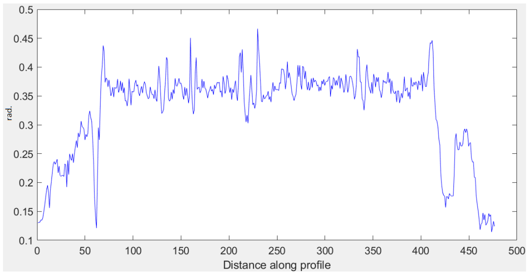

(c) Characteristic retardation graph of horizontal measurement of cube 2 calculated with Fourier polarimetry and taken with new camera.

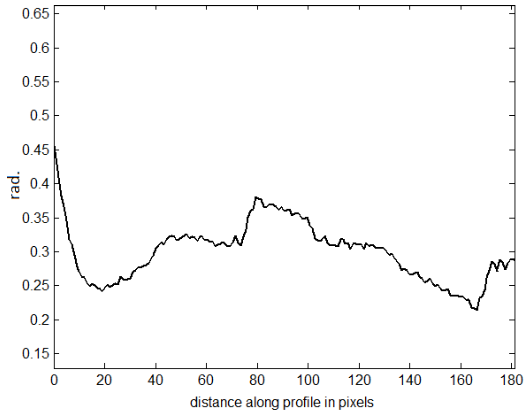

(b) Characteristic retardation graph of vertical profile measurement of cube 2 calculated with COPA.

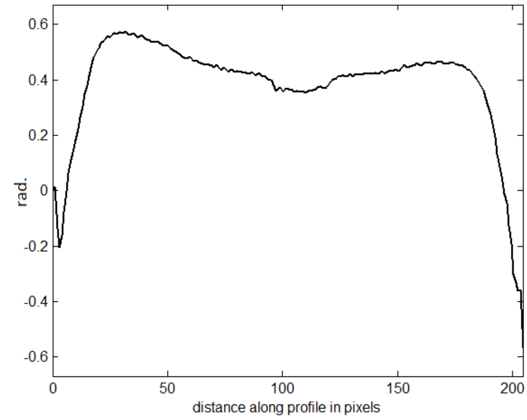

(d) Characteristic retardation graph of vertical profile measurement of cube 2 calculated with COPA.

Figure 6.24 Characteristic retardation direct comparison graphs between Fourier polarimetry (new camera) and COPA results for loaded cube 2 (29.43 N).

6.3 Reconstruction results with new camera implemented

In this section, the stress reconstruction results using the new camera, the re-positioning system, the new tank and the integration of the data acquisition programs are presented. The aim of this experiment is to test the impact of these improvements in comparison with the stress reconstructions obtained by using the old camera and the original rig presented in chapter 4. The specimen used for this test are the same as the one used for the experiments in chapter 4, therefore the load conditions of 8.82 N and 29.43 N are used as shown in Table 6.2. The complete data acquisition consisted of the collection of 180 light intensity images where the rotation of the sample from 0 to 180 degrees in the $''Z''$ axis, Figure 5.1, in increments of 1 degree were taken. Every time the specimen is rotated 1 degree a total of 18 images with different polarization states are captured as described in chapter 3, Figure 3.9. This process has to be repeated for 3 axis of the specimen as described in chapter 3, Figure 3.10. Then the automated cut and shift algorithm 3 presented in chapter 5, section 5.3 was used to remove the background information of the specimen. Then the averaging process at a number of pixels to reduce the amount of data processed by the program called "$Image - average.m$" was done, as explained in chapter 3, section 3.4.1. The results of the data acquisition, the cropped images and the averaged images for 2 of the 180 light intensity images acquired are presented in Figures 6.26, 6.29, 6.33, 6.37. The calculation of the characteristic parameters, using Fourier polarimetry as explained in section 2.7.2 are presented in Figures 6.26, 6.30, 6.34, 6.38. Finally the results of the reconstructions are shown in Figures 6.27, 6.31, 6.35 and 6.39 using the 3 by 3 pixels average. The results of the reconstructions using the 4 by 4 average is presented in Figures 6.28, 6.32, 6.36 and 6.40.

Table 6.2 Experimental work with conditions of PMMA samples after new camera and rig improvements implementation

Nº	Sample	Load	Immersion fluid	Averaging	Aim
1	PMMA 1 (batch 1)	8.82	Yes	3x3 pixels 4x4 pixels	To test: New camera Repositionig system New tank Automated cut_shift algorithm Integration of the programs
2	PMMA 2 (batch 1)	29.43	Yes	3x3 pixels 4x4 pixels	
3	PMMA 3 (batch 2)	8.82	Yes	3x3 pixels 4x4 pixels	
4	PMMA 4 (batch 2)	29.43	Yes	3x3 pixels 4x4 pixels	

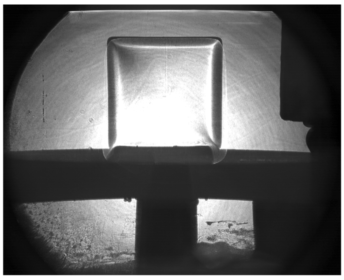

(a) 0 degrees light intensity image

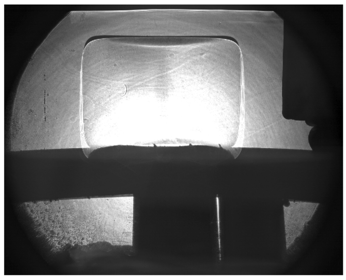

(e) 45 degrees light intensity image

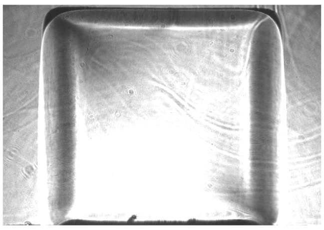

(b) 0 degrees cut light intensity image

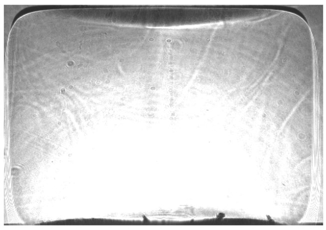

(f) 45 degrees cut light intensity image

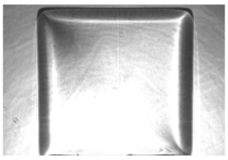

(c) 0 degrees 3 by 3 image average

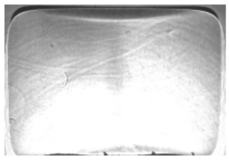

(g) 45 degrees 3 by 3 image average

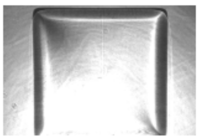

(d) 0 degrees 4 by 4 image average

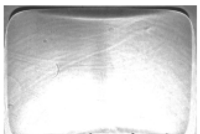

(h) 45 degrees 4 by 4 image average

Figure 6.25 Light intensity images for experiment 1 with new camera: stressed and no immersed specimen with the polariser and analyser set at 0 degrees and 20 degrees respectively. Where a) shows the data acquisition for PMMA 1 at 0 degrees and e) at 45 degrees, b) shows the cut image at 0 degrees and f) at 45 degrees, c) shows the 3 by 3 pixels averaged images at 0 degrees and g) at 45 degrees. Finally, d) shows the 4 by 4 pixels averaged images at 0 degrees and g) at 45 degrees.

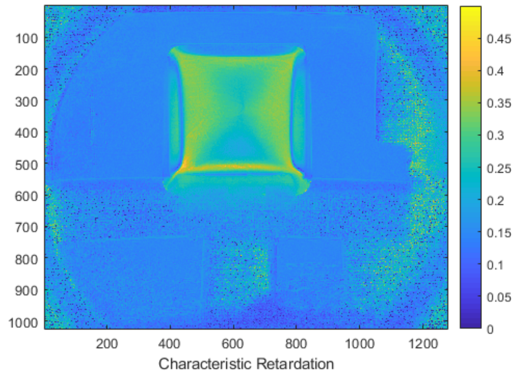

(a) Characteristic retardation at 0 degrees

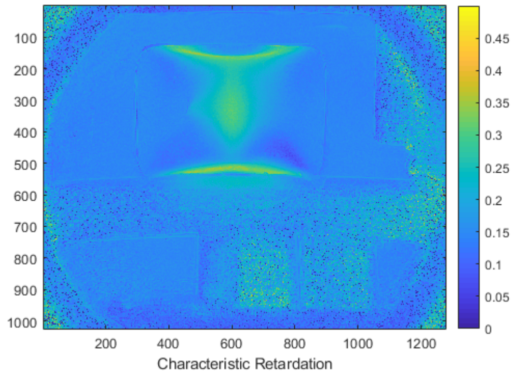

(d) Characteristic retardation at 45 degrees.

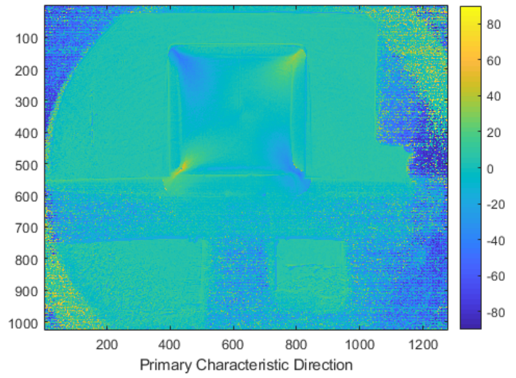

(b) Primary characteristic direction at 0 degrees

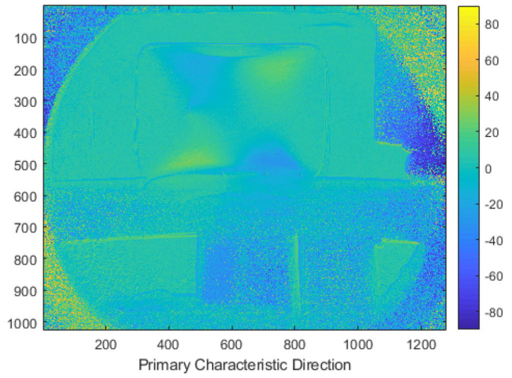

(e) Primary characteristic direction at 45 degrees

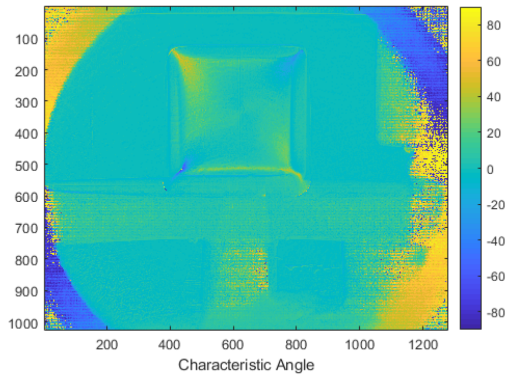

(c) Characteristic angle at 0 degrees

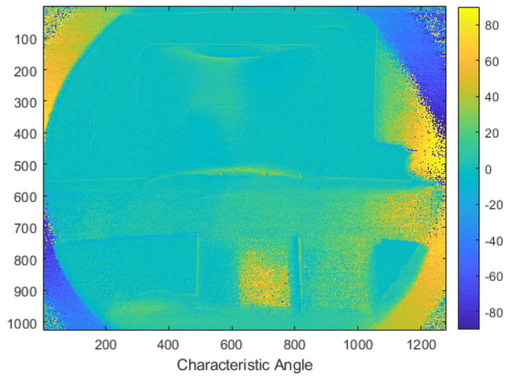

(f) Characteristic angle at 45 degrees

Figure 6.26 Characteristic parameters calculation for experiment 1 with new camera: stressed and immersed PMMA1 at 0 degrees and 45 degrees position

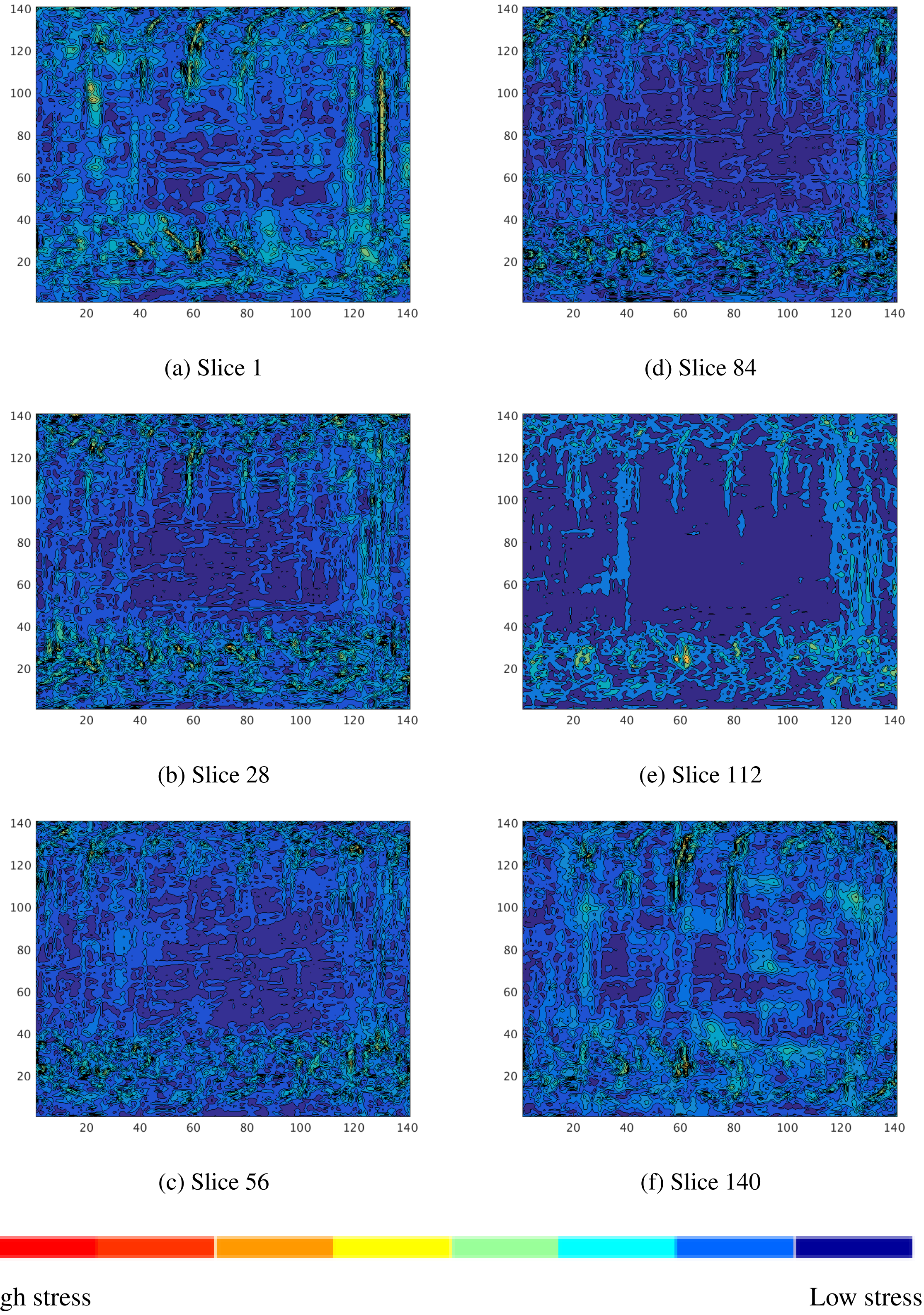

(a) Slice 1

(d) Slice 84

(b) Slice 28

(e) Slice 112

(c) Slice 56

(f) Slice 140

Figure 6.27 3-D reconstruction for PMMA 1: immersed and stressed using 3 by 3 averaged images.

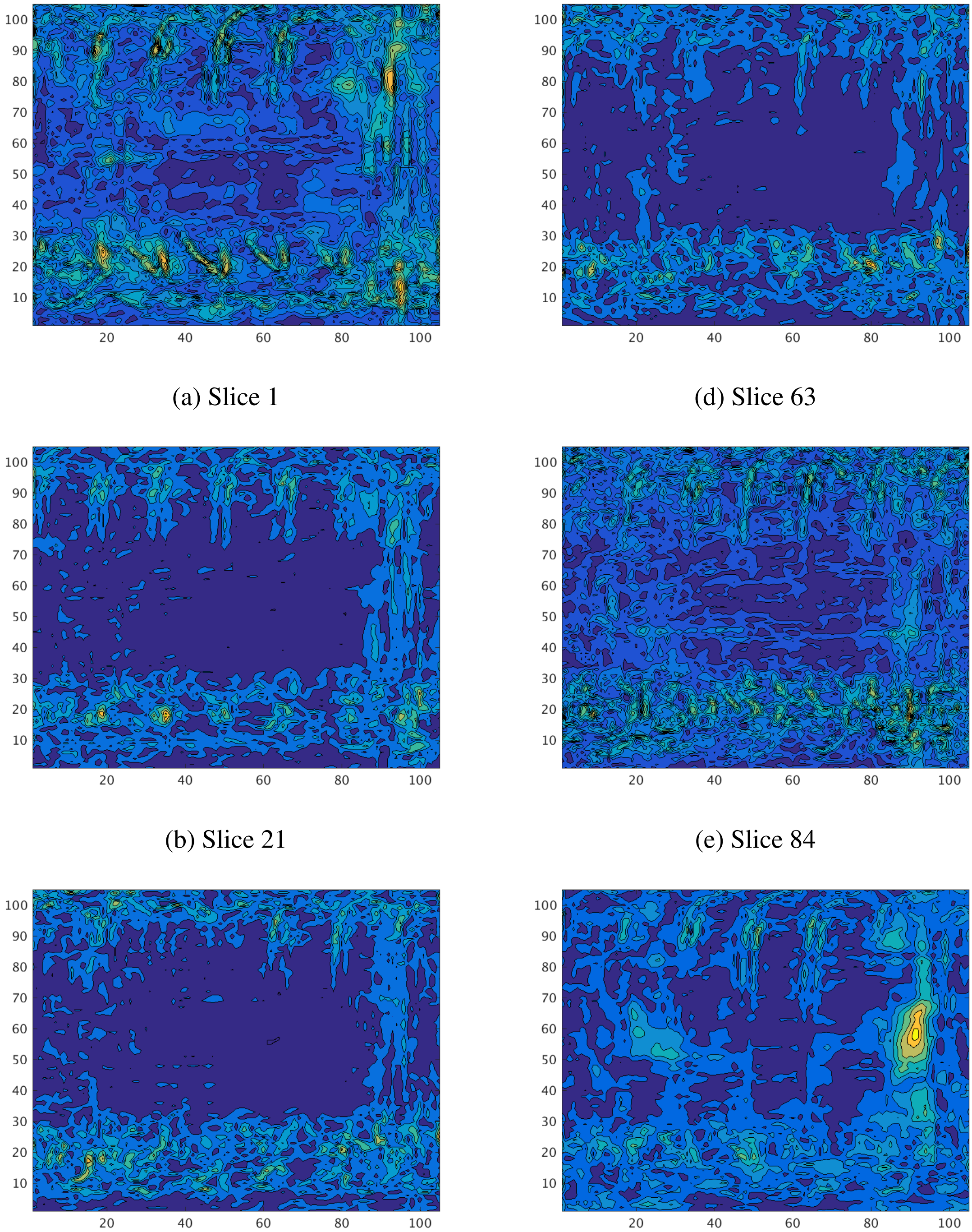

(a) Slice 1

(d) Slice 63

(b) Slice 21

(e) Slice 84

(c) Slice 42

(f) Slice 105

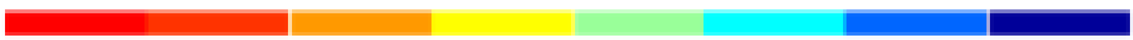

High stress Low stress

Figure 6.28 3-D reconstruction for PMMA 1: immersed and stressed using 4 by 4 averaged images.

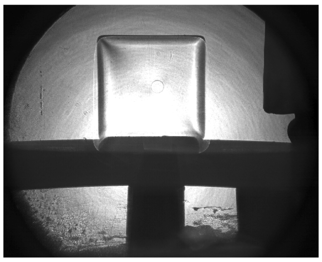

(a) 0 degrees light intensity image

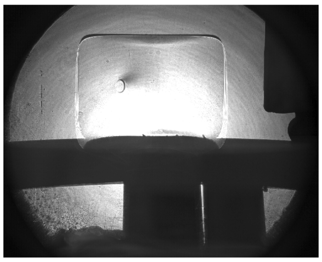

(e) 45 degrees light intensity image

(b) 0 degrees cut light intensity image

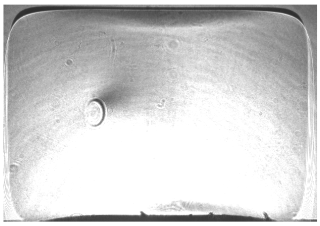

(f) 45 degrees cut light intensity image

(c) 0 degrees 3 by 3 image average

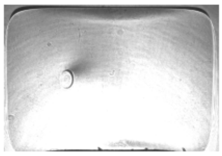

(g) 45 degrees 3 by 3 image average

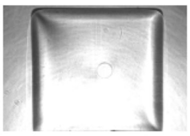

(d) 0 degrees 4 by 4 image average

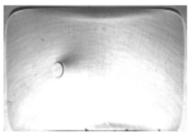

(h) 45 degrees 4 by 4 image average

Figure 6.29 Light intensity images for experiment 2 with new camera: stressed and no immersed specimen with the polariser and analyser set at 0 degrees and 20 degrees respectively. Where a) shows the data acquisition for PMMA 2 at 0 degrees and e) at 45 degrees, b) shows the cut image at 0 degrees and f) at 45 degrees, c) shows the 3 by 3 pixels averaged images at 0 degrees and g) at 45 degrees. Finally, d) shows the 4 by 4 pixels averaged images at 0 degrees and g) at 45 degrees.

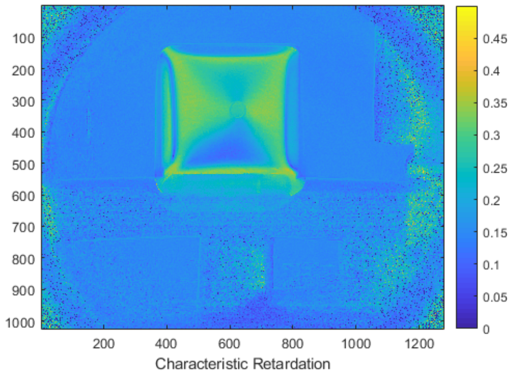

(a) Characteristic retardation at 0 degrees

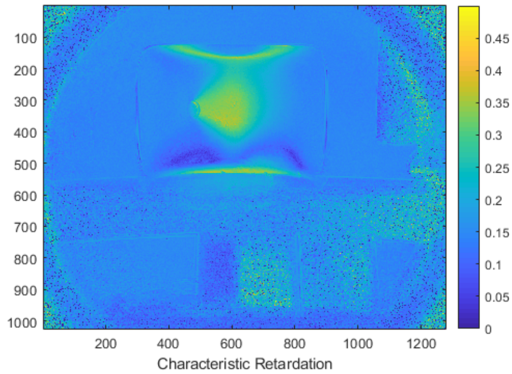

(d) Characteristic retardation at 45 degrees

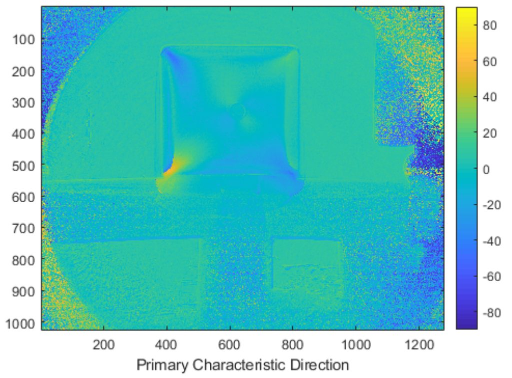

(b) Primary characteristic direction at 0 degrees

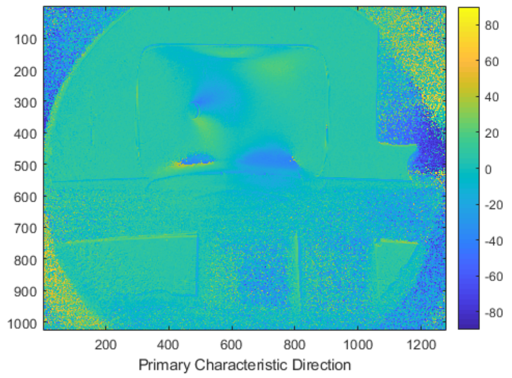

(e) Primary characteristic direction at 45 degrees

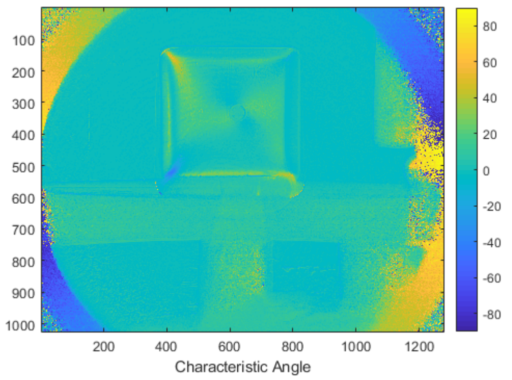

(c) Characteristic angle at 0 degrees

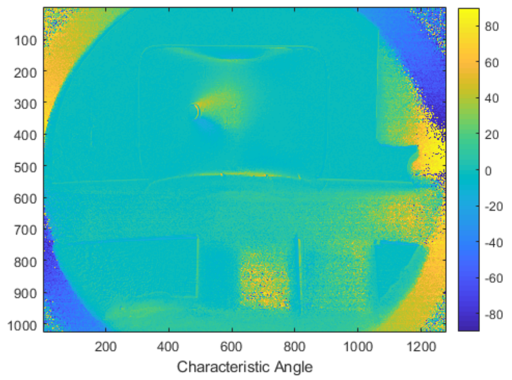

(f) Characteristic angle at 45 degrees

Figure 6.30 Characteristic parameters calculation for experiment 2 with new camera: stressed and immersed PMMA2 at 0 degrees and 45 degrees position

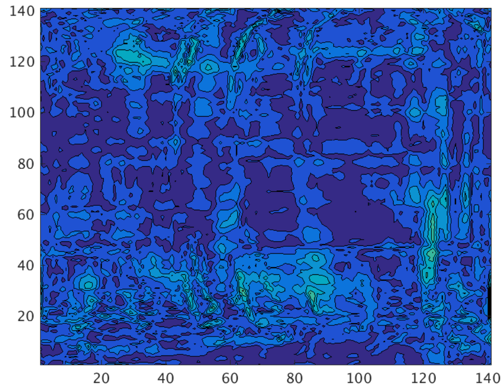

(a) Slice 1

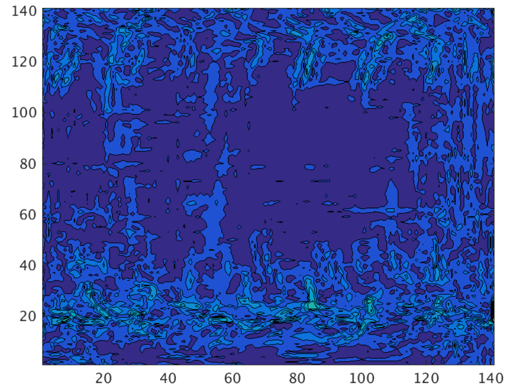

(d) Slice 84

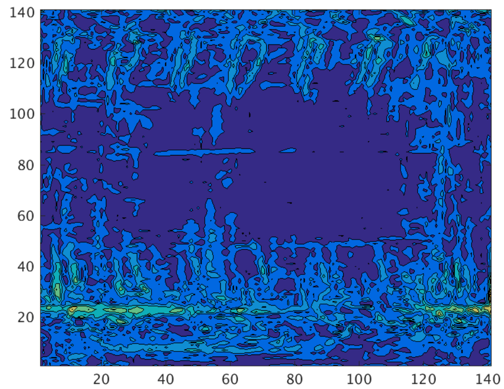

(b) Slice 28

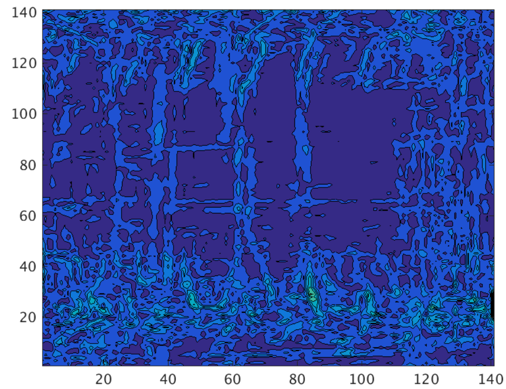

(e) Slice 112

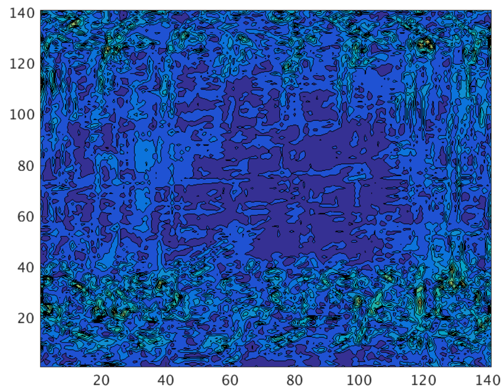

(c) Slice 56

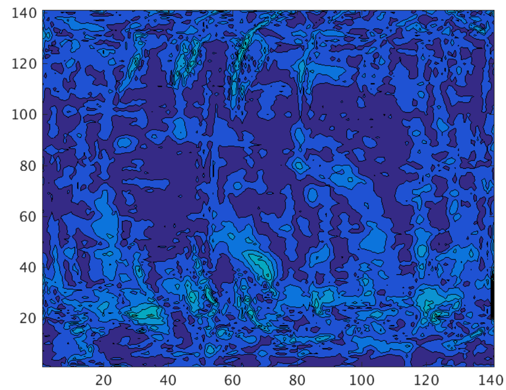

(f) Slice 140

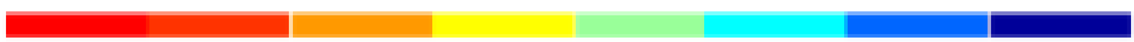

High stress Low stress

Figure 6.31 3-D reconstruction for PMMA 2: immersed and stressed using 3 by 3 averaged images.

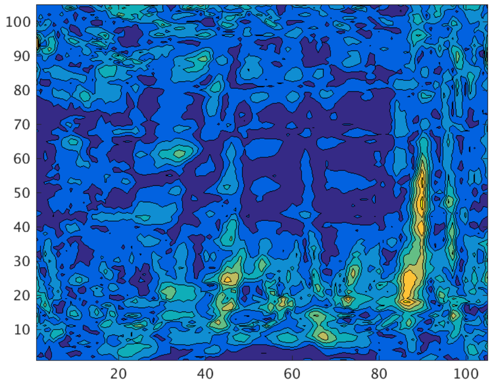

(a) Slice 1

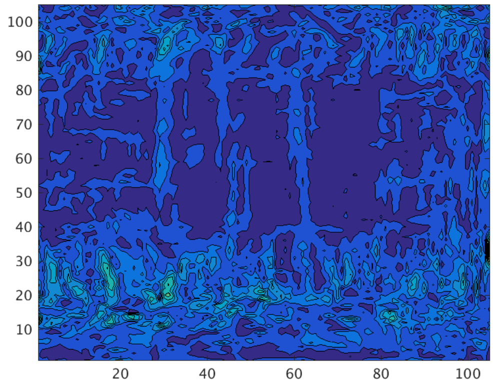

(d) Slice 63

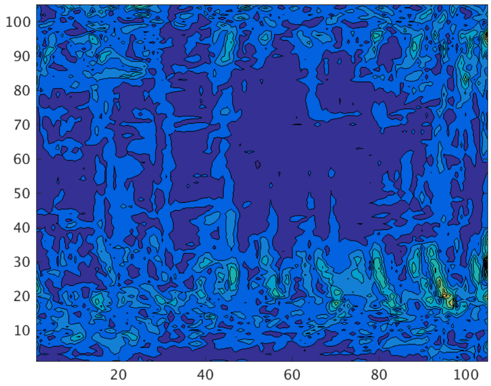

(b) Slice 21

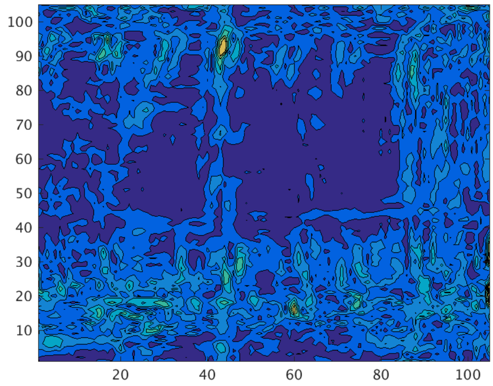

(e) Slice 84

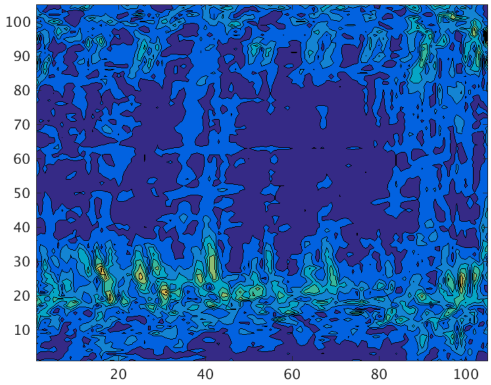

(c) Slice 42

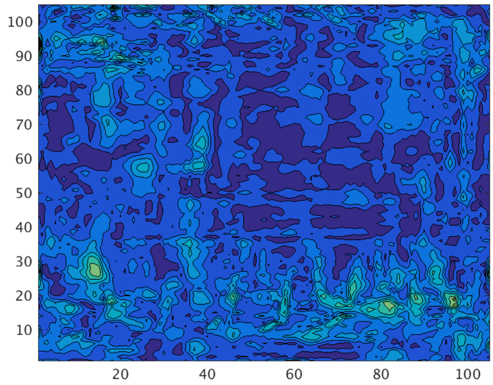

(f) Slice 105

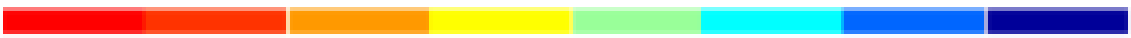

High stress Low stress

Figure 6.32 3-D reconstruction for PMMA 2: immersed and stressed using 4 by 4 averaged images.

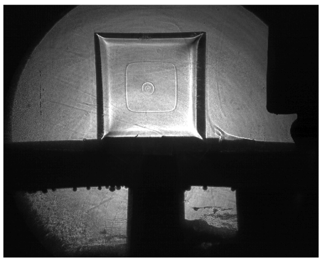

(a) 0 degrees light intensity image

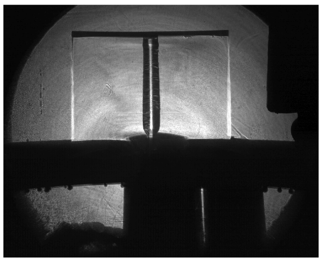

(e) 45 degrees light intensity image

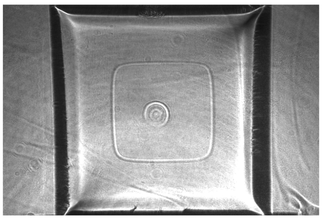

(b) 0 degrees cut light intensity image

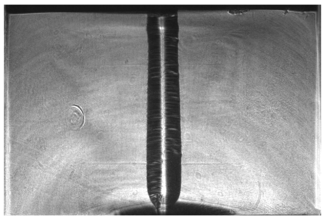

(f) 45 degrees cut light intensity image

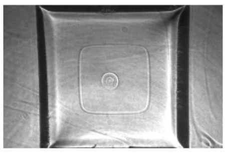

(c) 0 degrees 3 by 3 image average

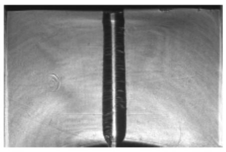

(g) 45 degrees 3 by 3 image average

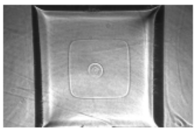

(d) 0 degrees 4 by 4 image average

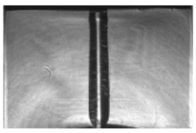

(h) 45 degrees 4 by 4 image average

Figure 6.33 Light intensity images for experiment 3 with new camera: stressed and no immersed specimen with the polariser and analyser set at 0 degrees and 20 degrees respectively. Where a) shows the data acquisition for PMMA 3 at 0 degrees and e) at 45 degrees, b) shows the cut image at 0 degrees and f) at 45 degrees, c) shows the 3 by 3 pixels averaged images at 0 degrees and g) at 45 degrees. Finally, d) shows the 4 by 4 pixels averaged images at 0 degrees and g) at 45 degrees.

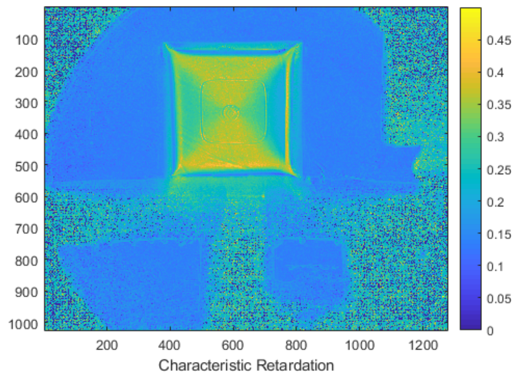

(a) Characteristic retardation at 0 degrees

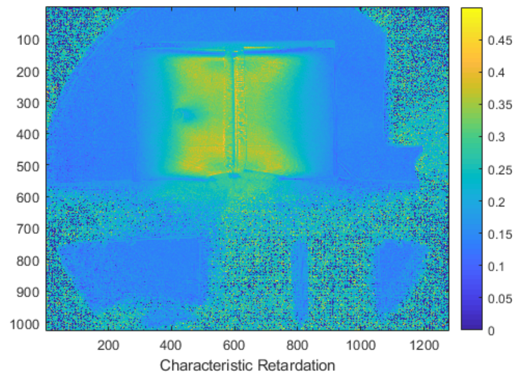

(d) Characteristic retardation at 45 degrees

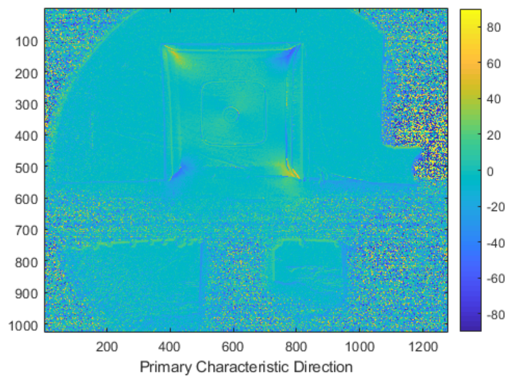

(b) Primary characteristic direction at 0 degrees

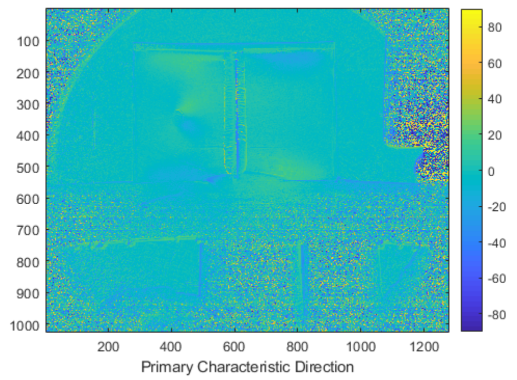

(e) Primary characteristic direction at 45 degrees

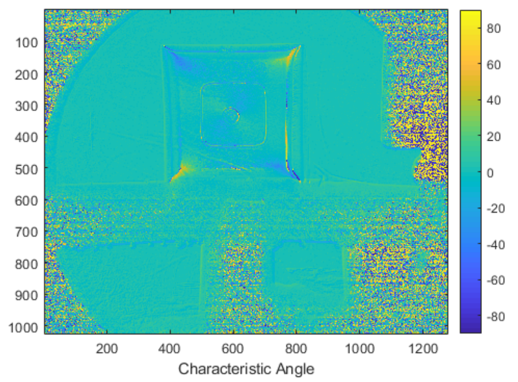

(c) Characteristic angle at 0 degrees

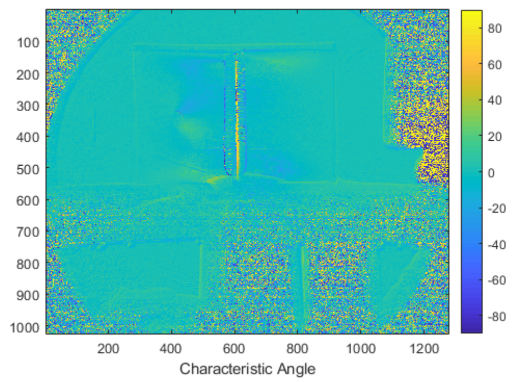

(f) Characteristic angle at 45 degrees

Figure 6.34 Characteristic parameters calculation for experiment 3 with new camera: stressed and immersed PMMA 3 at 0 degrees and 45 degrees position

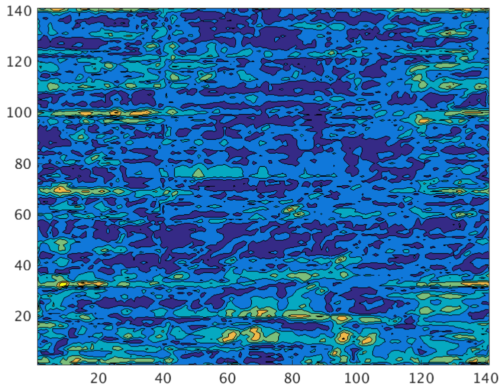

(a) Slice 1

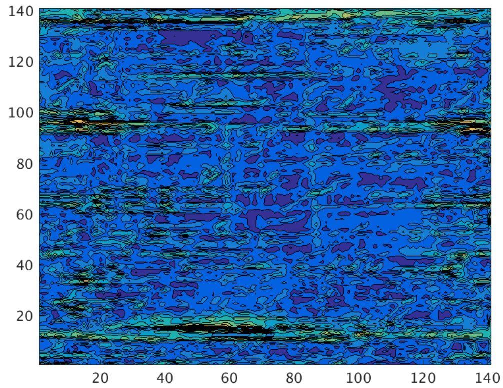

(d) Slice 84

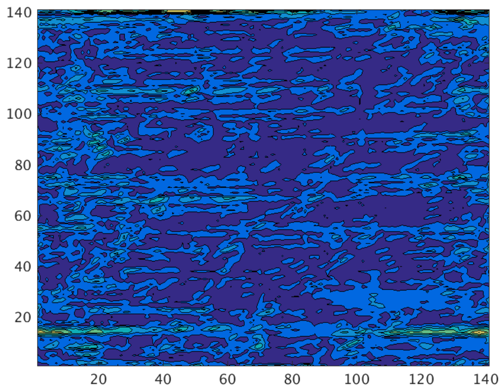

(b) Slice 28

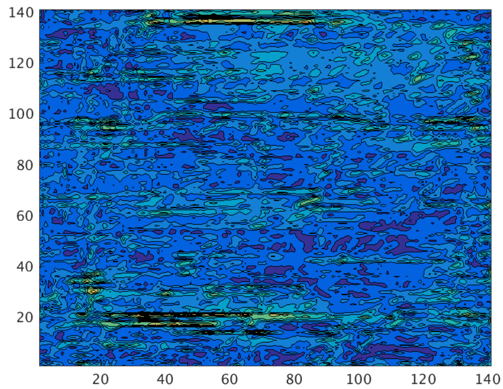

(e) Slice 112

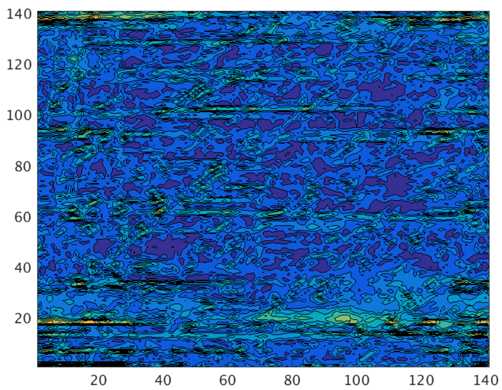

(c) Slice 56

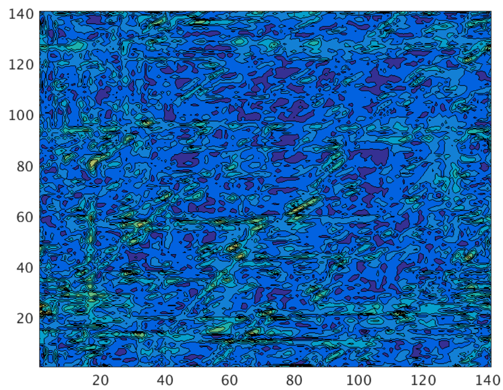

(f) Slice 140

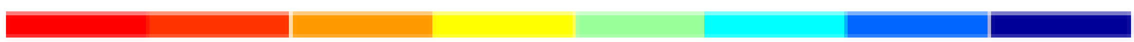

High stress Low stress

Figure 6.35 3-D reconstruction for PMMA 3: immersed and stressed using 3 by 3 averaged images.

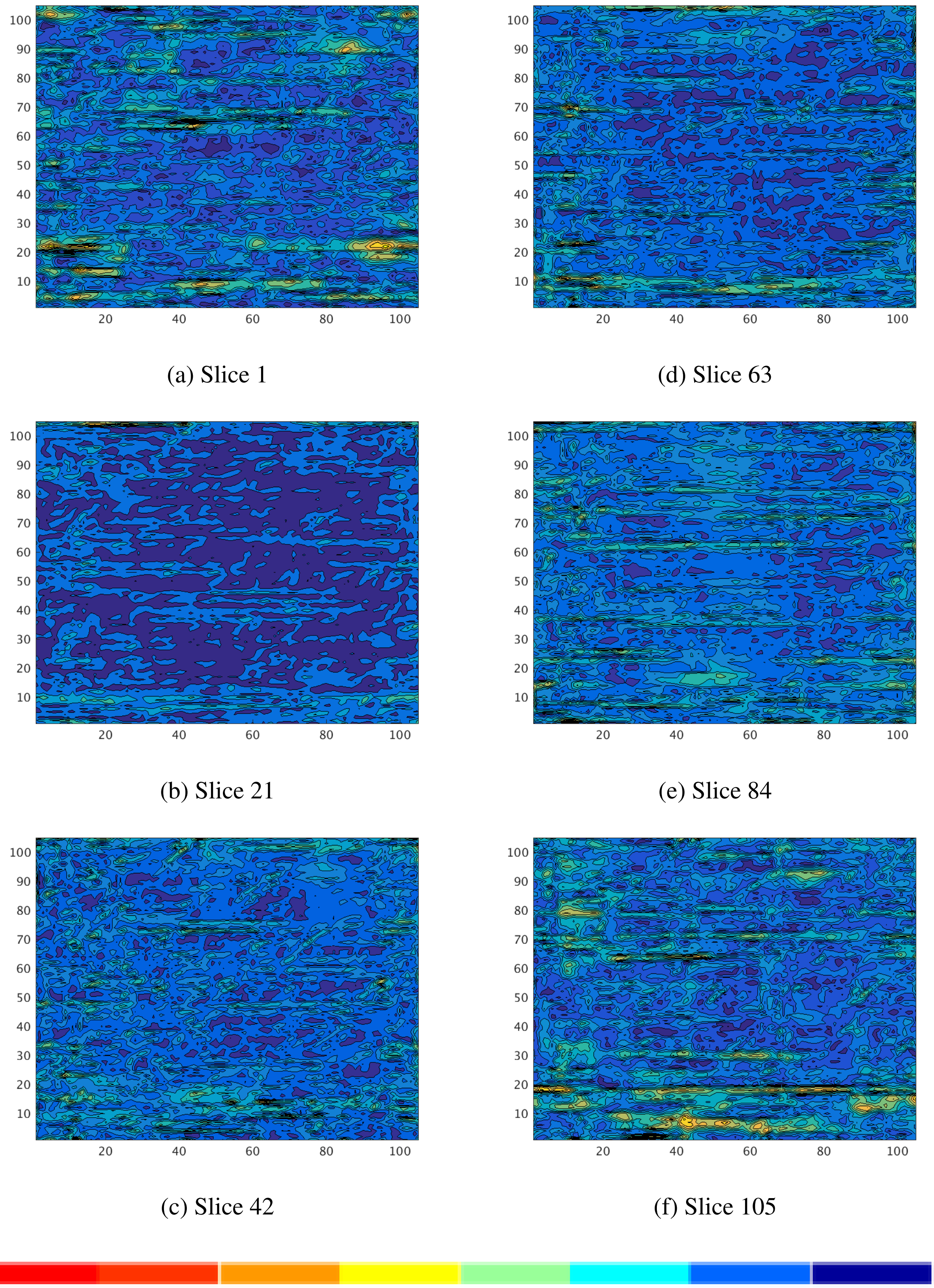

(a) Slice 1 (d) Slice 63

(b) Slice 21 (e) Slice 84

(c) Slice 42 (f) Slice 105

High stress Low stress

Figure 6.36 3-D reconstruction for PMMA 3: immersed and stressed using 4 by 4 averaged images.

(a) 0 degrees light intensity image

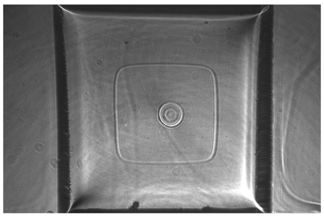

(b) 0 degrees cut light intensity image

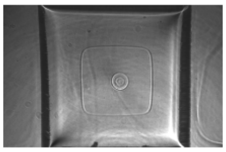

(c) 0 degrees 3 by 3 image average

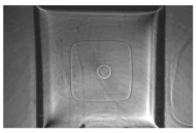

(d) 0 degrees 4 by 4 image average

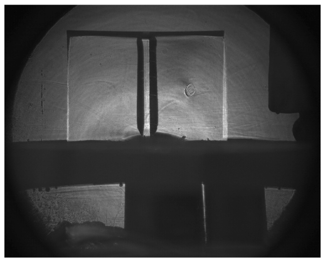

(e) 45 degrees light intensity image

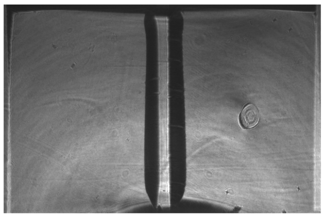

(f) 45 degrees cut light intensity image

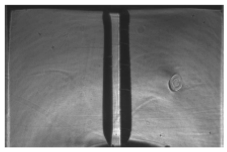

(g) 45 degrees 3 by 3 image average

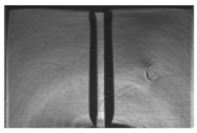

(h) 45 degrees 4 by 4 image average

Figure 6.37 Light intensity images for experiment 4 with new camera: stressed and no immersed specimen with the polariser and analyser set at 0 degrees and 20 degrees respectively. Where a) shows the data acquisition for PMMA 4 at 0 degrees and e) at 45 degrees, b) shows the cut image at 0 degrees and f) at 45 degrees, c) shows the 3 by 3 pixels averaged images at 0 degrees and g) at 45 degrees. Finally, d) shows the 4 by 4 pixels averaged images at 0 degrees and g) at 45 degrees.

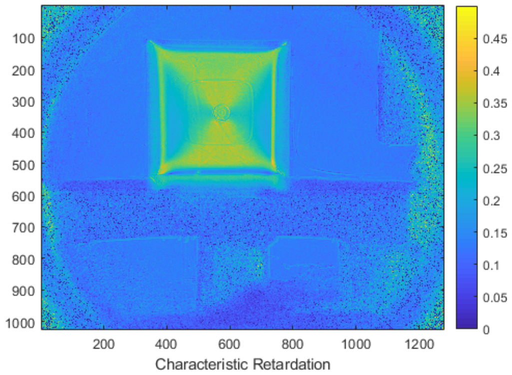

(a) Characteristic retardation at 0 degrees

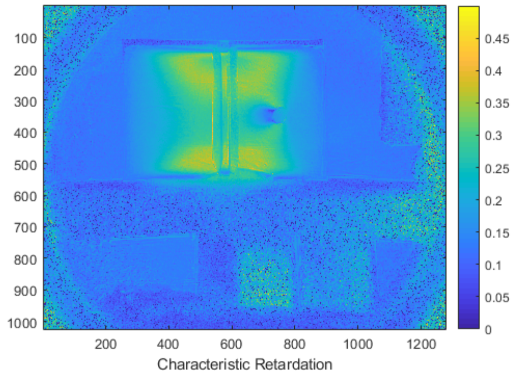

(d) Characteristic retardation at 45 degrees

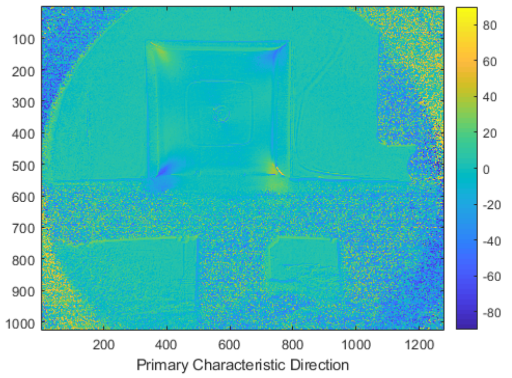

(b) Primary characteristic direction at 0 degrees

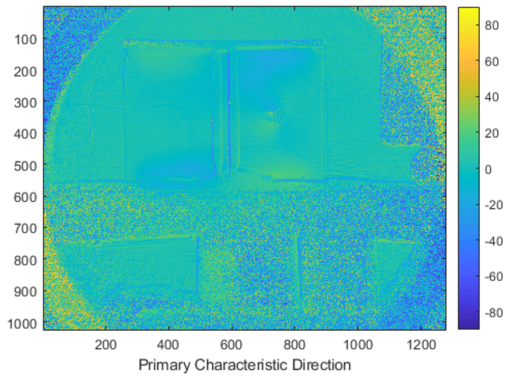

(e) Primary characteristic direction at 45 degrees

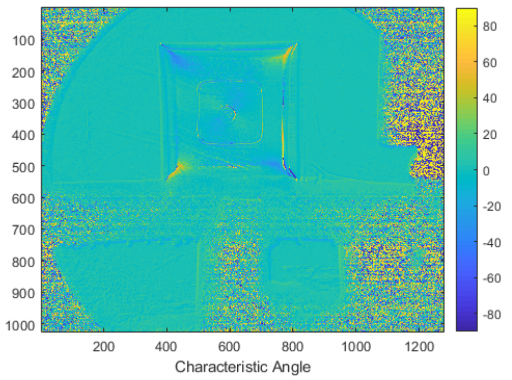

(c) Characteristic angle at 0 degrees

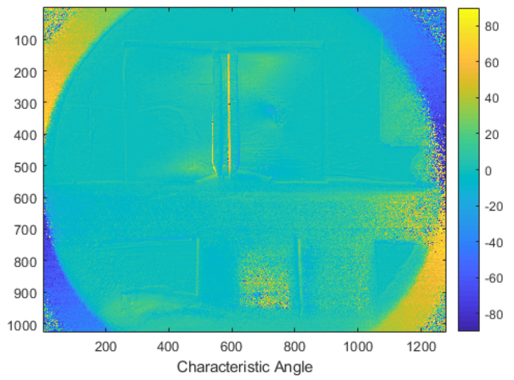

(f) Characteristic angle at 45 degrees

Figure 6.38 Characteristic parameters calculation for experiment 4 with new camera: stressed and immersed PMMA 4 at 0 degrees and 45 degrees position

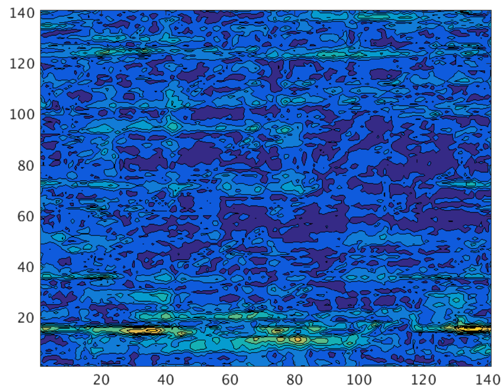

(a) Slice 1

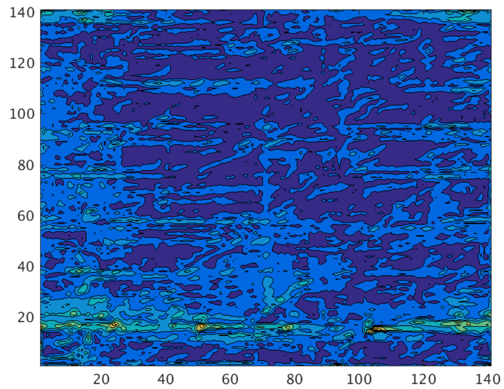

(b) Slice 28

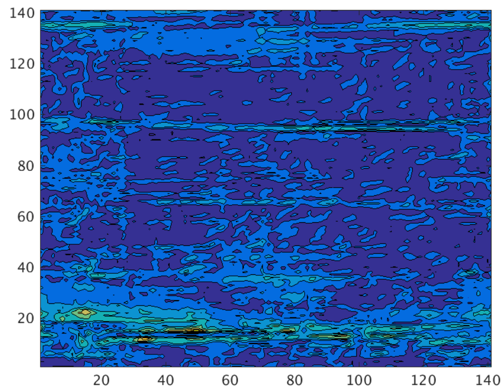

(c) Slice 56

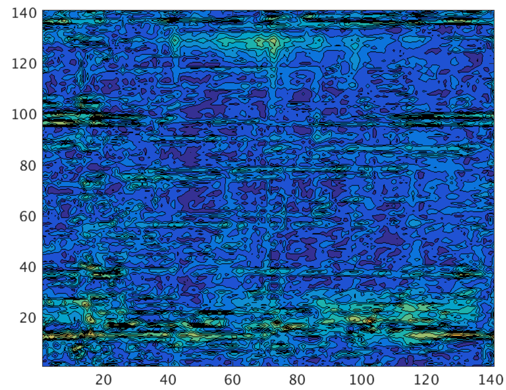

(d) Slice 84

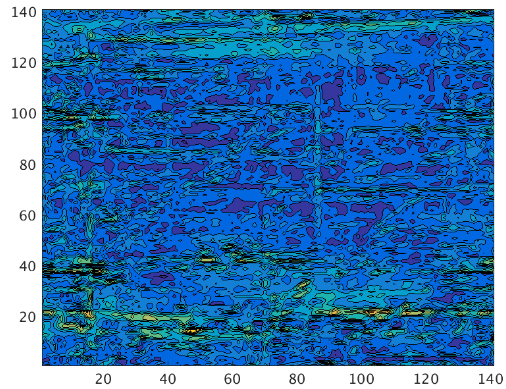

(e) Slice 112

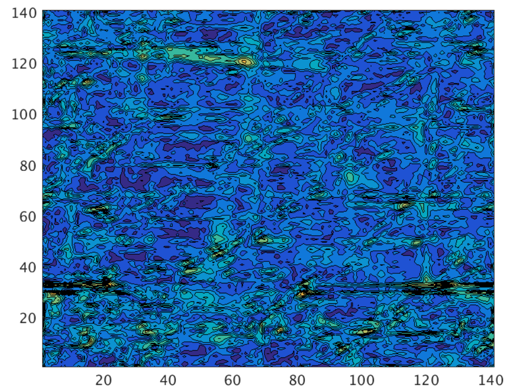

(f) Slice 140

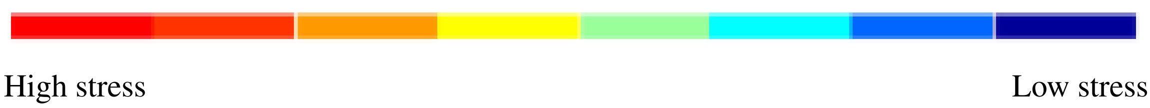

Figure 6.39 3-D reconstruction for PMMA 4: immersed and no stressed using 3 by 3 averaged images.

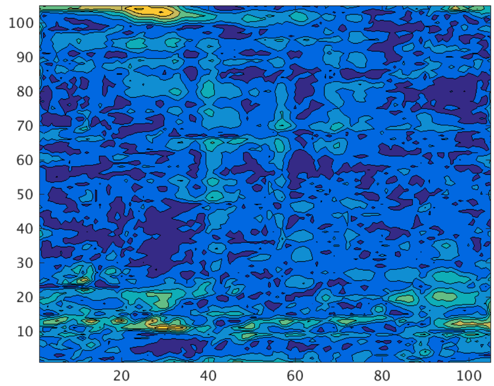

(a) Slice 1

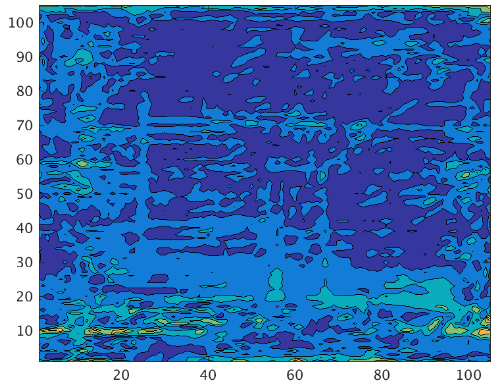

(b) Slice 21

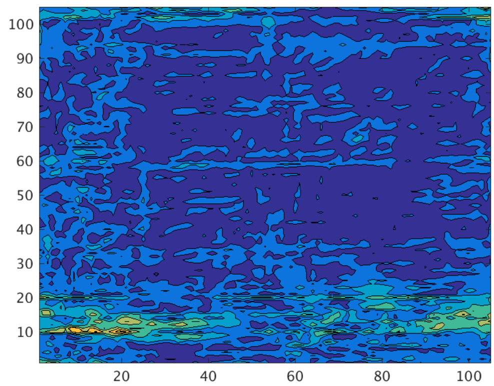

(c) Slice 42

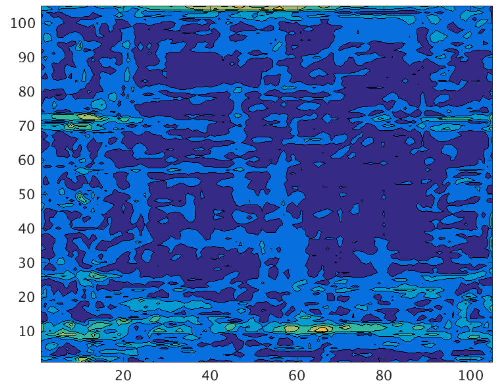

(d) Slice 63

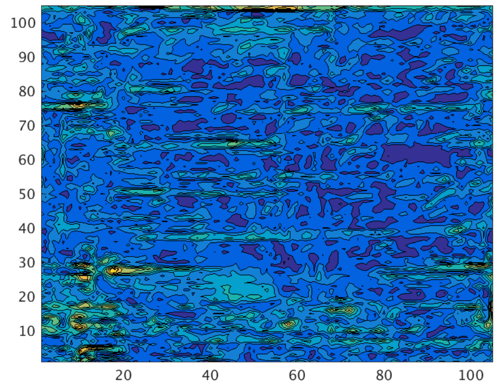

(e) Slice 84

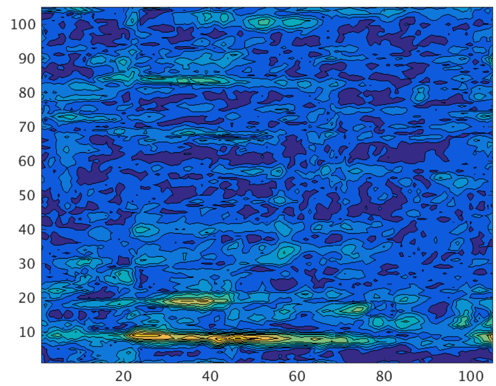

(f) Slice 105

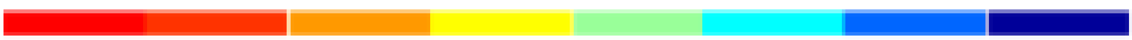

High stress Low stress

Figure 6.40 3-D reconstruction for PMMA 4: immersed and no stressed using 4 by 4 averaged images.

6.4 Discussion

In this section, the results of the experiments defined in Table 6.2 with the new camera, repositioning system, new tank and programs integration are discussed and compared with the previous experimental results obtained in chapter 4 with the old camera and the original rig. The experiments were performed on the PMMA samples which were made out of a manufactured cube or a square of PMMA. These specimens were loaded with a force of either 8.82 N or 29.43 N and immersed in the matching fluid that is inside the tolerance range defined by McKenzie [90]. However a dark shadow in the edges of the specimens at 0 degrees position were visible as Figure 6.25, 6.29, 6.33 and 6.37. This was attributed to the induced stress or perhaps the temperature changes resulting in a mismatch of the refractive index. It should be borne in mind that the tolerance is really narrow and even with the new tank there is not a way to control the temperature of this fluid.

The internal stress reconstructions performed for all the specimens in this chapter, Figures 6.27, 6.28, 6.31, 6.32, 6.35, 6.36, 6.39 and 6.40, showed noisy results and there is not a trend that indicates information regarding the internal stress.

The results in section 6.2 gave the author confidence that the Fourier polarimetry method was providing the correct values for the characteristic parameters. However it should be noted that the noise in the data was higher than those results using the phase stepping (see Figure 6.12 for example). Since the Fourier polarimetry method uses more images in the calculation process, the opposite would be expected. However the phase stepping method had many less optical components in the light path and, although every effort has been made to reduce the noise from these components in the FP method, it is clearly not enough to eliminate noise completely. It is considered likely that Szotten's reconstruction algorithms are sensitive to the noise and this is magnified throughout the reconstruction procedure and hence any noise masks the data signals. Another observation was made regarding the background data as can be seen in Figure 6.26, for example, where the area surrounding the specimen appears to have a positive value. In 2D photoelasticity, this is not a problem, since this area can be masked, and this is standard practice for phase-stepping software such as COPA [106]. In section 6.2 the manual masking technique was implemented for both Fourier polarimetry and COPA so that a direct comparison of the characteristic parameters could be made, and proved that the magnitudes were very similar. Masking the background is also not an issue for axisymmetric reconstructions such as those in the research by Aben and his team [8, 112, 73, 86], since the background remains the same size in the image and can be masked easily. However, for Photoelastic Tomography, the field of view for each image used in the reconstruction contains some of the background (see Figure 6.25 for example), and the size and shape of this background and the size and shape of the specimen varies as the sample rotates. It is postulated that if this background has a positive value, and these data are being used in the reconstruction algorithms, then it is possible that this is introducing an error to the reconstruction process. Although the cut and shift methodology removes some of the background, it does not eliminate it altogether. A solution to this problem would be to introduce a masking procedure for all "background" data, similar to that in COPA. However this would have to be automated, due to the large number of data images needed, and the variation in the relative size of the background and sample from image to image would make this process non-trivial, and is recommended for future work.

6.5 Conclusions

In this chapter the second round of experiments of this research was made by the validation of the characteristic parameters, specifically the characteristic retardation with a technique that uses phase stepping, COPA, instead of Fourier polarimetry. Furthermore, the comparison of two cameras with different length of time in operation was made. Better results in regards the characteristic parameters were obtained with the new camera. Therefore, 3-D internal reconstructions were performed with the light intensity images acquired with the new camera. In this point of the research the cleaning, alignment and the refractive index matching methodology had been implemented as it can be seen in the Appendix A and Chapter 4. In this chapter, in addition to the previous improvements, the system made use of the new repositioning system, new tank and the integrated data acquisition programs. Therefore, it was expected that the results were significantly less noisy. Nevertheless, the reconstructed results were as noisy as the ones obtained in chapter 4 and do not show any plausible stress pattern. Therefore it can be concluded that the improvements performed in this research for the experimental conditions tested did not impact directly within the noise in the stress reconstructions, which was the scope of this research. The algorithms developed to calculate the characteristic parameters [56] need further theoretical developments, perhaps addition of unwrapping filters, before they can be used in practice in the stress reconstruction.

Chapter 7

Conclusions

This chapter summarises the work and results obtained in this research. This work attempted experimental validation of the non-destructive internal stress reconstruction presented in Szotten's thesis 'Limited data problems in X-Ray and polarised light tomography'. A novel mathematical approach proposed the possibility of non-destructive internal stress reconstruction and concluded that it could be implemented experimentally. Preliminary results of previous research showed noisy results of the experimental implementation of this mathematical approach.
Therefore, the aim of this research was to experimentally test variables that could be affecting Szotten's mathematical approach. This testing process started in Chapter 2 with the performance an essential background review to understand the destructive and non-destructive experimental stress analysis techniques, such as photoelasticity, 3D photoelasticity, Integrated Photoelasticity, and Photoelastic Tomography, the polarimetry methods and the background of the computer tomography. It also presented a brief review of Szotten's work in order to give the reader an understanding of his methodology of stress reconstruction.

7.1 Critical audit

Chapter 3 provides a critical audit of the state of the original apparatus and software. This was done in order to identify the opportunity areas within the Photoelastic Tomography rig where improvements could be made. The opportunity areas identified were: the alignment and cleaning of the optical devices, matching of the refractive index fluid, which is one of the variables suspected to be affecting the stress reconstruction and the manual reposition of the specimen, which could lead to contamination of the refractive index matching fluid.
In addition, the algorithms used in previous research to perform the data acquisition, the im-

age processing, and the internal stress reconstruction were explained and critiqued. The areas of opportunity identified were focused on the data acquisition and image post-processing because this research aimed to test all the experimental variables involved before the stress reconstruction since it was assumed that the stress reconstruction works.
The cut and shift program that removes the irrelevant information of the specimen from the light intensity images taken was tedious, time-consuming and susceptible to human error; therefore, the development of an automated method was identified as a crucial improvement.

7.2 Experimental preparation

Chapter 4 introduced the refractive index methodology, this is important because the mathematical approach on which Photoelastic Tomography is based assumes minimal or no refraction of light at the specimen surfaces. In order to prove the impact of the refractive index on the reconstruction results, this thesis was focused to develop a methodology to perform a proper match according to the tolerance suggested. Work related to the refractive index matching has been previously attempted. However, in these studies, no prior measurements either from the specimen or the immersion fluid were taken and the accuracy of the matching index was not quantified after the blending. It was found in the literature review that the difference between the solid specimen and the blend of liquids to be immersed should not be greater than 0.002. Therefore, in this research, an accurate measurement of the specimen and the matching fluid was achieved with the use of a refractometer (Abbe 60 ED) capable of using an external light source to measure solids and liquids with an accuracy of ±0.00004 . The use of the same light source is important since the measurements of the refractive index are dependent on the wavelength of light. A calibration curve was successfully constructed which allowed for computation of the ratios of the blend of the Synesstic 5 and Synesstic 2 oils for the matching of the PMMA specimens. The found ratios for the PMMA specimens 1 and 2 were 65 % from Synestic 5 and 35 % from Synesstic 2. For the PMMA specimens 3 and 4, the ratios were 54% from Synestic 5 and 46 % of Synesstic 2. An example of matching results is displayed in detail in section 3.3, where the difference between the specimen and the blend from the stressed PMMA samples 1 and 2, which come from the same batch was 0.00060 and the difference for stressed PMMA sample 3 and 4 was 0.00070. Therefore it can be concluded that a proper refractive index matching methodology, according to the tolerance suggested, was set in this research. However, the experimentalist has to bear in mind that environmental conditions such as temperature and humidity loss can affect this matching.
After the refractive index preparation, the PMMA specimens were tested under different

loading conditions to make a comparison of the impact of these variables on the outcome results. However, it was concluded that the 3-D internal residual stress reconstructions under these improved conditions of the refractive index matching did not have an impact. It was also found that the stress level or the load applied to the specimens had little influence on the results. The research was redirected towards the validation of the calculation of characteristic parameters and the test of a new camera.

7.3 Automation of the Photoelastic Tomography rig and data processing

Before the validation of the characteristic parameters was carried out, the implementation of a repositioning system and the automated cut and shift program had to be implemented. This work is detailed in Chapter 5. This also focuses on overcoming the drawbacks identified in Chapter 3. Regarding the cut and shift program, several attempts to develop an algorithm that automates the measurement process, the specimen centring and the cropping was made. The first algorithm developed used Matlab's *regionprops* function. Once the coordinates of the edges of each image were obtained with this function, arithmetic operations were applied to centre the specimen. The algorithm worked well in instances where the specimen was not immersed. However, when the specimen was immersed, the algorithm incorrectly identified some of the fluid flow lines as image edges. A second attempt at measuring the light intensity with the *improfile* picture function was made.

However, for some of the images the edges were not visible enough since the light intensity was similar due to the correct refractive index matching. Therefore, the coordinates identified by the edge detection procedure were not correct for some of the images. While this algorithm worked better than the previous one, approximately 20% of the coordinates of the images were still mis-identified. A third attempt was made using the Hough transform function and Gaussian filter. This worked better than the *improfile* algorithm since less images were incorrectly centred. Therefore, this algorithm was successfully implemented within the Photoelastic Tomography post-processing to avoid the time-consuming and human error-prone process of the original methodology.

Additionally, a novel repositioning system composed of 4 waterproof servomotors was implemented in order to eliminate the manual handling, skin exposure and mostly importantly the refractive index contamination. This repositioning system was installed in a new tank that incorporates a lid to avoid evaporation losses which can affect the refractive index matching and contamination and a drainage system, which contributes to minimizing the risk of unsafe

practice within the laboratory.
A new GUI that controls the repositioning system was developed and is outlined in Chapter 5. The key point of the development of this new GUI was that it enabled the interfacing between all the different software routines in order to execute the test on all the axes without the experimentalist input until the reconstruction images are obtained . This was an important implementation because it has significantly increased the efficiency of the experiment in terms of facilitating user interaction and avoiding human error.

7.4 Characteristic parameters assessment

Once all these previous implementations were done this research moved forward to the characteristic parameters assessment in chapter 6. This was important because these parameters are the main raw data input that the reconstruction algorithms process to perform the internal reconstruction. Therefore a comparison with the phase stepping methodology was performed using the software developed by Siegmann and Patterson in addition to Fourier polarimetry. From the results of these comparisons, it was noted that the characteristic parameters followed a similar profile as it is shown in Figures 6.12 to 6.24. However, regarding the quantitative measurements they were different by 0.1 rad, but this was found to be due to the fact that light sources with different wavelengths were used in the two techniques. As previously said in chapter 3 it was suspected that this camera may be introducing noise to the system, therefore the implementation of a new camera was undertaken. The results with this new camera showed agreement with the stress patterns obtained by COPA, therefore it can be concluded that the characteristic parameters measurement are working.
The second round of experiments for the previous PMMA specimens followed the same methodology, but with the new repositioning system, new tank, the integration of software routines and the new camera. The reconstructed results were as noisy as the ones obtained in Chapter 4 and did not show any stress pattern. It was noted that while the cut and shift methodology eliminated the majority of the background data, some still remained, and it had a positive instead of null value. It was postulated that this the background data being included in the reconstruction could be the source of error. Therefore it can be concluded that the improvements made in this research, for the experimental conditions tested, did not resolve fully the noise in the stress reconstructions, which was the scope of this research. The reconstruction algorithms developed by Szotten [21] need further theoretical developments before they can be used in practice.

7.5 Future work

It has been a rewarding and full of knowledge journey, and the author would like to quote Sir Isaac Newton, “If I have seen a little further it is by standing on the shoulders of giants.” The author’s intention is not to call herself a giant, rather to acknowledge the fact that she began this research standing in giant’s shoulders and hope that her research could help future researchers to go further in this study. This thesis assessed the experimental variables that could be influencing the 3D internal reconstruction, e.g. refractive index, alignment of optical devices, and improve the methodology followed in previous research by automating manual processes that could lead to contamination of the specimen’s environment and human errors. Even though this thesis has come to the end, there is still a lot to explore in the 3-D internal stress reconstruction field. Therefore if someone else would like to undertake this research path, this section will present the future work.

Improvement of the refractive index matching was made. However, environmental conditions such as temperature and humidity loss, are not controlled in the experiment, hence the refractive index matching could be affected. Hence it is advised that a system that monitors and controls temperature within the tank is implemented.

To cut the intensity images and to centre the specimen in a more accurate way, research about image processing, to be able to identify the edges when the specimen is matched with the immersion fluid, must be carried out. This process must also fully mask any background data, so that only the sample data is used in the reconstruction.

Another factor that must be taken into account is the correction of possible barrel distortion and enclosure of the lenses to avoid dust and oil on the optical surfaces, which is beneficial for the image quality. Also, the implementation of a concentric calibration tool to ease the alignment of the optical components is necessary.

In Section 5.1.3, a repositioning system which helps increase the efficiency of the experiment is presented. However, it has to be taken into account that this system will be immersed in a liquid that is likely to have a higher viscosity than water, therefore the possibility of bubble-generation is expected. If this were to happen, the acquisition process could be delayed until the bubbles disappear in order to avoid the light refraction. In the current system, the tank does not have any way to speed up this process. Therefore, the addition of a vacuum pump could be helpful. Even though an original and water proof design made by the author was successfully implemented to completely automate the cubical specimens repositioning. There are improvements that could be made to the re-positioning system such as the redesigned of the gripper clamps so that different specimen’s geometries can be held and the addition of sensors to know the exact position of the specimen. Lastly the image results from the reconstruction section must be able to show quantitative rather than qualitative information. Hence, more research in this area to achieve more qualitative measures of the internal 3-D stresses must be carried out.

Bibliography

[1] Hillar Aben, Johan Anton, Andrei Errapart, Siim Hödemann, Jaak Kikas, Helina Klaassen, and Marko Lamp. On non-destructive residual stress measurement in glass panels. *Estonian journal of engineering*, 16(2):150, 2010.

[2] Warren Clarence Young and Richard Gordon Budynas. *Roark's formulas for stress and strain*, volume 7. McGraw-Hill New York, 2002.

[3] Ismail C Noyan and Jerome B Cohen. *Residual stress: measurement by diffraction and interpretation*. Springer, 2013.

[4] Alain Lodini M.E. Fitzpatrick. Analysis of residual stress by diffraction using neutron and synchrotron radiation. *Measurement Science and Technology*, 14(9):1739–1740, 2003. ISSN 0957-0233.

[5] Jan Cernosek. Three-dimensional photoelasticity by stress freezing. *Experimental Mechanics*, 20(12):417–426, 1980.

[6] Rajpal Sirohi. *Optical methods of measurement: wholefield techniques*. CRC Press, 2009.

[7] D. Swain, J. Philip, S.A. Pillai, and K. Ramesh. A revisit to the frozen stress phenomena in photoelasticity. *Experimental Mechanics*, 56(5):903–917, Jun 2016. ISSN 1741-2765. doi: 10.1007/s11340-016-0134-5. URL https://doi.org/10.1007/s11340-016-0134-5.

[8] H. K. Aben. *Integrated Photoelasticity as Tensor Field Tomography*, book section 30, pages 243–250. Springer Japan, 1986. ISBN 978-4-431-68041-3. doi: 10.1007/978-4-431-68039-0_30. URL http://dx.doi.org/10.1007/978-4-431-68039-0_30.

[9] K Ramesh. Digital photoelasticity, 2000.

[10] Hillar K Aben. Kerr effect tomography for general axisymmetric field. *Applied optics*, 26(14):2921–2924, 1987.

[11] H. Aben and A. Errapart. A non-linear algorithm of photoelastic tomography for the axisymmetric problem. *Experimental Mechanics*, 47(6):821–830, 2007. ISSN 0014-4851 1741-2765. doi: 10.1007/s11340-007-9057-5.

[12] Leo Ainola and Hillar Aben. Integrated photoelasticity for axisymmetric thermal stress measurement using the stress function. *Journal of Thermal Stresses*, 31(7):614–623, 2008.

[13] H Aben. On the existence of characteristic directions in three-dimensional photoelasticity. *Ingenieur-Archiv*, 52(3-4):245–250, 1982.

[14] Leo Ainola and Hillar Aben. Principal formulas of integrated photoelasticity in terms of characteristic parameters. *JOSA A*, 22(6):1181–1186, 2005.

[15] HK Aben. Characteristic directions in optics of twisted birefringent media. *JOSA A*, 3 (9):1414–1421, 1986.

[16] EA Patterson. Determination of characteristic parameters for integrated photoelasticity using phase stepping. In *Proc. Spring Conf. Experim. Mechanics*, pages 118–121, 1998.

[17] A Ajovalasit, Sandro Barone, and G Petrucci. A review of automated methods for the collection and analysis of photoelastic data. *The Journal of Strain Analysis for Engineering Design*, 33(2):75–91, 1998.

[18] H. Yang, S. Gibson, and R. A. Tomlinson. Improvement of fourier polarimetry for applications in tomographic photoelasticity. *Experimental Mechanics*, 46(5):619–626, 2006. ISSN 0014-4851 1741-2765. doi: 10.1007/s11340-006-9112-7.

[19] Eann A Patterson. Digital photoelasticity: Principles, practice and potential: Measurements lecture. *Strain*, 38(1):27–39, 2002.

[20] Euclid Seeram. *Computed Tomography-E-Book: Physical Principles, Clinical Applications, and Quality Control*. Elsevier Health Sciences, 2015.

[21] David Szotten. *Limited Data Problems in X-ray and Polarized Light Tomography*. PhD thesis, The University of Manchester, January 2011.

[22] ZF Wang and EA Patterson. Use of phase-stepping with demodulation and fuzzy sets for birefringence measurement. *Optics and Lasers in Engineering*, 22(2):91–104, 1995.

[23] EA Patterson and ZF Wang. Towards full field automated photoelastic analysis of complex components. *Strain*, 27(2):49–53, 1991.

[24] H. Aben, L. Ainola, and J. Anton. Integrated photoelasticity for nondestructive residual stress measurement in glass. *Optics and Lasers in Engineering*, 33(1):49–64, 2000. ISSN 0143-8166. doi: 10.1016/S0143-8166(00)00018-X.

[25] C.O. Harris. *Introduction to stress analysis*. Macmillan, 1959. URL https://books.google.co.uk/books?id=9iRSAAAAMAAJ.

[26] A.K. Singh. *Mechanics of solids*. PHI Learning, 2007. ISBN 9788120331907. URL https://books.google.co.uk/books?id=WaXTuC5dcbcC.

[27] S.I. Krishnamachari and L.J. Broutman. *Applied Stress Analysis of Plastics: A Mechanical Engineering Approach*. Springer US, 2013. ISBN 9781461531104. URL https://books.google.co.uk/books?id=IiQRBwAAQBAJ.

[28] M.I. Hetényi. *Handbook of Experimental Stress Analysis*. New York,: Wiley, 1950. URL https://books.google.co.uk/books?id=e4iHBwAAQBAJ.

[29] A. J. Durelli. *Introduction to photomechanics*. Englewood CLiffs ; London : Prentice-Hall, 1965, Englewood CLiffs ; London, 1965.

[30] Hartmann Römer. *Theoretical optics: an introduction*. John Wiley & Sons, 2006.

[31] Elizabeth Allen and Sophie Triantaphillidou. *The manual of photography and digital imaging*. Focal Press, 2012.

[32] Gary L. Cloud. *Optical methods of engineering analysis*. Cambridge : Cambridge University Press, 1998, Cambridge, 1998.

[33] Pericles S Theocaris and Emmanuel E Gdoutos. Two-dimensional photoelasticity. In *Matrix Theory of Photoelasticity*, pages 113–131. Springer, 1979.

[34] James W. Dally. *Experimental stress analysis*. New York ; London : McGraw-Hill, 1991, New York ; London, 3rd ed. edition, 1991.

[35] EG Coker. Photo-elasticity for engineers. *Proceedings of the Institution of Automobile Engineers*, 12(1):31–68, 1917.

[36] Arnold W Hendry. *An Introduction to Photo-elastic Analysis*. Blackie, 1948.

[37] Max Mark Frocht. *Photoelasticity*. New York : Wiley, 1948, New York, 1948.

[38] David G Patrick. *Laminated structures for sports mouthguards*. PhD thesis, University of Sheffield, 2005.

[39] Rachel Tomlinson. Lecture 04: Theory of photoelasticity, 2014. [Powerpoint slides].

[40] PS Theocaris and E Gdoutos. An interferometric method for the direct evaluation of principal stresses in plane-stress fields. *Journal of Physics D: Applied Physics*, 7(3): 472, 1974.

[41] MJ Turner. Stiffness and deflection analysis of complex structures. *journal of the Aeronautical Sciences*, 23(9):805–823, 1956.

[42] Andy MacKrell. Multiscale composite analysis in abaqus: Theory and motivations. *Reinforced Plastics*, 61(3):153–156, 2017.

[43] Xiaolin Chen and Yijun Liu. *Finite element modeling and simulation with ANSYS Workbench*. CRC Press, 2014.

[44] STRESS CHECK Mster Guide-V. 7. engineering software research and development, inc., 7750 clayton road, suite 204, st. louis, mo 63117, 2004.

[45] Nitin S Gokhale. *Practical finite element analysis*. Finite to infinite, 2008.

[46] Said Shakerin and Daniel D Jensen. Enhancement of mechanics education by means of photoelasticity and finite element method. *International Journal of Mechanical Engineering Education*, 29(4):307–320, 2001.

[47] E. J. Hearn. *Photoelasticity*. Watford 276 Hempstead Rd, Watford, Herts. : Merrow Publishing Co. Ltd, 1971, Watford (276 Hempstead Rd, Watford, Herts.), 1971.

[48] Paola Forte, Alessandro Paoli, and Armando Razionale. A cae approach for the stress analysis of gear models by 3d digital photoelasticity. *Int J Interact Des Manuf*, 9(1): 31–43, 2015. ISSN 1955-2513. doi: 10.1007/s12008-013-0201-4.

[49] Rickey J Seyler. *Assignment of the glass transition*, volume 1249. Astm International, 1994.

[50] Hanno Hammer. Characteristic parameters in integrated photoelasticity: An application of poincare's equivalence theorem. *Journal of Modern Optics*, 2003. doi: 10.1080/09500340310001631671.

[51] Hillar Aben. *Photoelasticity of glass*. Berlin ; New York : Springer-Verlag, c1993, Berlin ; New York, 1993.

[52] H. K. Aben, J. I. Josepson, and K. J. E. Kell. The case of weak birefringence in integrated photoelasticity. *Optics and Lasers in Engineering*, 11(3):145–157, 1989. ISSN 0143-8166. doi: 10.1016/0143-8166(89)90029-8.

[53] Hanno Hammer and William RB Lionheart. Reconstruction of spatially inhomogeneous dielectric tensors through optical tomography. *JOSA A*, 22(2):250–255, 2005.

[54] S. K. Mangal and K. Ramesh. Determination of characteristic parameters in integrated photoelasticity by phase-shifting technique. *Optics and Lasers in Engineering*, 31(4): 263–278, 1999. ISSN 0143-8166. doi: 10.1016/S0143-8166(99)00027-5.

[55] L. Ainola and H. Aben. Principal formulas of integrated photoelasticity in terms of characteristic parameters. *Journal of the Optical Society of America A: Optics and Image Science, and Vision*, 22(6):1181–1186, 2005. ISSN 10847529.

[56] Eann A. Patterson. Digital photoelasticity: Principles, practice and potential. *Strain*, 38(1):27–39, 2002. ISSN 0039-2103. doi: 10.1046/j.0039-2103.2002.00004.x.

[57] Rachel Tomlinson and Eann Patterson. The use of phase-stepping for the measurement of characteristic parameters in integrated photoelasticity. *Experimental Mechanics*, 42 (1):43–50, 2002. ISSN 0014-4851. doi: 10.1007/BF02411050.

[58] J. Hsieh. *Computed Tomography Principles, Design, Artifacts, and Recent Advances*. Wiley, 2009. ISBN 9780470563533. URL https://books.google.co.uk/books?id=uX-bQgAACAAJ.

[59] Prabhat Munshi. Tomography. *Journal of Science Education*, 12(11):54–62, 2007. ISSN 0971-8044. doi: 10.1007/s12045-007-0114-2.

[60] Trevor A York. Status of electrical tomography in industrial applications. *Journal of Electronic Imaging*, 10(3):608–620, 2001.

[61] GN Ramachandran and AV Lakshminarayanan. Three-dimensional reconstruction from radiographs and electron micrographs: application of convolutions instead of fourier transforms. *Proceedings of the National Academy of Sciences*, 68(9):2236–2240, 1971.

[62] J Radon. On the determination of functions from their integrals along certain manifolds. *Ber. Verh, Sachs Akad Wiss.*, 69:262–277, 1917.

[63] Computed Tomography and ASTRA Toolbox training course. What is computed tomography? Vision Lab at the University of Antwerp, Belgium, September 2015. URL https://www.youtube.com/watch?v=JKf1Q4DOfs0&feature=youtu.be. [Video File].

[64] Computed Tomography and ASTRA Toolbox training course. The projection model of ct expressed using analytical mathematics. Vision Lab at the University of Antwerp, Belgium, September 2015. URL https://www.youtube.com/watch?v=MA2y_2YySq0&feature=youtu.be. [Video file].

[65] Computed Tomography and ASTRA Toolbox training course. The projection model of ct expressed using algebra. Vision Lab at the University of Antwerp, Belgium, September 2015. URL https://www.youtube.com/watch?v=r5ZIzog2JlE&feature=youtu.be. [Video file].

[66] Avinash C Kak and Azriel Rosenfeld. Digital picture processing. *New York*, 1982.

[67] Avinash C.. Kak and Malcolm Slaney. *Principles of computerized tomographic imaging*. IEEE press New York, 1988.

[68] Computed Tomography and ASTRA Toolbox training course. The fourier slice theorem is the basis of the filtered backprojection reconstruction method. Vision Lab at the University of Antwerp, Belgium, September 2015. URL https://www.youtube.com/watch?v=YIvTpW3IevI&feature=youtu.be. [Video file].

[69] Computed Tomography and ASTRA Toolbox training course. The filtered backprojection (fbp) is a very efficient, and therefore widely used, reconstruction method. Vision Lab at the University of Antwerp, Belgium, September 2015. URL https://www.youtube.com/watch?v=YIvTpW3IevI&feature=youtu.be. [Video file].

[70] TH Farquhar, A Chatziioannou, G Chinn, M Dahlbom, and EJ Hoffman. An investigation of filter choice for filtered back-projection reconstruction in pet. *IEEE transactions on nuclear science*, 45(3):1133–1137, 1998.

[71] William Lionheart and Vladimir Sharafutdinov. Reconstruction algorithm for the linearized polarization tomography problem with incomplete data. *Contemporary Mathematics*, 14:137, 2009.

[72] Vladimir Altafovich Sharafutdinov. *Integral geometry of tensor fields*, volume 1. Walter de Gruyter, 2012.

[73] Hillar Aben. *Integrated Photoelasticity*. McGraw Hill International Book Company, 1979.

[74] David Szotten, William RB Lionheart, and Rachel A Tomlinson. Tomographic reconstruction of stress from photoelastic measurements using elastic regularization. 2006.

[75] Robert L Siddon. Fast calculation of the exact radiological path for a three-dimensional ct array. *Medical physics*, 12(2):252–255, 1985.

[76] Filip Jacobs, Erik Sundermann, Bjorn De Sutter, Mark Christiaens, and Ignace Lemahieu. A fast algorithm to calculate the exact radiological path through a pixel or voxel space. *Journal of computing and information technology*, 6(1):89–94, 1998.

[77] Simon Fleming. Photoelastic tomography:stress analysis of an epoxy resin sample. Master's thesis, The University of Manchester,UK, 2013.

[78] Aniela Rodak. Photoelastic tomography. Master's thesis, The University of Manchester,UK, 2013.

[79] Ciara Barrett Smith. Photoelastic tomography: A non-destructive method for recovering 3d stress distributions experimentally. Master's thesis, The University of Manchester,UK, 2014.

[80] Elizabeth Brown. Determination of stress using non-destructive photoelastic tomography. Master's thesis, The University of Manchester,UK, 2014.

[81] Daniel Naylor. An application of three dimensional photoelastic tomography for the measurement of stress in polycarbonate samples. Master's thesis, The University of Manchester,UK, 2015.

[82] Rachel A Tomlinson, Hui Yang, David Szotten, and William RB Lionheart. The design and commissioning of a novel tomographic polariscope. In *Proceedings of the SEM Annual Conference on Experimental and Applied Mechanics, St Louis, USA, Paper*, number 244, 2006.

[83] J. L Comstock. *Youth's book of natural philosophy*. Reed and Barber,, 1838. URL http://hdl.handle.net/2027/hvd.hn5wzr.

[84] G.D. Boreman. *Basic Electro-optics for Electrical Engineers*. SPIE Optical Engineering Press, 1998. ISBN 9780819428066. URL https://books.google.co.uk/books?id=aKCgh3go-sYC.

[85] H. Aben and A. Puro. Photoelastic tomography for three-dimensional flow birefringence studies. *Inverse Problems*, 13(2):215–221, 1997. ISSN 0266-5611.

[86] H. Aben and J. Josepson. On the precision of integrated photoelasticity for hollow glassware. *Optics and Lasers in Engineering*, 22(2):121–135, 1995. ISSN 0143-8166.

[87] RL Burguete and EA Patterson. Photomechanical properties of some birefringent polymers around their glass transition temperatures. *Experimental mechanics*, 36(4): 399–403, 1996.

[88] Alternative plastics. Specifications of alt cast acrilic, 2018. URL http://www.alternativeplastics.co.uk/files/tolerances/e67e18ad82.pdf. Accesed:15/02/2018.

[89] RL Burguete and EA Patterson. A photoelastic study of contact between a cylinder and a half-space. *Experimental Mechanics*, 37(3):314–323, 1997.

[90] H. W McKenzie. *Basic optical stress measurement in glass*. Society of Glass Technology, Sheffield, 1999. ISBN 0900682272.

[91] Sébastien Wiederseiner, Nicolas Andreini, Gaël Epely-Chauvin, and Christophe Ancey. Refractive-index and density matching in concentrated particle suspensions: a review. *Experiments in Fluids*, 50(5):1183–1206, May 2011. ISSN 0723-4864.

[92] Rita Mehra. Application of refractive index mixing rules in binary systems of hexadecane and heptadecane with n -alkanols at different temperatures. *Journal of Chemical Sciences*, 115(2):147–154, April 2003. ISSN 0253-4134.

[93] Masahiko Daimon and Akira Masumura. Measurement of the refractive index of distilled water from the near-infrared region to the ultraviolet region. *Applied optics*, 46(18):3811–3820, 2007.

[94] Exxon mobile synesstic 5 product data sheet, 2017. URL https://exxonmobilchemical.ides.com/en-US/ds244637/Synesstic%E2%84%A2%205.aspx?I=30156&U=1. [Accessed:09/2018].

[95] Exxon mobile spectrasyn 2 product datasheet, 2017. URL https://exxonmobilchemical.ulprospector.com/en-US/ds244637/Synesstic%E2%84%A2%205.aspx?I=30156&U=1. [Accessed:09/2018].

[96] ASTM International. Standard test method for refractive index and refractive dispersion of hydrocarbon liquids, 2016. URL https://www.astm.org/Standards/D1218.htm.

[97] Cornelia Margarete Keck. Cyclosporine nanosuspensions : Ciclosporin nanosuspensionen : Optimised size characterisation & oral formulations : Optimierte partikelgrößencharakterisierung & orale formulierungen, February 2010.

[98] Richard Hodgkinson. *The effect of extensional flow on shear viscosity*. PhD thesis, University of Sheffield, 2017.

[99] Mathworks. Custom add on library concepts (r2018), . URL https://uk.mathworks.com/matlabcentral/answers/18336-how-to-cite-a-user-s-guide. Last updated: 28 Jan 2018.

[100] Mathworks. Servo control (r2018), . URL https://uk.mathworks.com/help/supportpkg/arduino/ref/servo-control.html. Last updated: 28 Jan 2018.

[101] Camera Thornlab DC1545X. Camera thornlab dc1545x. URL https://www.thorlabs.com/software_pages/viewsoftwarepage.cfm?code=ThorCam. [Accessed:09/2018].

[102] Alice Allen, Cecilia Aragon, Christoph Becker, Jeffrey Carver, Andrei Chis, Benoit Combemale, Mike Croucher, Kevin Crowston, Daniel Garijo, Ashish Gehani, et al. Lightning talk:" i solemnly pledge" a manifesto for personal responsibility in the engineering of academic software. In *Fourth Workshop on Sustainable Software for Science: Practice and Experiences (WSSSPE4)*, volume 1686. CEUR, 2016.

[103] RSES. Research software engineering sheffield. URL https://rse.shef.ac.uk/. [Accessed:09/2018].

[104] P Siegmann, D Backman, and EA Patterson. A robust approach to demodulating and unwrapping phase-stepped photoelastic data. *Experimental Mechanics*, 45(3):278–289, 2005.

[105] Mark D Pritt. Phase unwrapping by means of multigrid techniques for interferometric sar. *IEEE Transactions on Geoscience and Remote Sensing*, 34(3):728–738, 1996.

[106] Philip Siegmann and Eann Patterson. Operating instructions for copa 1.0, 2004. URL http://agamenon.tsc.uah.es/Personales/philip/software/Operating%20Instructions%20for%20COPA%20version%203.pdf. Accessed: 2018-09-25.

[107] Jacob Benesty, Jingdong Chen, Yiteng Arden Huang, and Simon Doclo. Study of the wiener filter for noise reduction. In *Speech Enhancement*, pages 9–41. Springer, 2005.

[108] WH Press, BP Flannery, SA Teukolsky, and WT Vetterling. Optimal (wiener) filtering with the fft. *Numerical recepies in pascal: The art of scientific computing*, pages 459–462, 1986.

[109] M Heredia-Ortiz and EA Patterson. On the industrial applications of moiré and fringe projection techniques. *Strain*, 39(3):95–100, 2003.

[110] Junichi Nakamura. *Image sensors and signal processing for digital still cameras*. CRC press, 2016.

[111] Thornlabs. Dcx camera functional description and sdk manual, 2016. URL https://www.thorlabs.com/drawings/f7ad924ac215d731-60030603-A9BE-C80E-F21802498DE7C32E/DCC1545M-Manual.pdf.

[112] Aben, H., Ainola, L., and Errapart, A. Photoelastic tomography as hybrid mechanics. *EPJ Web of Conferences*, 6:32009, 2010. doi: 10.1051/epjconf/20100632009. URL https://doi.org/10.1051/epjconf/20100632009.

[113] TRIOPTICS GmbH . Optical Instruments. Inspection, alignment,cementing and assembly of optics. Hafenstr. 35-39 . D-22880 Wedel / Germany. URL http://trioptics-usa.com/wp-content/uploads/OptiCentric_E_2010_web.pdf.

[114] Thornlabs. N-bk7 plano-convex lenses (uncoated), 2017. URL https://www.thorlabs.com/thorproduct.cfm?partnumber=LA1002.

Appendix A

Photoelastic Tomography components cleaning

Optical devices are exposed to dirt from different sources such as dust, fingerprints, grease, residual chemicals used for its cleaning and even fibers from clothes. This dirt affects the image quality, therefore it is important to identify what kind of dirt exist within the system in order to be able to clean it properly. For instance, in the case of dust, it is important to identify if the particles are attached to the optical surface or if it can be easily removed with a gun air. Besides, the kind of surface within the experiment must be identified since it's cleaning will depend on this. For example, concave or convex surfaces are cleaned with cotton or new polyester swabs and a solution, on the other hand, flat surfaces are cleaned with soft wipes in order to avoid scratches or residual chemicals in the surface of the devices. Within the Photoelastic Tomography devices, convex surfaces from the lenses and flat surfaces from the filters (polarizer and analyser) can be found. The first step to clean these components started by blowing up air in order to remove dust particles as it can be seen in Figure A.1 and A.2. Then swabs immersed in a cleaning solution were needed. In this case, it was advised by Dr. Darren Robinson from The Wolfson Light Microscopy Facility in the University of Sheffield the use of petroleum ether 40-60°C, boiling point. Once the swab has been immersed in the cleaning solution the lenses must be cleaned in an spiral motion way as depicted in Figure A.2 it is not recommended to do the cleaning in a zig-zag way. .

The key points to consider in the cleaning of the Photoelastic Tomography optical devices are A.2:

- Avoid the usage of dry swabs or wipes, because it could lead to scratching of the optical elements.

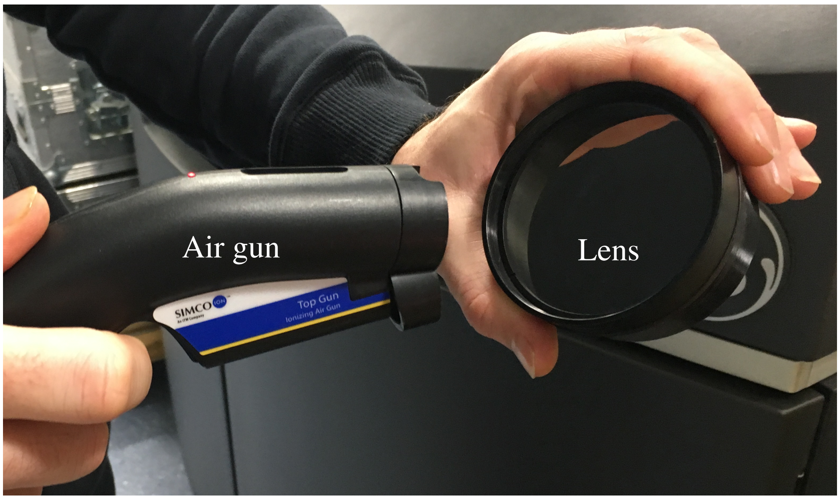

Figure A.1 Dust particles removal from a lens using an air blow gun.

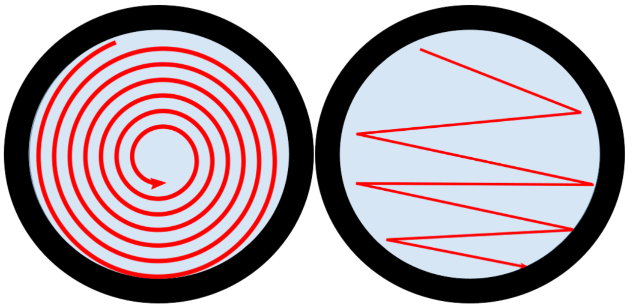

a) b)

Figure A.2 lens cleaning: a) proper way and b) improper way.

- Avoid the usage of spray pressurized air since it leaves a residue that could be difficult to remove.
- Finally do not clean internal optical surfaces such as the camera sensor.

A.1 Photoelastic tomography alignment

The optical devices,described in section 3.1 and shown in Figure 3.2, after being cleaned need to be aligned with the optical axis of the system. In this section the suggested methodology of the optical devices alignment used for the Photoelastic Tomography experiment is presented.

A.1.1 Laser and camera alignment

The first step is to set up the camera and the laser height at the centre of the polarizer and analyser. Once this step is done, the laser is placed in the exit guide line ahead of the camera as shown in Figure A.3. Pictures were taken to know the current state of the laser beam as shown in Figure A.4 a). The adjustments are made until a totally centred beam is reached as

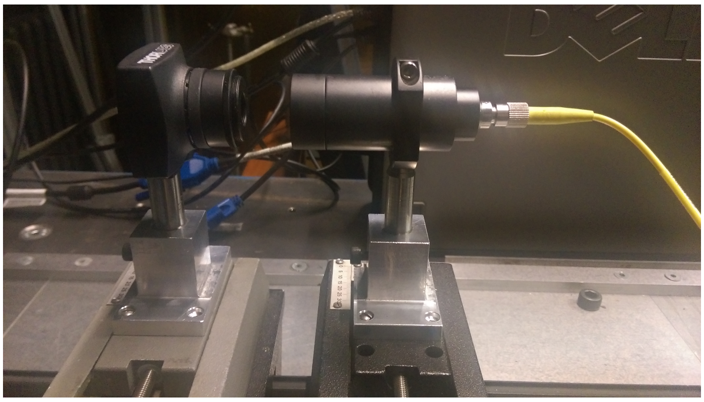

Figure A.3 Laser positioned at the exit of the rig to align it with the camera

shown in Figure A.4 b).
Finally, the laser is placed in the entrance of the apparatus and the camera is positioned in the exit of the apparatus,as shown in Figure 3.2. The procedure to align all the optical devices starts from these references (camera and laser) passing the light beam through the polarizer A.5 a) and analyser A.5 b) centres by the use of a semi opaque screen.

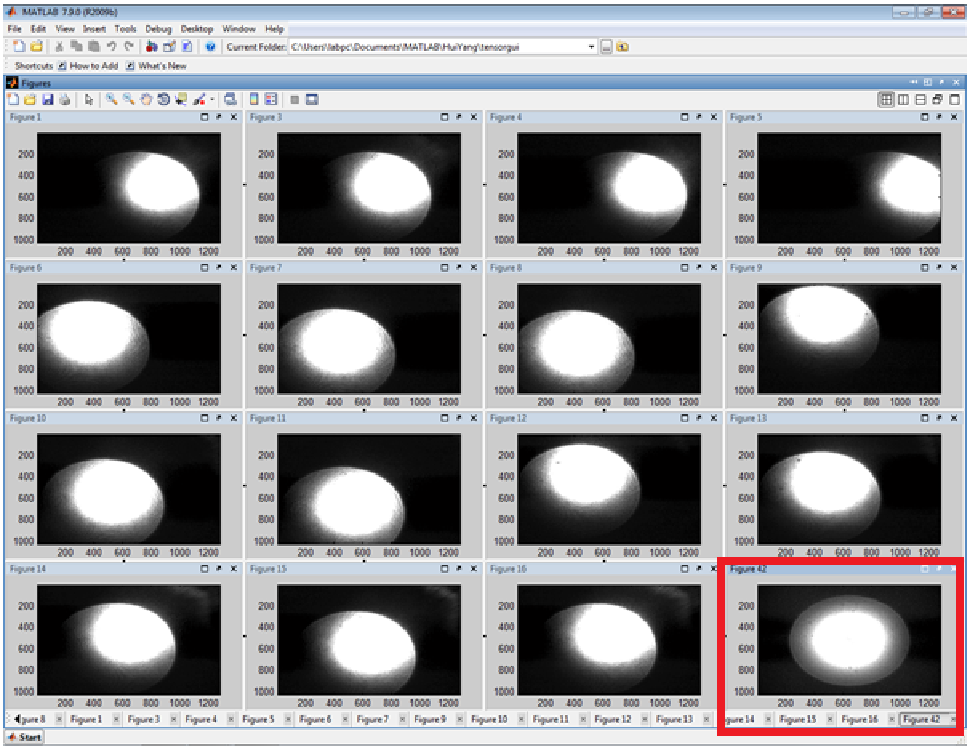

a)

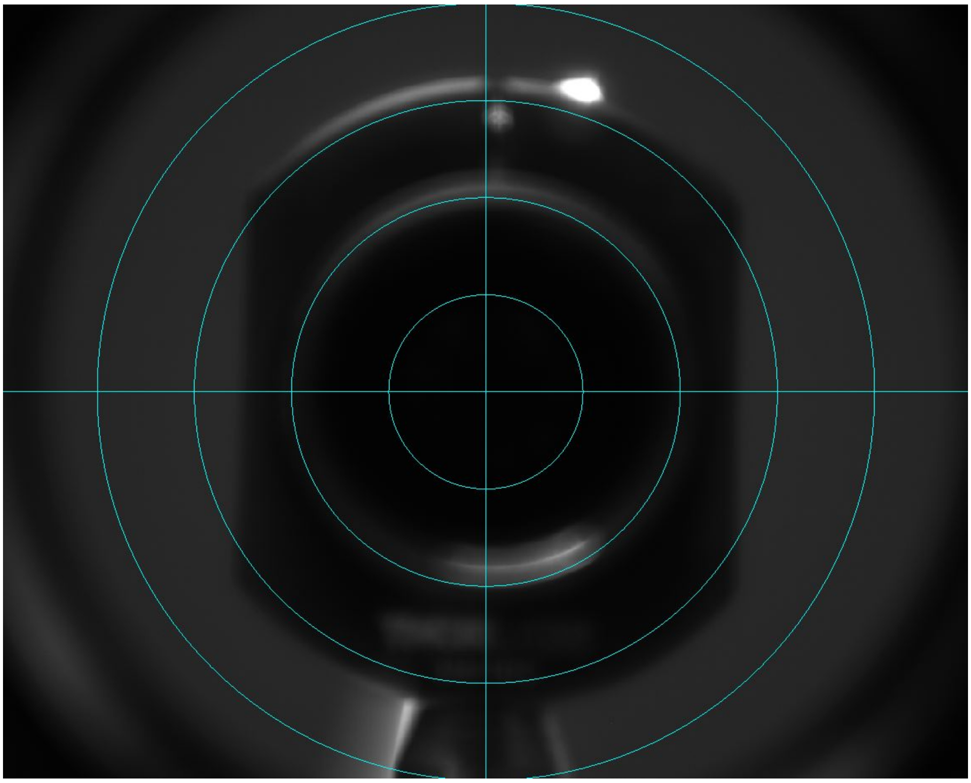

b)

Figure A.4 Images from the camera and the laser alignment procedure where the red window shows an image of the correct alignment, b) Image of the laser and camera alignment result with laser off.

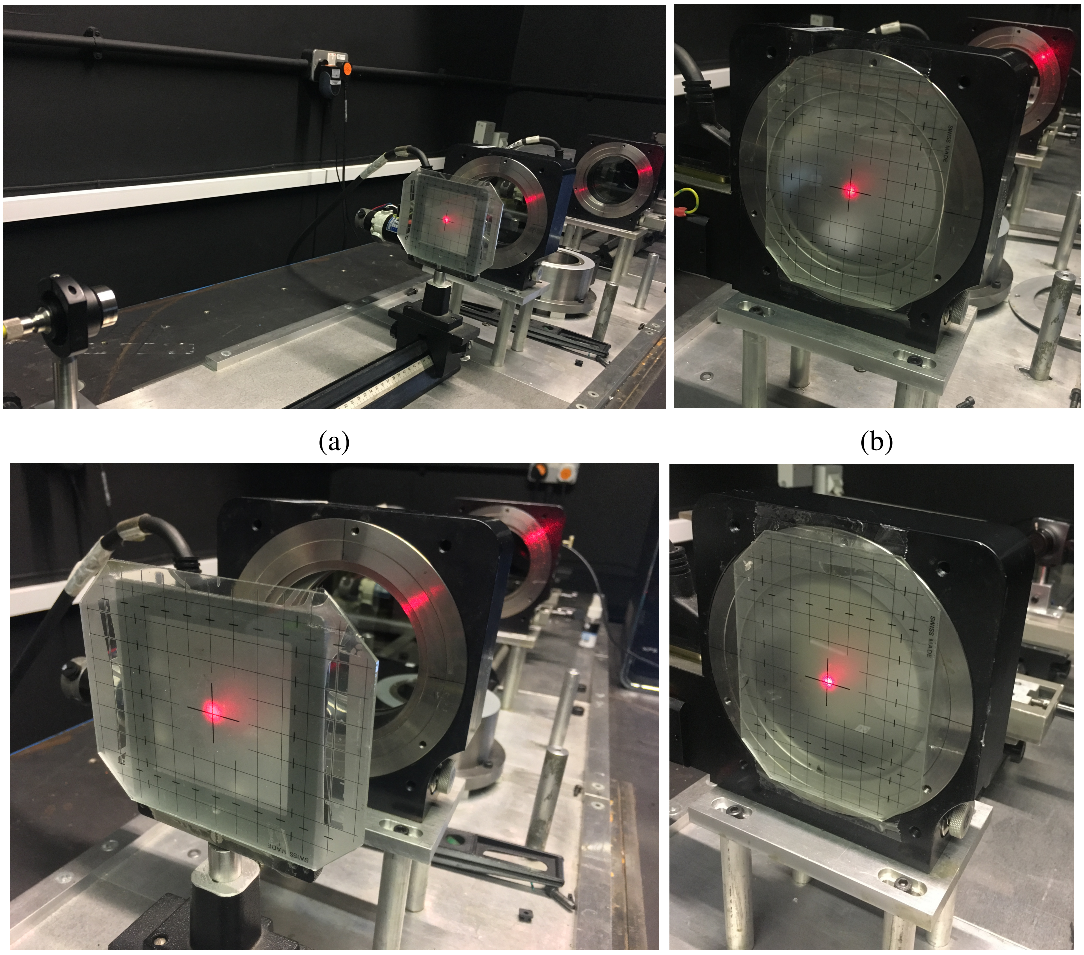

(a) (b)

(c) (d)

Figure A.5 Laser beam path measuring through a) the polariser, b) analyser and c) the second plano-convex lens centre.

A.1.2 Spatial filter:

As mentioned in 3.1 the spatial filter used in the experiment, is composed of by a lens and a pin hole. The procedure to align the spatial filter starts with focusing the lens with the pin hole. To perform this, it is necessary to take the spatial filter out of its base plate, subsequently move the lens along the axis of the point 2 as shown in Figure A.6 a) and then observe through the peephole against a light source until some focused light beam is visible as shown in the Figure A.6 b). Once this is obtained, the screw from Figure A.6 a) needs to be tightened.

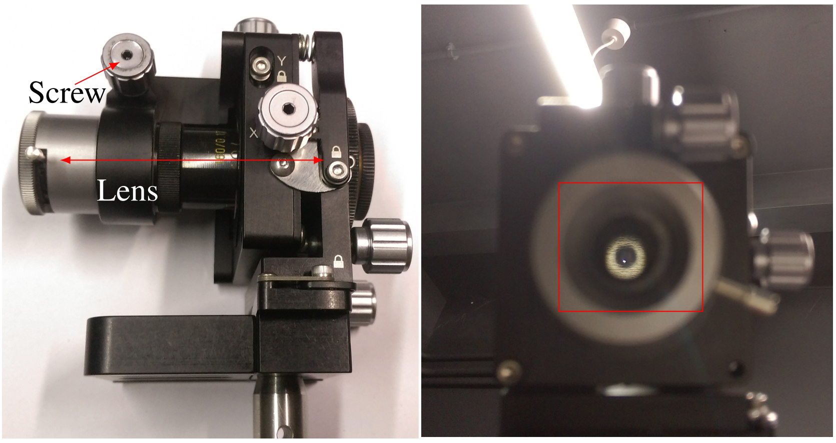

a) b)

Figure A.6 a)Spatial filters lens and screw to fix the lens position,b)Spatial filter lens focused with pin hole.

The next step, is to place the spatial filter in its base plate as shown in Figure A.7 , adjust the height similarly to the laser as shown in Figure A.5.

For the next step the screws X and Y need to be adjusted, presented in Figure A.9 a), until Airy disks are obtained, as shown in Figure A.9. Once the Airy disks are obtained is essential that the screws remain in the same position throughout the experiment.

To remove the Airy disks, the adjustment on the Z axis must be done as displayed in the Figure A.10 a), giving as a result the light beam, Figure A.10 b).

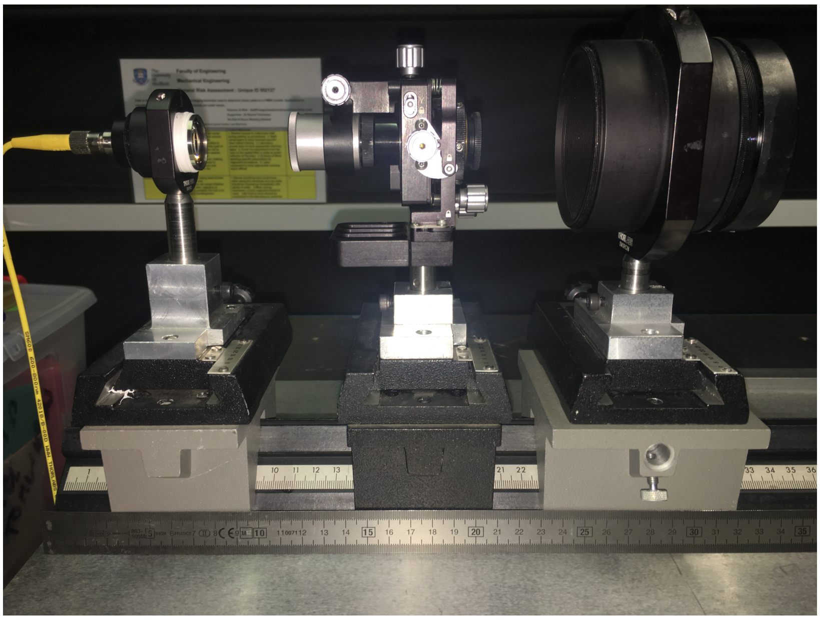

Figure A.7 Spatial filter placed in its base.

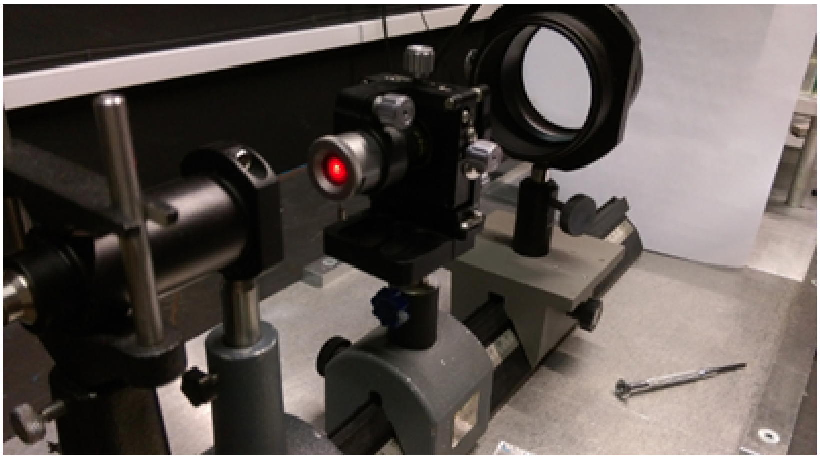

Figure A.8 Spatial filter and laser coincident height.

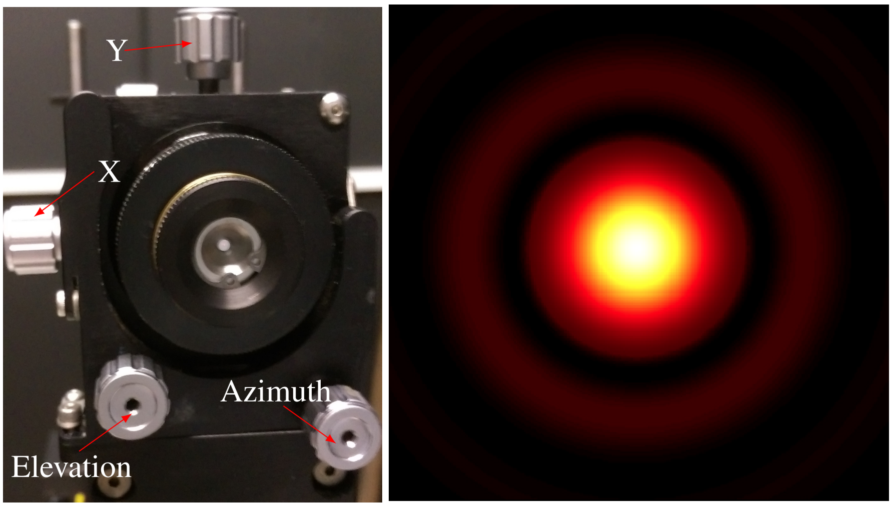

a) b)

Figure A.9 a) Spatial filter screws for : X axis, Y axis, elevation and azimuth axis control, b)Airy disks.

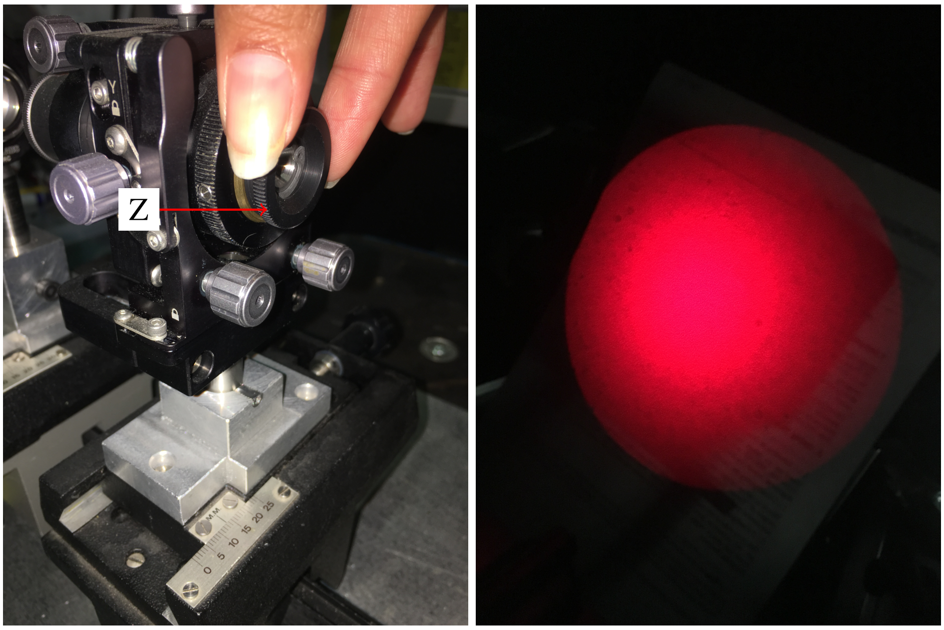

(a) (b)

Figure A.10 a) Z axis adjustment and b) Airy disk elimination.

A.1.3 Lens alignment

The definition of a lens can be stated as a transparent material, which have a curved, plane or both, polished surfaces, that manipulates the light beams to create images. When performing a lens alignment an optical reference axis must be followed, when the position of the devices do not meet this reference axis, a misalignment is the result. The most common misalignments are the translational displacement, tilt, surface tilt error of a spherical surface, cementing error, tilt of the aspherical axis, air gaps and centre thicknesses [113].
Within its system, Photoelastic Tomography has three Plano-convex lenses, which must be aligned concentrically with the polarizer's centre. To achieve this, the lenses heights and positions in the X axis of the base plate must be adjusted.Additionally, it is needed to assure that no tilt variation is present on the lens. To ensure this, a plane surface was used as a reference as shown in FigureA.11. Taking as reference the working table it was possible to adjust the angle of the lenses with the aid of a spirit level as shown in Figure A.12

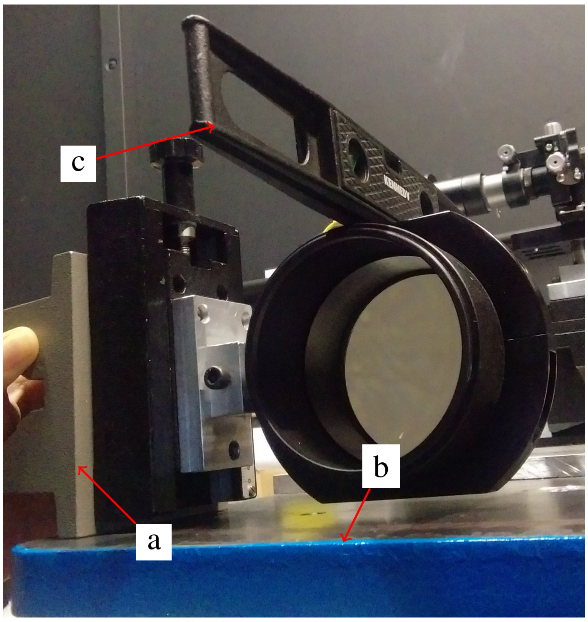

Figure A.11 Lens alignment: a) base plate b) working table c) spirit level.

With the aid of the spirit level, the lens was aligned, as FigureA.12 shows.line width=0.8mm, . After the alignment, the focal length of the lenses must be known. However, in this case no part number identification was found on the lenses used for the Photoelastic Tomography experiment. Measurements of the focal length was made as shown in Figure A.13 giving a result of 15 cm. This technique only recover an approximate focal length. To have a precise focal length it is needed to consider the distance to the lights in the ceiling of the laboratory. However, with this approximate measurement, it was possible to consult the manufacturer

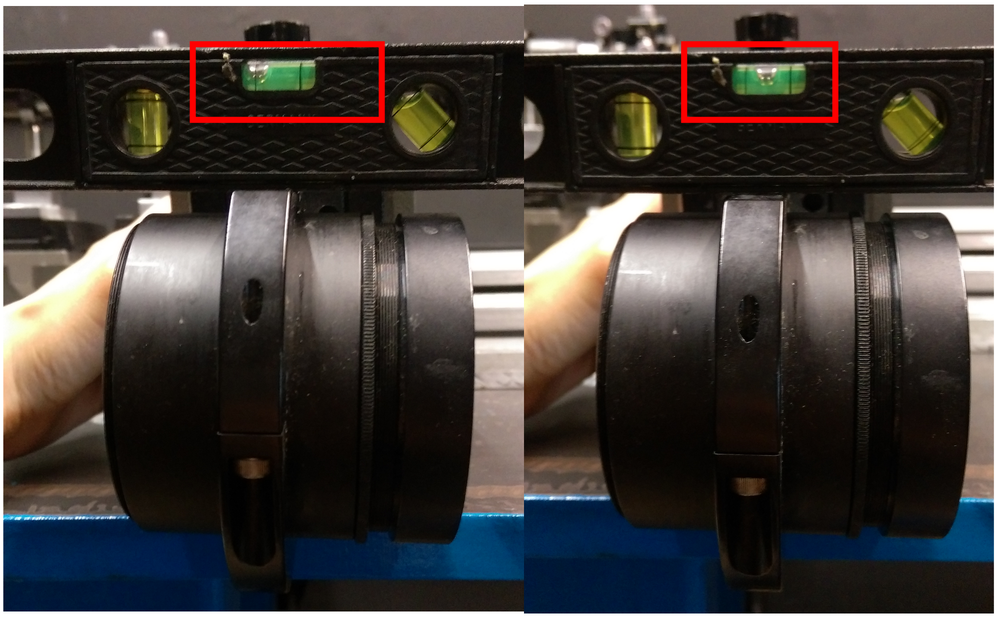

a) b)

Figure A.12 Lens tilt adjustment a) Tilted b) Not tilted.

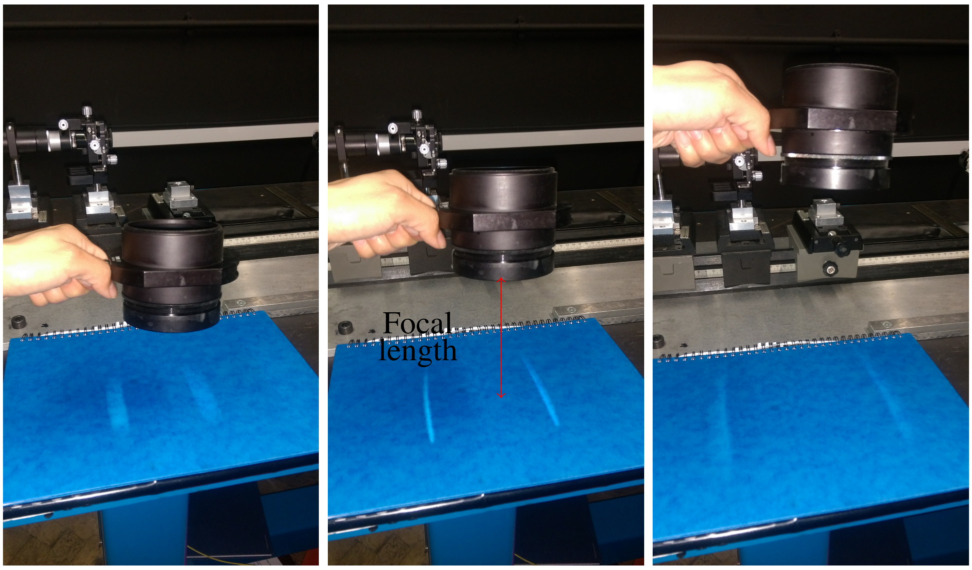

a) b) c)

Figure A.13 Experimental focal lens measurement where a) and c) shows the lens with a not appropriate focal lens due to the blurred lines whereas b) shows defined lines.

specifications to review focal distance of this lens model and make the comparison with what was measured. This measurement matched the model N-BK7 Plano-Convex 75 mm diameter uncoated lenses [114].

A.2 Alignment improvements within the Photoelastic Tomography rig

During the optical devices alignment performed by the experimentalist, it was observed that the optical devices such as the laser were placed in a base plate that did not fit the diameter of their stalk. Variations of the laser height through the optical system were observed when the screw that tights the stalk of the laser was fixed. Figure A.14 shows an overemphasised example.

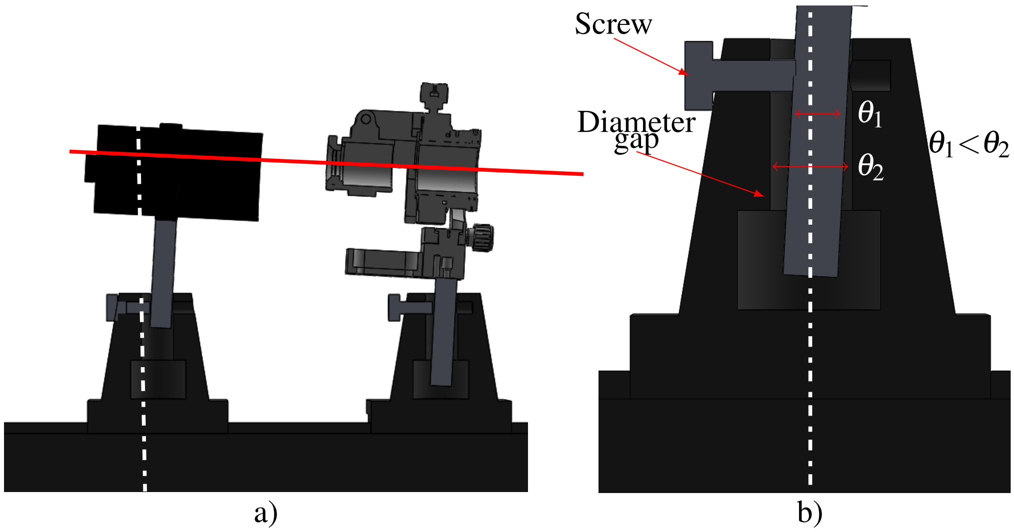

Figure A.14 Laser's base plate with unsuitable diameter

This misalignment was observed when measurements of the height position of the laser beam with a semi opaque screen, before entering and after exiting the polarizers were taken. In order to avoid this variance of approximately 2 mm in "Z" axis, or height, new base plates with a coincident diameter were built as shown in Figure A.15 giving as a result the same height for the laser beam through the system. Even when the previous improvement was implemented, the procedures used in the experimental alignment are not able to be repeated; they are based in lots of assumptions and measurements with tools that cannot assure the consistency of this alignment.

Figure A.15 New base plates with fitting diameter.

Appendix B

Cut and shift program developed by previous research

		How sample moves		Order of size	Formula		
		On paper	On screen				
(x,y)	x > y	LRR	RLL	a > b > c	a=b+c	$\Delta y = \frac{b}{2} = \frac{a-c}{2}$	$\Delta x = \frac{a+c}{2}$
	y > x	LLR	RRL	b > a > c	b=a+c	$\Delta y = \frac{b}{2} = \frac{a+c}{2}$	$\Delta x = \frac{a-c}{2}$
(-x,-y)	|x| > |y|	RLL	LRR	a > b > c	a=b+c	$\Delta y = \frac{b}{2} = \frac{a-c}{2}$	$\Delta x = \frac{a+c}{2}$
	|y|> |x|	RRL	LLR	b > a > c	b=a+c	$\Delta y = \frac{b}{2} = \frac{a+c}{2}$	$\Delta x = \frac{a-c}{2}$
(-x,y)	|x| > y	RLL	LRR	c > b > a	c=a+b	$\Delta y = \frac{b}{2} = \frac{c-a}{2}$	$\Delta x = \frac{a+c}{2}$
	y> |x|	LLR	RRL	b > c > a	b=a+c	$\Delta y = \frac{b}{2} = \frac{a+c}{2}$	$\Delta x = \frac{c-a}{2}$
(x,-y)	x > |y|	LRR	RLL	c > b > a	c=a+b	$\Delta y = \frac{b}{2} = \frac{c-a}{2}$	$\Delta x = \frac{a+c}{2}$
	|y|> x	RRL	LLR	b > c > a	b=c+a	$\Delta y = \frac{b}{2} = \frac{a+c}{2}$	$\Delta x = \frac{c-a}{2}$

Figure B.1 Formulas for determining position for each situation L and R stands for left and right.

Algorithm 1: Cut and shift program developed in previous research part A

Input : Light intensity image acquisition
Output : Cropped and centered light intensity images

```
function imageArr = intensity2characparams(directory) if nargin == 0 directory with
  intensity files
directory = uigetdir('C:\Bill\ImageBank\hlc3a3data\2015_04_23_01');
end
if directory(end)  = filesep
path = [directory filesep];
end
files = dir([path '*.mat']);
nFiles = length(files);
if nFiles == 0
error('No .mat files found')
end
load first file to get dimensions (one var called pic): fileName = files(1).name;
load([path fileName]);
only one axis of rotation for now imageArr = zeros(3, size(pic,1), size(pic,2), nFiles);
warning(['Assuming low res and cropping pic. ' ...
'TODO: figure out how to make thor driver notice subsampling']);
NOTE: see also pic cropping below
we require mod(height,3) == 0:
and height:width = 3:4
imageArr = zeros(3, 120, 160, nFiles);
pic=zeros(382,496,18,uint8);
disp('Warning: using new (non-Hui) folder format to save data'); acquiredate=clock;
folder_base = sprintf('C:\Bill\ImageBank\hlc3a3data\2015_04_23_01', ...
acquiredate(1), ...
acquiredate(2), ...
acquiredate(3));
folder_postfix = 1;
folder_name = sprintf('s_.2d ', folder_base, folder_postfix);
while(exist(folder_name, 'dir'))
folder_postfix = folder_postfix + 1;
folder_name = sprintf(%s_.2d%, folder_base, folder_postfix);
end
mkdir(folder_name);
```

Algorithm 2: Cut and shift program developed in previous research part B

Input : Light intensity image acquisition

Output : Cropped and centered light intensity images

```
r= (Value calculated from equation 4.2 in chapter 3);Put angles in radians!!!
theta= Value calculated from equation 4.3 in chapter 3;
acquiredate=clock;
for n=1:nFiles
nrad=(n-1)*pi/180;
a= (Center of the picture at 45 degrees) + r*sin(theta+(nrad)) -(Width of the
  specimen divided by 2); from 90 and 270 image, work out centre of plate. use
  maximum size of cube to determine start and end points of x values.
c=round(a);
b=Center of the picture at 45 degrees + r*sin(theta+(nrad)) + (Width of the specimen
  divided by 2);
d=round(b);
fileName = files(n).name;
load([path fileName]);
pic = pic(50:323,c:d,:);
acquiredate=clock;
filename = sprintf('%s
pic_%.3d ', folder_name, n);
save(filename, 'pic ');
end
```

Appendix C

Automated cut and shift algorithms

Algorithm 3: Automated cut and shift program using *improfile* function part A

Input : Light intensity image acquisition

Output : Cropped and centered light intensity images

```
I = imread('pic1','png'); Load the converted RGB image og the light intensity
imshow('pic1.png') Show the RGB image.
BW=im2bw(I,0.5); Converts the RGB image to black and white.
x2 = [200 ,600]; Defining the points where the profile picture will be taken.
y2 = [360 ,760]; for the left side of the specimen
improfile(BW,x2, y2); improfile function and the defined points.
h = findobj(gca,'Type','line');
x=get(h,'Xdata');
y=get(h,'Ydata');
P=table((transpose(x)),(transpose(y)));
The next lines perform the iteration of the mean value of the pixels in the previously
  profile defined. When point is out of the mean value, it will be detected as the left
  edge of the specimen.
npoints = 20;
n_after =50;
Left_edge = zeros(3,1);
jj = 1;
for ii=40:size(y,2)-40
data = y(ii:ii+npoints);
mean = sum(data)./npoints;
if y(ii+npoints+1)<mean*0.5
Left_edge(jj) = ii+npoints+1;
iii = ii+npoints+n_after;
jj = jj + 1;
break
end
end
for iii = ii:size(y,2)-40
data = y(ii:ii+npoints);
mean = sum(data)./npoints;
if y(ii+npoints+1)<mean*0.5
Left_edge(jj) = ii+npoints+1;
iii = ii+npoints+n_after;
jj = jj + 1;
break
end
end
for iiii = iii:size(y,2)-40
data = y(ii:ii+npoints);
mean = sum(data)./npoints;
if y(ii+npoints+1)>mean*2
Left_edge(jj) = ii+npoints+1;
break
end
end
```

Appendix D

Camera settings

[Versions]
uc480.dll=4.80.5
uc480.sys=4.80.5
uc480 _boot.sys=4.80.5
[Sensor]
Sensor=C1285R12M
[Image size]
Start X=0
Start Y=0
Start X absolute=1
Start Y absolute=1
Width=1280
Height=1024
Binning=0
Subsampling=0
[Scaler]
Mode=0
Factor=0.000000
[Multi AOI]
Enabled=0
Mode=0
x1=0
x2=0
x3=0
y1=0
y2=0
y3=0
[Shutter]
Mode=0
Linescan number=0
[Timing]
Pixelclock=25
Framerate=14.543796
Exposure=0.576720
[Selected Converter]
IS_SET_CM_RGB32=1
IS_SET_CM_RGB24=1
IS_SET_CM_RGB16=1
IS_SET_CM_RGB15=1
IS_SET_CM_Y8=1
IS_SET_CM_RGB8=1
IS_SET_CM_BAYER=8
IS_SET_CM_UYVY=1
IS_SET_CM_UYVY_MONO=1
IS_SET_CM_UYVY_BAYER=1
IS_CM_CBYCRY_PACKED=0
IS_SET_CM_RGBY=8
IS_SET_CM_RGB30=8
IS_SET_CM_Y12=8
IS_SET_CM_BAYER12=8
IS_SET_CM_Y16=8
IS_SET_CM_BAYER16=8
IS_CM_RGBA8_PACKED=1
IS_CM_RGB8_PACKED=1
IS_CM_RGBY8_PACKED=8

IS_CM_RGB10V2_PACKED=8
[Parameters]
Colormode=6
Brightness=100
Contrast=215
Gamma=1.600000
Hardware Gamma=0
Blacklevel Mode=1
Blacklevel Offset=0
Hotpixel Mode=2
Hotpixel Threshold=0
Sensor Hotpixel=0
GlobalShutter=7
[Gain]
Master=0
Red=0
Green=0
Blue=0
GainBoost=1
[Processing]
EdgeEnhancement=0
RopEffect=0
Whitebalance=0
Whitebalance Red=1.000000
Whitebalance Green=1.000000
Whitebalance Blue=1.000000
Color correction=0
Color_correction_factor=1.000000
Color_correction_satU=100
Color_correction_satV=100
Bayer Conversion=1
[Auto features]
Auto Framerate control=0
Brightness exposure control=1
Brightness gain control=0
Auto Framerate Sensor control=0
Brightness exposure Sensor control=0
Brightness gain Sensor control=0
Brightness exposure Sensor control =0
Brightness gain Sensor control photometry=0
Brightness control once=0
Brightness reference=70
Brightness speed=50
Brightness max gain=100
Brightness max exposure=68.693760
Brightness Aoi Left=0
Brightness Aoi Top=0
Brightness Aoi Width=1280
Brightness Aoi Height=1024
Brightness Hysteresis=2
Brightness Skip Frames=0
Auto WB control=0
Auto WB offsetR=0
Auto WB offsetB=0
Auto WB gainMin=0
Auto WB gainMax=100
Auto WB speed=50
Auto WB Aoi Left=0
Auto WB Aoi Top=0
Auto WB Aoi Width=1280
Auto WB Aoi Height=1024
Auto WB Once=0
Auto WB Hysteresis=2
Auto WB Skip Frames=0
[Trigger and Flash]
Trigger delay=0
Trigger debounce mode=0
Trigger debounce delay time=0
Flash strobe=0
Flash delay=0
Flash duration=0